Towards Isolation of Alkane and CO_2 Complexes

Aaron Insley

Thesis submitted to the University of Nottingham for the degree of Doctor of Philosophy

24th September 2022

0.1 Abstract

Chapter 1

This Chapter gives an introduction to the series of compounds that are investigated and the techniques used in this Thesis. A brief outline of transition metal carbonyl complexes is given along with a brief outline on the main techniques used to detect reactive intermediates. These techniques were: matrix isolation, low temperature solution studies and fast spectroscopic techniques such as time resolved infrared (TRIR). The final part of this Chapter introduces the theory behind computational chemistry.

Chapter 2

The photophysical and photochemical properties of $Co(CO)_3(NO)$ have been probed in Chapter 2, using both picosecond and nanosecond TRIR, run in *n*-heptane at two different excitation wavelengths. These results were compared to a previous study performed by Harris *et al.* in 2008 where they reported a picosecond TRIR experiment on $Co(CO)_3(NO)$ following 400 nm excitation.[1] A clear concentration disparity was observed between our experiments and those reported by Harris. To address this, experiments were performed at both a high and low concentration of $Co(CO)_3(NO)$. There was a clear concentration dependence, with the kinetics of the various photoproducts both forming and decaying much quicker in high concentration experiments when compared with low concentration experiments. $Co(CO)_3(NO)$ displays both CO loss and NO loss upon irradiation of each excitation wavelength used in our experiments which allows for

the observation and assignment of both $Co(CO)_3$ and $Co(CO)_2(NO)$(*n*-heptane) as observed photoproducts. A very tentative reaction pathway was suggested, which includes many unknown species.

The various observed photoproducts whose identity were unknown, were further investigated by density functional theory (DFT). A set of DFT calculations were performed where some possible dimeric structures were geometry optimised and their vibrational frequencies were calculated. These calculated vibrational frequencies were then compared with the observed IR bands from the TRIR experiments and attempted tentative assignments were made to some species.

Chapter 3

In this Chapter, a theoretical investigation into the strength and nature of the binding of weakly coordinating ligands to various organometallic fragments is described with a focus on CO_2 coordination to manganese and rhenium.

Most of the investigated organometallic complexes, both neutral and cationic, are predicted to display η^1-OCO binding between the metal and CO_2. The functionalisation of the organic moiety of the organometallic complexes was found to be more influential for the pianostool complexes than for the α-diimine complexes. The effect of this functionalisation also showed that, due to the nature of η^1-OCO binding of CO_2, the introduction of electron withdrawing groups would increase the metal to CO_2 binding strength, while electron donating groups would decrease the metal to CO_2 binding strength. It was also found that the cationic complexes were found to bind to CO_2 more strongly than neutral complexes. The change in HOMO-LUMO separation between metal fragments and ligands is also investigated where it is found that the lowering in energy of the metal LUMO, in both cationic complexes and complexes containing a greater number of elec-

tron withdrawing groups, allows for better orbital overlap with the HOMO of the CO_2 ligand. It is found that for both pianostool and α-diimine complexes, that rhenium is a better choice of metal than manganese when trying to maximise the metal to ligand bond strength. The various isomers of the octahedral complexes explored, were also investigated to look for trends in different isomer stability. It was found that for both cationic and neutral complexes, a stronger metal to CO_2 bond is formed when the CO_2 is located *cis* to the bpy ligand.

A large number of calculated vibrational frequencies of CO_2 bound complexes are also reported in this Chapter, along with corresponding bond lengths, which may act as benchmarks for other calculations and also allow for comparison to future experimental work.

Chapter 4

In this Chapter, the synthesis and characterisation of a range of group seven organometallic complexes is described with a focus on rhenium pianostools and α-diimine complexes.

The synthesis of $[BnMn(CO)_3][OTf]$, $[(Mes)Re(CO)_3][PF_6]$, $[(HMB)Re(CO)_3][PF_6]$ (HMB = Hexamethylbenzene) and $[(HEB)Re(CO)_3][PF_6]$ (HEB = Hexaethylbenzene) are reported. Anion exchanges with $[Al(OC(CF_3)_3)_4]^-$ were attempted on the isolated complexes, but all had issues.

The synthesis of a series of neutral rhenium α-diimine complexes, $[(bpy)Re(CO)_3Cl]$, $[(dmbpy)Re(CO)_3Cl]$, $[(dtbpy)Re(CO)_3Cl]$, $[(dfbpy)Re(CO)_3Cl]$, $[(dnb\text{-}F_{34})Re(CO)_3Cl]$ and $[(dnb\text{-}F_{34})Re(CO)_3Br]$ is reported. The synthetic route for the dfbpy ligand is reported along with the synthesis and characterisation of the dnb-F_{34} ligand. $[(dnb\text{-}F_{34})Re(CO)_3Cl]$ was

photolysed in THF, but CO loss was not easily induced, owing to the aggregation of the fluorinated chains present on the dnb-F_{34} ligand. [(dnb-F_{34})Re(CO)$_3$Cl] was found to be soluble in liquid CO_2, but the observed peaks displayed very minimal absorbance due to solubility limitations.

The synthesis of a series of a cationic rhenium α-diimine complexes, [(bpy)Re(CO)$_4$][OTf], [(dmbpy)Re(CO)$_4$][OTf], [(dtbpy)Re(CO)$_4$][OTf] and [(dfbpy)Re(CO)$_4$][OTf] are reported. The synthesis of [(dnb-F_{34})Re(CO)$_4$][OTf] was also attempted, but could not be isolated in a pure form. A matrix isolation experiment on [(dtbpy)Re(CO)$_4$][Al(OC(CF$_3$)$_3$)$_4$] in a polyethlyene disc was performed in CO_2 and two main features were noted which were the growth of an extra peak at 2270 cm^{-1} and the rotational restriction of CO_2. Further experiments were then performed to better understand these observations, which included an identical experiment on a blank polyethlyene disc where both these features were observed again and the photolysis of [(dtbpy)Re(CO)$_4$][Al(OC(CF$_3$)$_3$)$_4$] in a polyethlene disc under an N_2 atmosphere where no observation of a coordinated N_2 band could not be made. [(dmbpy)Re(CO)$_4$][PF$_6$] was photolysed in THF and a noticeable difference in photostability between the cationic and neutral complexes was observed.

Some preliminary work involving using ionic liquids as a cosolvent to aid in solubility of organometallic complexes in non-polar, non-coordinating solvents was performed and the key features of the FTIR spectra were noted. Based on these results there is potential for this area to develop further but more work would be needed on synthesis of a less coordination ionic liquid and removal of water from ionic liquids.

Chapter 5

The summaries and future work of the results obtained from the work in this Thesis are given in this Chapter. These discuss the implications that have arisen from these results and areas of research that could be investigated in the future.

Chapter 6

The experimental methods and spectroscopic techniques used throughout this Thesis are described in this Chapter. This includes detailed descriptions of the equipment, along with procedures and materials used.

0.2 Acknowledgements

First and foremost I would like to thank Professor Michael George for all his constant support and endless patience with me throughout my PhD. He has been there for me both academically but also provided me with a much needed morale boost whenever it was needed. I also thoroughly enjoyed the numerous conversations about music and teaching him about the wonderful world of metal.

I also must individually thank Dr Ashley Love for his extensive help with interpreting spectra, matrix experiments and helping with all the work involving CO and CO_2 in Chapter 4. I need to also thank Dr Surajit Kayal for his incredible amount of help with all my TRIR data in Chapter 2 and his aid in helping me understand anything to do with excited states. Extra thanks must also go to Dr David Tiemessen for all his help with MATLAB scripts, Dr Johnny Moore for his help with purification of the fluorinated ligand and Dr Magnus Hanson-Heine for helping with any queries I had on DFT. The final postdoc I would like to thank is Dr Katherine Reynolds for her helpful suggestions when I was having various synthetic issues and her help with all the various risk assessments and COSHH forms.

I would like to thank Agata for all her help when I first joined the group and Nasiru for teaching me about the disc making process for matrix isolation. I would also like to thank the rest of the Fort; Xue, Jorge, Taran, Ed, Bijol, Gen, Matt, Andrew and Nat over the four years for being fantastic company and all their various bits of help here and there. My project students both Jen and Chloe should also be both thanked and applauded for being able to deal with me for a whole year!

My thanks must also go to Matthew McAdam, Clive Dixon, Conor Bennett and the rest of the workshops for all their help in repairing the various pieces of equipment that were broken due to my clumsiness. My thanks go to Shaz for entrusting me access to the special 500 MHz NMR machine to enable me to get ^{13}C NMR of my ligand and to Ben from the Mass Spec team for helping me to

identify mysterious peaks in the mass spectra.

Additional thanks must go to Professor Johnathan McMaster for his help with ADFinput and both helpful and enjoyable discussions towards the end of my third year. Extra thanks must also go to Professor Martyn Poliakoff for helpful discussions in my first year.

Most importantly I would like to thank my friends and family, especially my parents, for their endless and continuous morale support during these four years. They have been the main reason I am still (somewhat) sane after this PhD.

Lastly I'd like to thank the University of Nottingham for access to their high performance computing service.

0.3 Abbreviations

BDE	- bond dissociation energy
Bn	- benzene, η^6-C_6H_6
bpy	- 2,2'-bipyridine
BSSE	- basis set superposition error
Cp	- cyclopentadienyl, η^5-C_5H_5
Cy	- cyclohexyl
dfbpy	- 4,4'-perfluorodimethyl-2,2'-bipyridine
dftbpy	- 4,4'-bis(1,1,1,3,3,3-hexafluoro-2-(trifluoromethyl)propan-2-yl)-2,2'-bipyridine
DFT	- density functional theory
diars	- 1,2-bis(dimethylarsino)benzene, $C_6H_4(As(CH_3)_2)_2$
dmbpy	- 4,4'-dimethyl-2,2'-bipyridine
dtbpy	- 4,4'-di-tert-butyl-2,2'-bipyridine
dnb-F_{34}	- 4,4'-bis [1H,1H,2H,2H,3H,3H-perfluoroundecyl]-2,2'-bipyridine
dnb-F_{42}	- 4,4'-bis [1H,1H,2H,2H,3H,3H-perfluorotridecyl]-2,2'-bipyridine
ECP	- effective core potential
FTIR	- fourier transform infrared
HEB	- hexaethylbenzene
HMB	- hexamethylbenzene
HOMO	- highest occupied molecular orbital
LUMO	- lowest unoccupied molecular orbital
Mes	- 1,3,5-trimethylbenzene
MLCT	- metal to ligand charge transfer
MO	- molecular orbital
MOM	- maximum overlap method
OTf	- trifluoromethanesulfonate
PES	- potential energy surface
PFMCH	- perfluoromethylcyclohexane
PFTEA	- perfluorotriethylamine
TRIR	- time-resolved infrared
ν(C-O)	- carbonyl stretching vibration

Table of Contents

Chapter 1

Introduction

The work reported in this Thesis focuses on working towards the isolation of long-lived alkane and CO_2 organometallic complexes. This is done by generating a reactive intermediate by dissociation of a CO ligand from an organometallic carbonyl complex *via* UV-Vis photolysis. These resulting reactive species can then form a reactive solvent or dopant complex. The mechanism of these reactions can often seem simple, but complicated mechanistic pathways involving a large number of different reactive intermediates are often involved.

Many photochemically-generated species are extremely reactive and have lifetimes on the fast and ultrafast timescale ($<<$1 s at room temperature).[2] These timescales are too short for detection using conventional laboratory techniques and analytical techniques and as such investigation of these species raises a challenge. There are a number of ways in which these compounds can still be studied by use of either ultrafast spectroscopy or utilising realtime techniques where the reaction is slowed down. Both of these concepts are covered in this introduction.

Much of the experimental work in this Thesis is complemented by DFT calculations to support or aid with spectroscopic assignments and this was initiated due to changes imposed due to the COVID pandemic. Computational chemistry, specifically DFT, is a very powerful tool that has changed the way people can think about and undertake chemistry. This section briefly introduces computational chemistry as a technique and covers the different methods and functionals

used in this Thesis.

All the species investigated in this work, both theoretically and experimentally, are organometallic carbonyl complexes. This family of compounds are briefly introduced in this Chapter.

1.1 Transition Metal Carbonyl Complexes

This type of species is often used in organic chemistry as a catalyst or as a catalyst precursor and are usually quite toxic.[3,4] The carbonyl ligand makes for a remarkably useful reporter ligand in FTIR spectroscopy, due to the fact the carbonyl region for organometallics appears mostly between 1850 to 2250 cm^{-1}, which does not clash with many popular organic solvents.[5–10] This is one of the reasons why the carbonyl ligand is a popular spectroscopic reporter group in organometallic chemistry.[11,12]

Another one of the main reasons carbonyls are so useful for FTIR analysis, is the nature of their bonding to the metal centre. The carbonyl ligand engages in "synergic" bonding with the metal centre. There is a σ bond formed from the overlap of the nonbonding sp-hybridised electron pair on carbon and the metal orbitals. A π bond also arises from overlap between the filled metal d-orbitals and the carbonyl π^* orbitals. The electron density from the metal orbitals being donated into the carbonyl π^* orbitals, π back donation, requires that both the metal has d electrons and that it is also in a relatively low oxidation state ($<$ +2) otherwise it will not be sufficiently favourable. A schematic overview of this synergic bonding can be seen in Figure 1.1. As the back donation fills up the C-O π^* orbital this weakens and therefore lengthens the C-O bond while strengthening the M-C bond.[13–18] This change in carbonyl bond strength and length is reflected in the IR spectrum of these complexes. If the back-bonding is happening with an electron rich metal centre there will be a red shift in the band position. This red shift occurs because there will be a greater electron density in the π^* orbital from the metal, therefore weakening the C-O bond. If the C-O bond is weaker,

it will therefore have a lower force constant, which means that it will vibrate at a lower wavenumber and hence absorb longer wavelengths of IR radiation, which are lower in energy. The reverse is also true where if back-bonding is occuring with a more electron deficient metal centre, there will be a blue shift in the band position. This effect can be invaluable when probing excited states of carbonyl complexes, as the shifting can reflect the nature of charge transfers.

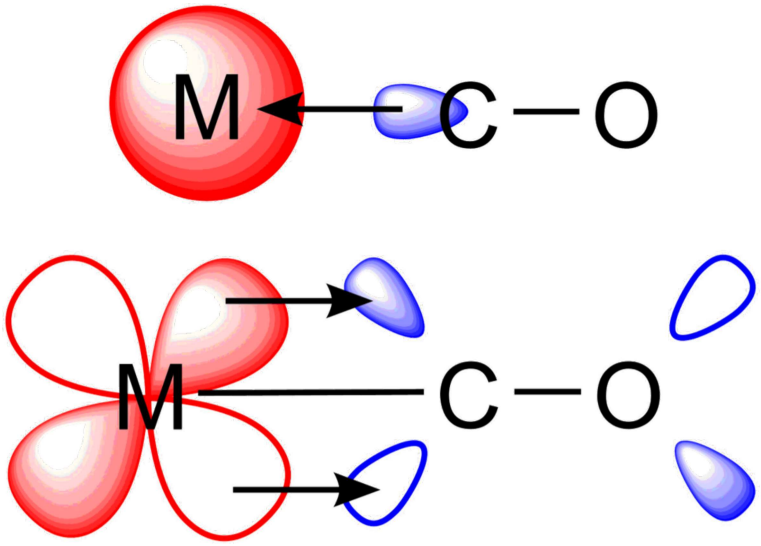

Figure 1.1: A schematic orbital diagram showing the synergic bonding found between metals and carbonyl ligands.

As two of the Chapters in this Thesis have a focus on transition metal carbon dioxide carbonyl complexes, this section will briefly talk about using IR spectroscopy to probe carbon dioxide coordination in a similar way to that of CO in metal carbonyl complexes.

Free CO_2 is a linear molecule that exhibits three fundamental modes, two of which are IR active. There is a degenerate band at 667 cm^{-1} and an antisymmetric stretch at 2349 cm^{-1}. The bands for free CO_2 and for coordinated CO_2 will be at different wavenumbers and may also occur at different frequency depending on the coordination mode. In both η^1-C and η^2-C,O coordination modes the CO_2 is bent and as such the expectation is to find the IR band closer to that of the $CO_2^{\cdot -}$ radical anion around 1671 cm^{-1}. In the η^1-O end-on coordination, the CO_2 is more linear and you would expect to find the band much closer to that of

free CO_2. In the study of [(1,4,7-tris(3-adamantyl-5-tert-butyl-2-hydroxybenzyl)-1,4,7-triazacyclononane)U(CO_2)], covered in the introduction of Chapter 3, an η^1-O end-on coordination complex was isolated, the CO_2 band was reported at 2188 cm^{-1}.[19] In many cases, CO_2 coordinated complexes are synthesised while solubulised in CO_2, which will have a very broad solvent band in the IR and may hide any bands around 2188 cm^{-1}. Coordination of CO_2 would make the IR-inactive symmetric stretch of free CO_2 become active. This is because after coordination, the symmetric stretch would still result in a change of dipole moment on the CO_2. This band would expect to be found around 1480 cm^{-1}.

1.2 Detection of Reactive Intermediates

There are two main principles that can be used in order to make these reactive intermediates easier to probe. The first is to increase the lifetime of the intermediate by slowing down its reactions to the point they can be probed with more conventional laboratory spectroscopic techniques. This forms the basis of the idea of matrix isolation and low temperature solution studies. The other principle is to use fast spectroscopic techniques, where the intermediate is created and then probed almost instantly before it has chance to return to its initial state.

1.2.1 Matrix Isolation

Matrix isolation uses the principle of increasing the lifetime of the photoproducts of interest in a rigid matrix of inert material at cryogenic temperatures. Due to the low temperatures, the reactive intermediates and excited states recombine and relax at a much slower rate, compared to those at room temperature, allowing for investigation using conventional laboratory spectroscopic techniques, such as IR spectroscopy.[20] A large variety of materials have been reported as suitable matrices including noble gases, frozen hydrocarbons and polymers.[21–26] Due to the intense and distinctive nature of carbonyl bands in IR spectroscopy this

combination of methods for investigation of the photochemistry of organometallic carbonyls is particularly powerful as low concentrations of intermediates can be detected.

Matrix isolation does have some disadvantages. Firstly, some matrices, usually hydrocarbon-based, can have intense IR bands, which can hide the IR bands belonging to the compounds of interest. This can be avoided by use of noble gas matrices as these have no IR bands of their own, however noble gases have their own limitations such as their melting points and their low solubilising ability. It has also been reported that sometimes photogenerated reactive intermediates can interact with the matrix, which changes the mechanism of the reaction being probed.[27]

1.2.2 Low Temperature Solution Studies

Low temperature solution studies have also been widely used to increase the lifetime of unstable photogenerated species.[28] Liquefied noble gases, CO_2, alkanes and perfluorinated alkanes are common solvents for these studies as they are relatively inert and non-coordinating. In the solution phase, the compounds of interest can move in the solvent media, which allows for use of conventional analytical techniques such as FTIR and NMR spectroscopy to be used for characterisation.[29–32]

The primary limitation of this technique is that the solubility of many compounds are very limited in these solvents. This means the photogenerated compounds of interest are limited to those with soluble parent compounds and can only be formed in very low concentrations, which can often not be high enough to be probed by spectroscopic techniques. To solve this issue, new synthetic approaches can be utilised to modify the structure of compounds, while leaving their electronic nature unaltered, to improve their solubility.[33–35] The synthetic attempts in this work are covered in Chapter 4 of this Thesis. Large numbers of CF_2 groups are added to a ligand to increase solubility in CO_2, while using

a number of CH_2 groups to create distance between fluorinated chain and the remainder of the ligand.

1.2.3 Fast Spectroscopic Techniques

Often given the name 'pump-probe' techniques, these fast spectroscopic techniques involve photochemically exciting the complex (the pump) followed by another photon after a small delay (the probe), which gathers the information on the excited sample. Due to the typical lifetimes of the species in this type of work, time-resolved nanosecond and picosecond spectroscopy are popular techniques.[36,37] Additionally, because of the previously mentioned complementary nature of carbonyl chemistry and vibrational spectroscopy time-resolved infrared spectroscopy can be a powerful tool. A schematic setup for this technique is given in Figure 1.2.

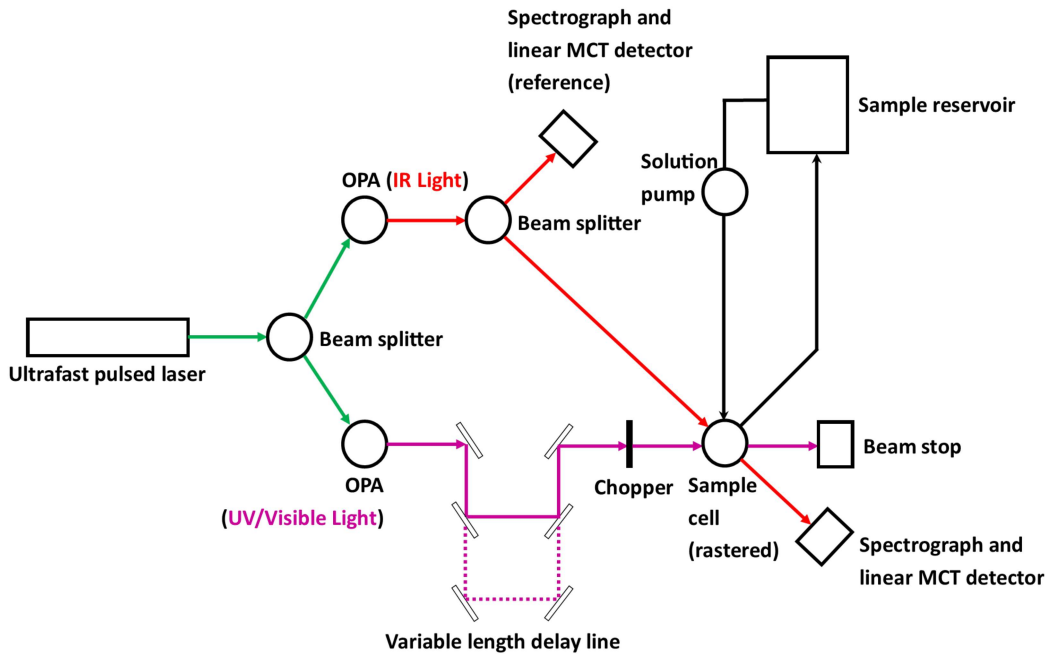

Figure 1.2: A schematic setup for a TRIR experiment similar to the one used at Nottingham. The UV-pump pulse goes along the bottom and the IR probe pulse goes along the top of the diagram.

Here, a pulsed laser leading to a beam splitter to release two rays of light is described. On the bottom of the diagram in Figure 1.2 there is the pump beam, this first goes to an optical parametric amplifier (OPA), which gives the

desired wavelength of light (usually in the UV/Vis region). This beam then enters a variable length delay line where the time difference between the pump beam hitting the sample and the probe beam analysing the sample is tuned. This beam then leads to a chopper which rotates at half the time difference between the laser pulses to help isolate just an excited state spectrum. This beam then leads into the sample cell and is stopped by a beam stop. On the top of the diagram in Figure 1.2 there is the probe pulse, which also first goes to an OPA to give the desired IR wavelength of light. This IR light then leads to a beam splitter where one beam goes to a detector, this is used as a reference so it is possible to correct for any differences in the beam due to things like power fluctuations. The other beam goes to the sample cell, which is scanned in a rastered fashion to avoid damage to the CaF_2 cell, and then the light finally hits another detector where the excited state signal is detected.

1.3 Computational Theory

1.3.1 The Shrödinger Equation

The time-independent Shrödinger wave equation is the cornerstone of modern theoretical chemistry and accounts for the quantum mechanical behaviour of molecular and atomic systems. It takes the mathematical form

$$\hat{H}\Psi = E\Psi \tag{1.1}$$

where $\hat{H}$ is the Hamiltonian operator for the system, E is the energy and Ψ is the wavefunction or eigenfunction, containing the coordinates of all the components that make up the system from which all observable properties may be extracted.

The form of the molecular Hamiltonian is given by the sum of the nuclear kinetic energy, $\hat{T}_N$, nuclei-nuclei repulsion, $\hat{V}_{NN}$, electronic kinetic energy, $\hat{T}_e$, electron-nuclei attraction, $\hat{V}_{Ne}$, and electron-electron repulsion, $\hat{V}_{ee}$, potential en-

ergies

$$\hat{H} = \hat{T}_N + \hat{V}_{NN} + \hat{T}_e + \hat{V}_{Ne} + \hat{V}_{ee} \tag{1.2}$$

which when written in atomic units can be written as

$$\hat{H} = -\sum_I \frac{1}{2M_I}\nabla_I^2 + \sum_I \sum_{J>I} \frac{Z_I Z_J}{|R_I - R_J|} - \sum_i \frac{1}{2}\nabla_i^2 - \sum_i \sum_I \frac{Z_I}{|r_i - R_I|} + \sum_i \sum_{j>i} \frac{1}{|r_i - r_j|} \tag{1.3}$$

where M_I and Z_I are the nuclear masses and charges, respectively, and $R_I - R_J$, $r_i - R_I$ and $r_i - r_j$ are the differences between the particle positions where i and j label electrons and I and J label nuclei. ∇^2 is defined in Cartesian coordinates by

$$\nabla^2 = \frac{\delta^2}{\delta x^2} + \frac{\delta^2}{\delta y^2} + \frac{\delta^2}{\delta z^2} \tag{1.4}$$

1.3.2 The Born-Oppenheimer Approximation

The molecular wavefunction, Ψ, is a function of the positions of all nuclei and electrons in a given system. The Born-Oppenheimer approximation allows for the separation of the nuclear and electronic structure based on the assumption that the nuclei within a molecule are stationary compared to the electrons and that the electrons can respond to changes in nuclear potential instantaneously.[38] This is true as nuclei are much heavier than electrons and as a result the nuclei move much more slowly than the electrons. Quantum chemistry is mostly concerned with the electronic Hamiltonian and the electronic Shrödinger equation and as such the Hamiltonian takes the form

$$\hat{H}_{elec} = -\sum_i \frac{1}{2}\nabla_i^2 - \sum_i \sum_I \frac{Z_I}{|r_i - R_I|} + \sum_i \sum_{j>i} \frac{1}{|r_i - r_j|} \tag{1.5}$$

The full wavefunction depends on the coordinates of all nuclei and electrons

but within the Born-Oppenheimer approximation the wavefunction is a product of nuclear and electronic wavefunctions where the electronic wavefunction is defined for a fixed set of nuclear coordinates as shown in Equation 1.6.

$$\Psi(R,r) = \Psi_{nuc}(R)\Psi_{elec}(R;r) \tag{1.6}$$

1.3.3 Hartree-Fock Theory

The simplest *ab initio* quantum chemical method for solving the Shrödinger equation is Hartree-Fock theory, which is based upon constructing the electronic wavefunction for a many-electron system as a product of one-electron independent wavefunctions, or molecular orbitals.[39] These wavefunctions are dependent on both spatial and spin components

$$\chi^{\uparrow}(x) = \psi(r)\alpha(\omega) \tag{1.7}$$

$$\chi^{\downarrow}(x) = \psi(r)\beta(\omega) \tag{1.8}$$

The majority of studies are performed on closed-shell systems that have electrons of opposite spin paired together with the same spatial components. If just these situations are considered, this leads to restricted Hartree-Fock theory.

To construct a many-electron wavefunction from a set of molecular orbitals a product of orbitals can be used, which is known as a Hartree product that can be expressed as

$$\Psi(x_1,x_2) = \chi_1(x_1)\chi_2(x_2) \tag{1.9}$$

However, this product does not obey the Pauli exclusion principle, which states that the total wavefuction must be anti-symmetric with respect to the interchange of any pair of electrons. This wavefunction must be anti-symmetrised by considering a linear combination of products, which for two electrons can be

written as

$$\Psi(x_1, x_2) = \chi_1(x_1)\chi_2(x_2) - \chi_1(x_2)\chi_2(x_1) \tag{1.10}$$

and now if two electrons are interchanged the Pauli principle is obeyed. The anti-symmetrized form of the wavefunction can be expressed as a determinant which for the two electron case is

$$\Psi(x_1, x_2) = \begin{vmatrix} \chi_1(x_1) & \chi_2(x_1) \\ \chi_1(x_2) & \chi_2(x_2) \end{vmatrix} \tag{1.11}$$

This type of wavefunction is known as a Slater determinant and is an expression that describes the wavefunction of a multi-fermonic system that satisfies anti-symmetry requirements and consequently, the Pauli principle upon exchange of two electrons.[40] Hartree-Fock theory uses a Slater determinant for N-electron wave functions which take the form

$$\Psi_{HF}(x_1, x_2, ..., x_N) = \frac{1}{\sqrt{N!}} \begin{vmatrix} \chi_1(x_1) & \chi_2(x_1) & ... & \chi_N(x_1) \\ \chi_1(x_1) & \chi_2(x_2) & ... & \chi_N(x_2) \\ \vdots & \vdots & & \vdots \\ \chi_1(x_N) & \chi_2(x_N) & ... & \chi_N(x_N) \end{vmatrix} \tag{1.12}$$

Upon using this wavefunction in the electronic Shrödinger equation an expression for the electronic energy containing terms corresponding to the kinetic energy of the electrons is found to be

$$E_T = \frac{1}{2} \sum_{i=1}^{N} \int \phi_1^*(r) \nabla_i^2 \phi_i(r) dr \tag{1.13}$$

The expression for the attraction between electrons and nuclei is

$$E_{Ne} = -\sum_{i=1}^{N} \sum_{I=1}^{M} Z_I \int \frac{\phi_i^*(r)\phi_i(r)}{|r_i - R_I|} dr \tag{1.14}$$

A term corresponding to the classical Coulomb expression for each electron

interacting with each of the the other electrons of the form

$$E_{ee} = \frac{1}{2}\sum_{i=1}^{N}\sum_{j=1}^{N}\int\int \frac{\phi_i^*(r_1)\phi_i(r_1)\phi_j^*(r_2)\phi_j(r_2)}{|r_i - r_j|}dr_1 dr_2 \tag{1.15}$$

This evaluation of electron-electron interactions is the most time-consuming part of a Hartree-Fock calculation. There is an additional term, known as the exchange energy, which is a purely quantum effect that arises when two or more electrons with the same spin exchange their positions in the degenerate orbitals of a subshell. When the orbitals are half-filled or completely filled then the number of exchanges is maximum. Therefore, the systems stability is maximum. The effect of exchange is that in order to avoid occupying the same physical state, electrons are repelled even more strongly than predicted by the Coulomb force, and the net effect is to slightly push apart the electron density clouds, thus slightly decreasing their repulsion energy because they are further apart. This exchange energy has the form

$$E_X = -\frac{1}{2}\sum_{i=1}^{N}\sum_{j=1}^{N}\int\int \frac{\phi_i^*(r_1)\phi_j(r_1)\phi_j^*(r_2)\phi_i(r_2)}{|r_i - r_j|}dr_1 dr_2 \tag{1.16}$$

There is an additional nuclear-nuclear repulsion energy term, which can be accounted for by

$$E_{NN} = \sum_{I}\sum_{J>I}\frac{Z_I Z_J}{|R_I - R_J|} \tag{1.17}$$

This E_{NN} term is a constant thanks to operating under the Born-Oppenheimer approximation where nuclei within a molecule are stationary. E_{NN} may be easily calculated based on fixed nuclear charges and positions and simply added to the final energy.

Closed-shell systems possess electrons of opposite spin paired together with the same spatial components as described above. They are often treated by assuming that there is just one set of doubly-occupied orbitals, which is characteristic of the restricted Hartree-Fock method. It is possible to allow the spatial

component of an orbital with α-spin to be different from the spatial component of an orbital with β-spin, which leads to unrestricted Hartree-Fock theory. This is crucial for calculations on radical or ion species. From equations 1.7 and 1.8 it can be seen that in restricted Hartree-Fock theory the spin-orbitals, $\chi(x)$, have the same spatial orbital, $\psi(r)$, for up and down spin electrons, but for unrestricted Hartree-Fock theory, the up and down spin electrons have their own different spatial orbitals shown in Equations 1.18 and 1.19.

$$\chi^{\uparrow}(x) = \psi^{\uparrow}(r)\alpha(\omega) \tag{1.18}$$

$$\chi^{\downarrow}(x) = \psi^{\downarrow}(r)\beta(\omega) \tag{1.19}$$

Equations in Hartree-Fock theory are solved in an iterative process that minmises the energy, allowing an approximate wavefunction and electronic energy to be determined. However, in Hartree-Fock theory equation 1.15 is solved in such a way that each electron only sees an averaged potential of the other electrons. This introduces a minor error which is known as correlation energy, E_C

$$E_C = E_{exact} - E_{HF} \tag{1.20}$$

where E_{exact} is the exact-non-relativistic energy within the basis set used. Despite the correlation energy accounting for a very small percentage of the total energy the correct calculation of this energy can be important as interactions between electrons are a very important quantity when investigating chemical behaviour. There are multiple methods that go beyond the Hartree-Fock method to calculate the correlation energy the most popular by far is DFT which is the focus of the work in this Thesis.

1.3.4 Roothaan-Hall Equations

To solve the Shrödinger equation by minimising the total energy each atomic orbital can be expressed as a linear combination of K basis functions, ϕ, each multiplied by an MO coefficient.

$$\psi_i(r) = \sum_{\nu=1}^{K} C_{\nu i}\phi_\nu(r) \tag{1.21}$$

where the MO coefficient can be expressed as a matrix

$$C = \begin{vmatrix} C_{11} & C_{12} & \cdots & C_{1K} \\ C_{21} & C_{22} & \cdots & C_{2K} \\ \vdots & \vdots & & \vdots \\ C_{K1} & C_{K2} & \cdots & C_{KK} \end{vmatrix} \tag{1.22}$$

Expanding the molecular orbitals using the result of equation 1.21, the Hartree-Fock energy can then be expressed as the matrix equation of Roothaan and Hall,[41,42]

$$FC = \epsilon SC \tag{1.23}$$

where F is the Fock matrix, ϵ contains the orbital energies and S is elements of the overlap matrix, which is used in quantum chemistry to describe the inter-relationship of a set of basis vectors.

$$S_{\mu\nu} = \int \phi_\mu^* \phi_\nu d\tau \tag{1.24}$$

The Fock matrix is a matrix approximating the single-electron energy operator of a given quantum system in a given set of basis vectors. This Fock matrix is an approximation to the true Hamiltonian operator of the quantum system and includes effects of the electron-electron repulsion in an average way described previously where each electron only sees an averaged potential of the other electrons. The Fock operator does not include calculation of the electron correlation energy

because it is a one-electron operator.

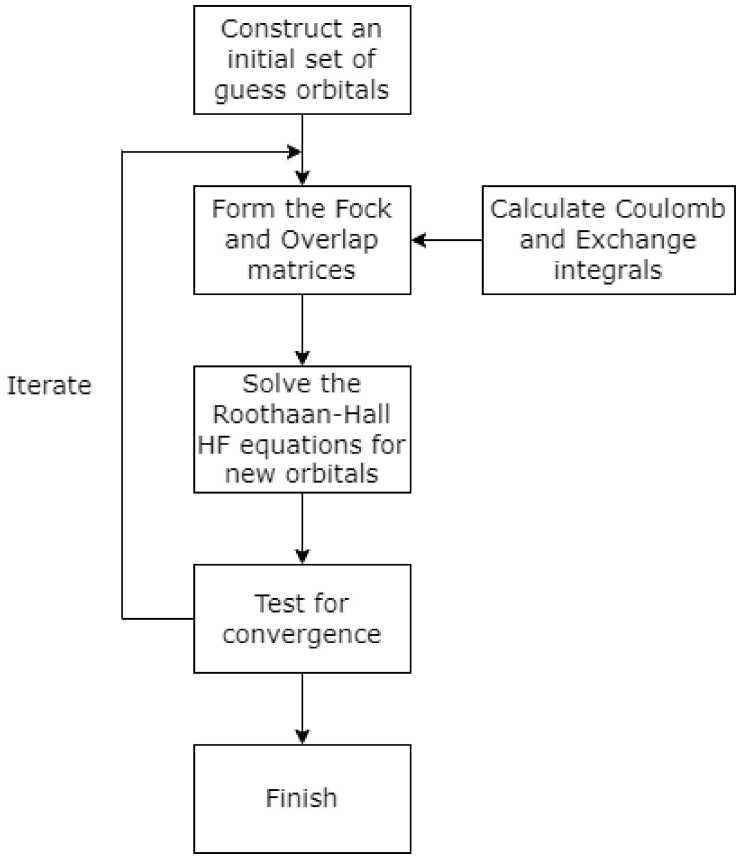

Figure 1.3: Flow chart showing the different steps of the iterative SCF method

The elements of the Fock matrix contain the molecular orbital coefficients and therefore to solve the resulting equations an iterative approach is required, which is known as self-consistent field (SCF) method as described in Figure 1.3.

1.3.5 Basis Sets

The complete set of basis functions used to model a system is called a basis set. This process was first employed by Slater whereby exponential basis functions (STOs) were fitted to resemble hydrogen-like atomic orbitals.[43] There are two main criteria to select the most suitable basis and a balance must be found between providing the best representation of the orbitals while also allowing rapid evaluation of the two-electron integrals. These STO basis functions consist of an angular part, given by spherical harmonic functions and a radial part, which for STOs have a general radial form

$$R_{1s}^{STO}(r) = Ne^{-\zeta r} \tag{1.25}$$

The radial 1s solution is

$$R(r) = 2\left(\frac{1}{a_0}\right)^{\frac{3}{2}} e^{-\frac{r}{a_0}} \tag{1.26}$$

where a_0 is the bohr radius. The radial solution has the form of a Slater function and illustrates that the orbitals decay exponentially and provide a good representation of features of the molecular orbitals. Evaluation of two-electron integrals are computationally intensive as when using a basis set the two-electron integrals must be evaluated over all basis functions and this can be very time consuming with Slater functions.

This technique was later refined by Boys who used Gaussian functions to speed up the calculation of two-electron integrals.[44] These functions had a general radial form of

$$R_{1s}^{GTO}(r) = Ne^{-\zeta r^2} \tag{1.27}$$

These Gaussian functions (GTOs) provide a less accurate description of the exponential decay of molecular orbitals than the STOs. Both the Slater and Gaussian functions contain an exponent, ζ, which controls the speed of decay of the functions. The exponent of the Gaussian function can be optimised to give the best match to a Slater function and with a single optimised Gaussian a reasonable decay can be obtained but there will be a much poorer description of the near nucleus behaviour. One solution is to use a linear combination of many Gaussian functions but the computational burden would be substantially larger. Contracted basis functions are fixed linear combinations of primitive functions and these have the form

$$\phi_\mu = \sum_\nu d_{\nu\mu} g_\nu \tag{1.28}$$

where $d_{\nu\mu}$ are the contraction coefficients and g_ν are primitive Gaussian functions. The most popular family of contracted basis sets are the STO-nG basis sets where n Gaussians are used and the exponents and contraction coefficients and optimised to reproduce STO orbitals.[45]

While small sets of contracted GTO functions provide a qualitatively accurate description of the wavefunction, the more basis functions that a wavefunction is built from, the greater the flexibility in modelling the true form of the wavefunction. Most chemistry takes place between valence atomic orbitals and as such all work in this Thesis has multiple basis functions describing each valence atomic orbital.[46]

Basis sets can also be expanded to include sets of basis functions of higher angular momentum than the valence atomic orbitals, these are called polarisation functions.[47] These polarisation functions allow for the electron density to be polarised away from the basic atomic orbital shapes, which can be vital when trying to model chemical bonds. The presence of polarisation functions in common basis sets are indicated by adding either * or ** to the basis set names. One * indicates polarisation functions are present on all atoms except H and He and two ** indicates polarisation functions are present on all atoms. Sometimes these * symbols are replaced by either a p, d or f representing the extra angular momentum level shown in parentheses.

Additional functions with greater spatial extent can be included in order to describe long range interactions which can be very important for treatment of anions and excited states.[48] These types of functions are called diffuse functions and their inclusion in the basis functions of a basis set is often indicated by the presence of a (+) symbol or the letters *aug*.

1.3.6 Effective Core Potentials

As the number of electrons in a system increases, the computational cost of the calculation can start to increase quite dramatically and often these deep core

electrons are not directly involved in the chemistry being investigated. They also cannot be totally ignored as these core electrons still interact with the valence electrons in electron-electron repulsions. This problem is often tackled by using an effective core potential (ECP), also known as a pseudopotential, which only describes the outer core and valence orbitals using basis functions.[49,50] This means that the core electrons are not explicitly treated in the calculation, but instead are approximated to an overall potential. These ECPs can also be parameterised to include the effects of relativity and are therefore particularly useful for calculations including heavy metals and atoms beyond the second row of the periodic table.[51]

1.3.7 Density Functional Theory

Another approach to solving the electronic Shrödinger equation is by using electron density. The electron density may be defined by integrating the probability density for a wave function over all coordinates, except the spatial coordinates of one electron and then normalising to the number of electrons. The Hohenberg-Kohn theorems of 1964 proved that the ground state electronic energy of any system is uniquely determined by a functional of the electron probability density,

$$E[p] = T[p] + E_{ee}[p] + E_{ext}[p] \tag{1.29}$$

where $E[p]$, $T[p]$, $E_{ee}[p]$ and $E_{ext}[p]$ are energy density functionals for the total energy, kinetic energy, electron-electron interaction energy and the electron-nuclei interaction energy respectively.[52] This is one of the two primary Hohenberg-Kohn theorems that make up the foundation of DFT. The second Hohegnberg-Kohn theorem is that if a functional is known, then the best electron density fit can be determined by minimising the energy with respect to variations in the density. This is because any approximate electron density will lead to an energy greater than or equal to the true ground state energy, but never lower energy.[53]

The Kohn-Sham DFT scheme proposed using a model system comprised of

non-interacting electrons, which leads to a much simpler and lower computational cost calculation, as for any non-interacting system the wave function is a single Slater determinant. The approximations used in Hartree-Fock theory allow for electrons to interact with a mean-field electron field instead of explicitly interacting with all other electrons. The kinetic energy for the non-interacting electron system, $T_s[p]$, can be considered as a sum of the individual orbital kinetic energies obtained from equation 1.13. The electron-nuclei interaction energy, $E_{ext}[p]$, can be expressed by using equation 1.14 and the electron-electron field interaction can be expressed using equation 1.15.

The remaining unknown components of the density functional can then be collected into a single exchange-correlation term, $E_{XC}[p]$, and the resulting energy expression from equation 1.30, can be solved using a Slater determinant and SCF procedure, similar to the one from Figure 1.3.[53]

$$E[p] = T_s[p] + E_{ext}[p] + E_J[p] + E_{XC}[p] \tag{1.30}$$

The accuracy of the energy calculated this way for a given basis set depends on how accurately the exchange-correlation energy is approximated. Unlike Hartree-Fock theory where the exchange-correlation energy is never calculated, DFT usually includes an approximation for this energy and as such can be highly accurate while having only a slight computational cost increase when compared with a Hartree-Fock calculation. Many different methods for approximating the exchange-correlation energy have been developed with different approximation methods found to be better suited to different chemical problems.[54]

1.3.8 Local Density Functionals

The simplest functionals used to approximate the exchange-correlation energy are known as local density functionals, which are derived using the uniform electron gas model. This is where a model system of N electrons are placed in a cube and a uniformly spread positive charge is applied to make the system neutral.

These local density functionals consider the exchange-correlation energy as a function of the local electron density at each point in space, which works as a good approximation for systems where the electron density is mostly uniform, but performs poorly for molecular systems where density will vary rapidly.[55] A very commonly used example of a local density functional is SVWN where the S stands for Slater and was developed by Vosko, Wilk and Nusair and in many programs SVWN is simply called LDA (local density approximation).[56]

1.3.9 Gradient Corrected Functionals

The next commonly used advancement on LDAs is to not only include the local value of the electron density but also the gradient of the density at each point.[57] This method is known as generalised gradient approxmation (GGA) and, for the most part, these are constructed in a way that simply corrects the LDA functional and works well for qualitative descriptions of bonding in molecules. The most popular GGA functional is BLYP where B stands for Becke and describes the exchange functional and LYP stands for Lee, Yang and Parr and describes the correction functional.[58] There is another category of GGA functionals known as meta generalised gradient approxmations (mGGA), which try to improve on the accuracy by adding more non-local information such as higher order density gradients and often also kinetic energy density, however these calculations are often too costly for larger practical computations.

1.3.10 Hybrid Functionals

The most commonly used functionals for calculating molecular properties are called hybrid functionals and combine approximate density-based exchange-correlation functionals with a fraction of orbital dependant exchange from equation 1.16. The B3LYP functional is the most widely used functional in all of chemistry and was developed by Becke in 1993 and generally outperforms equivalent pure density functionals.[59] This functional takes the form

$$E_{XC}^{B3LYP} = E_X^{LDA} + a_0(E_X^{HF} - E_X^{LDA}) + a_X(E_X^{B88} - E_X^{LDA}) + E_C^{VWN} + a_C(E_C^{LYP} - E_C^{VWN}) \tag{1.31}$$

where for B3LYP, E_C^{VWN}, is the SVWN functional and E_X^{B88} is the BLYP functional, with the empirical parameters set to $a_0 = 0.20$, $a_X = 0.72$ and $a_C = 0.81$.

1.3.11 The Potential Energy Surface

The main focus of this introduction so far has been on calculation of the energy of molecular systems, but it is equally important to be able to calculate molecular properties. These properties can be calculated as derivatives of the energy with respect to 'perturbations'. Common perturbations considered include changes in nuclear geometry, application of an external electric field or magnetic field, and interaction of electrons with nuclear magnetic moments. A very important example of a property that can be calculated through these derivative techniques is harmonic vibrational frequencies and intensities.[60,61]

One of the central themes of the work presented in this Thesis is calculation of infra-red spectra, which in order to compute, it is necessary to consider the nuclear part of the Shrödinger equation, as how the nuclei are expected to move is crucial. Using electronic structure methods, the energy of electrons moving under the potential generated by a specific arrangement of nuclei can be calculated. The nuclei-nuclei repulsion energy can be added on afterwards as a constant term. Comparing the energies of different arrangements of nuclei leads to a surface which describes the relationship between changes in nuclear positions and changes in the energy called the potential energy surface (PES). This PES contains nuclei-nuclei repulsion potentials as well as the external potential acting on the nuclei due to changes in electron configuration, for all possible nuclear coordinates. This means the nuclear Hamiltonian can be greatly simplified by substituting the term for

nuclear-electron interaction energy with the PES which can be seen in equation 1.32 where the summation runs over M nuclei in the system.

$$\hat{H} = -\sum_{I}^{M} \frac{1}{2M_I}\nabla_I^2 + V_{PES} \tag{1.32}$$

1.3.12 The Harmonic Approximation

The nuclear vibrational states of a molecule correspond to the bands observed by IR and Raman spectroscopy and therefore quantum mechanics can be useful for assigning the vibrational spectrum for a known molecular geometry. Solving the nuclear equation 1.32 would require evaluation of all possible nuclear configurations and therefore is only feasible for very small systems. In order to simplify this task, the PES can be expanded using a Taylor series about a minimum energy geometry of the form

$$E_{nuc} = E_0 + \sum_{I}^{3M} \frac{\partial E}{\partial R_I} R_I + \frac{1}{2!}\sum_{I,J}^{3M} \frac{\partial^2 V}{\partial R_I \partial R_J} R_I R_J + \frac{1}{3!}\sum_{I,J,K}^{3M} \frac{\partial^3 V}{\partial R_I \partial R_J \partial R_K} R_I R_J R_K ... \tag{1.33}$$

where R_i represents the $3M$ cartesian displacement coordinates corresponding to displacements in the x, y and z axes of the M nuclei from their minimum energy positions and E_0 is a constant which is set to zero by convention. The gradient of the PES at a minimum geometry is zero and therefore the term $\frac{\partial E}{\partial R_i} R_I$ is zero and so the simplest approach to approximating the PES is to take the first non-zero term of the Taylor series and assume the PES is equal to that.

$$E_{nuc} = \frac{1}{2!}\sum_{I,J}^{3M} \frac{\partial^2 V}{\partial R_I \partial R_J} R_I R_J \tag{1.34}$$

From equation 1.32, the nuclear Hamiltonian can be expressed in cartesian displacement coordinates including the nuclear kinetic energy operator as

$$\hat{H}_{nuc} = -\sum_{I}^{3M}\left(\frac{1}{2M_I}\frac{\partial^2}{\partial x_i^2}\right) + \frac{1}{2}\frac{\partial^2 V}{\partial R_i \partial R_j}R_i R_j \tag{1.35}$$

which means the nuclear Shrödinger equation can now be expressed as

$$\left[-\frac{1}{2}\sum_{I}\left(\frac{1}{M_I}\nabla_I^2\right) + \boldsymbol{\Delta x}^{\dagger}\boldsymbol{F}\boldsymbol{\Delta x}\right]\Psi_n = E_n\Psi_n \tag{1.36}$$

where $\mathbf{F}$ is a 3M $\times$ 3M force constant (Hessian) matrix containing second derivatives of the energy with respect to the coordinates $\boldsymbol{\Delta x}$.[62] This can be separated into 3M one dimensional Shrödinger equations where the nuclear Hamiltonian has the form

$$\hat{H}_{nuc} = \frac{1}{2}\sum_{I}^{3M}\left(-\frac{1}{M_I}\nabla_I^2 + \epsilon_i q_i^2\right) \tag{1.37}$$

from Wilson in 1939 where each harmonic oscillator is vibrating at a frequency related in Hz to the corresponding eigenvalue by $\omega = \sqrt{\epsilon}/2\pi$ and in wavenumbers by $\epsilon = 4\pi^2 c^2 \omega^2$.[63] This form of the Shrödinger equation for a harmonic oscillator can be solved.[62]

It is also necessary to calculate the probability that vibrational transitions will occur in order to compare with experimental data. Infrared transition probabilities are given by the change in the electric dipole moment, $\hat{\mu}$, during molecular vibration, which can be calculated within the harmonic approximation from the proportionality shown in equation 1.38 where q_i corresponds to mass-weighted vibrational normal coordinates.[64]

$$I_i \propto \left(\left|\frac{\partial \hat{\mu}}{\partial q_i}\right|\right)^2 \tag{1.38}$$

1.3.13 Anharmonic Corrections

There are numerous reasons why spectra calculated using the harmonic approximation will vary from those obtained in experiments. These can range from incomplete electronic structure methods, insufficient modelling of the surround-

ing environment and sometimes even temperature effects. The corrections to improve agreement briefly covered here refer to correcting for incomplete modelling of the PES due to the truncation of the Taylor series from equation 1.34. Harmonic frequencies are systematically too high as a consequence of the approximation of the PES. This has been shown to be around a 10 % increase for Hartree-Fock theory and around 4 % for hybrid DFT.[65] It is common practice to apply scaling factors to these frequencies, derived for each electronic structure method to obtain improved values.[66] The main drawback of this approach is that the appropriate scale factor can even vary within the same molecular species although multiple scale factors have been used in the past to attempt to address this limitation.[67] The vibrational analysis work in this Thesis is primarily on that of carbonyl bonds and as such this approach of making use of empirical scaling factors is sufficient.

1.3.14 Bond Dissociation Energy Calculations

Many of the calculations performed in this Thesis are computations in order to work out a bond dissociation energy, often between CO_2 or some other ligand and a metal centre. For the following section fragment 'A' refers to a ligand and fragment 'B' refers to the rest of the complex containing the metal atom. The term $E_Y^X(Z)$ corresponds to the energy of system Z with basis set X and geometry Y.

When calculating bond dissociation energies, a basic calculation will simply subtract the energy of individual fragments at their preferred geometry away from the energy of the full complex as shown in Equation 1.39. The problem with this method is that this difference in energies between two monomer units and a dimer is not entirely due to the complexation energy; some of the difference will be due to something called basis set superposition error (BSSE).[62]

$$\Delta E(AB) = E_{AB}^{AB}(AB) - E_A^A(A) - E_B^B(B) \tag{1.39}$$

This BSSE occurs because a finite basis function is used and as the atoms of the interacting molecules, or in some cases parts of the same molecule, approach one another, their basis functions start to overlap.[62] This results in each monomer 'borrowing' functions from the other nearby components, effectively altering the basis set and changing the calculation of some properties, such as energy. Consequently, calculating bond dissociation energies, if the total energy is minimised as a function of the system geometry, the short-range energies from the mixed basis sets must be compared with the long-range energies from unmixed basis sets and this introduces the BSSE.

To correct for this BSSE, four additional calculations are required, two of them use each fragment, A and B, frozen into the geometry they possess in the full complex. The other two involve the fragments frozen in the complex geometry, but using a full AB basis set for fragment. This means that the energy of A will be calculated in the presence of both the normal A basis functions, but also with the basis functions of fragment B despite it not actually being present in the calculation. These basis functions representing non present atoms are often called ghost orbitals and the equation for this more complex calculation can be seen in equation 1.40. When using ghost functions the energy of the fragment is lowered such that $\mathrm{E}_{AB}^{AB}(A) < \mathrm{E}_{AB}^{A}(A)$ and this results in an energy that will be closer to the energy obtained using a true wavefunction. This is called the counterpoise (CP) correction method.[62,68]

$$\Delta E^{CP}(AB) = [E_{AB}^{AB}(AB) - E_{AB}^{AB}(A) - E_{AB}^{AB}(B)] + [E_{AB}^{A}(A) - E_{A}^{A}(A)] + [E_{AB}^{B}(B) - E_{B}^{B}(B)] \quad (1.40)$$

The CP correction works by estimating the size of the BSSE and simply subtracting it away from the final bond energy calculation. The first part of the equation, $[E_{AB}^{AB}(AB) - E_{AB}^{AB}(A) - E_{AB}^{AB}(B)]$ describes the energy of bringing both

fragments together to form the complex, with the geometry of all fragments fixed in the complex geometry using a consistent full AB basis set. The second term, $[E^A_{AB}(A) - E^A_A(A)]$, and the third term, $[E^B_{AB}(B) - E^B_B(B)]$, describe the energy required to distort each of the individual fragments from its preferred geometry to the geometry it has in the full complex, this can also be known as the relaxation correction.[62,68]

This introduction covering transition metal carbonyls, detection of reactive intermediates and computational theory aims to cover the background knowledge required to fully understand the work conducted in this Thesis. The overall aim of this work is to continue research focussing on trying to isolate stable alkane and CO_2 organometallic complexes by a variety of techniques.

Chapter 2

Time-Resolved Studies of $Co(CO)_3(NO)$ in *n*-heptane

2.1 Introduction

This Chapter focuses on time-resolved infra red studies of $Co(CO)_3(NO)$ in *n*-heptane and was carried out just at the beginning of the COVID lockdown. This system has been studied with the aim of both gaining a better understanding of the photophysics and photochemistry of $Co(CO)_3(NO)$ while also trying to better understand the mechanism behind the formation and decay of $Co(CO)_2(NO)$(*n*-heptane) as an alkane complex of interest.

2.1.1 Organometallic Nitrosyl Complexes

The chemistry of transition metal-NO complexes, or metal nitrosyls, has taken on added significance in recent years because of the important role that nitric oxide has been found to play as a signalling molecule in biological systems, especially plants.[69–72] Recent work has also shown that the characteristic chemistry of nitrosyl compounds is often different to that exhibited by their isoelectronic carbonyl analogues.[73] The unusual reactivity of transition metal nitrosyl complexes is attributed to the unpaired electron on the NO radical.[74–76] The NO ligand is

most commonly found to bind linearly to a metal centre through the N atom, but can also bind in a bent geometry.[74] This change from linear to bent geometry is accompanied by a change in the electron spin density which describes the interaction between the NO ligand and the metal centre. This change from linear to bent is considered to change the NO ligand from a three electron donating ligand to a one electron donating ligand.[74] Other possible binding modes such as ON and side-on η^2-NO coordination have also been detected.[77] These less common binding modes are more frequently associated with metastable products of photochemical reactions, where stable nitrosyl complexes are irradiated to form a complex with ON or η^2-NO coordination.[77–79] In Figure 2.1 the differences in back-bonding, geometry and M-N-O angle between these four different binding modes are represented.

Within a given complex, the stretching frequencies of the bent-NO, ON and η^2-NO ligands are red-shifted relative to the infrared frequency of the linear-NO ligand. The η^2-NO stretching mode is generally ~ 400 cm^{-1} lower in wavenumber than the linear-NO mode. The ON stretching mode is generally ~ 100 cm^{-1} lower in wavenumber than the linear-NO mode. The stretching frequency of bent-NO ligands are also approximately 100 cm^{-1} lower in wavenumber than the linear-NO stretch. A linear-to-bent NO conversion can be thought of as rehybridisation of nitrogen from sp to sp^2, which corresponds to a weakened NO bond, which in turn decreases the frequency of the NO stretch.

2.1.2 Characteristics of $Co(CO)_3(NO)$

One of the most commonly investigated nitrosyl complexes is $Co(CO)_3(NO)$, which is a linear-NO complex in its ground state.[80,81] Figure 2.2 shows the electronic absorption spectrum of $Co(CO)_3(NO)$, which has two main bands, a very intense band around 200 nm and a much weaker band around 380 nm. According to Hackett *et al.* the band centred around 200 nm can be assigned to a transition that leads to the breaking of the Co-NO or Co-CO bonds and the band around

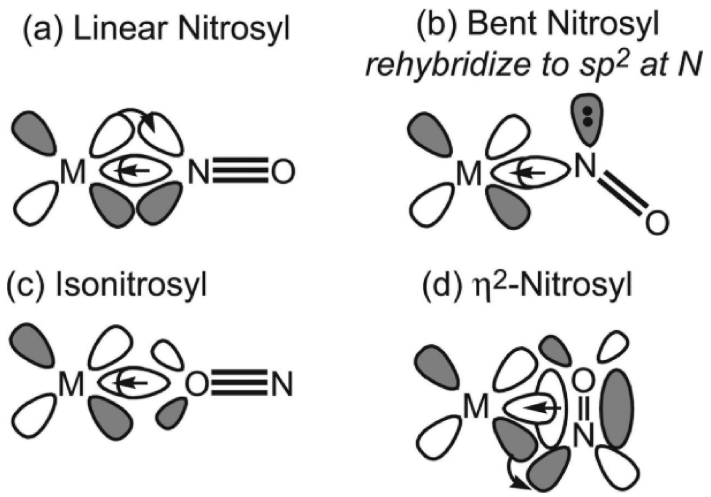

Figure 2.1: Binding modes of a nitrosyl ligand to a transition metal where the nitrosyl ligands are lying in the same place as the metal atom. (a) Linear MNO: the σ(NO) orbital is bound to the metal d_{z^2} orbital, and the π^*(NO) orbital participates in π back-bonding with the metal. (b) Bent MNO: the N is sp^2 hybridised, and there is a σ-donation between the d_{z^2} orbital on the metal and as sp^2 orbital on the NO. Additionally, there is a lone pair on the NO ligand in this geometry. The amount of π back-bonding with the metal centre is reduced in this geometry because there is no longer an interaction between the π^*(NO) orbital and the d orbitals in the plane of the paper; however, there is π back-bonding between the π^*(NO) orbital and the d orbitals that are perpendicular to the page. (c) MON: identical to the backbonding between a metal and a linear NO, except that there is less back-bonding because of the smaller lobes of the oxygen π^* orbitals. (d) M(η^2-NO): the metal is bound in a σ-fashion to the NO bond so that is is oriented in a side-on geometry. From Harris *et al.*[1]

380 nm can be assigned to a cobalt-to-nitrosyl charge-transfer transition.[82] This charge transfer is also proposed to lead to a bent-NO complex.[81]

In Figure 2.3 a molecular orbital diagram of the different bent and linear NO bonding modes is given as predicted by Enemark and Feltham.[83] In the ground electronic state the HOMO is labelled $4a_1$, which has primarily d_{z^2} character and the LUMO, labelled as 4e, is primarily composed of π^* orbitals of NO and both d_{xz} and d_{xy} orbitals from Co and is antibonding in nature. Irradiation with 400 nm light causes an excitation from the $4a_1$ to 4e MO, resulting in the energies of both the 4e and 3e molecular orbitals changing. The molecule then decays into a triplet state, which causes the molecule to rearrange, both causing the NO ligand to become bent and causing an overall geometry change of the molecule

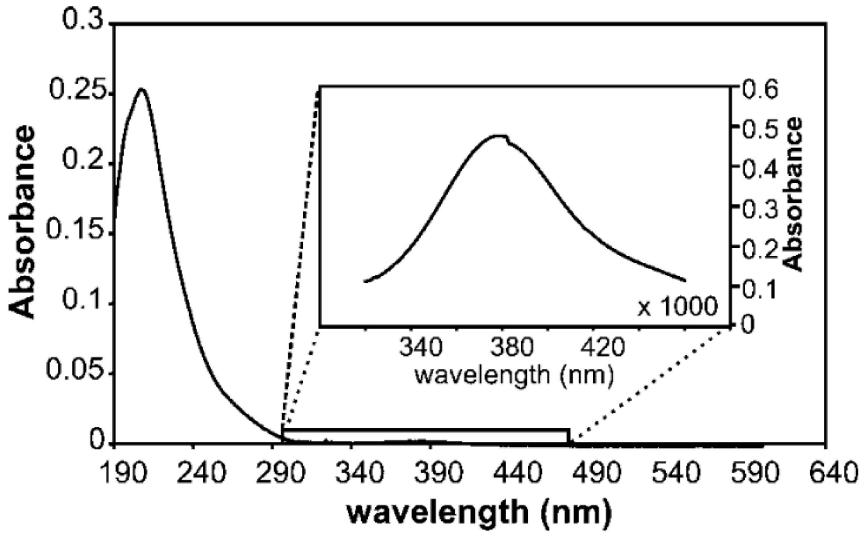

Figure 2.2: Electronic absorption spectrum of $Co(CO)_3(NO)$ in a neat hexane solution from Harris *et al.*[1]

from tetrahedral to pseudo-square planar.[81]

Numerous investigations involving the most common cobalt nitrosyl complex, $Co(CO)_3(NO)$, have been reported with some of these also being photochemical studies.[84–86] Some of these photochemical studies involve carbonyl substitutions in solution phase of a variety of ligands such as 1,3-butadiene, PEt_3, pyridine and PH_3.[81,87,88] In this Chapter, the photochemical reaction of interest is the substitution reaction in *n*-heptane which forms $Co(CO)_2(NO)$(*n*-heptane).

2.1.3 Direct Observation of Photoinduced Bent Nitrosyl Excited-State Complexes

A key paper for this Chapter is the picosecond TRIR study by Harris *et al.* on $Co(CO)_3(NO)$. TRIR studies were interpreted to show the presence of two bent NO excited state complexes and no evidence for either linear or bent ON or η^2-NO isomers following photolysis. This TRIR study was complemented by DFT calculations and is summarised in this introduction.[1]

Figure 2.4 shows the ultrafast time-resolved visible-pump, mid-IR probe spectra of $Co(CO)_3(NO)$ (**A**) in a hexane solution along with dynamics and peak assignments in Table 2.1. Figure 2.4a,b shows the NO stretching re-

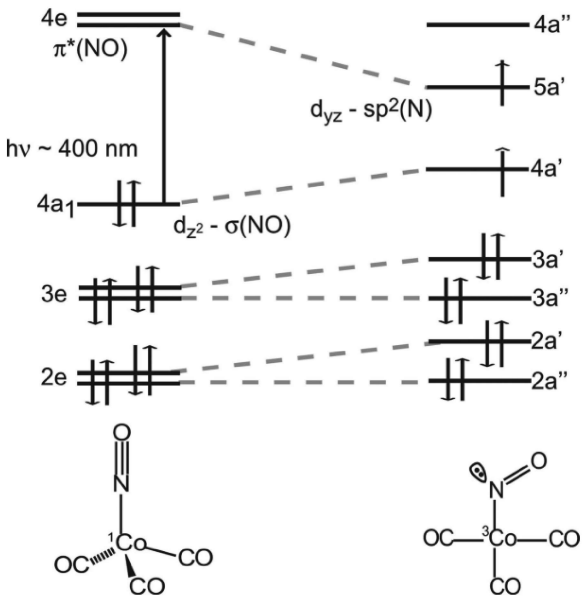

Figure 2.3: The molecular orbital correlation diagram of the CoNO structural unit in the linear-NO and bent-NO forms of $Co(CO)_3(NO)$, as predicted by Enemark and Feltham.[83]

gion and Figure 2.4c shows the CO stretching region. Peaks assigned to (**A**), $^1Co(CO)_2(NO)$(hexane) and $Co(CO)_3$ are excluded from Figure 2.4, but their assignments can be seen in Table 2.1.

The spectra and assignments from Figure 2.4 show species that are not attributable to either CO or NO loss pathways, which confirms that there are intermediates formed *via* nondissociative photochemical pathways.[89,90] As shown in Figure 2.4a,b there are three different peaks at 1684, 1715 and 1755 cm^{-1}, which are all assigned to NO stretching modes and labelled $\mathbf{C}_{NO}$, $\mathbf{B}_{NO}$ and $\mathbf{D}_{NO}$.

The peak labelled $\mathbf{D}_{NO}$ is assigned to vibrational cooling of the NO ligand based on its decay with a time constant of $\tau = 11 \pm 1$ ps being similar to the recovery of the NO stretch of **A** (23 ± 1 ps) and the decay of the NO stretch of the vibrationally hot parent molecules (17 ± 2 ps).

Both peaks $\mathbf{B}_{NO}$ and $\mathbf{C}_{NO}$ have dynamics that are separate from vibrational cooling where $\mathbf{B}_{NO}$ decays with a time constant of $\tau = 359 \pm 150$ ps and $\mathbf{C}_{NO}$ rises with a time constant of $\tau = 350 \pm 100$ ps. This agreement between time constants suggests that species **B** converts to species **C** in approximately 350 ps. The kinetics of these processes can be seen in Figure 2.5 where peak intensities

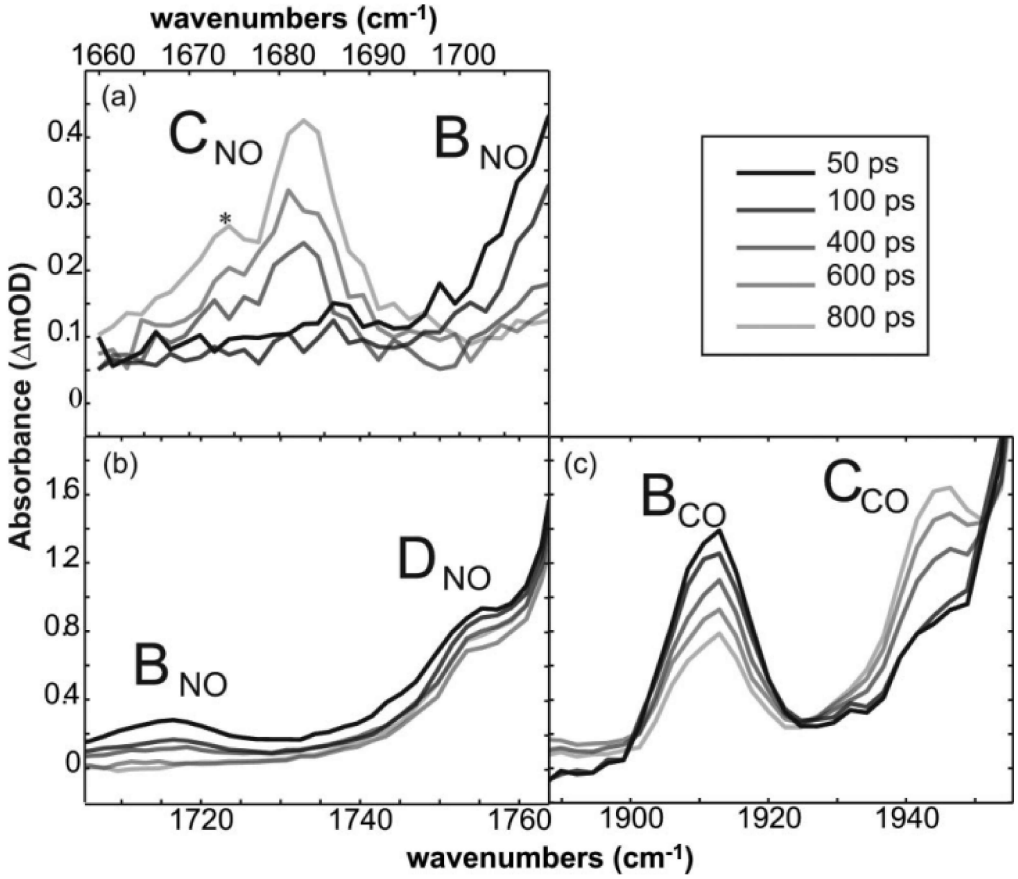

Figure 2.4: Ultrafast time-resolved visible-pump, mid-IR probe spectra of the (a) NO stretching region of $\sim$ 20 mM $Co(CO)_3(NO)$, (b) NO stretching region of $\sim$ 5 mM $Co(CO)_3(NO)$ and (c) CO stretching region of $\sim$ 5 mM $Co(CO)_3(NO)$ in neat hexane solution. The additional feature labelled * appears to be a shoulder for the B_{NO} peak. From Harris *et al.*[1]

at 1715 and 1684 cm^{-1} are plotted over time.

Figure 2.4c shows peaks in the carbonyl region at 1913 and 1949 cm^{-1} and kinetic plots following the intensities of these peaks can be seen in Figure 2.6. The $\mathbf{B}_{CO}$ band decays with a time constant of $\tau = 206 \pm 78$ ps and $\mathbf{C}_{CO}$ grows in with a time constant of $\tau = 297 \pm 18$ ps which are similar to the time constants from Figure 2.5 assigned to $\mathbf{B}_{NO}$ and $\mathbf{C}_{NO}$. This similarity in time constants meant Harris *et al.* proposed that the peaks labelled $\mathbf{B}_{CO}$ and $\mathbf{C}_{CO}$ corresponded to the CO stretching modes of species **B** and **C**. No CO stretches of species **D** were observed as the peaks were hidden by the larger peaks from the CO and NO loss pathways.

Species **B**, **C** and **D** have wavenumber values lower than that of **A** by 92, 113

Species	Obs Frequency / cm^{-1}	τ / ps	Trend
$Co(CO)_3(NO)$	1807 (NO)	17 ± 1	rise
	2037 (CO)	not resolvable	
	2103 (CO)	3 ± 4	rise
		191 ± 26	rise
hot $Co(CO)_3(NO)$	1775 (NO)	23 ± 3	decay
	2025 (CO)	170 ± 12	decay
	2085 (CO)	4 ± 4	decay
		155 ± 20	decay
$^1Co(CO)_2(NO)$(hexane)	1775 (NO)	10 ± 7	rise
		32 ± 20	decay
	1992 (CO)	7 ± 2	decay
		162 ± 13	decay
	2062 (CO)	137 ± 20	decay
$Co(CO)_3$	1973 (CO)	38 ± 15	decay
$^3Co(CO)_3(NO)$ (T_2 or T_3)	1715 (NO)	9 ± 2	decay
		350 ± 150	decay
	1913 (CO)	5 ± 2	rise
		209 ± 78	decay
$^3Co(CO)_3(NO)$ (T_1)	1684 (NO)	12 ± 3	decay
		350 ± 100	rise
	1949 (CO)	8 ± 3	decay
		297 ± 18	rise
$^3Co(CO)_2(NO)$ (T_1)	1755 (NO)	11± 1	decay

Table 2.1: Peak assignments and dynamics for species from Figure 2.4 and other species observed. From Harris *et al.*[1]

and 52 cm^{-1}, respectively. From earlier in this Chapter this means these species could correspond to either a complex with a linear-ON or bent-NO ligand. Due to the lack of literature examples of observation of these linear-ON or bent-NO species, Harris *et al.* employed DFT computations to determine their structures.

In Figure 2.7 a calculated partial Kohn-Sham orbital diagram for **A** with a tetrahedral geometry and a linear-NO is shown. The HOMO-LUMO gap is an almost perfect match in energy with a 400 nm pump pulse (71 kcal/mol), but a $2a_1 \rightarrow 4e$ transition would also be possible as these orbitals are 76 kcal/mol (375 nm) apart. The DFT calculations by Harris *et al.* showed that both transitions were weak, but that the $2a_1 \rightarrow 4e$ transition moment is half as intense as the transition moment for $3e \rightarrow 4e$. It is predicted that, provided the former transition is not dissociative, that both these transitions will result in the same

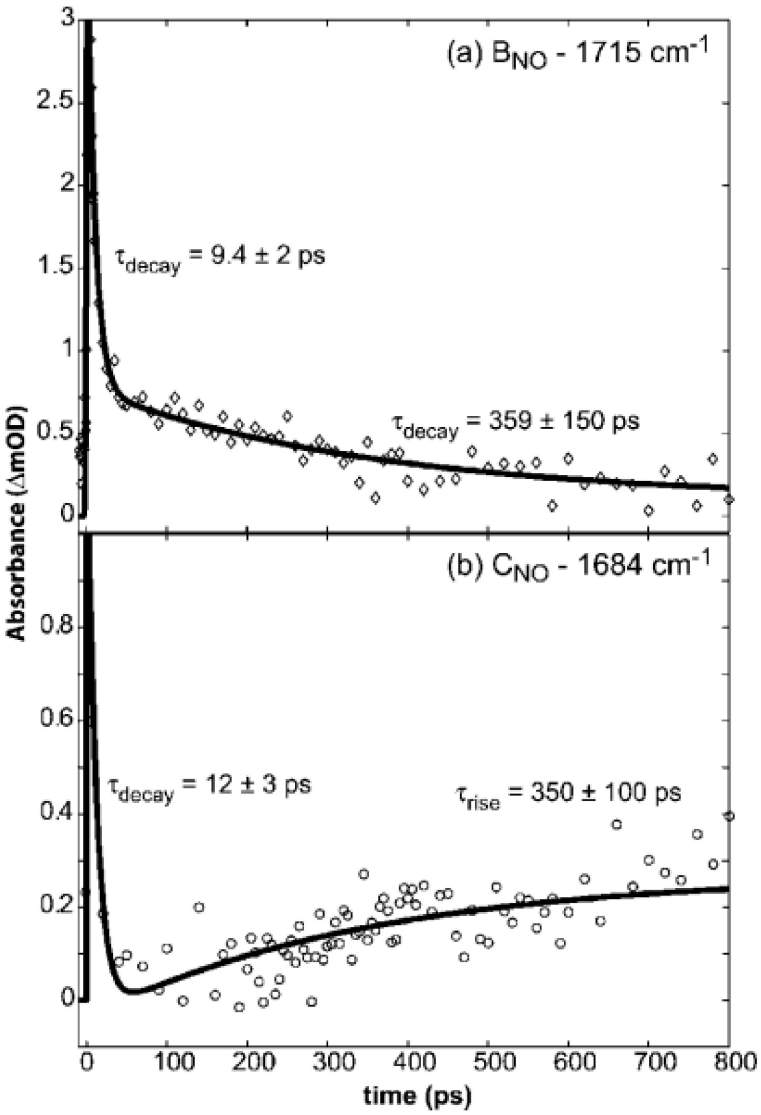

Figure 2.5: Kinetic plots following the intensities of the peaks at (a) 1715 cm^{-1} ($\mathbf{B}_{NO}$) and (b) 1684 cm^{-1} ($\mathbf{C}_{NO}$) in hexane solution. From Harris *et al.*[1]

dynamics on the picosecond timescale.

Figure 2.8 shows that as the Co-N-O angle is decreased the symmetry goes from C_{3V} to C_s and the 3e and 4e molecular orbitals split into nondegenerate pairs labelled a' and a". In this new C_s geometry the three CO groups are arranged non-symmetrically as the angle between two of the CO groups is larger, which creates a space into which the NO ligand can bend into. The a' orbital which stems from the HOMO rises in energy, due to a smaller degree of π back-bonding. The a' and a" orbitals from the LUMO decrease in energy as the Co-N-O angle decreases. This suggests that S_1 and T_1, which correspond to the lowest energy

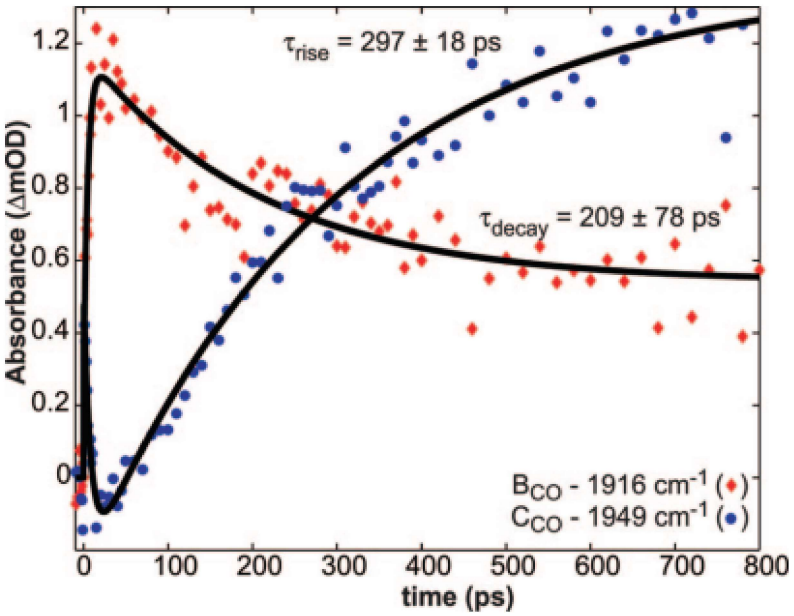

Figure 2.6: Kinetic plots of the carbonyl stretches of peaks at 1917 cm^{-1} ($\mathbf{B}_{CO}$) and 1949 cm^{-1} ($\mathbf{C}_{CO}$) in solution. From Harris *et al.*[1]

singlet and triplet excited states, will have structures notably different from that of the S_0 ground state.

Past studies have indicated that the most significant pathway upon 400 nm photolysis of $Co(CO)_3(NO)$ is CO dissociation.[89] The singlet species $^1Co(CO)_2(NO)(S)$ was observed in the experiments discussed above for which DFT predicts that the NO ligand is slightly bent and has a vibrational frequency of 1803 cm^{-1}. This is 39 cm^{-1} lower in wavenumber than the experimental observed stretch of the NO band for the complex S_0. The triplet CO-loss complex, $^3Co(CO)_2(NO)$, is also accessible by 400 nm photolysis of $Co(CO)_3(NO)$, and for this system DFT predicts a linear NO ligand, which has a stretching frequency of 1773 cm^{-1}. This agreement with the experimentally observed band at 1755 cm^{-1} is further evidence for the assignment of species **D**. This photoproduct is long-lived on the duration of the picosecond experiments due to the singlet-triplet gap being 20 kcal/mol, which is large enough that coupling between these states should be small enough to allow the triplet complex $^3Co(CO)_2(NO)$ to have a long lifetime.

Figure 2.9 shows optimised structures and harmonic frequencies for the NO

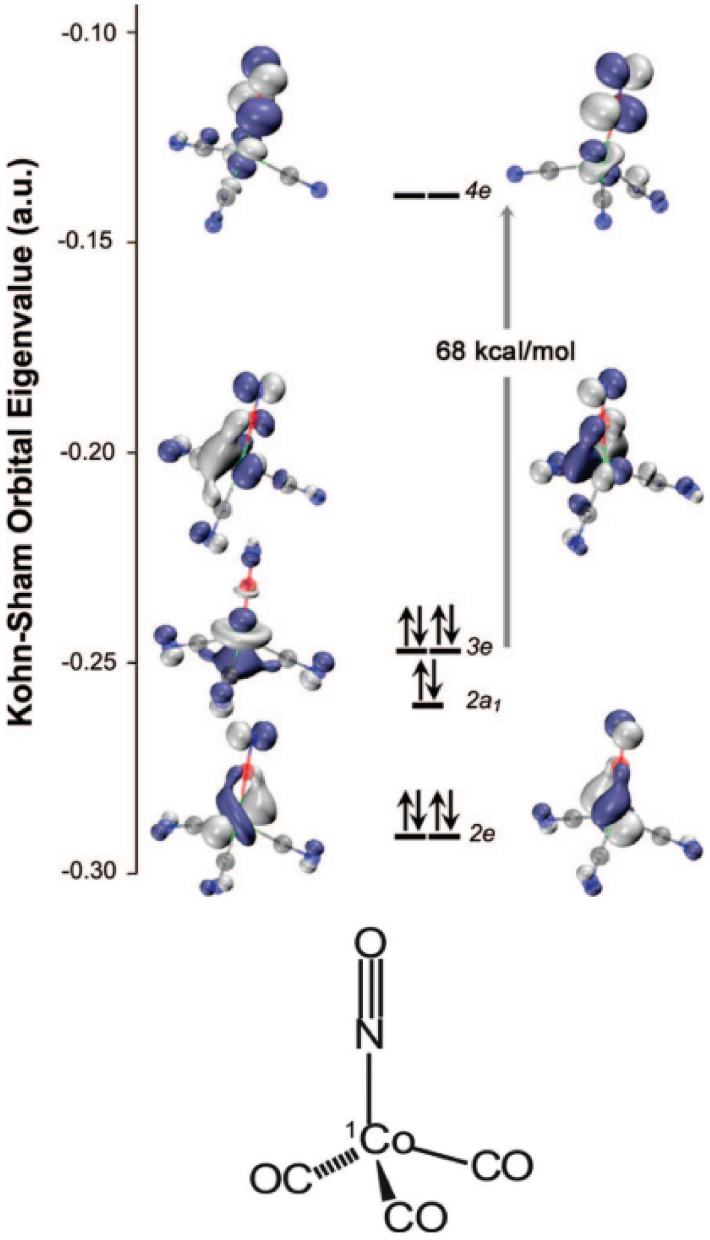

Figure 2.7: Calculated Kohn-Sham orbital diagram for $Co(CO)_3(NO)$ where the NO is pointing up (as pictured). From Harris *et al.*[1]

stretching frequency for seven different complexes. The first three of these are three ground-state structural isomers, linear-NO, η^2-NO and ON complexes labelled as S_0, η^2-S_0 and iso-S_0, respectively. The iso-S_0 and η^2-S_0 structures are higher in energy than S_0 by 42.0 and 38.4 kcal/mol, respectively, and have a redshifted NO stretch from that of the S_0 complex. The optimised structures for the first excited triplet and singlet excited states (T_1 and S_1) can also be seen in Figure 2.9, which both contain bent NO ligands that are 0.02 Å longer than the

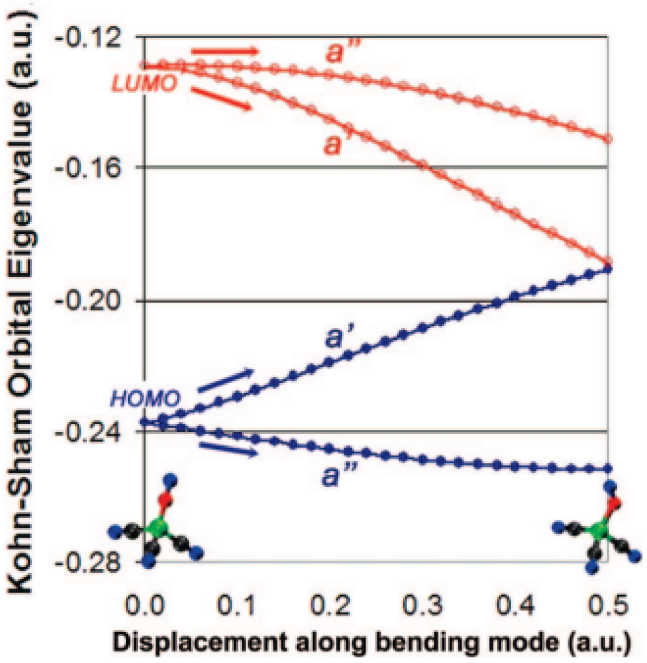

Figure 2.8: Frontier orbitals (occupied, closed blue circles; unoccupied, open red circles) along the positive half of the NO bending mode (588 cm^{-1}). From Harris *et al.*[1]

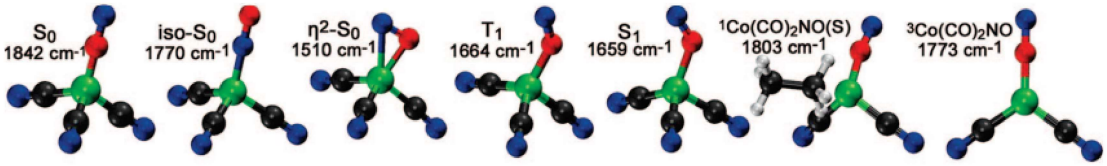

Figure 2.9: Optimised molecular structures and harmonic NO stretching frequencies of the structural isomers of ground-state $Co(CO)_3(NO)$, the lowest energy structures on the lowest-lying triplet (T_1) and singlet (S_1) excited-state potentials and the associated CO-loss species. From Harris *et al.*[1]

NO bond in S_0 due to the decrease in bond order. This longer NO bond again has caused a redshift of the NO vibrational frequency in T_1 and S_1 compared with S_0 and the Co-N bonds in T_1 and S_1 are also 0.15 and 0.17 Å longer, respectively, because of reduced back-bonding. This confirms that the NO bond is weaker when bound to the metal centre in a bent configuration when compared with a linear configuration.

These DFT calculations conducted by Harris *et al.* indicate that their experimentally-observed peaks cannot be assigned to a η^2-S_0 species as the frequency of its NO stretch falls outside of the limits of the range their experimental

setup can detect, but they do not rule out the potential formation of the η^2-S_0 species. The calculated NO stretching frequencies for iso-S_0, S_1 and T_1 do however all fall within the error of their experimentally-observed peaks and as such are all candidates for the identities of both **B** and **C**.

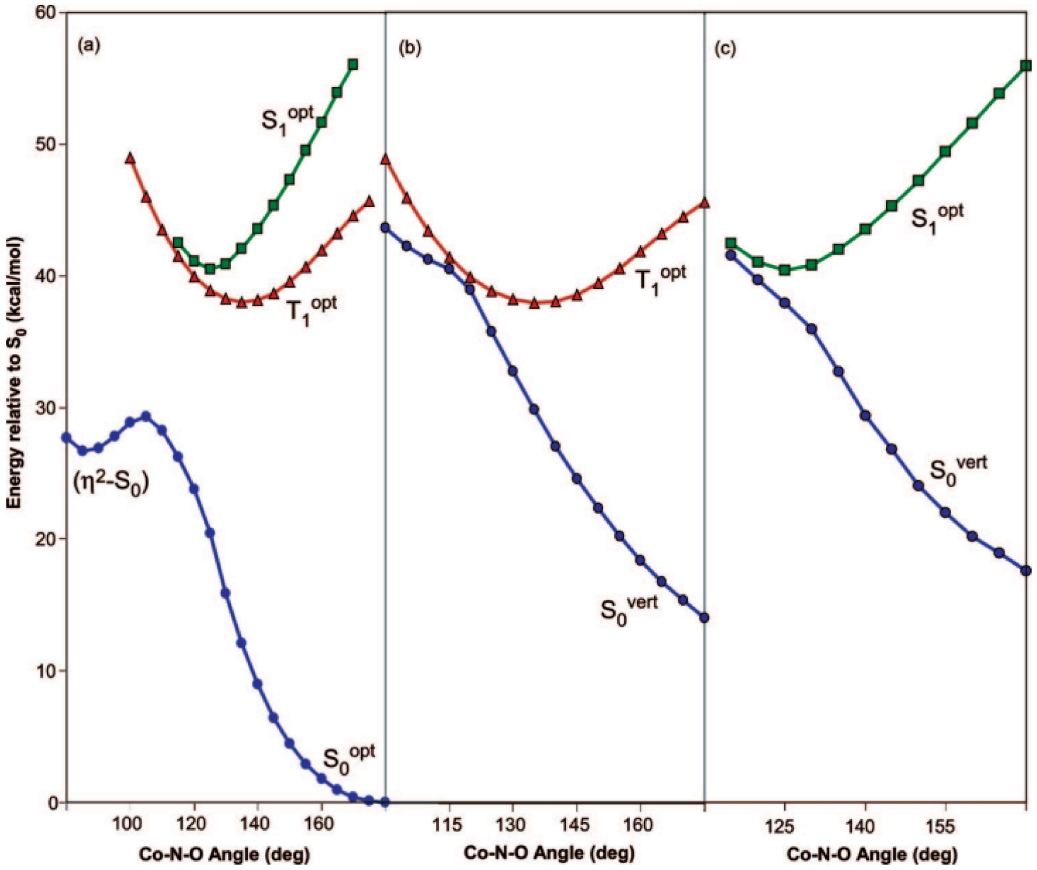

Figure 2.10: S_0, T_1 and S_1 potential energy surfaces along the Co-N-O bending angle of $Co(CO)_3(NO)$, calculated with BP86/6-31G*. (a) Constrained potential energy scan calculated while fixing the Co-N-O bending angle at successive values ranging between 80 and 180° ; (b) single-point energy calculation of S_0^{vert} performed at the optimised structures on the T_1^{opt} state; (c) single-point energy calculation of S_0^{vert} performed at the optimised structures on the S_1^{opt} state. The 'opt' superscript denotes constrained optimisation at a given bending angle. The 'vert' superscript signifies a single-point energy calculation on a different potential energy surface, with the same molecular structure as that of the paired opt state. From Harris *et al.*[1]

Figure 2.10a shows one-dimensional slices of the ground and two lowest energy excited potential energy surfaces (S_0, T_1 and S_1) of $Co(CO)_3(NO)$ and confirms that the global minimum on the S_0 potential has a linear NO structure aswell as predicting a 28 kcal/mol barrier connecting S_0 to η^2-S_0 where the reverse

barrier is only 3 kcal/mol. This much smaller reverse barrier suggests that if η^2-S_0 were to form then it would quickly isomerise back to S_0. Iso-S_0 (not shown on this diagram) is less stable than S_1 and T_1 and a significant barrier exists to accessing it from either S_0 or η^2-S_0 and therefore neither **B** nor **C** is due to iso-S_0. This is supported by other literature which has shown that multiple photons are required to access iso-S_0 and requires formation of a stable intermediate species, η^2-S_0.[79,91,92]

Now both η^2-S_0 and iso-S_0 have been excluded from the assignments of **B** and **C** this only leaves excited state bent-NO complexes. The calculated NO stretching frequencies for both T_1 and S_1 (1664 and 1659 cm^{-1}) are close to that of $\mathbf{C}_{NO}$ at 1684 cm^{-1}, so can tentatively be assigned as either T_1 or S_1. Figure 2.10b,c can be used to help distinguish between these two different species, and shows vertical energies of S_0, which are single point energy calculations that were performed at the optimised structures of the paired optimised state. Figure 2.10c shows that S_1 and S_0 are close in energy at the minimum on the S_1 potential energy surface with an estimated 2 kcal/mol energy barrier to accessing the 'point of closest approach' from the minimum-energy structure of S_1. Harris *et al.* concludes that the coupling between the S_0 and S_1 states is strong and the nonadiabatic transition may occur before the classical barrier is crossed and therefore S_1 must be short lived and cannot be assigned to **C**, which is a long-lived species.

Figure 2.10b shows that T_1 and S_0 have a close approach along the Co-N-O angle but because T_1 is a high-spin state, it is reasonable that it is longer lived than S_1 due to exchange energy stabilisation. The spin-orbit coupling in this vicinity would be a lot smaller than it was for the situation in Figure 2.10c as $T_1 \rightarrow S_0$ is a spin-forbidden transition. There is again also a small classical barrier of around 3 kcal/mol to accessing the point of closest approach. The combination of all these factors suggests that before the system can undergo a nonadiabatic transition to the ground state, it must pass over the classical barrier to access the crossing point and as a result the T_1 species is expected to be long-lived.

This long-lived nature of T_1, combined with the good match between calculated stretching frequency and that observed in experiment means that species **C** is assigned to T_1, the bent NO complex in the ground triplet state.

Now that Harris *et al.* have assigned both species **C** and **D**, only species **B** remained unidentified. The NO stretch of species **B** is slightly blueshifted compared with that of **C** but significantly redshifted compared with that of **A** and suggests that **B** should be assigned to a species with a bent NO ligand, but less bent than the 137° NO present in **C**. The S_1 species can therefore be discounted as its NO stretch is redshifted when compared to species **C**. Also since it is known that **B** decays into **C**, if S_1 were to form, it is significantly more likely that a $S_1 \rightarrow S_0$ transition would occur as opposed to a spin forbidden $S_1 \rightarrow T_1$ transition.

Due to the lack of evidence for a bent-NO complex, which is less bent than **C** on any of the S_0, S_1 or T_1 it is expected that **B** corresponds to a complex on a higher excited state. Species **B** corresponds to an excited state complex that decays to form T_1 with a time constant of $\tau = 350$ ps due to a classical barrier or a very small amount of nonadiabatic coupling between the states. Figure 2.11 contains plotted vertical TD-DFT excited states of the higher singlet and triplet states along the 588 cm^{-1} bending mode. Four states that arise from the original, doubly degenerate HOMO and LUMO of **A** can be seen where the singlets are shown as green circles and the triplets as red triangles. Based on these potentials, all but one of the states in Figure 2.11 have at least one local minimum with a structure containing a bent NO group and all are less bent than the 137° NO present in T_1.

There are three singlet states, S_1, S_2 and S_3, which all have energies close to that of the pump photon at 71 kcal/mol and the calculations by Harris *et al.* found that among the singlet states, only S_1 and S_3 have nonzero oscillator strengths suggesting that the 400 nm photolysis will only populate these states. However, all three of these singlet excited states have potentials that intersect with another

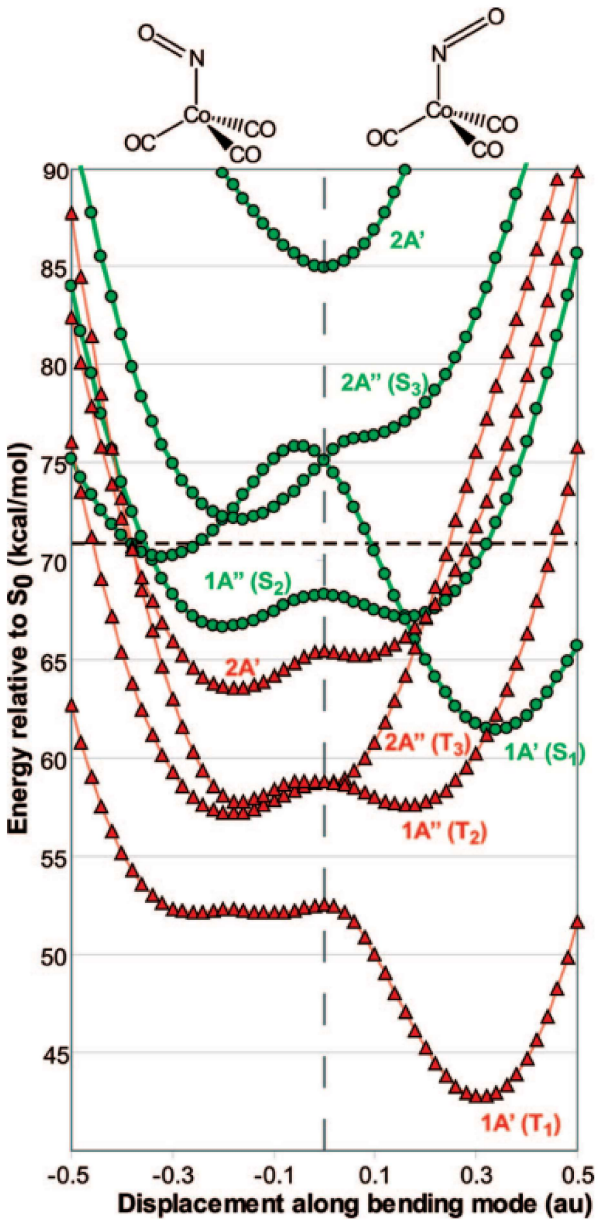

Figure 2.11: TD-DFT vertical excited states along the bending mode of the parent complex. Shown are the four single-excitation states of each spin symmetry arising from the original doubly degenerate HOMO and LUMO. Singlet states are shown in green (circles) and the triplet states are shown in red (triangles). The symmetries (A' and A") correspond to the symmetries for the individual states with positive bending modes and the numbering of the states is based on the energy ordering of the states when the complex has a bent-NO geometry. In the positive bending mode (right), the NO ligand bends so that it bisects two of the CO ligands, in the negative bending mode (left), the NO ligand is bent directly towards the remaining CO group. The horizontal dashed line (71 kcal/mol) corresponds to the 400 nm photon energy. From Harris *et al.*[1]

singlet excited state, and often near the local minima too. This suggests that any species which undergoes excitation to these states would rapidly relax back to S_0

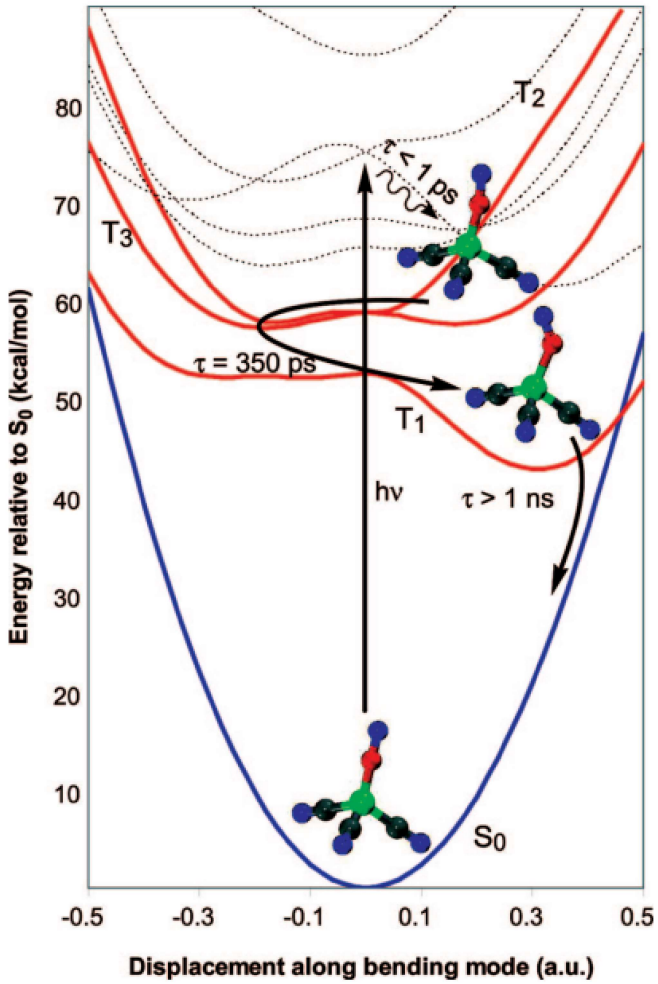

Figure 2.12: Photochemical mechanism for the formation of excited-state bent-NO complexes of $Co(CO)_3(NO)$. From Harris *et al.*[1]

on a timescale much quicker than the experimentally observed 350 ps decay of species **B** thus none of these species are expected to be assigned to **B**.

The excited triplet states, T_2 and T_3 are separated from T_1 by quite a large energy gap which suggests the stability of either of these states will be quite high. The point of closest approach between T_1 and the other two triplet states occurs along a negative bending mode where the structure is trending towards an eclipsed structure where T_1 is 5 kcal/mol lower in energy than the higher states. T_2 and T_3 are almost isoenergetic in the region of the point of closest approach and as such distinguishing between T_2 and T_3 is near impossible and therefore one structure cannot be assigned to species **B**.

Figure 2.12 shows the mechanism proposed by Harris *et al.* for these photo-

chemical formation of the bent NO complexes. Photolysis of $Co(CO)_3(NO)$ with a 400 nm photon leads to many very short-lived (under 1 ps) excited states which decay to either T_2 or T_3. This structure is stable for 350 ps before nonadiabatic coupling induces a transition to T_1 which is observable on a long timescale. It is expected that T_1 will decay back to S_0, but is not observed on the picosecond timescale.

2.1.4 Aims and Objectives

In this Chapter, we build on the work of Harris *et al.* to further grow our understanding of the photophysics of $Co(CO)_3(NO)$ in alkane solvents.[1] This is done by both nanosecond and picosecond TRIR experiments using 400, 355 and 266 nm pump pulses and performed over a larger window than the previously reported work. We have used the following strategy to address the aims above:

1) TRIR spectra were first taken on the nanosecond timescale using a 355 nm pump pulse to look for evidence of the predicted decay from the T_1 species back to S_0 proposed by Harris.[1]

2) Further TRIR experiments were conducted on the picosecond timescale using a 400 nm pump pulse to aid in comparison of our work to that of the original experiments performed by Harris.

3) The previous TRIR experiments were then repeated at a much higher concentration to try to better understand and more closely replicate the results of Harris.

4) Some final TRIR experiments were performed using a 266 nm pump pulse in an attempt to investigate the wavelength dependence on the formation of $Co(CO)_2(NO)$(*n*-heptane) and further study the overall photophysics and photochemistry of $Co(CO)_3(NO)$.

This research was initiated during the COVID-19 shutdown and the constraints of the pandemic hampered the study of the photophysics and photochemistry of this complex and did not allow for the time required to run high

concentration experiments using a 266 nm pump pulse.

2.2 Results and Discussion

2.2.1 TRIR Studies of $Co(CO)_3(NO)$ in *n*-Heptane Using 355 and 400 nm Excitation

The initial aim was to examine the decay of the $Co(CO)_3(NO)$ (T_1) theorised by Harris *et al.*, which was believed to have a lifetime exceeding 1 ns. Their TRIR experiments were limited by the optical delay line used to determine the time resolution whereas the Nottingham apparatus contains a kHz ns pump laser with an ultra fast IR probe producing a spectrometer, which can obtain IR from <1 ps to 200 μs. The ns-TRIR of $Co(CO)_3(NO)$ was recorded in *n*-heptane, which is similar to the *n*-hexane used in the experiments of Harris.

The TRIR spectrum, obtained 1 ns after 355 nm excitation of $Co(CO)_3(NO)$ clearly shows a bleach of the three parent bands at 2101, 2034 and 1808 cm^{-1}, and the growth of some new peaks at 2057, 1992, 1970 and 1775 cm^{-1} as shown in Figure 2.13. The peak at 1970 cm^{-1} can be possibly assigned to $Co(CO)_3$ formed following the loss of NO by comparison to the results of Harris and previous matrix isolation experiments.[82] The peaks at 1775, 1992 and 2057 cm^{-1} are also tentatively assigned to $Co(CO)_2(NO)$(*n*-heptane) based on previous work.[1,82,89]

The assignment of the band at 1970 cm^{-1} to $Co(CO)_3$ is not supported by previous experiments since the analogous experiment by Harris observed a decay on the picosecond timescale.[1] The peak at 1970 cm^{-1} decays away at the nanosecond timescale with a similar time to the growth of the peaks 2052, 2038 and 1953 cm^{-1} (27 $\pm$ 2) as seen in Figure 2.14. The $Co(CO)_3$ species formed is theorised to be a 15 electron radical quartet or doublet species, which is highly reactive and would react with the parent to form a dimeric species, something that is tentatively assigned to the bands at 2052, 2038 and 1953 cm^{-1} peaks. We will return to this assignment later.

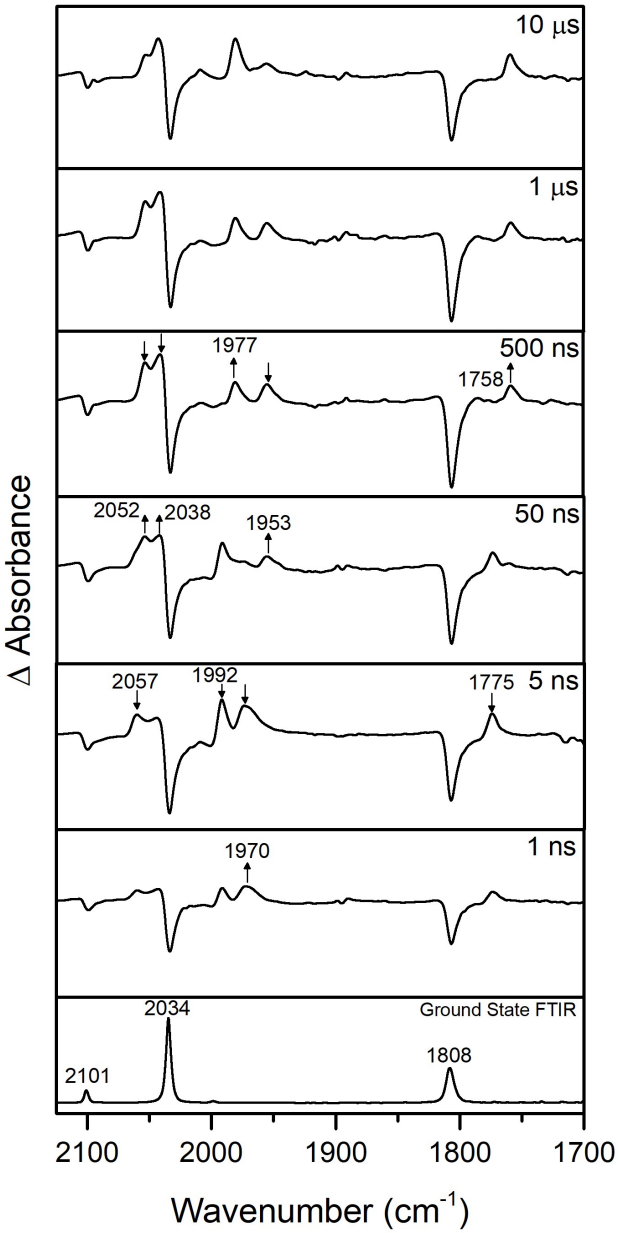

Figure 2.13: ns-TRIR of $Co(CO)_3(NO)$ in *n*-heptane following a 355 nm excitation.

The rate of decay of the $Co(CO)_2(NO)$(*n*-heptane) species can be seen in Figure 2.15 along with the decay of the original parent complex, $Co(CO)_3(NO)$. This decay does not match with the measurable growth of any of the observed bands in this experiment. As such we assume the presence of another species, which displays no clear bands in the IR spectrum at this concentration. This

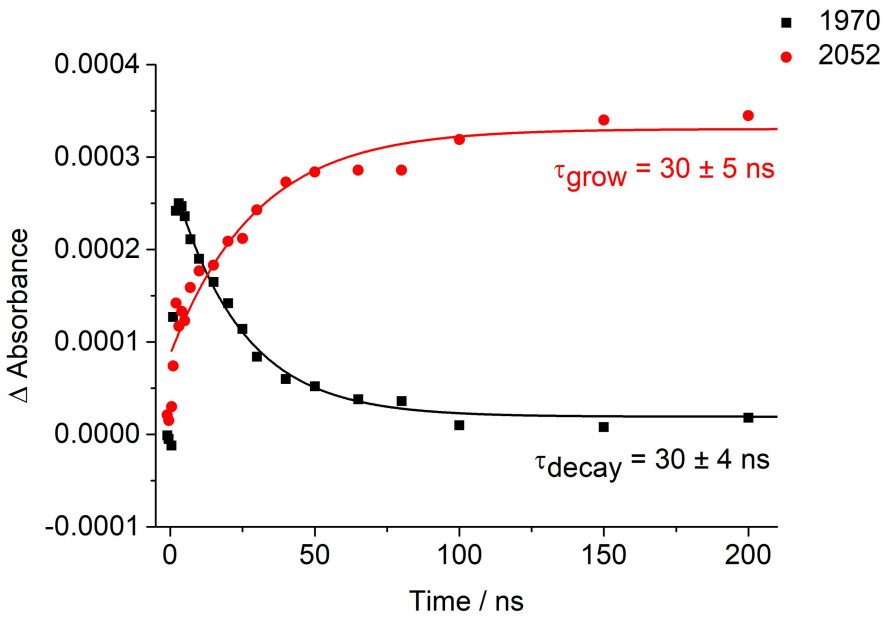

Figure 2.14: Kinetic traces from ns-TRIR of $Co(CO)_3(NO)$ in *n*-heptane following a 355 nm excitation of peaks at 1970 cm^{-1} ($Co(CO)_3$) and 2052 cm^{-1}.

can be done as when a species decays, due to the law of conservation of mass, it must decay to another species. These bands are likely broad and featureless with much lower extinction coefficients than the visible bands. It should be noted though that the parent bleach at 2034 cm^{-1} displays some gradual recovery during the first 250 ns of the experiment, which suggests a band growing in at this wavenumber.

The peaks at 2052, 2038 and 1953 cm^{-1}, assigned to a dimeric species, also decay during the course of the experiment on a microsecond timescale. The last two peaks at 1977 and 1758 cm^{-1} both grow in over the timeframe of the experiment and do not decay and as such are due to a long-lived species. The kinetics of this species along with the decay of the dimeric species from earlier are shown in Figure 2.16.

From the analysis of this TRIR experiment, an early tentative reaction pathway seen in Figure 2.17 is proposed. There are both similarities and differences between these ns-TRIR and the conclusions drawn from the picosecond experiments carried out by Harris. One notable difference is that our experiment did not observe the peaks at 1949 and 1684 cm^{-1} assigned to the T_1 state by Harris

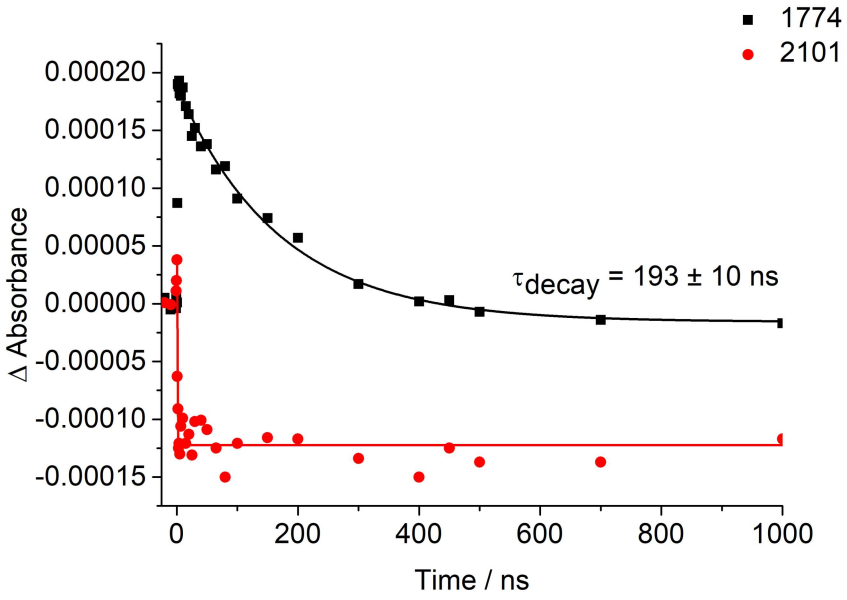

Figure 2.15: Kinetic traces from ns-TRIR of $Co(CO)_3(NO)$ in *n*-heptane following a 355 nm excitation of a peak at 1774 cm^{-1} assigned to $Co(CO)_2(NO)$(*n*-heptane) and following the bleach of a peak at 2101 cm^{-1} assigned to $Co(CO)_3(NO)$.

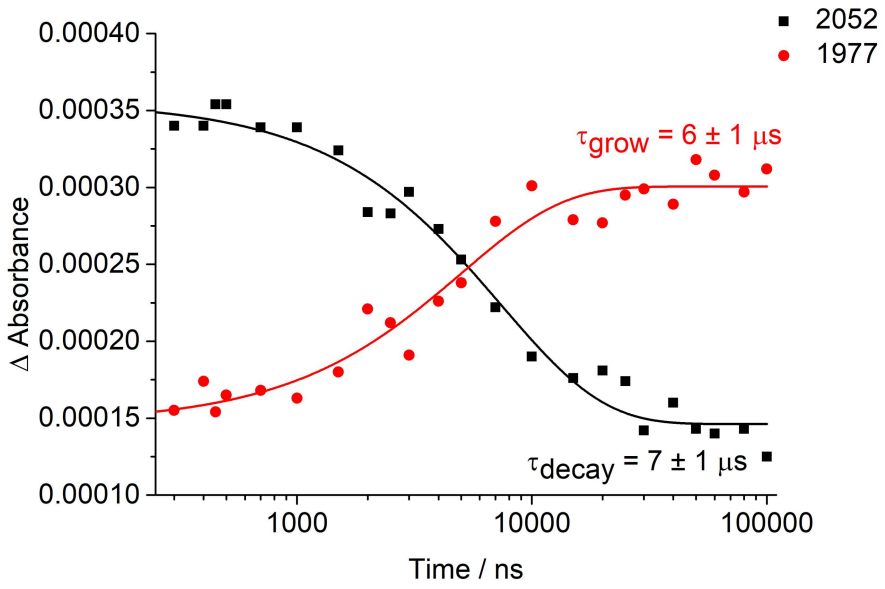

Figure 2.16: Kinetic trace from ns-TRIR of $Co(CO)_3(NO)$ in *n*-heptane following a 355 nm excitation of the peak at 2052 cm^{-1} assigned to a dimeric species and a peak at 1977 cm^{-1} assigned to a long-lived species.

and so additional experiments were carried out to repeat their experiment on the picosecond timescale using a 400 nm pump pulse on the Nottingham apparatus.[1]

The TRIR spectrum, obtained 1 ps after 400 nm excitation of $Co(CO)_3(NO)$

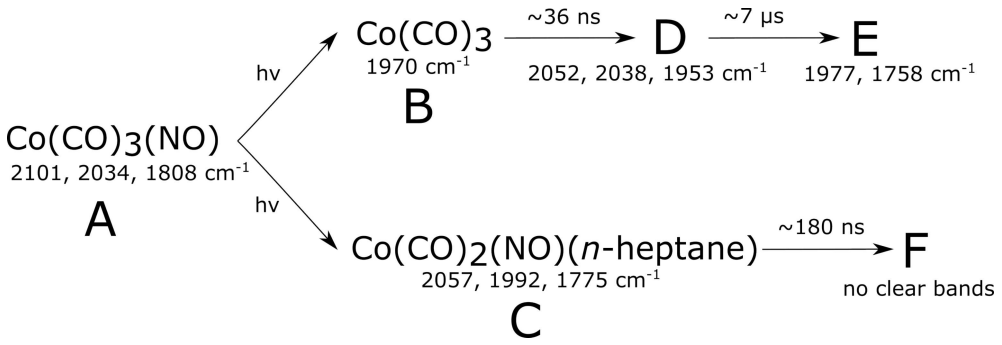

Figure 2.17: Proposed reaction pathway observed following irradiation of $Co(CO)_3(NO)$ in *n*-heptane following a 355 nm excitation on the nanosecond timescale.

clearly shows a bleach of the three parent bands at 2101, 2034 and 1808 cm^{-1} and the growth of a new peak at 1970 cm^{-1} as shown in Figure 2.18. This peak at 1970 cm^{-1} grows in <1 ps, which matches the observations of Harris and is again, based off previous work, tentatively assigned $Co(CO)_3$.[1] Harris observed a 11 ± 1 ps decay of this species, but in our experiment, consistent with our previous nanosecond experiment, no decay of this peak is observed on the picosecond timescale.

There is additionally a peak at 2007 cm^{-1}, also growing in <1 ps, which has a decay time of 20 (± 4) ps as seen in Figure 2.19. Harris did not report this band, but did note a peak at 1755 cm^{-1}, which had a growth of <1 ps and decay of 11 (± 1) ps assigned to $^3Co(CO)_2(NO)$ (T_1). No carbonyl peak was reported for this species in Harris' work due to intense peaks from both CO and NO loss pathways observed at the higher concentrations used in their experiments.[1] The 1755 cm^{-1} peak detected by Harris had an absorbance of 0.0005 A at a concentration 35 times greater than we used in our experiments so it is possible that this peak may not be detected in our experiments. DFT calculations predict that the carbonyl bands for $^3Co(CO)_2(NO)$ (T_1) would be at 1999 and 2055 cm^{-1} and there is a very small broad and featureless bump around 2067 cm^{-1} in our experiment, which could be possibly attributed to $^3Co(CO)_2(NO)$ as could the peak at 2007 cm^{-1}.

A peak was observed to grow in at 2025 cm^{-1}, and the TRIR kinetic trace is

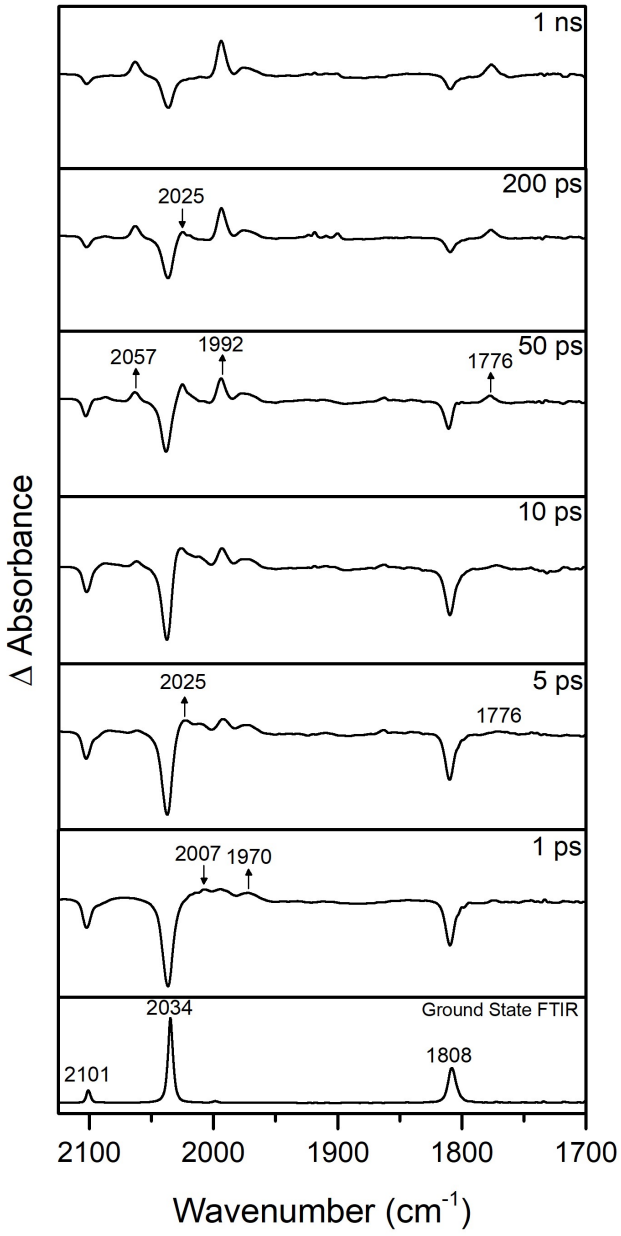

Figure 2.18: ps-TRIR of $Co(CO)_3(NO)$ in *n*-heptane following a 400 nm excitation.

shown in Figure 2.20. A band at 2025 cm^{-1} was also observed by Harris with a decay of 170 ($\pm$ 12) ps and was assigned to vibrationally hot $Co(CO)_3(NO)$.[1] A hot species is a compound which has a vibrational state centred on a transition between two excited vibrational states.[93] In the experiment by Harris other bands at 2085 and 1775 cm^{-1} were assigned to vibrationally hot $Co(CO)_3(NO)$, but

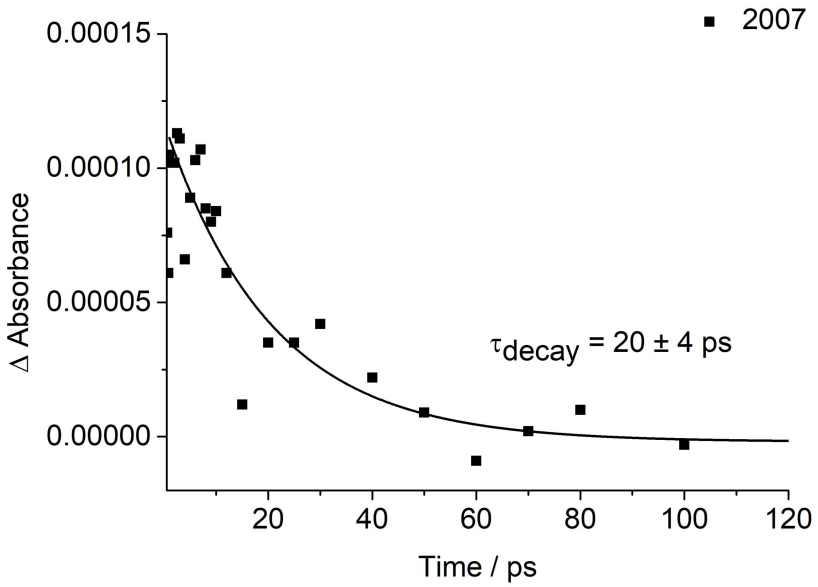

Figure 2.19: Kinetic trace from ps-TRIR study of $Co(CO)_3(NO)$ in *n*-heptane following a 400 nm excitation of a peak at 2007 cm^{-1} tentatively assigned to $^3Co(CO)_2(NO)$.

possibly due to lower concentration in our experiment, a peak at 2085 cm^{-1} may not be visible due to signal to noise issues. The parent bleach at 1808 cm^{-1} displays an apparent slower decay (2 ps) than the other two parent bands at 2101 and 2034 cm^{-1} (0.8 ps) which is consistent with a band at this location due to another species growing in under the parent bleach.

The final three peaks observed in our experiment are at 2059, 1992 and 1776 cm^{-1}, which were long-lived on the timescale of this experiment and can be assigned to $Co(CO)_2(NO)$(*n*-heptane) based on matching wavenumbers with that of the work by Harris. The kinetics of this species are shown in Figure 2.21 and no decay is observed, which is consistent with our nanosecond experiment. Harris observed the decay of this species on the picosecond timescale.[1]

As noted above, our experiments were performed at a concentration at least an order of magnitude lower than the experiments carried out by Harris and we notably did not observe any detectable signals due to the $^3Co(CO)_3(NO)$ T_1 (1949 and 1684 cm^{-1}), T_2, or T_3 (1913 and 1715 cm^{-1}) species that were reported by Harris. We tentatively assigned $^3Co(CO)_2(NO)$ and the observation of the decay

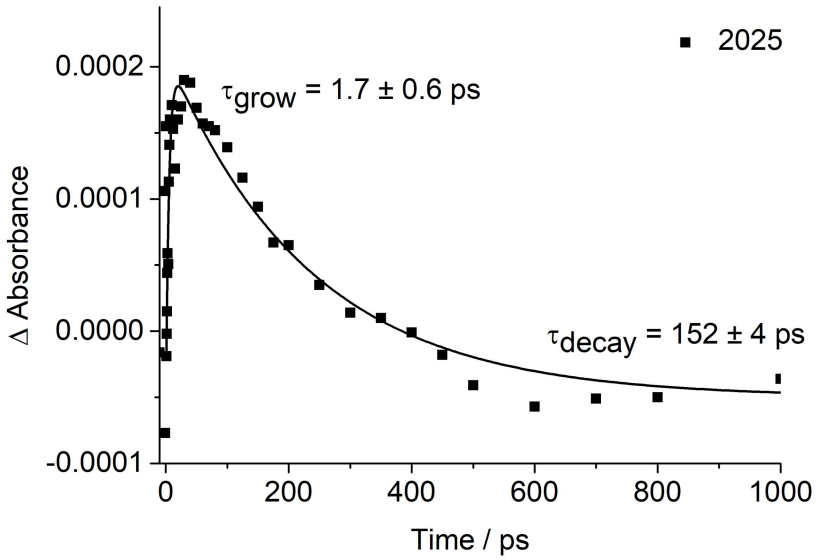

Figure 2.20: Kinetic trace from ps-TRIR of $Co(CO)_3(NO)$ in *n*-heptane following a 400 nm excitation of a peak at 2025 cm^{-1} assigned to vibrationally hot $Co(CO)_3(NO)$.

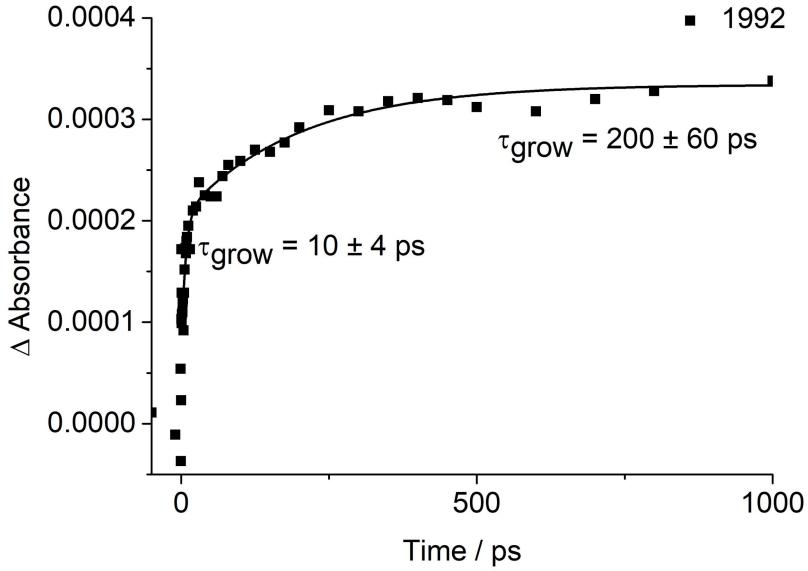

Figure 2.21: Kinetic trace from ps-TRIR of $Co(CO)_3(NO)$ in *n*-heptane following a 400 nm excitation of a peaks at 1992 cm^{-1} assigned to $Co(CO)_2(NO)$(*n*-heptane).

of $^3Co(CO)_2(NO)$ T_1 was made. There are again both similarities and differences between these ps-TRIR conducted here and the experiments reported by Harris. The one difference between our experiments and those conducted by Harris is

the large variation in concentration. To investigate this further, 400 nm ps-TRIR experiments were repeated, but at a much higher concentration than previously used in this work to try to closer replicate the concentration of the experiments reported by Harris.

The ps-TRIR spectra of the higher concentration solution can be seen in Figure 2.22 where more peaks are visible when compared with the order of magnitude lower concentration experiment. The band at 1970 cm^{-1} assigned to $Co(CO)_3$, observed in both Harris work and our previous experiments, is seen again along with the previously observed band at 2007 cm^{-1} tentatively assigned to $^3Co(CO)_2(NO)$. In this higher concentration experiment a peak at 1747 cm^{-1} is now observable, which has very similar kinetics to the band at 2007 cm^{-1} and could possibly be the missing NO band of $^3Co(CO)_2(NO)$ that was not detected in the order of magnitude lower concentration experiment. Harris reported a band assigned to $^3Co(CO)_2(NO)$ at 1755 cm^{-1} and the apparent difference could be due to the different experimental set-ups and possibly calibration in the Harris experimental setup. We re-checked the calibration and our values of parent bleach are consistent with FTIR measurements.

In the higher concentration experiment, a band at 1633 cm^{-1} is now observed, which has a growth of 3 ($\pm$ 1) ps and then decays away at 10 ($\pm$ 2) ps. This peak grows in with a similar kinetic profile to the band at 2017 cm^{-1} meaning they could be assigned to the same species. DFT calculations of the S_1 state of $Co(CO)_3(NO)$ were performed by both Harris and us utilising the new maximum overlap method to optimise towards this excited state singlet structure.[94] The maximum overlap method works by modifying the orbital selection step in the SCF procedure by choosing orbitals that most resemble those from the previous cycle rather than those with lowest energies. This allows for more easy optimisation towards an excited state. The computationally predicted values reported by Harris are 2067, 2040, 1998 and 1659 cm^{-1} and our predicted values are 2053, 2024, 1989 and 1643 cm^{-1}. There is some expected variation between the com-

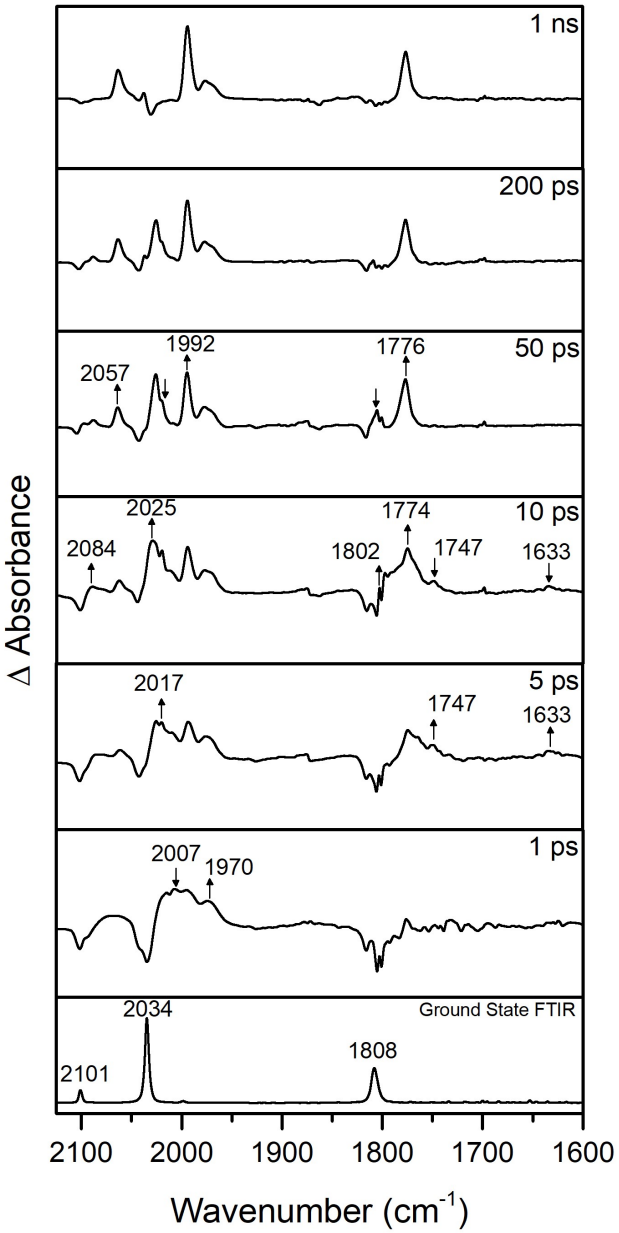

Figure 2.22: ps-TRIR of an order of magnitude higher concentration solution of $Co(CO)_3(NO)$ in *n*-heptane following a 400 nm excitation.

putational results of us and Harris due to a difference in methods and basis sets used. Some of these calculated values display reasonable agreement with the experimentally observed peaks at 1633 and 2017 cm^{-1}. Given the error of DFT calculations, particularly for excited state singlets, and the fact that in the region between 1965 to 2090 cm^{-1} there are many overlapping bands, a possible

very tentative proposed structure for both the 2017 and 1633 cm^{-1} peaks is the S_1 state of $Co(CO)_3(NO)$ due to similarity to predicted values of 2024 and 1643 cm^{-1}.

In the order of magnitude lower concentration experiment, a peak at 2025 cm^{-1} was observed which was assigned to vibrationally hot $Co(CO)_3(NO)$. Based on the previous work by Harris it was proposed that two other bands, not visible in that experiment, should also be observed which were at 2085 and 1775 cm^{-1}. In this order of magnitude higher concentration experiment bands at both 2084 and 1774 cm^{-1} are observed, which have similar kinetic profiles to that of the peak at 2025 cm^{-1}. This allows for a confident assignment of the peaks at 2085, 2025 and 1775 cm^{-1}, growing in at 1.7 ($\pm$ 0.6) ps and decaying away at 152 ($\pm$ 4) ps, being assigned to vibrationally hot $Co(CO)_3(NO)$.

The previous two assignments of the S_1 state of $Co(CO)_3(NO)$ and vibrationally hot $Co(CO)_3(NO)$ both decaying back to the parent species can be further supported by inspection of the parent recovery kinetics of the peak at 2101 cm^{-1}, which are shown in Figure 2.23. The parent recovery kinetics of this peak can be fitted with a biexponential growth, with an initial growth time of 8 ($\pm$ 3) ps and a later growth time of 170 ($\pm$ 60) ps. The initial growth of 8 ps matches the decay of the S_1 state of $Co(CO)_3(NO)$ and the later growth of 170 ps matches the decay of vibrationally hot $Co(CO)_3(NO)$.

There is a peak at 1802 cm^{-1} that overlaps with the parent bleach at 1808 cm^{-1} and as such is very difficult to untangle, but the kinetics of this peak grow in around 20 ps and decay away around 100 ps. The assignment of this peak requires further work and this was not possible due to COVID restrictions.

The last bands examined in this experiment are the set at 2057, 1992 and 1776 cm^{-1} which are the peaks assigned to the long-lived alkane species, $Co(CO)_2(NO)$(*n*-heptane). The kinetic trace of the peaks at 2007 and 1776 cm^{-1}, assigned to $^3Co(CO)_2(NO)$ and $Co(CO)_2(NO)$(*n*-heptane) respectively, can be seen in Figure 2.24. It is clear that $^3Co(CO)_2(NO)$ decays to form

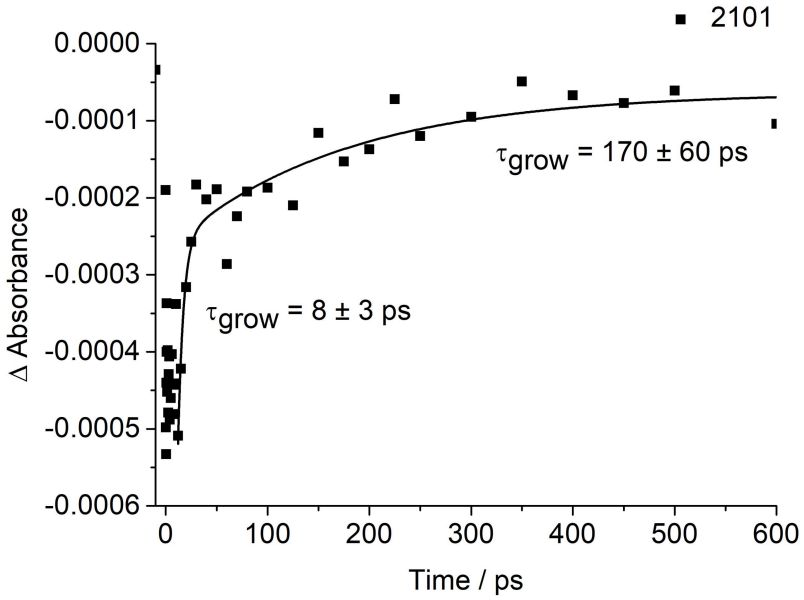

Figure 2.23: Kinetic trace from ps-TRIR of a order of magnitude higher concentration solution of $Co(CO)_3(NO)$ in *n*-heptane of the parent recovery after a 400 nm excitation of a peak at 1992 cm^{-1} assigned to $Co(CO)_3(NO)$.

$Co(CO)_2(NO)$(*n*-heptane) and this is in agreement with previous experiments.

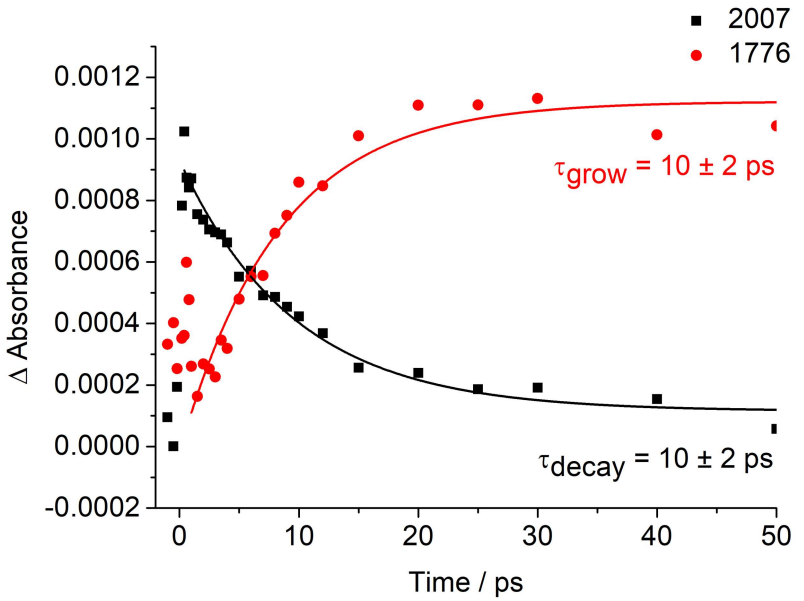

Figure 2.24: Kinetic trace from ps-TRIR of a order of magnitude higher concentration solution of $Co(CO)_3(NO)$ in *n*-heptane following a 400 nm excitation of the peak at 2007 cm^{-1} assigned to $^3Co(CO)_2(NO)$ and the peak at 1776 cm^{-1} assigned to $Co(CO)_2(NO)$(*n*-heptane).

Our order of magnitude higher concentration TRIR experiments have many

more similarities with the results reported by Harris compared with our low concentration data but there is also some differences, *i.e* the triplet states of $Co(CO)_3(NO)$ were not observed in our experiments. To further investigate, we have performed a high concentration experiment on the nanosecond timescale following 355 nm excitation.

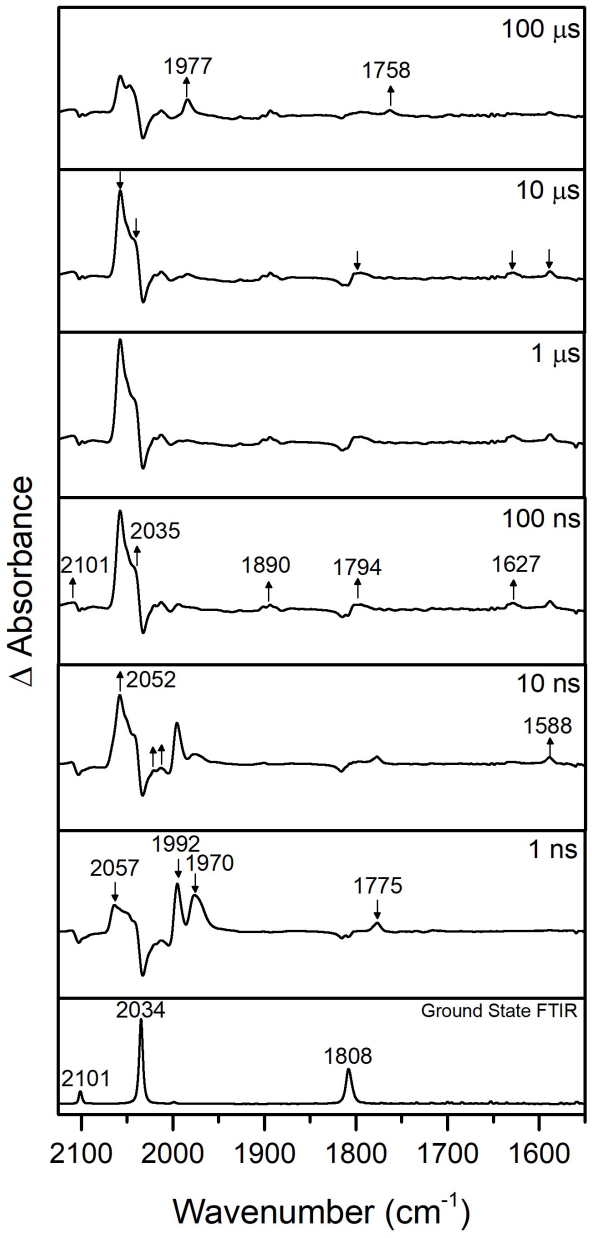

Figure 2.25: ns-TRIR of a order of magnitude higher concentration solution of $Co(CO)_3(NO)$ in *n*-heptane following a 355 nm excitation.

The ns-TRIR spectra of the order of magnitude higher concentration solution can be seen in Figure 2.25 where more peaks are observable when compared with the order of magnitude lower concentration experiment. The decay of the peaks assigned to both $Co(CO)_3$ (1970 cm^{-1}) and $Co(CO)_2(NO)$(*n*-heptane) (2057, 1992 and 1775 cm^{-1}) can be seen, but their decay is significantly faster than in our low concentration experiments. The decay time constant for $Co(CO)_3$ is now 7 ns (30 ns in low concentration experiment) and for $Co(CO)_2(NO)$(*n*-heptane) is approximately 35 ns (193 ns in low concentration experiment). The 7 ns decay of $Co(CO)_3$ again matches well with the growth of new peaks at 2052 and 2035 cm^{-1}, but in this experiment no band at 1953 cm^{-1} can be observed suggesting there may be two secondary photoproducts. There is an additional peak present at 1588 cm^{-1} that also has a similar kinetic profile to that of the bands at 2052 and 2035 cm^{-1} and suggest it is due to the same species. The band at 1588 cm^{-1} is possibly assigned to either a bent nitrosyl or potentially an η^2-side on coordination. The faster decay of both $Co(CO)_3$ and $Co(CO)_2(NO)$(*n*-heptane) compared with the order of magnitude lower concentration experiment is consistent with either dimerisation of $Co(CO)_3$ or reaction with the parent. For $Co(CO)_2(NO)$(*n*-heptane), like many metal carbonyl alkane intermediates, it is likely to be forming a dimer by reaction with the parent. The exact structure of these complexes can vary but their general structure is usually just a combination of the parent molecule and the decaying reactive species.

There are some additional weak absorbances at 2105, 1890, 1794 and 1627 cm^{-1}, which are not observed in the low concentration experiment that are not reported in the previous experiments of Harris. The peaks at 2105 and 1890 cm^{-1} grow in over approximately 40 ns and then partially decay away to around 60 % intensity at approximately 120 ns where a constant absorbance is then maintained for the remainder of the experiment. There are also some peaks that grow in around 2015 and 2007 cm^{-1} which also grow in around 40 ns and potentially partially, decay but they are slighty obscured by the parent bleach

and so are very difficult to analyse. The peaks at 1794 and 1627 cm^{-1} both grow in over approximately 50 ns and then decay away around 30 μs.

Finally, two peaks at 1977 and 1758 cm^{-1} start to grow in around 30 μs that continue to grow in for the duration of the experiment. These peaks were also observed in the order of magnitude lower concentration experiment growing in around 6 μs. The much later growth time of these peaks in the high concentration experiments suggests that this photoproduct is potentially the product of a reaction between two other photoproducts as opposed to a reaction between a photoproduct and the parent molecule.

From our experiments it is clear that there is a concentration dependence on the reaction pathway upon irradiation of $Co(CO)_3(NO)$ in *n*-heptane. This can affect the reaction kinetics, what IR peaks are visible and also potentially which products are formed.

Although there are some differences with the experiments of Harris, one of the assignments is that of $Co(CO)_2(NO)$(*n*-heptane) where we have observed its formation and decay. We wish to investigate the wavelength dependence on its formation along with the overall photophysics and photochemistry of $Co(CO)_3(NO)$. To achieve this we have repeated both ns and ps-TRIR experiments on $Co(CO)_3(NO)$ following 266 nm excitation.

2.2.2 TRIR Studies of $Co(CO)_3(NO)$ in *n*-Heptane Using 266 nm Excitation

The TRIR spectrum, obtained 1 ns after 266 nm excitation can be seen in Figure 2.26 where the parent bleach can be seen along with the previously observed peaks at 2058, 1992, 1970 and 1775 cm^{-1} assigned to $Co(CO)_3$ and $Co(CO)_2(NO)$(*n*-heptane).

The peak at 1970 cm^{-1} assigned to $Co(CO)_3$ decays away at 45 ($\pm$ 7) ns and another set of bands at 2052, 2038 and 1952 grow in at 50 ($\pm$ 5) ns which can be seen in Figure 2.27. In our previous ns-TRIR following 355 nm excitation

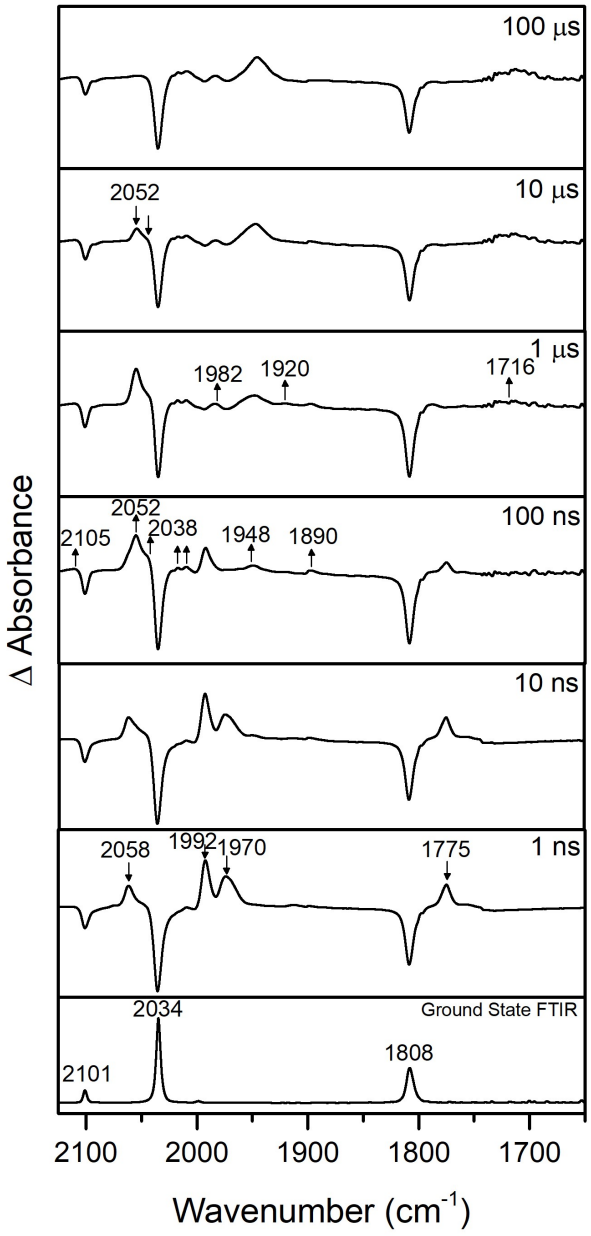

Figure 2.26: ns-TRIR of $Co(CO)_3(NO)$ in *n*-heptane following a 266 nm excitation.

the same decay and growth pattern was noted, but on a very slightly faster time scale of 30 ns, which might be due to either difference in wavelength of excitation or variation in parent concentration. There are peaks also observed at 2105, 2015, 2007 and 1890 cm^{-1} that follow a similar pattern to that seen in our previous order of magnitude higher concentration 355 nm ns-TRIR where both

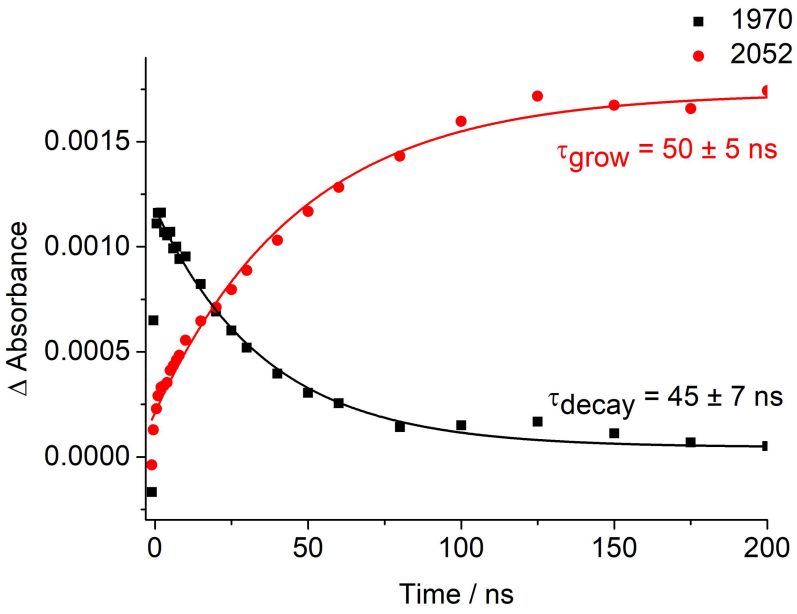

Figure 2.27: Kinetic traces from ns-TRIR of $Co(CO)_3(NO)$ in *n*-heptane following a 266 nm excitation of peaks at 1970 cm^{-1} ($Co(CO)_3$) and 2052 cm^{-1}.

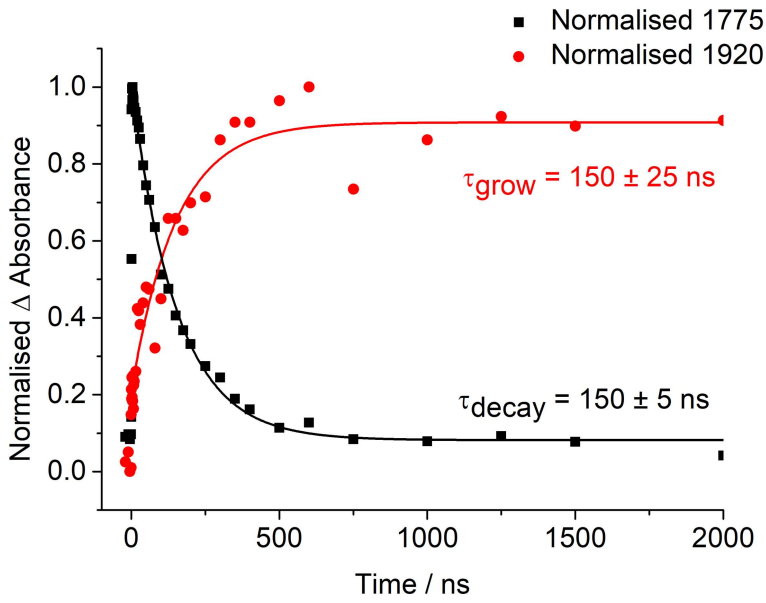

Figure 2.28: Normalised kinetic traces from ns-TRIR of $Co(CO)_3(NO)$ in *n*-heptane following a 266 nm excitation of a peak at 1775 cm^{-1} assigned to $Co(CO)_2(NO)$(*n*-heptane) and a peak at 1920 cm^{-1}.

2105 and 1890 cm^{-1} grow in and then partially decay, but they are at different band positions and both 2015, 2007 cm^{-1} do not decay and are due to unknown secondary photoproducts. These peaks also grow in slightly slower in this 266 nm experiment (70 ns) compared with the previous 355 nm experiment (40 ns).

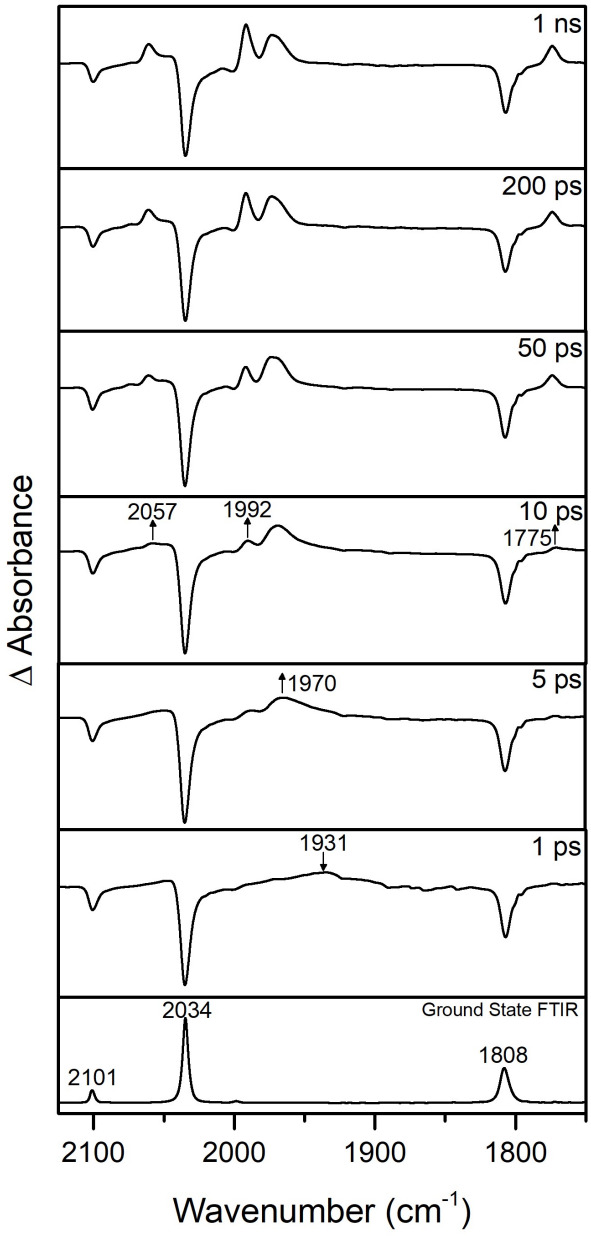

Figure 2.29: ps-TRIR of $Co(CO)_3(NO)$ in *n*-heptane following a 266 nm excitation.

The rate of decay of the $Co(CO)_2(NO)$(*n*-heptane) species can be seen in Figure 2.28 along with the growth kinetic of the peak at at 1920 cm^{-1}. There were no other observable peaks that displayed the same kinetic profile as the peak at 1920 cm^{-1} so it is possible that the other peaks for this species were hidden by other bands or parent bleaches.

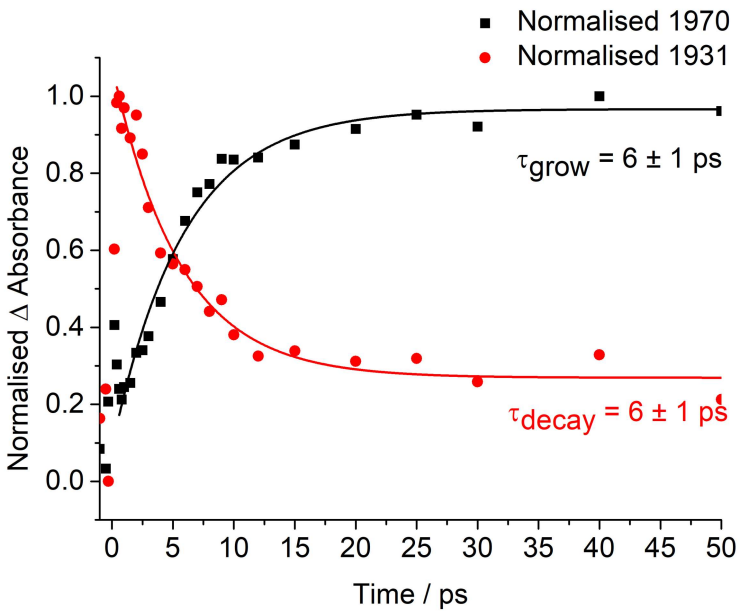

Figure 2.30: Normalised kinetic traces from ps-TRIR of $Co(CO)_3(NO)$ in *n*-heptane following a 266 nm excitation of a peak at 1931 cm^{-1} and 1970 cm^{-1} assigned to $Co(CO)_3$.

The other long-lived peaks in this experiment can be seen at 1982, 1948 and 1716 cm^{-1}, which are all still visible at 100 μs. Both 1943 and 1716 cm^{-1} have matching kinetics that can be fitted with a biexponential growth with time constants of 95 ($\pm$ 20) ns and 4.5 ($\pm$ 0.8) μs. The kinetic profile of the peak at 1982 cm^{-1} are difficult to untangle as there is significant overlap with the peaks at 1992 and 1970 cm^{-1} at early times.

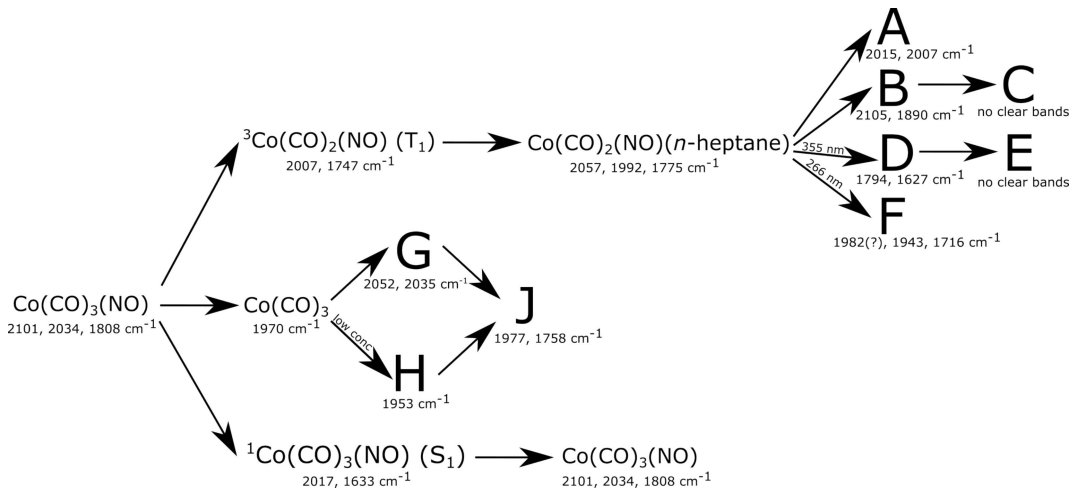

Figure 2.31: Proposed reaction pathway observed following irradiation of $Co(CO)_3(NO)$ in *n*-heptane following excitation on the picosecond and nanosecond timescale.

The final experiment conducted with $Co(CO)_3(NO)$ was a ps-TRIR experiment following a 266 nm excitation, shown in Figure 2.29. At 1 ps there is a very broad growth centred at 1931 cm^{-1}, which appears to decay away at 6 ($\pm$ 1) ps.

One of the notable differences between this 266 nm excitation experiment compared with our previous 400 nm excitation is that the peak at 1970 cm^{-1} assigned to $Co(CO)_3$ appears to grow in much slower. In both the 400 nm excitation experiments the peak at 1970 cm^{-1} grows in <1 ps whereas in this experiment the band at 1970 cm^{-1} appears to grow in at 6 ($\pm$ 1) ps, which matches with the decay of the broad band centred around 1931 cm^{-1} shown in Figure 2.30.

The only other peaks present in this experiment are 2057, 1992 and 1775 cm^{-1} assigned to $Co(CO)_2(NO)$(*n*-heptane) which is best fitted with a biexponential growth with an intial growth of 9 ($\pm$ 2) ps and a later growth of 167 ($\pm$ 21) ps which is mostly consistent with the time constants from our ps-TRIR following 400 nm excitation.

To summarise, an initial tentative reaction pathway is suggested here in Figure 2.31. It is acknowledged that this is very likely an incomplete picture with a few peaks having kinetics obscured by other peaks and the potential for many other peaks to not be observable.

2.2.3 DFT Calculations to Aid the Assignments of $Co(CO)_3(NO)$ Dimers

As shown in Figure 2.31 we have able to detect some new intermediates formed following irradiation of $Co(CO)_3(NO)$ in *n*-heptane that were not observed or reported by Harris. However, it is clear that many of the species formed still remain unassigned. The observed IR bands of these species and their kinetics in both high and low concentration experiments are given in Table 2.2.

In order to support possible assignments of the unknown species summarised in Figure 2.31, potential structures of the various long-lived species observed in these TRIR experiments were investigated using DFT calculations. The geome-

Complex	Wavenumber / cm^{-1}	Z_{grow}		Z_{decay}	
		Low	High	Low	High
A	2015, 2007, 1982, 1943, 1716	193 ns	40 ns	long-lived	
B	2105, 1890	N/A	40 ns	N/A	120 ns
C	N/A	N/A			
D	1794, 1627	N/A	50 ns	N/A	30 μs
E	N/A	N/A			
F	2052, 2035	30 ns	7 ns	7 μs	40 μs
G	1977, 1758	7 μs	40 μs	long-lived	

Table 2.2: Table of unassigned species from Figure 2.31 showing wavenumbers of observed peaks in our TRIR experiments along with their kinetic profiles.

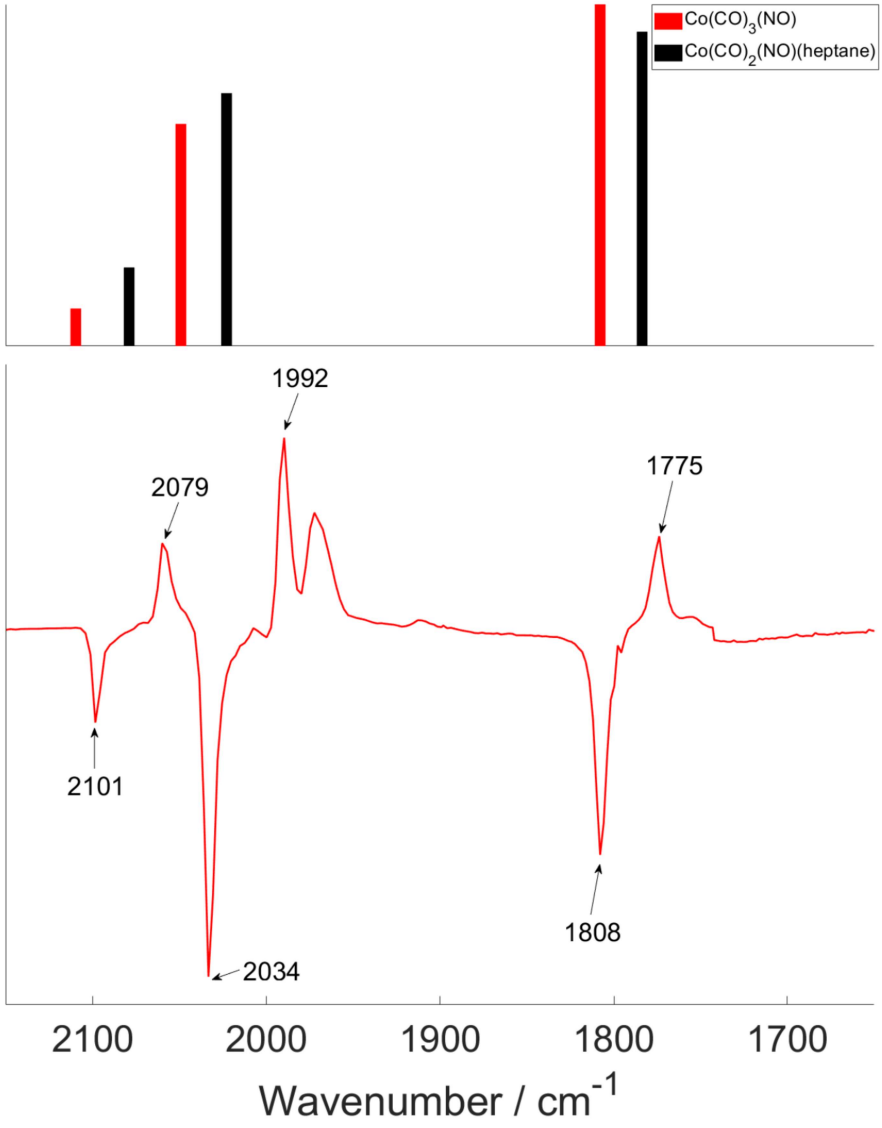

Figure 2.32: Bottom: experimental spectra from the TRIR experiments with the peaks assigned to both $Co(CO)_3(NO)$ and $Co(CO)_2(NO)$(*n*-heptane) labelled. Top: calculated vibrational frequencies of both $Co(CO)_3(NO)$ (red) and $Co(CO)_2(NO)$(*n*-heptane) (black).

tries of these structures were optimised and then their IR frequencies calculated to allow for comparison to experimentally observed bands. The first step is to obtain an approximate benchmark for the calculations we are performing by comparison of a calculated set of IR bands for $Co(CO)_3(NO)$ and $Co(CO)_2(NO)$(*n*-heptane), where the assignment is not in doubt, then compare them to experimental FTIR bands. The experimentally observed bands for $Co(CO)_3(NO)$ are 2101, 2034 and 1808 cm^{-1} and from the calculation were 2199, 2134 and 1966 cm^{-1}. As covered in the Chapter 1 introduction on computational theory and the section on anaharmonic corrections, it is common practice to apply scale factors to calculated IR frequencies as they are often systematically too large. For the M06 method used along with the basis sets used in these calculations the appropriate scale factor is 0.96.[65,66,95] Using this scale factor gives calculated IR frequencies of 2111, 2048 and 1887 cm^{-1} for $Co(CO)_3(NO)$, which is a slightly better fit for the CO ligands, but still quite far off for NO ligands. It is found that if a scale factor of 0.92 for just the NO ligands is used instead of 0.96 then a much better match is achieved. The calculated IR frequencies are then found to be 2111, 2048 and 1808 cm^{-1}, which is a much better match for the NO ligand as it is closer to the experimentally observed value. The $Co(CO)_2(NO)$(*n*-heptane) has experimentally observed peaks at 2057, 1992 and 1775 cm^{-1} in both our TRIR and the experiments reported by Harris and our scaled DFT calculations give values of 2079, 2022 and 1784 cm^{-1}. A comparison of these calculated vibrational frequencies with the experimental spectra is given in Figure 2.32. It can be seen that the shift to lower wavenumber upon *n*-heptane coordination is correctly predicted by DFT and agrees with the experimental data and both the CO and NO bands show a reasonable agreement.

A variety of structures were optimised, their vibrational frequencies calculated scale factors applied and the results are shown in Table 2.3. The data in this table can be compared with those in Table 2.2 to make tentative suggestions as to the structures of some of the intermediate species formed in these TRIR experiments.

Complex	Charge	Multiplicity	NO Geometry	ν (CO and NO) /cm^{-1}
$(CO)_2(NO)Co(\mu\text{-}CO)Co(CO)_2(NO)$ (Eclipsed)	0	1	Linear	2111, 2079, 2054, 2049, 1929, 1822, 1751
$(CO)_2(NO)Co(\mu\text{-}CO)Co(CO)_2(NO)$ (Staggered)	0	1	Linear	2106, 2071, 2048, 2041, 1937, 1803, 1788
$(CO)_3Co(\mu\text{-}CO)Co(CO)_2(NO)$ (Eclipsed)	0	2	Linear	2115, 2069, 2055, 2053, 2049, 1903, 1771
$(CO)_3Co(\mu\text{-}CO)Co(CO)_2(NO)$ (Staggered)	0	2	Linear	2104, 2058, 2045, 2042, 2020, 1933, 1772
$(CO)_4Co\text{-}Co(CO)_3(NO)$	0	2	Bent	2119, 2065, 2056, 2046, 2037, 2027, 2015, 1684
$(CO)_3Co\text{-}Co(CO)_3$ (Eclipsed)	0	1	N/A	2124, 2063, 2043, 2042, 2024, 1998
$(CO)_3Co\text{-}Co(CO)_3$ (Staggered)	0	1	N/A	2120, 2064, 2041, 2031, 2021, 2019
$(CO)_3Co(\mu\text{-}CO)_2Co(CO)_2(NO)$	0	2	Bent	2118, 2080, 2061, 2058, 2054, 1917, 1898, 1687
$(NO)Co(\mu\text{-}CO)_3(NO)$	0	1	Linear	1989, 1814
$Co(CO)_4$	-1	1	N/A	1898
$Co(CO)(NO)(CH_4)_2$	0	1	Linear	2032, 1776

Table 2.3: Table of DFT optimised potential structures of intermediate species in the TRIR experiments of $Co(CO)_3(NO)$. The IR frequencies have been scaled by 0.96 for CO ligands and 0.92 for NO ligands.

Our starting point is to examine the reactivity and subsequent chemistry observed following the decay of $Co(CO)_2(NO)$(*n*-heptane). $Co(CO)_2(NO)$(*n*-heptane) decays at a faster rate (Z = 30 ns) at order of magnitude higher concentration compared to lower concentration (Z = 193 ns) and decay into a range of different species (A-E in Table 2.2). The increasing rate of decay of $Co(CO)_2(NO)$(*n*-heptane) with increasing parent concentration is consistent with the intermediate reacting with the parent, which is often observed in metal carbonyl photochemistry.[96–99]

Complex A from Table 2.2 has five observable peaks, some of which were only observable at the order of magnitude higher concentrations or using 266 nm excitation due to low peak absorbances. This is a fairly unique situation in that 2015 and 2007 cm^{-1} are visible following both 355 and 266 nm excitation whereas the bands at 1982, 1943 and 1716 cm^{-1} are only visible following 266 nm excitation. The peaks at 2015 and 2007 cm^{-1} grow in faster in the order of magnitude higher concentration experiments and all are long-lived on the timescale of the experiments meaning the resulting complex is fairly stable. A possible candidate for this complex could be $(CO)_2(NO)Co(\mu\text{-}CO)Co(CO)_2(NO)$ as this contains two 18 electron metal centres and would contain peaks in the carbonyl region, both terminal and bridging, along with the nitrosyl region. This complex could be formed by reaction of the alkane complex with the parent complex, after uncoordinated of the bound *n*-heptane.

Figure 2.33 shows an experimental spectrum from the order of magnitude higher concentration 266 nm experiment along with calculated vibrational frequencies of both staggered and eclipsed isomers of $(CO)_2(NO)Co(\mu\text{-}CO)Co(CO)_2(NO)$. There is reasonable agreement with multiple terminal carbonyl peaks, a peak in the staggered isomer attributed to the bridging carbonyl and also some signals in the nitrosyl region. It seems unlikely that only a single isomer would be formed in experiment and as such complex A is tentativley suggested to an isomeric mix of both staggered and eclipsed $(CO)_2(NO)Co(\mu\text{-}$

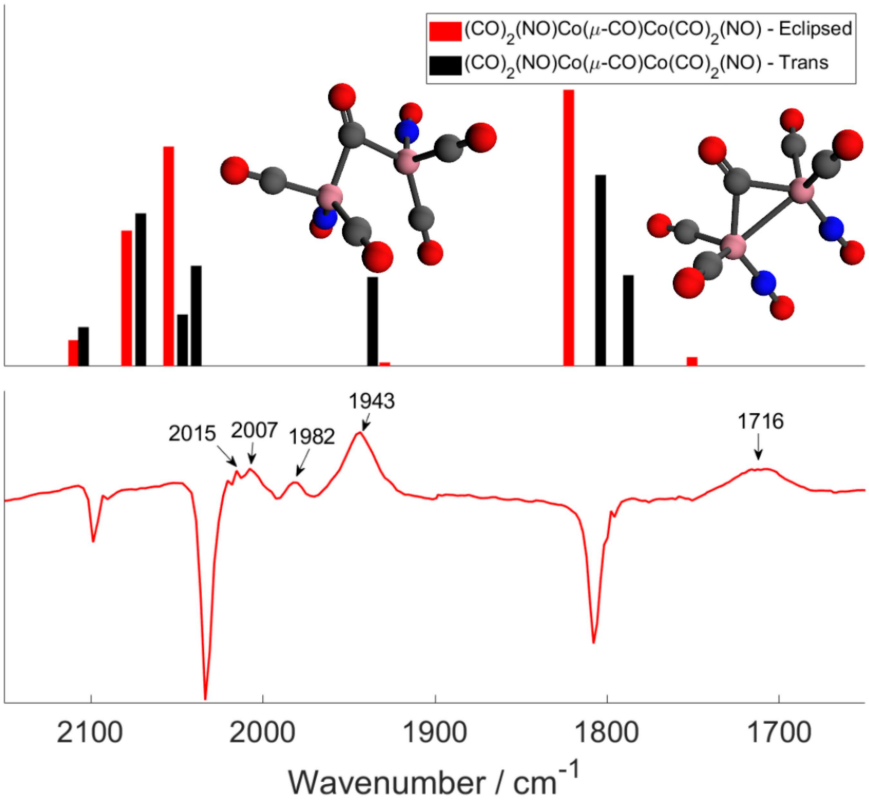

Figure 2.33: Bottom: experimental spectra from the TRIR experiments with the peaks assigned to 'Complex A' labelled. Top: calculated vibrational frequencies of both $(CO)_2(NO)Co(\mu\text{-}CO)Co(CO)_2(NO)$ - Eclipsed (red) and $(CO)_2(NO)Co(\mu\text{-}CO)Co(CO)_2(NO)$ - Staggered (black).

$CO)Co(CO)_2(NO)$. The most obvious difference between the two calculated spectra is the intensity of the peak attributed to the bridging carbonyl band close to 1950 cm^{-1}, which is much larger in the staggered isomer than the eclipsed one.

A possible reason why the peaks at 1982, 1943 and 1716 cm^{-1} are not visible in any of the 355 nm excitation experiments involving irradiation of $Co(CO)_3(NO)$ is due to the lesser amount of $Co(CO)_2(NO)$(n-heptane) being formed. If a smaller amount of $Co(CO)_2(NO)$(n-heptane) is formed then, in turn, the products which decay from $Co(CO)_2(NO)$(n-heptane) will also be produced in lower concentrations. In the order of magnitude lower concentration 355 nm experiment the peak at 1992 cm^{-1}, which is assigned to $Co(CO)_2(NO)$(n-heptane), has a max absorbance of around 0.0003 A. In the 266 nm experiments, which were only done at low concentration, the peak at 1992 cm^{-1} has a max absorbance of around 0.002 A. This much higher concentration of $Co(CO)_2(NO)$(n-heptane)

would allow for a larger amount of complex A to be formed as well as potentially a different isomeric mix following different excitation wavelength.

Complex B from Table 2.2 has two observable peaks at 2105 and 1890 cm^{-1}, which are both low in intensity and are only visible in the high concentration experiments. This species is fairly short-lived as it grows in around with a growth constant of around 40 ns and decays away with a decay constant of around 120 ns. These time constants suggest that this complex would be quite unstable and as such could potentially be assigned to one of the complexes from Table 2.3 with a multiplicity of two and a linear nitrosyl ligand. The only calculated species from Table 2.3 which fits this description are the eclipsed and staggered isomers of $(CO)_3Co(\mu\text{-}CO)Co(CO)_2(NO)$. The way in which this molecule would form from $Co(CO)_2(NO)$(*n*-heptane) is unclear though as it would require a reaction with $Co(CO)_4$. $Co(CO)_4$ has been isolated in a high pressure CO matrix during the study of $Co_2(CO)_8$ and it has an experimentally observed band at 2012 cm^{-1}.[100] $Co(CO)_4$ has also been isolated in an Ar matrix before where it was found to have two FTIR bands, at 2025 and 2014 cm^{-1}.[82] Work by Moskovich *et al.* in 2006 on UV flash photolysis of $Co_2(CO)_8$ in solution and found that the species $Co(CO)_4$ displayed a very intense peak at 2011 cm^{-1} and was stable for around 40 μs. There is no visible intense peak in this area which has kinetics to match evidence suggesting the formation of $Co(CO)_4$

Figure 2.34 contains an experimental spectrum from the high concentration 355 nm experiment along with calculated vibrational frequencies of both staggered and eclipsed isomers of $(CO)_3Co(\mu\text{-}CO)Co(CO)_2(NO)$. There is reasonably good agreement with the terminal and bridging carbonyls, and the large number of peaks in one area could help to explain the broad looking nature of the band at 2105 cm^{-1}. Unfortunatley there is no nitrosyl peaks present in the experimental spectrum, which is assigned to complex B, and the predicted intensity of the nitrosyl band for both isomers of $(CO)_3Co(\mu\text{-}CO)Co(CO)_2(NO)$ is quite high. It could potentially be possible that its nitrosyl band is hidden behind either

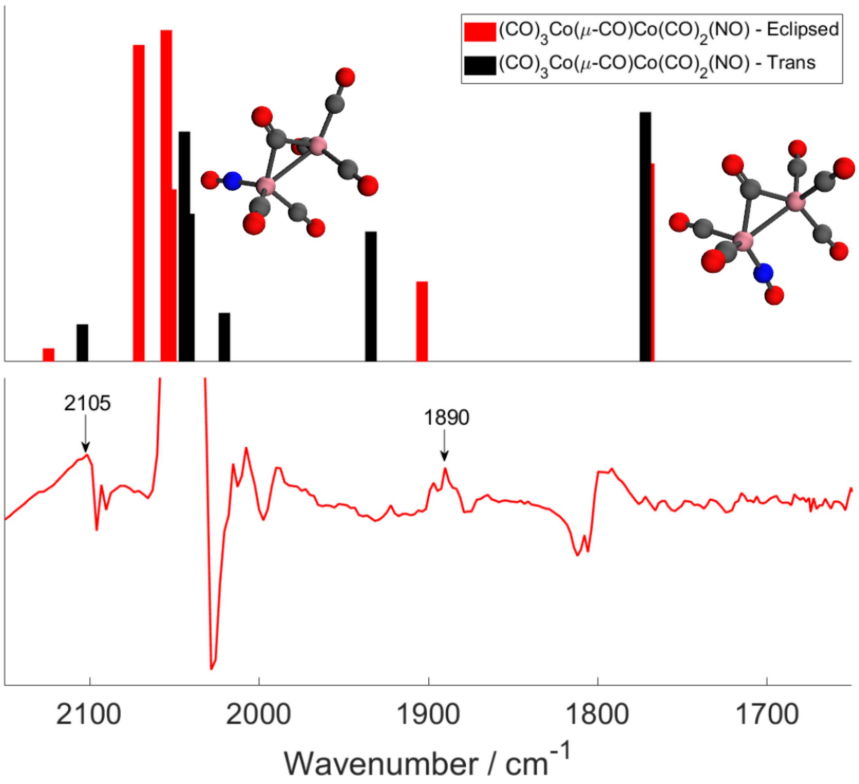

Figure 2.34: Bottom: experimental spectra from the TRIR experiments with the peaks assigned to 'Complex B' labelled. Top: calculated vibrational frequencies of both $(CO)_3Co(\mu\text{-}CO)Co(CO)_2(NO)$ - Eclipsed (red) and $(CO)_3Co(\mu\text{-}CO)Co(CO)_2(NO)$ - Staggered (black).

the parent bleach or the small positive growth at 1794 cm^{-1}, which is assigned to Complex D, which has a lifetime far greater than complex B. The missing nitrosyl peak, along with it not being entirely clear how $(CO)_3Co(\mu\text{-}CO)Co(CO)_2(NO)$ would be formed from $Co(CO)_2(NO)$(n-heptane) means that more work would be required in the future to allow for assignment of Complex B.

Complexes C and E display no observable bands in our TRIR experiments, but their formation is suggested by the decay of the complexes B and D whose decay does not match the growth of any observed peaks. Due to the lack of observable peaks to assign to these species they can also unfortunately not be assigned based on the data collected so far.

Complex D from Table 2.2 has two observable peaks at 1794 and 1627 cm^{-1} which can again only be seen in the high concentration experiments. Both of these peaks are outside of the terminal carbonyl region and as such could only be

assigned to bridging carbonyls or terminal nitrosyls, potentially linear or bent. Given the parent molecule of the system it is almost a certainty that this product contains terminal carbonyl ligands but the IR bands of this complex are likely hidden behind either parent bleaches or peaks of other intermediates in the experiment. It is a longer lived species than complex B by a significant margin with a decay 30 μs. Without any observable terminal carbonyl bands with matching kinetics to these peaks it is tough to make any kind of assignment with the data available so far but the peak at 1627 cm^{-1} potentially suggests a bent nitrosyl ligand being present in the molecule.

The next set of species to assign are formed following the decay of $Co(CO)_3$ which decays away faster than $Co(CO)_2(NO)$(*n*-heptane) and similarly decays at a faster rate (Z = 7 ns) at higher concentration compared to lower concentration (Z = 40 ns). This time $Co(CO)_3$ appears to decay into just one species, which is complex F in Table 2.2.

Complex F from Table 2.2 has three observable peaks at 2052, 2035 and 1953 cm^{-1}. The peak at 1953 cm^{-1} is not observable in the order of magnitude higher concentration experiment, which could again be potentially an isomeric effect or could potentially be due to a different species entirely. Given the instability of $Co(CO)_3$ due to being a radical it seems reasonable to assume that it could react with another molecule of $Co(CO)_3$ to quench and form a more stable dimer of the structure $(CO)_3Co\text{-}Co(CO)_3$.

Figure 2.35 shows an experimental spectrum from the order of magnitude lower concentration 355 nm experiment along with calculated vibrational frequencies of both staggered and eclipsed isomers of $(CO)_3Co\text{-}Co(CO)_3$. There is agreement between the calculated spectra and the experimentally observed peaks at 2052 and 2035 cm^{-1}, especially with the eclipsed isomer. There are no peaks in the calculated vibrational frequencies which align very well with the peak at 1953 cm^{-1} for either of the isomers. This is potentially further evidence that the peak at 1953 cm^{-1} is simply due to another species, with similar kinetics to

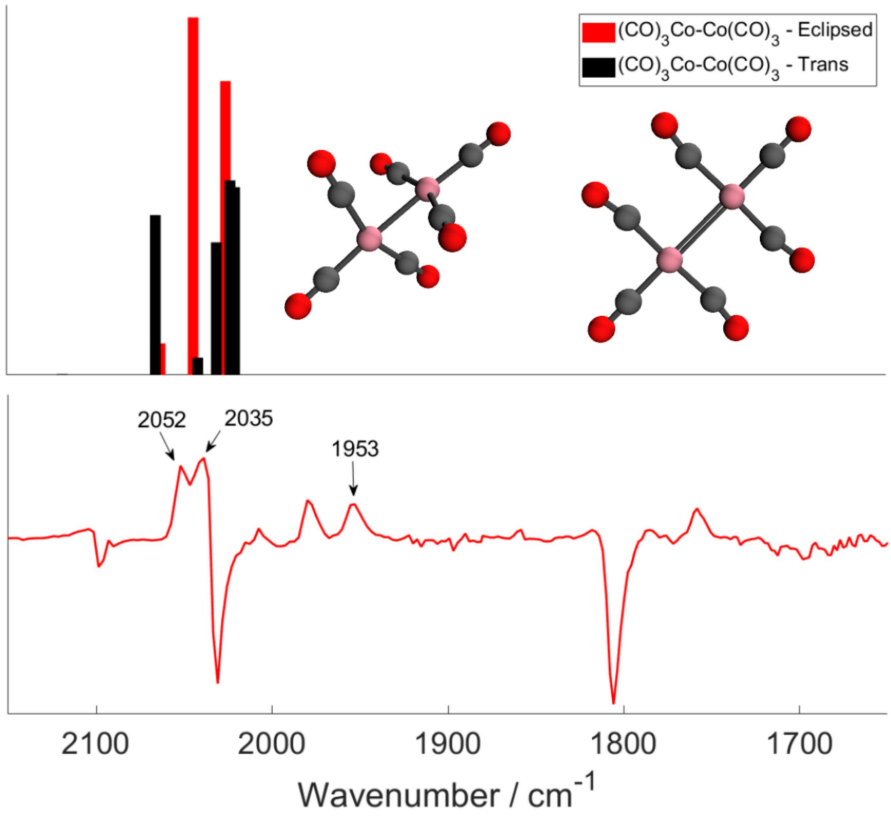

Figure 2.35: Bottom: experimental spectra from the TRIR experiments with the peaks assigned to 'Complex F' labelled. Top: calculated vibrational frequencies of both $(CO)_3Co(\mu\text{-}CO)Co(CO)_2(NO)$ - Eclipsed (red) and $(CO)_3Co(\mu\text{-}CO)Co(CO)_2(NO)$ - Staggered (black).

that of $(CO)_3$Co-Co$(CO)_3$. A tentative suggestion for the structure of complex F is $(CO)_3$Co-Co$(CO)_3$, based on the peaks at 2052 and 2035 cm^{-1} and their agreement with the calculated spectra, but its more likely that additional species are also forming.

The peak at 1953 cm^{-1} is only visible in the low concentration experiment and also appears to form from the decay of $Co(CO)_3$. This peak at 1953 cm^{-1} is an almost perfect match with the species Co(CO) isolated in an Ar matrix, which was reported to appear at 1952 cm^{-1}.[101] In this scenario of a room temperature solution it seems unlikely that Co(CO) is a stable molecule in solution on the microsecond timescale so this assignment would appear incorrect. Further work is required to understand the exact origins of the peak at 1953 cm^{-1}.

Complex G from Table 2.2 has two observable peaks at 1977 and 1758 cm^{-1}

and is seen in both the high and low concentration TRIR experiments following 355 nm excitation. It grows in on the microsecond timescale, appearing to grow in from complex F and does not decay on the timescale of our experiments. This species also forms quicker in the high concentration experiments compared with the low concentration experiments which could suggest a reaction between complex F and a parent molecule. The exact structure of this complex would be very challenging to predict as there would be a whole multitude of potential structures and isomers. More work is also needed here to gather more evidence to help elucidate the exact structure of complex G.

2.3 Conclusions and Future Perspectives

The photochemical behaviour of $Co(CO)_3(NO)$ in *n*-heptane have been observed in both picosecond and nanosecond TRIR experiments using 400, 355 and 266 nm excitation wavelengths. The initial experiments performed in order to probe the decay of the T_1 species observed by Harris revealed there were both similarities and differences between our experiments and theirs. Both Harris and ourselves observed the formation of $Co(CO)_3$ and $Co(CO)_2(NO)$(*n*-heptane), but on different timescales, but many of the triplet states of the parent molecule, which Harris reported, were not observed in our experiments. A few extra unknown species were also observed in our initial nanosecond experiment, one of which appeared to grow in from $Co(CO)_2(NO)$(*n*-heptane) which then decayed away further. Another unknown species which appeared to grow in from $Co(CO)_3$ was also observed which also decayed on the microsecond timescale and formed a new species which was stable on the timescale of our experiment.

Due to the differing observed kinetic profiles of both $Co(CO)_3$ and $Co(CO)_2(NO)$(*n*-heptane), an experiment on the same timescale of the original, reported by Harris, was then performed and again there were both similarities and differences. The decay of $^3Co(CO)_2(NO)$ was observed, which had a matching kinetic profile to that of the growth of $Co(CO)_2(NO)$(*n*-heptane) which was

stable on the picosecond timescale. $Co(CO)_3$ was also observed, which grew in <1 ps, but was also stable on the picosecond timescale. Other species such as vibrationally hot $Co(CO)_3(NO)$ and the S_1 state of $Co(CO)_3(NO)$ were also tentatively assigned, but they simply appeared to just decay back to the parent on the picosecond timescale. A concentration difference was then suggested as the reasoning for the different kinetics of our experiments compared with those of Harris.

A picosecond experiment following 400 nm excitation using a significantly higher concentration of $Co(CO)_3(NO)$ in *n*-heptane was then performed in order to try and more closely match the results observed by Harris. In this higher concentration experiment, the same species as before in $^3Co(CO)_2(NO)$, $Co(CO)_3$, $Co(CO)_2(NO)$(*n*-heptane), $^1Co(CO)_3(NO)$ and vibrationally hot $Co(CO)_3(NO)$ were all observed again. In this experiment a few additional bands assigned to $^3Co(CO)_2(NO)$, $^1Co(CO)_3(NO)$ and vibrationally hot $Co(CO)_3(NO)$, which were missing in the order of magnitude lower concentration experiment were now observable aswell as an additional peak at 1802 cm^{-1}, which had kinetic profile that could not be untangled due to overlap with the parent bleach.

There were still differences between our experiment and those reported by Harris at this higher concentration, but there are now also more similarities. Due to this increased degree of similarity at higher concentration the original nanosecond experiment using 355 nm excitation was repeated. In this experiment the decay of both $Co(CO)_3$ and $Co(CO)_2(NO)$(*n*-heptane) was found to be a lot faster (Z = 7 ns ($Co(CO)_3$) 35 ns ($Co(CO)_2(NO)$(*n*-heptane))) than in the lower concentration experiments (Z = 30 ns ($Co(CO)_3$) 193 ns ($Co(CO)_2(NO)$(*n*-heptane))). There were also many additional peaks observed, not previously seen in our low concentration experiments and a peak at 1953 cm^{-1}, observed in the low concentration experiment, that was not observed in this high concentration experiment. The growth and decay of complexes F and G were also faster in the high concentration experiment. This experiment displayed a clear concen-

tration dependence on the reaction kinetics upon irradiation of $Co(CO)_3(NO)$ in *n*-heptane.

To further probe the formation and decay of $Co(CO)_2(NO)$(*n*-heptane), both nanosecond and picosecond TRIR experiments were conducted following 266 nm excitation. Many of the same peaks observed in the low concentration 355 nm experiments were observed again with pretty similar kinetics and three additional peaks at 1982, 1943 and 1716 cm^{-1} were also noted. These additional peaks appeared to grow in from the decay of $Co(CO)_2(NO)$(*n*-heptane) and continued to grow in over the timescale of the experiment. In the picosecond experiment following 266 nm excitation the peak corresponding to $Co(CO)_3$ appeared to grow in from a broad featureless band centred at 1931 cm^{-1}, which was the first experiment where the band at 1970 was not observed <1 ps. The only other peaks observed in this experiment could be assigned to $Co(CO)_2(NO)$(*n*-heptane) which had mostly consistent kinetic profiles to the picosecond experiments following 400 nm excitation.

DFT calculations were performed in an attempt to help assign unknown species and it was found that using a scale factor of 0.96 for carbonyls and 0.92 for nitrosyls resulted in much better agreement between calculated and experimentally observed vibrational frequencies. A tentative assignment of complex A as both staggered and eclipsed isomers of $(CO)_2(NO)Co(\mu\text{-}CO)Co(CO)_2(NO)$ and for complex F as both staggered and eclipsed isomers of $(CO)_3Co\text{-}Co(CO)_3$ was made.

It is understood that there are still many gaps in our understanding in the photochemistry of $Co(CO)_3(NO)$ in *n*-heptane as there are still many unassigned species and a few peaks with kinetics which could not be resolved or understood. More TRIR experiments would be required to work towards a more complete understanding of this system.

There are a number of future experiments that would potentially shed light on the photochemistry of $Co(CO)_3(NO)$. A wider range of variable $Co(CO)_3(NO)$

concentration experiments including repeating those performed above in order to untangle the complex reaction dynamics. Another set of experiments to perform would be using different pump lasers, which may help to investigate if any photoproducts formed were due to 2-photon processes. A wider range of wavelength of pump excitation may also be used in order to explore the wavelength dependence on the photochemistry of $Co(CO)_3(NO)$. Experiments in a wider range of solvents, of different coordination ability and polarity, may be useful to further understand the kinetics of various photoproducts and their stability in different systems. Another important factor to consider would be the temperature that the experiments were conducted at and the effect of variations of this temperature and its ability to influence kinetics. Due to the nature of the disruptions caused by the COVID-19 pandemic, many of the above experiments could not be performed.

Chapter 3

Computational Study of Rhenium and Manganese Pianostool and α-Diimine CO_2 Complexes

3.1 Introduction

3.1.1 Bonding in Carbon Dioxide

CO_2 is a linear triatomic molecule with a $D_{\infty h}$ point group that possesses two equivalent C=O bonds of 1.16 Å length.[102] Due to the difference in electronegativity between the C and O atoms there is a partial charge transfer from the carbon atom to the oxygen atoms resulting in the carbon centre being electrophillic and both of the oxygen atoms being nucleophillic.[103] There are two π-bonds of CO_2 that can be involved in bonding meaning that along with the previously mentioned charge distribution there is a multitude of ways CO_2 can bind to metal centres.[104] For a single molecule of CO_2 there are currently four known ways in which it can coordinate to a metal centre shown as in Figure 3.1.[105]

CO_2 possesses 16 valence electrons that occupy a set of 12 molecular orbitals

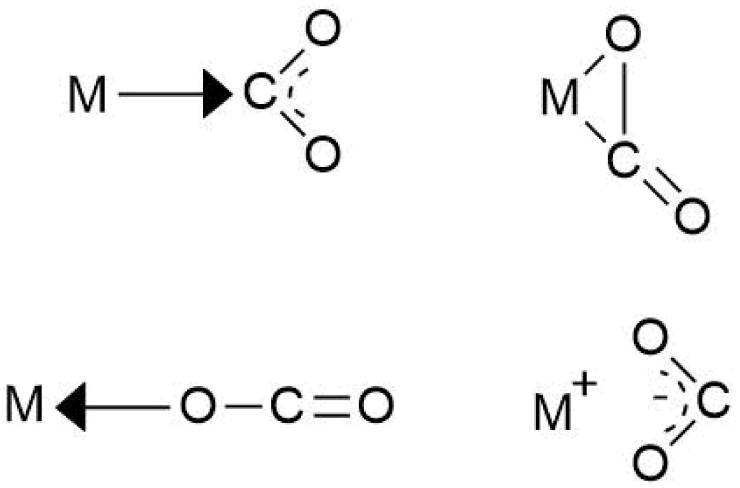

Figure 3.1: The four binding modes displayed by a single CO_2 molecule when coordinating to metal centres: η^1-C (top left), η^2-C,O (top right), η^1-O (bottom left) and η^2-O,O (bottom right).[106]

generated by 12, 2s and 2p orbitals of the carbon and oxygen atoms. The s and p_z orbitals combine to form the six σ molecular orbitals. The p_x and p_y atomic orbitals combine to form two equivalent sets of three π molecular orbitals where one set is in the xz plane and the other is rotated 90° in the yz plane. When considering bonding between CO_2 and organometallic complexes there are four orbitals that will be the most important. These four are the "O-end lone pair" and the 'parallel' π, nπ and π^* MO's. The word 'parallel' is used to refer to the set of these orbitals that lie in the plane of the metal during η^1-C and η^2-C,O side on coordination. The 'perpendicular' set of π orbitals will be orthogonal to this set and will not play as much of an important role in bonding due to a much lesser degree of overlap with the metal orbitals.[109,110] The molecular orbital diagram for CO_2 can be seen in Figure 3.2 where the four most important orbitals for coordination with organometallic complexes are highlighted.

There are different molecular orbital requirements for different modes of CO_2 bonding, this report will briefly talk about these requirements for η^1-C, η^2-C,O and η^1-O coordination.

For the η^1-C mode of coordination there is a previously mentioned strong charge transfer interaction from the metal to the CO_2. This occurs from a

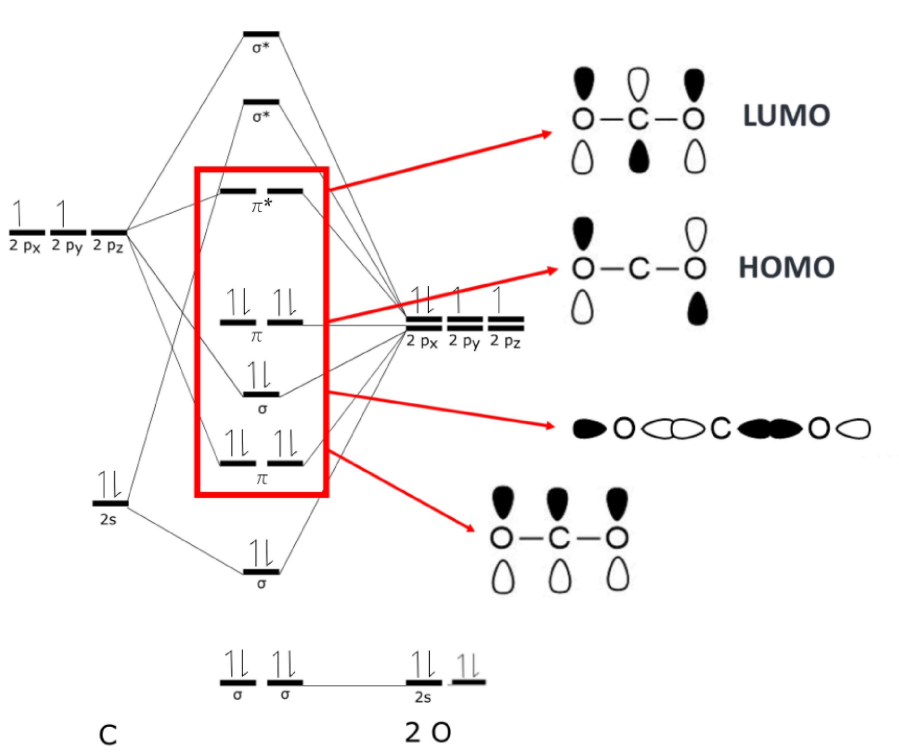

Figure 3.2: Molecular orbital diagram for CO_2 highlighting the four most important orbitals for coordination with organometallic complexes.[107,108]

metal d_{z^2} orbital to an empty π^* orbital on CO_2 shown in Figure 3.3. The most favourable situation for this interaction is when the metal is in a low oxidation state and also when the metal HOMO is mainly composed of a d_σ orbital.

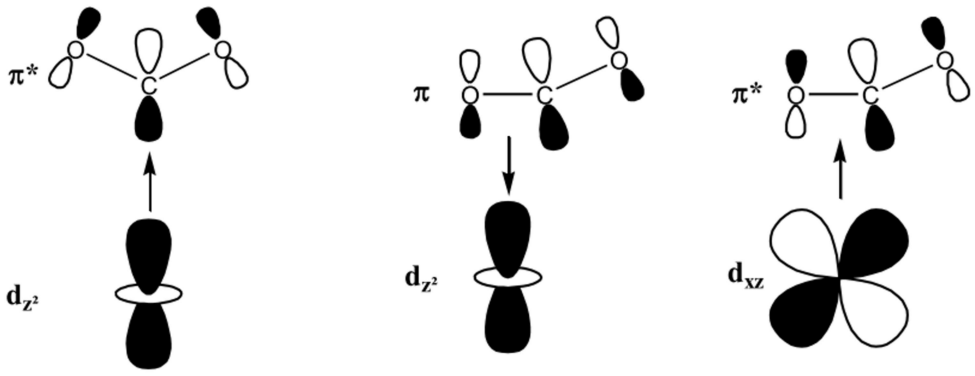

Figure 3.3: Coordination of CO_2 to a transition metal centre. Left: η^1-C Right: η^2-C,O[107,108]

For the η^2-C,O mode of coordination there are two major components: σ bonding from the occupied π orbital of CO_2 to an empty d_{z^2} metal orbital, together with π back-donation from an occupied metal d_{xz} to the empty π^* orbital

of the CO_2 as seen in Figure 3.3. The most favourable situation for this coordination mode would therefore be when there is a d_π orbital as the HOMO of the metal and an empty d_σ orbital pointing towards the CO_2 ligand. This will enhance the π back-bonding between the CO_2 and the metal and also eliminate the four-electron destabilising interaction that would occur between a filled d_σ orbital and the π and $n\pi$ orbitals of CO_2.

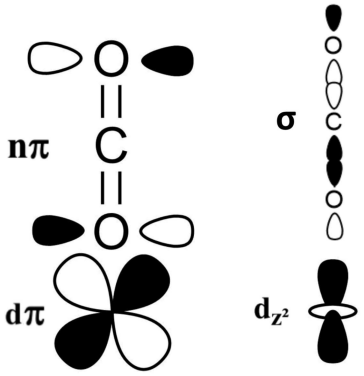

Figure 3.4: The two pairs of four-electron destabilising interactions for the η^1-O coordination mode of CO_2 to a transition metal centre.[107,108]

For the η^1-O mode of coordination there is a large reliance on there being a favourable electrostatic type interaction present. Since the oxygen atoms on CO_2 carry a partial negative charge this means that the metal centre will preferably be positively charged or possess a reasonably high oxidation state. If the metal has a high-lying occupied d_{z^2} and d_π orbitals, and also an absence of a good electron acceptor among its co-ligands, then the η^1-O mode will suffer from two pairs of four-electron destabilising interactions. These destabilising interactions are shown in Figure 3.4. The ideal orbital situation for η^1-O coordination is to minimise these destabilising interactions.

3.1.2 Organometallic CO_2 Complexes

Coordination of CO_2 to organometallic complexes is a growing area of interest due to their ability to help catalyse the breakdown of CO_2 to other, useful molecules such as CO and methanol.[111–115] A variety of different CO_2 coordinated complexes

have been isolated and in this Chapter an example of each coordination mode is described.

η^1-C coordinated complexes are most favourable in complexes with electron rich metals. This is because of the electron transfer from the metal to the electrophillic carbon atom which then leads to an even greater partial negative charge on the oxygen atoms. The first structurally characterised η^1-C coordinated complex was found in 1983 by Herskovitz *et al.* of the formula $[(diars)_2Rh(CO_2)(Cl)]$.[116] This complex was synthesised by pressurising a solution of $[(diars)_2Re]Cl$, a 16 electron complex, in CH_3CN at 19 psi with CO_2. The crystal structure of this complex can be seen in Figure 3.5. This CO_2 complex displays new IR bands 1610 and 1210 cm^{-1} due to the coordinated CO_2 C-O stretches and the Rh-C bond.[116]

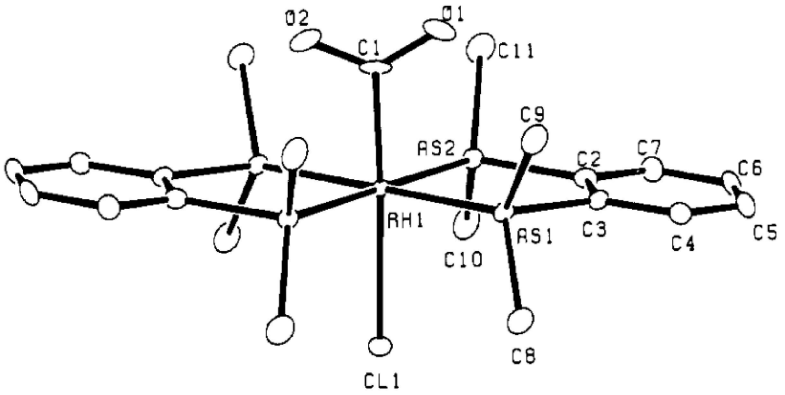

Figure 3.5: The molecular structure for the complex $[(diars)_2)Rh(\eta^1\text{-}CO_2)(Cl)]$ discovered by Herskovitz *et al.* in 1983.[116]

The η^1-C can clearly be seen at the top of Figure 3.5 along with the long Rh-Cl bond, which is due to a *trans* influence from the bound CO_2 due to its high π acidity. The OCO plane is rotated by 4° from an exact bisection of the diars ligands, this is to minimise the nonbonding repulsions with the methyl groups. This rotation of the OCO plane is also believed to be caused by intermolecular interaction of the oxygen atoms with the hydrogen atoms on the phenyl groups. Both these factors are believed to help influence the CO_2 into the η^1-C binding mode over the equally possible η^2-C,O binding mode. To investigate further

Herskovitz *et al.* also performed theoretical calculations on this system which indicated a large electronegative character on the oxygen atoms of the CO_2 which agreed with previous theories at the time. These calculations also suggested that the binding mode preference was likely due to the relatively high electron density on the metal centre. This is due to both the diars ligands binding through donation of two lone pairs each to the metal centre.

η^2-C,O side on coordinated complexes are the most common complexes with many examples of them being isolated in the past.[117–119] They are often pure π complexes or metallacycles where there is a donor-acceptor bond, with electron transfer from M→C and O→M. The π back-bonding is a large stabilising factor for η^2-C,O side on coordination when compared with η^1-C end-on coordination. When the metal has strong Lewis basicity along with a small positive charge, η^2-C,O will often be more electronically favourable, but in some situations due to things like coordination numbers or steric crowding the η^1-C coordination mode will end up actually occurring.

The first structurally characterised η^2-C,O side on coordinated complex was found eight years before the first η^1-C complex back in 1975 by Aresta *et al.*[120] The complex, $[Ni(CO_2)(PCy_3)_2]\bullet 0.75\ C_6H_5CH_3$, was isolated by treating either $[Ni(PCy_3)_3]$ or $[Ni(PCy_3)_2(N_2)]$ with CO_2 in toluene at room temperature to give red-orange crystals, which are air-stable for a few hours. Aresta *et al.* performed X-ray crystallography to confirm the planarity of the complex and verify the η^2-C,O side on coordination mode of CO_2.[120]

In 1985 Dohring *et al.* managed to structurally characterise the solvent-free complex $[Ni(CO_2)(PCy_3)_2]$ by dissolving [Ni(cyclododecatriene)] and PCy_3 in diethyl ether and reacting with a constant stream of CO_2 at 0 °C for 20 h.[121] The crystal structure of this complex can be seen in Figure 3.6.

η^1-O end-on coordination is favoured by metals which are electron deficient. In these η^1-O end-on complexes there is electron transfer from O→M as the O atoms of CO_2 are quite electron rich due to the previously mentioned partial

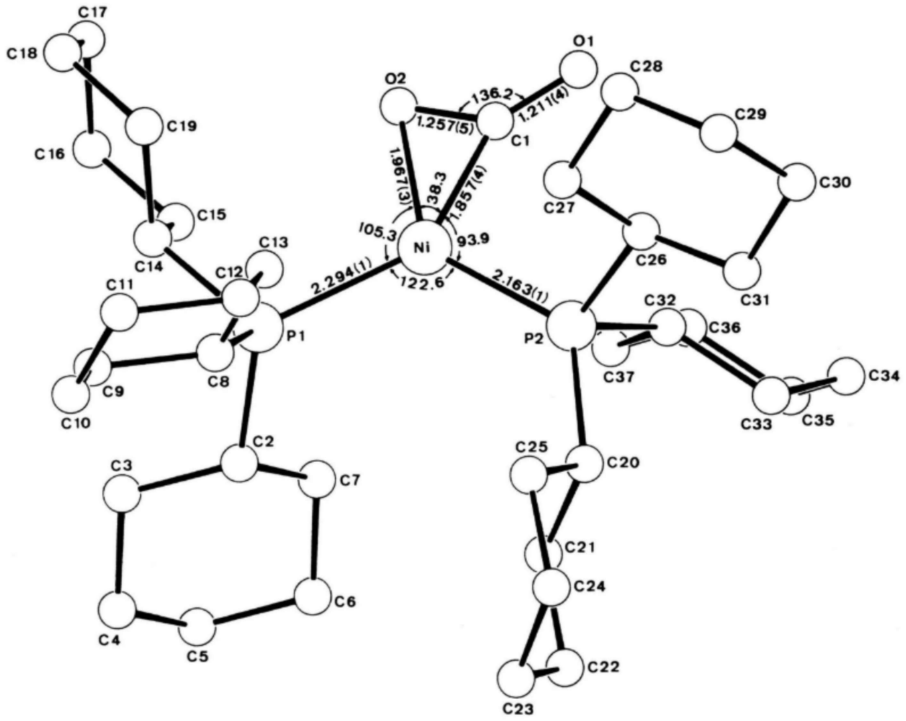

Figure 3.6: The molecular structure of the complex $[Ni(CO_2)(PCy_3)_2]$ isolated by Dohring *et al.* in 1985.[121]

charge transfer. Stable η^1-O end-on coordinated CO_2 complexes are a lot less common than both η^2-C,O side on and η^1-C complexes and as such there are limited structurally characterised examples.

A fairly recent example of an η^1-O end-on coordinated CO_2 complexes was isolated by Meyer *et al.* in 2004, which is a uranium complex made by exposing the sterically stabilised [(1,4,7-tris(3-adamantyl-5-^{t}Bu-2-hydroxybenzyl)-1,4,7-triazacyclononane)U] complex in toluene to a CO_2 environment of just 1 atm.[19] This process reportedly instantly discoloured the solution and you could then concentrate and filter the toluene solution to get the product, [(1,4,7-tris(3-adamantyl-5-^{t}Bu-2-hydroxybenzyl)-1,4,7-triazacyclononane)U(CO_2)] shown in Figure 3.7.

The η^1-O end-on coordination can be seen in Figure 3.7 where the molecular structure showing near linear U-O-C and O-C-O bond angles. This is unique as in both η^2-C,O side on coordination and η^1-C coordination the CO_2 is bent upon coordination to the metal centre.

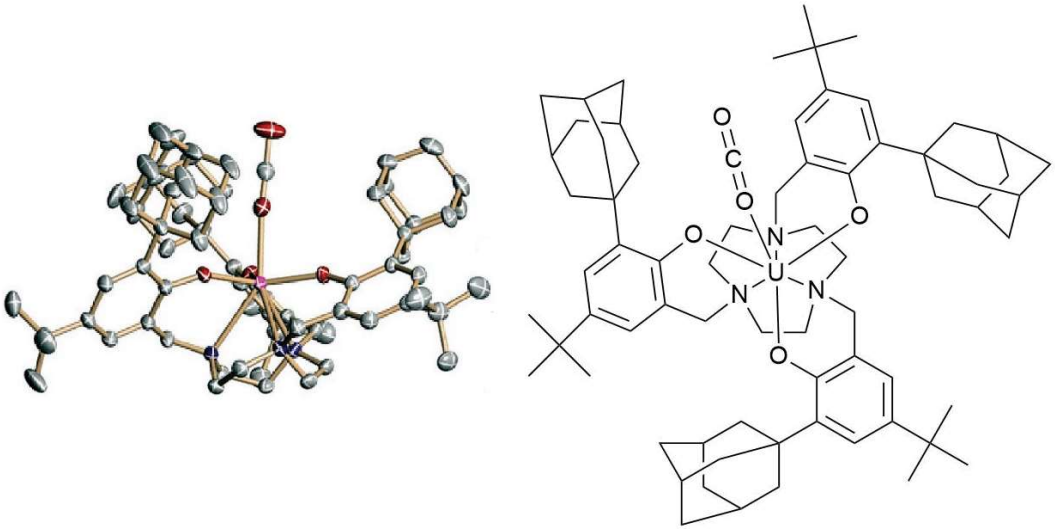

Figure 3.7: An η^1-O end-on CO_2 coordination complex, [(1,4,7-tris(3-adamantyl-5-tert-butyl-2-hydroxybenzyl)-1,4,7-triazacyclononane)U(CO_2)], isolated by Meyer *et al.* in 2004. Left: The molecular structure. Right: The structural formula.[19]

In this complex the uranium is in the +4 oxidation state owing to the high favourability of the η^1-O end-on coordination mode. This is further supported by the bulky adamantyl substituents sterically crowding the area around the CO_2 molecule but leaving a space suitable for the linear CO_2 molecule to comfortably fit. The U-O bond length is reported as 2.351(3)Å and the neighbouring C-O bond length as 1.122(4)Å, while the terminal C-O bond has a length of 1.277(4)Å. The UOC bond angle is 171.1° and the OCO angle is 178.0°, which are both quite close to linear. The UOC bond angle would not be expected to be quite as linear since the electron donation from the CO_2 comes from a lone pair but the presence of the adamantyl substituents stops the CO_2 from bending too far from its linear geometry. The nujol FTIR band for the coordinated CO_2 was found at 2188 cm^{-1}. These bond lengths combined with the near linearity of the coordination suggest a bonding structure along the lines of U-O≡C-O^-.

Yang *et al.* detected the presence of a linear bound CO_2 to [$CpMn(CO)_2(CO_2)$] in 2008 using time-resolved infrared spectroscopy.[122] This was an unusual result as the complex [$CpRe(CO)_2(CO_2)$] had η^2-C,O side on coordination of the CO_2 molecule. DFT calculations were performed in an attempt

to explain this and it was found that for [CpRe(CO)$_2$(CO$_2$)] there was significant charge transfer from the rhenium d_π HOMO to the π^* orbital on the CO_2 resulting in a partial oxidation of the rhenium centre. There was an additional two-electron stabilising interaction present between the complex LUMO orbital, which has d_σ character, and the CO_2 occupied n_π orbital. For [CpMn(CO)$_2$(CO$_2$)] the d_σ orbital is much lower in energy and as such the d_σ orbital and CO_2 σ lone pair interaction takes over leading to the η^1-O coordination mode with a major component being an electrostatic interaction. The Mn-O-C bond angle was not found to be linear here but instead 167.4° suggesting further that the CO_2 bound in the uranium complex was sterically forced into that angle.

The η^2-O,O mode of coordination is by far the least common and has not yet been seen forming a stable complex at room temperature and pressure. It has primarily been observed in alkali metal complexes, $M^+CO_2^-$ (M = Li, Na, K and Cs) in low temperature matrices.[123,124] Formation of these complexes involves reducing the CO_2 to the radical anionic species $CO_2^{\cdot-}$ which was first achieved by Hartman *et al.* in 1966.[125] This was accomplished by irradiating pressed alkali halide disks containing the formate ion in solution with gamma rays and then using IR spectroscopy to analyse the structure of the ion. The recorded wavenumber of the $CO_2^{\cdot-}$ radical anion was 1671 cm^{-1}, which is a huge red shift from the usual CO_2 stretching frequency region of around 2300 cm^{-1}. This is due to the weaker C-O bonds as there is now an extra electron on the CO_2 occupying a π orbital. This intermediate could be of great interest as this weakens the C-O bond strength, this could make the task of "activating" the CO_2 for further reduction far easier.

3.1.3 Computationally-Investigated CO_2 Organometallic Complexes

DFT has been used extensively to probe CO_2 and its properties in a number of different reactions, many with focusses on surface adsorption and its roles in

chemical reactions.[126–131] There is also significant DFT-driven research probing the reactions of CO_2 with metal atoms and metal complexes, primarily in the context of catalysis.[132–137] There has even been theoretical research on probing the mechanism of CO_2 reduction by use of rhenium metal complexes.[138,139] There is very little theoretical research specifically focussing on probing the lesser observed η^1-OCO binding mode. Before 2004, the η^1-OCO end-on binding mode of CO_2 complexes had only been predicted theoretically and isolated in low temperature matrices. In 1982 Morokuma *et al.* performed a theoretical investigation of CO_2 coordination to both $Ni(PH_3)_2$ and $Cu(PH_3)_2^+$, where it was seen that side-on coordination of CO_2 is favoured for $Ni(PH_3)_2$ whereas end-on OCO coordination is favoured for $Cu(PH_3)_2^+$.[140] This difference was found to be due to the ability of the Ni^0 metal centre to provide π back-donation causing the side-on binding mode to be most favourable. For $Cu(PH_3)_2^+$, the strong electrostatic interaction between Cu^I and the partially negatively charged O atom causes the η^1-OCO end-on binding mode to be most favourable.

In 1995 Pidun and Frenking conducted a theoretical investigation into side-on π bonded ligands to $W(CO)_5L$ and WCl_4L and in both cases CO_2 was predicted to bind weaker than C_2H_4, HCCH and CH_2O.[141] For the WCl_4L complexes, the CO_2 is predicted to bind in a side-on fashion but for $W(CO)_5L$ the CO_2 is predicted to bind end-on. This is because the side-on coordination is better suited for the development of covalent bonds and the WCl_4L M-L bonds are covalent in nature whereas for $W(CO)_5L$ the W-L bonds are donor-acceptor bonds. Their work also showed that the inclusion of correlation energy was vital for accurate descriptions of transition metal donor-acceptor complexes.

In 2019 George *et al.* were investigating the effect of coordination of alkanes, Xe and CO_2 (η^1-OCO) on changes in spin state and reactivity in organometallic chemistry and as part of this they calculated energies of coordination between η^1-OCO and different spin states of $CpMn(CO)_2$ fragments.[142] They reported relative binding energies compared with a reference of $^3CpMn(CO)_2$ + ligand and it was

found that when examining the binding between ^{1}CpMn(CO)$_2$ and various ligands that *n*-heptane was predicted to bind most strongly at 56 kJ mol^{-1}. The next strongest ligand was ethane at 45 kJ mol^{-1} followed by both CO_2 and Xe, which were quite similar at 36 kJ mol^{-1}, and lastly was two different perfluorinated solvents, PFMCH and pFCyc which had a strength of 25 kJ mol^{-1}. This general trend of alkane > CO_2 ≈ Xe > perfluorosolvents was found to be true for all spin states where the only exception was ethane, which was found to coordinate more closely in energy with CO_2 and Xe as the spin state of CpMn(CO)$_2$ got higher in energy.

The work in this Chapter is influenced by the previously mentioned work reported by Yang *et al.* in 2009 and their investigation into the formation and reactivity of CpM(CO)$_2$(CO_2) (M = Mn or Re) in CO_2.[122] This work is summarised in more detail in the results section below.

3.1.4 Aims and Objectives

The question to be examined in this Chapter is to examine the strength and nature of binding of CO_2 to various organometallic fragments. Specifically, how changing from neutral to cationic organometallic fragments alters the HOMO-LUMO separation between the fragments and probe the effect on both the nature and strength of the bonding CO_2 to the metal centre. This will open-up for more extensive characterisation and potential isolation of CO_2 complexes particularly η^1-OCO complexes. Therefore, the aim is to explore, with DFT and plan future chemical synthesis and spectroscopic measurements. We have used the following strategy to address the aims above:

1) Undertake DFT calculations of CO_2 complexes formed following photolysis of CpM(CO)$_3$ (M = Mn or Re) since these have differing CO_2 binding modes and there are historic published DFT calculations in order to benchmark our calculations.

2) Undertake DFT calculations of possible neutral and cationic organometal-

lic CO_2 complexes to evaluate the binding strength of these weakly coordinating ligands to benchmark them against reported complexes in the literature and investigate the nature of the CO_2 binding in these complexes.

3) Use these calculations to help guide synthesis of organometallic carbonyl precursors designed to be soluble in non-coordinating solvents such as perfluorinated alkanes, alkanes and liquid CO_2.

3.2 Results and Discussion

3.2.1 DFT Investigation of $CpM(CO)_3$ (M = Mn or Re)

The starting point for our studies was to examine the reported bonding of CO_2 to the $CpM(CO)_2$ (M = Mn or Re) moiety. Geometry optimisations of both $CpMn(CO)_2(CO_2)$ and $CpRe(CO)_2(CO_2)$ were performed together with frequency calculations to ensure the optimised structures were at the true energy minimum. The resulting structures from these calculations are shown in Figure 3.8.

The previous experimental and theoretical studies on $CpM(CO)_2(CO_2)$ (M = Mn or Re) have shown that CO_2 adopts different binding modes depending upon the metal centre.[122] Our new calculated structures agree with this and show that $CpMn(CO)_2(CO_2)$ would display a preference for the η^1-OCO binding mode while $CpRe(CO)_2(CO_2)$ would possess a side on η^2-CO_2 coordination mode. These findings are consistent with those reported by Yang *et al.* who in 2009 photolysed both $CpRe(CO)_3$ and $CpMn(CO)_3$ in liquid CO_2 to form their corresponding CO_2-bound photoproducts and characterised them using TRIR spectroscopy.[122]

Calculated bond lengths can be used to examine the bonding of the CO_2 ligand to the metal centre. A useful benchmark to understand bonding for $CpRe(CO)_2(CO_2)$ is to examine the carbonyl bonds found in $CpRe(CO)_3$. The Re-C bonds are on average 1.922 Å and the C-O bond lengths are on average 1.150 Å long. The bond lengths for $CpRe(CO)_2(CO_2)$, in Table 3.1, show that

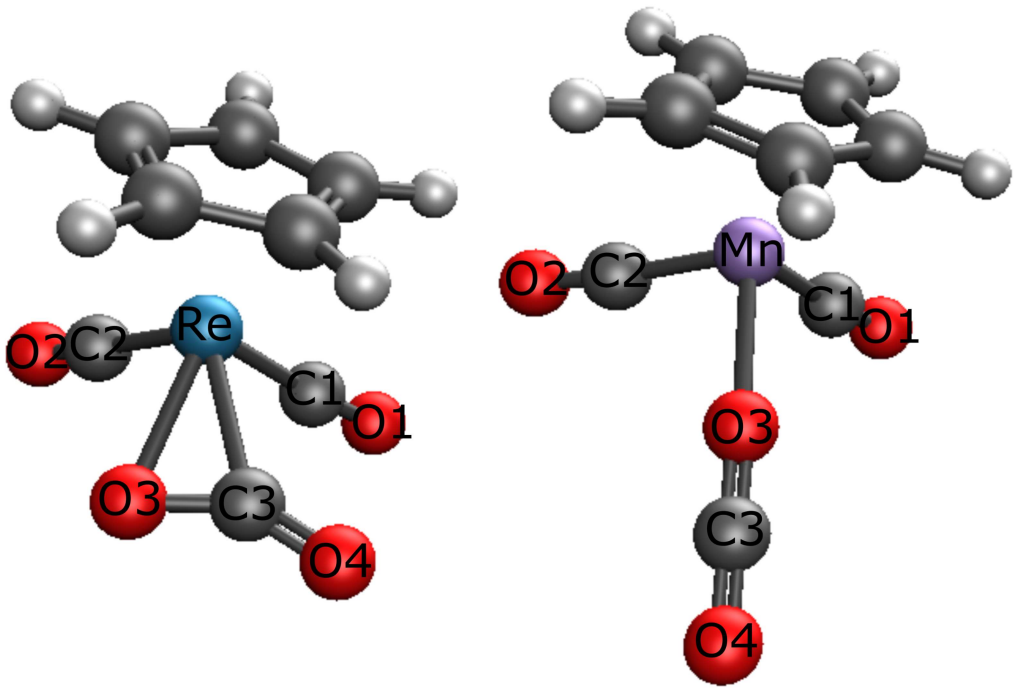

Figure 3.8: Optimised structures obtained at the DFT-M06/LANL08(f) (metals) and 6-311++G** level for $CpRe(CO)_2(CO_2)$ (left) and $CpMn(CO)_2(CO_2)$ (right) showing the difference in preferential CO_2 binding mode.

Bond Length /Å	$CpRe(CO)_2(CO_2)$	$CpMn(CO)_2(CO_2)$
M-C1	1.906	1.782
M-C2	1.939	1.782
M-C3	2.194	-
M-O3	2.218	2.151
C1-O1	1.151	1.153
C2-O2	1.146	1.153
O3-C3	1.235	1.155
C3-O4	1.182	1.153

Table 3.1: Table of non-arene bond lengths for $CpRe(CO)_2(CO_2)$ and $CpMn(CO)_2(CO_2)$ from DFT calculations.

two carbonyl ligands have different lengths, C1-O1 = 1.151 Å whereas C2-O2 = 1.146 Å. The Re-C bond lengths for each of these two carbonyl bonds is also found to vary where Re-C1 = 1.906 Å and Re-C2 = 1.939 Å. When comparing the carbonyl bond lengths to those found in $CpRe(CO)_3$ it can be seen that Re-C1 is found to be a shorter length by 0.016 Å and Re-C2 is found to be a longer length by 0.017 Å. This can be explained by a different amount of carbonyl backbonding in each of the two different carbonyls. A greater amount of carbonyl backbonding found in 'carbonyl 1' means that both the CO to metal n $\rightarrow$ d_σ and $d_\pi \rightarrow \pi^*$

interactions are stronger. The opposite is true for 'carbonyl 2' where the Re-C2 bond is found to be lengthened and the C2-O2 bond shortened.

The other bonds examined in $CpRe(CO)_2(CO_2)$ are those in the CO_2 moiety. The O3-C3 = 1.235 Å and the C3-O4 = 1.182 Å. The Re-C3 and Re-O3 bond lengths are 2.194 and 2.218 Å, respectively. This trend of a longer O3-C3 bond than C3-O4 and a longer Re-O3 bond than Re-C3 bond is in agreement with the experimental values from the X-ray crystal structures of the η^5:η^1-$C_5H_4CH_2CH_2N(CH_3)_2Re(CO)(\eta^2$-$CO_2)$ complex from literature.[143] They are also consistent with the associated charge transfer from an occupied d_π orbital to the π^* orbital of CO_2, which can be viewed as corresponding to partial oxidation of the rhenium atom. The data in Figure 3.9 can also aid in this explanation where it can be seen there is a two-electron stabilising interaction between the d_π HOMO of the $CpRe(CO)_2$ fragment and the empty π^* orbital on the CO_2. This interaction is accountable for the dihapto binding mode of CO_2 found in this complex. This interaction weakens the C-O bond interacting with the metal centre explaining why this C-O bond has a calculated length of 1.24 Å compared with the other CO bond of length 1.18 Å.

The bond lengths of $CpMn(CO)_2(CO_2)$ from Table 3.1 can also be investigated in order to learn the difference between these two binding modes. A useful benchmark would be to first of all examine the bond lengths for $CpMn(CO)_3$ where the Mn-C bond lengths were found to be 1.787 Å and the C-O bond lengths are 1.148 Å. The two carbonyl bands in $CpMn(CO)_2(CO_2)$ are found to be identical, both 1.153 Å, which is 0.005 Å longer than in $CpMn(CO)_3$. Mn-C1 and Mn-C2 in $CpMn(CO)_2(CO_2)$ are found to be the same at 1.782 Å which are both 0.005 Å shorter than than the Mn-C bond lengths found in $CpMn(CO)_3$. Both of these trends can be explained by carbonyl backbonding caused by the manganese atom in $CpMn(CO)_2(CO_2)$ to be more electron rich than in $CpMn(CO)_3$. This means there is a larger amount of CO to metal $n \rightarrow d_\sigma$ donation and metal to CO_2 $d_\pi \rightarrow \pi^*$ interactions. This greater amount of electron density present on the

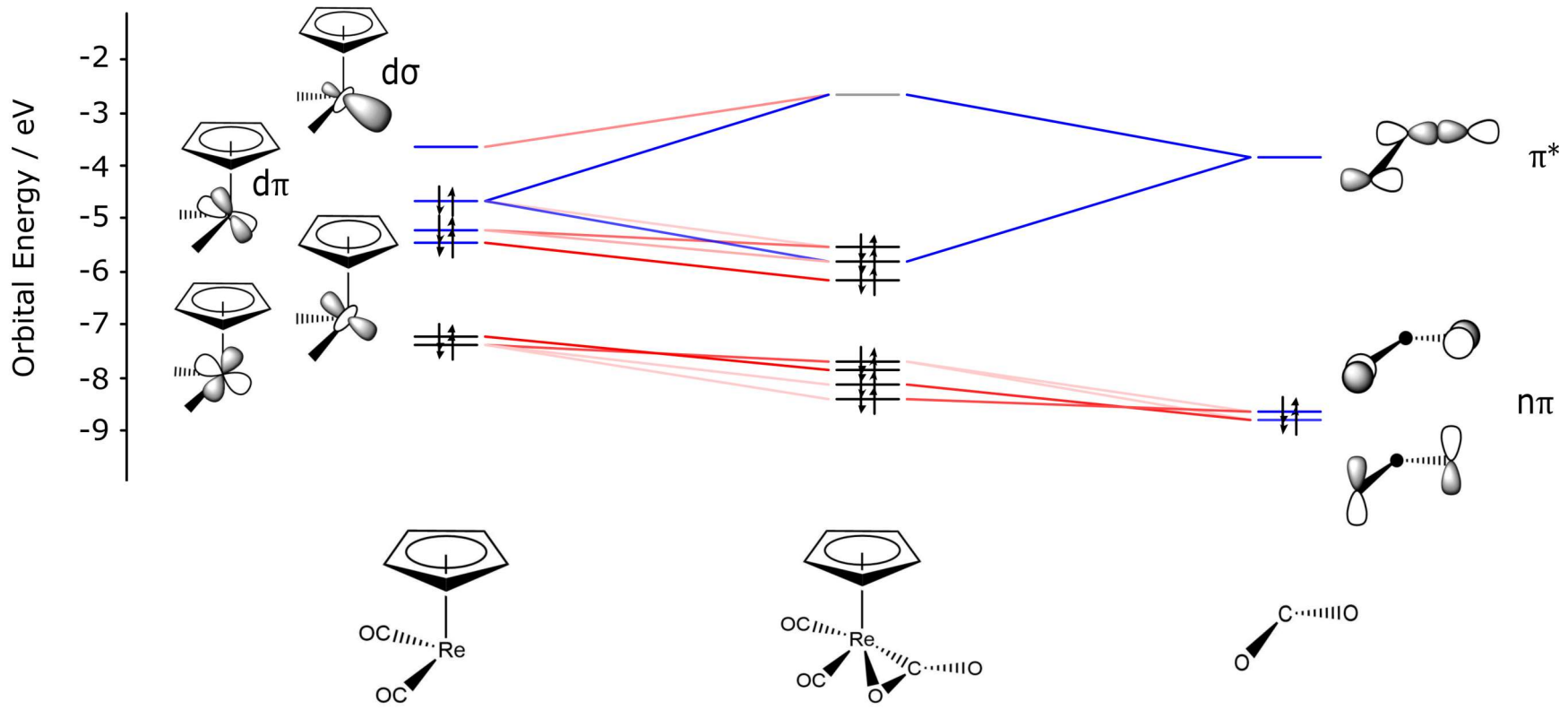

Figure 3.9: Schematic orbital interaction diagram between the orbitals of the $CpRe(CO)_2$ fragment and the orbitals of a bent CO_2 molecule. Generated using the data obtained from DFT calculations and plotted using ADFInput.

metal in the η^1-OCO coordinated system can be explained by the binding mode of CO_2 in this system donating electron density onto the metal.

The bonding interaction between the $CpMn(CO)_2$ fragment and the CO_2 ligand is quite different to the bonding between the $CpRe(CO)_2$ fragment and CO_2 as shown in Figure 3.10. The d_σ orbital in the $CpMn(CO)_2$ fragment is lower in energy than in the $CpRe(CO)_2$ fragment enough so that the triplet state, in which both the d_σ and d_π frontier orbitals are both singly occupied, is known as the ground state.[144] The interaction between the d_σ orbital and the σ lone pair on the CO_2 is a prominent interaction, leading to the η^1-OCO binding mode. This interaction involves a large degree of transfer of electron density from the CO_2 molecule onto the metal atom, which explains why the metal centre was found to be more electron rich in $CpMn(CO)_2(CO_2)$ when compared with $CpMn(CO)_3$. The antibonding interaction between the d_σ orbital and CO_2 σ lone pair is high enough that the situation is equivalent to having a two-electron stabilising interaction.

These calculations match with the findings from Yang *et al.* and as such provide a useful benchmark to be able to move forward with into more novel areas of work.[122]

3.2.2 DFT Investigation of Mn and Re Pianostool Complexes

Geometry Optimisations and Bond Lengths

The next step in our studies involves examining the bonding of CO_2 to a set of novel complexes. Geometry optimisations were performed on a set of pianostool complexes, along with complementary frequency calculations, to ensure the optimised structures were correct with the aim of then calculating some theoretical bond dissociation energies for the complexes of interest. These calculations will help us to learn more about the trends that may be displayed in this family of molecules. Two of these complexes, $[BnRe(CO)_2(CO_2)]^+$ and

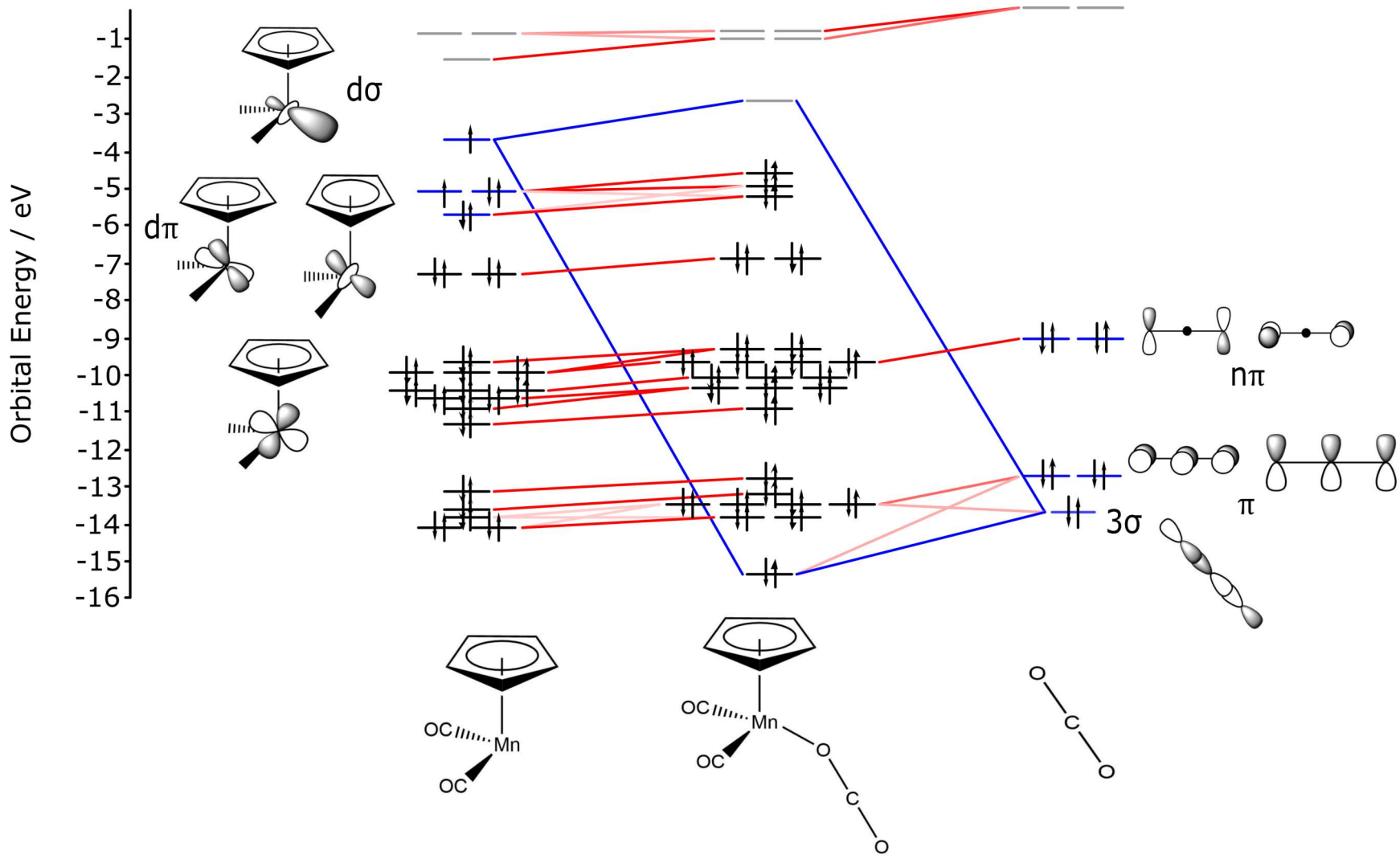

Figure 3.10: Schematic orbital interaction diagram between the orbitals of the $CpMn(CO)_2$ fragment and the orbitals of a linear CO_2 molecule.

$[BnMn(CO)_2(CO_2)]^+$ are shown in Figure 3.11 where it can be noted that both complexes have optimised towards an η^1-OCO end-on binding mode. It is believed that changing these complexes to be cationic instead of neutral is likely to dramatically increase the stability of the η^1-OCO end-on binding mode when compared with the η^2-CO_2 side-on coordination mode.

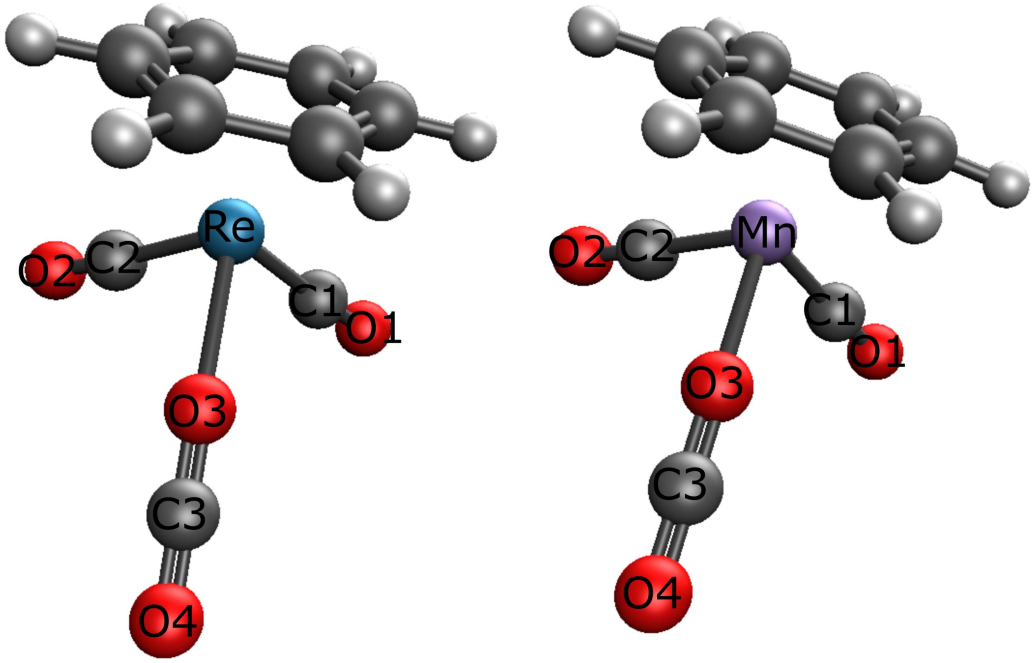

Figure 3.11: Optimised structures obtained at the DFT-M06/LANL08(f) (metals) and 6-311++G** level for $[BnRe(CO)_2(CO_2)]^+$ (left) and $[BnMn(CO)_2(CO_2)]^+$ (right) showing the preferential η^1-OCO end-on binding mode.

Calculated bond lengths can be used to further examine the bonding for the CO_2 ligand to these cationic metal centres as for $CpM(CO)_2(CO_2)$. The bond lengths for $[BnRe(CO)_2(CO_2)]^+$ and $[BnMn(CO)_2(CO_2)]^+$ in Table 3.2 show that for each complex, the M-C and C-O bonds in the carbonyl ligands are the same. If we compare these numbers to those of their tricarbonyl derivatives it is found that for $[BnRe(CO)_3]^+$ the M-C bond length is 1.955 Å and the C-O bond length is 1.136 Å and for $[BnMn(CO)_3]^+$ the M-C bond length is 1.836 Å and C-O bond length is 1.134 Å. For both systems the CO_2 bound complex is found to have shorter M-C bonds but a longer C-O bonds which is the same trend found for the neutral $CpMn(CO)_2(CO_2)$ investigated previously in this report. The reasoning

for these bond length differences can again be explained by carbonyl backbonding caused by the manganese atom in $[BnMn(CO)_2(CO_2)]^+$ to be more electron rich than in $[BnMn(CO)_3]^+$ meaning there is a large degree of CO to metal n→d_σ donation and a greater degree of metal to CO_2 $d_\pi \rightarrow \pi^*$ interactions.

Bond Length /Å	$[BnRe(CO)_2(CO_2)]^+$	$[BnMn(CO)_2(CO_2)]^+$
M-C1	1.950	1.832
M-C2	1.950	1.832
M-O3	2.283	2.148
C1-O1	1.139	1.135
C2-O2	1.139	1.135
O3-C3	1.165	1.164
C3-O4	1.142	1.144

Table 3.2: Table of non-arene bond lengths for $[BnRe(CO)_2(CO_2)]^+$ and $[BnMn(CO)_2(CO_2)]^+$.

To analyse the M-CO_2 bond lengths the most direct comparison that can be made between these complexes and their neutral Cp analogues is between $[BnMn(CO)_2(CO_2)]^+$ and $CpMn(CO)_2(CO_2)$ due to the matching η^1-OCO end-on binding mode present in both complexes. It can be seen that the Mn-O bond length is shorter for the cationic complex by 0.003 Å, which can be explained by a stronger M-O interaction, due to the fact that cationic complexes are less electron rich. There is a much larger difference between the neutral and cationic bonding scenarios when comparing the difference in lengths between the O3-C3 and C3-O4 bonds. For the neutral complex they differ in length by just 0.002 Å, but for the cationic complex they vary in length by a much larger 0.02 Å. Performing a composition analysis on the molecular orbital of interest (HOMO-26) it can be noted that there is a more even electron distribution over the CO_2 ligand in the neutral example when compared with the cationic example, this could explain why the variation in bond length for O3-C3 and C3-O4 is much greater in the cationic complex when compared with the neutral complex.

Orbital Interactions and Bond Strengths

The bonding interaction between the $[BnMn(CO)_2(CO_2)]^+$ fragment and linear CO_2 molecule is shown in Figure 3.12 and it can be noted that the orbitals involved in the bonding are the same as the bonding orbitals between $CpMn(CO)_2$ and CO_2 from Figure 3.10. The primary difference of note is that now the d_σ orbital in the $[BnMn(CO)_2]^+$ fragment is 5.7 eV lower in energy and closer to the -13.7 eV of the interacting CO_2 σ orbital. This decrease in energy causes the interaction between the σ lone pair on the CO_2 and the metal d_σ orbital to occur more favourably than for the neutral complex, and as such results in a stronger M-CO_2 interaction.

The DFT results show that oxidising these pianostool complexes by changing the arene from Cp to Bn, which in turn changes the complexes from neutral to cationic, increases the strength of the M-CO_2 interaction and therefore increases the lifetime of short lived CO_2 bound complexes. This increase in lifetime is due to the decreased HOMO-LUMO separation between the metal LUMO and CO_2 σ orbital. Further calculations were therefore conducted on more pianostool complexes, investigating their bond dissociation energies for the M-CO_2 bond, these results can be seen in Table 3.3. It can also be investigated how functionalisation of the arene can effect the strength of the M-CO_2 interaction.

Complex	BDE / kJ mol^{-1}	ν(CO_2 and CO) /cm^{-1}
$[CpMn(CO)_2(\eta^1\text{-}OCO)]$	39	2432, 1982, 1930
$[CpRe(CO)_2(\eta^2\text{-}CO_2)]$	45	2030, 1979, 1953
$[BnMn(CO)_2(\eta^1\text{-}OCO)]^+$	43	2433, 2079, 2049
$[BnRe(CO)_2(\eta^1\text{-}OCO)]^+$	70	2434, 2064, 2023
$[(Mes)Re(CO)_2(\eta^1\text{-}OCO)]^+$	68	2428, 2043, 2003
$[(HMB)Re(CO)_2(\eta^1\text{-}OCO)]^+$	64	2421, 2026, 1983
$[(HEB)Re(CO)_2(\eta^1\text{-}OCO)]^+$	64	2420, 2025, 1980
$[(C_6F_6)Re(CO)_2(\eta^1\text{-}OCO)]^+$	80	2439, 2099, 2066
$[(C_6(CF_3)_6)Re(CO)_2(\eta^1\text{-}OCO)]^+$	81	2441, 2114, 2071

Table 3.3: Table of BDE values for the M-CO_2 bond between $[(arene)M(CO)_2]^+$ and CO_2 and their calculated ν(CO) values.

The trends seen in Table 3.3 confirm the theory that the cationic

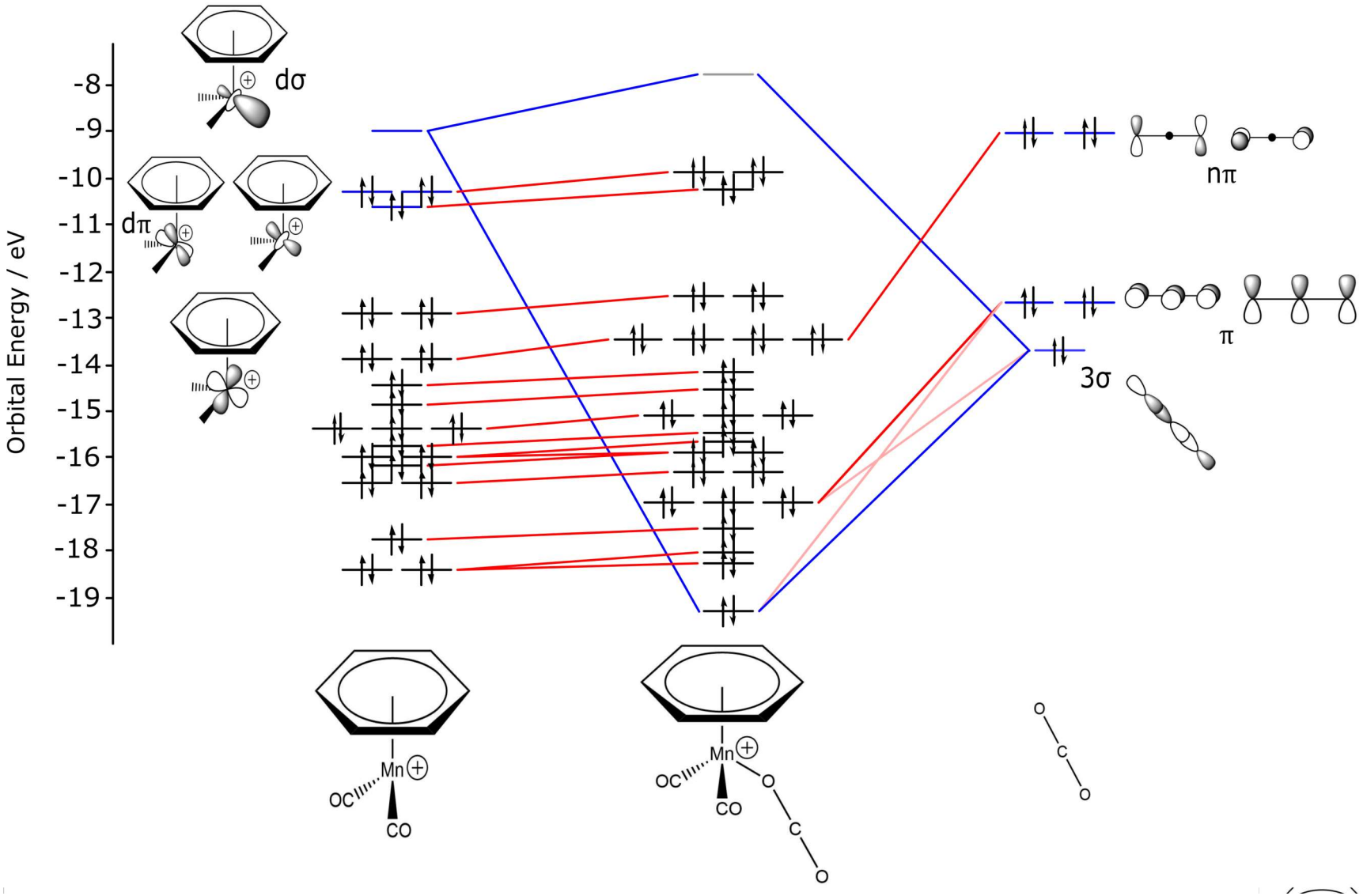

Figure 3.12: Schematic orbital interaction diagram between the orbitals of the $[BnMn(CO)_2]^+$ fragment and the orbitals of a linear CO_2 molecule.

complexes,$[BnM(CO)_2(CO_2)]^+$, interact more strongly with CO_2, when coordinating through the η^1-OCO end-on binding mode, than the neutral counterparts, $CpMn(CO)_2(CO_2)$. It can also be seen that the rhenium complexes, $[(arene)Re(CO)_2(CO_2)]^+$, interact with CO_2 significantly more strongly than the manganese, $[BnMn(CO)_2(CO_2)]^+$, complex. For the neutral Cp complexes the rhenium complex, $CpRe(CO)_2(CO_2)$, was found to coordinate to the CO_2 molecule 6 kJ mol^{-1} more strongly when compared with the manganese complex, $CpMn(CO)_2(CO_2)$. This can be attributed to the very large energy gap between the interacting orbitals for $CpMn(CO)_2(CO_2)$ as seen previously in Figure 3.10 compared with a smaller energy gap for $CpRe(CO)_2(CO_2)$. The change to cationic complexes over neutral ones caused a small increase in binding strength for the manganese complex but a much larger strengthening of the M-CO_2 bond for the rhenium systems along with a change from the previous η^2-CO_2 side-on coordination to η^1-OCO end-on binding. The remarkable stability of short lived rhenium complexes when compared with other Group V, VI and VII metals has been previously noted in the literature and this trend is found to continue here with the cationic rhenium complexes displaying far greater M-CO_2 binding strengths than the $[BnMn(CO)_2(\eta^1\text{-OCO})]$ complex.[145]

Figure 3.13 shows an MO diagram displaying the orbital interaction of the $[BnRe(CO)_2]^+$ fragment and the orbitals of a linear CO_2 molecule. It can be noted that this diagram looks similar to that given in Figure 3.12 for $[BnMn(CO)_2(CO_2)]^+$ showing that regardless of the metal the coordination of CO_2 in the η^1-OCO end-on fashion uses the same sets of orbitals on both molecules. The orbitals that interact between the metal fragment and the linear CO_2 molecule also do not change as the arene becomes more electron withdrawing or donating but there are shifts in the orbital energies of the metal fragment. This trend can be seen in Figure 3.14 displaying all of the cationic rhenium complexes, $[(arene)Re(CO)_2(\eta^1\text{-OCO})]$, from Table 3.3. The electron donating substituents on the arene cause a greater amount of electron density to be donated from the

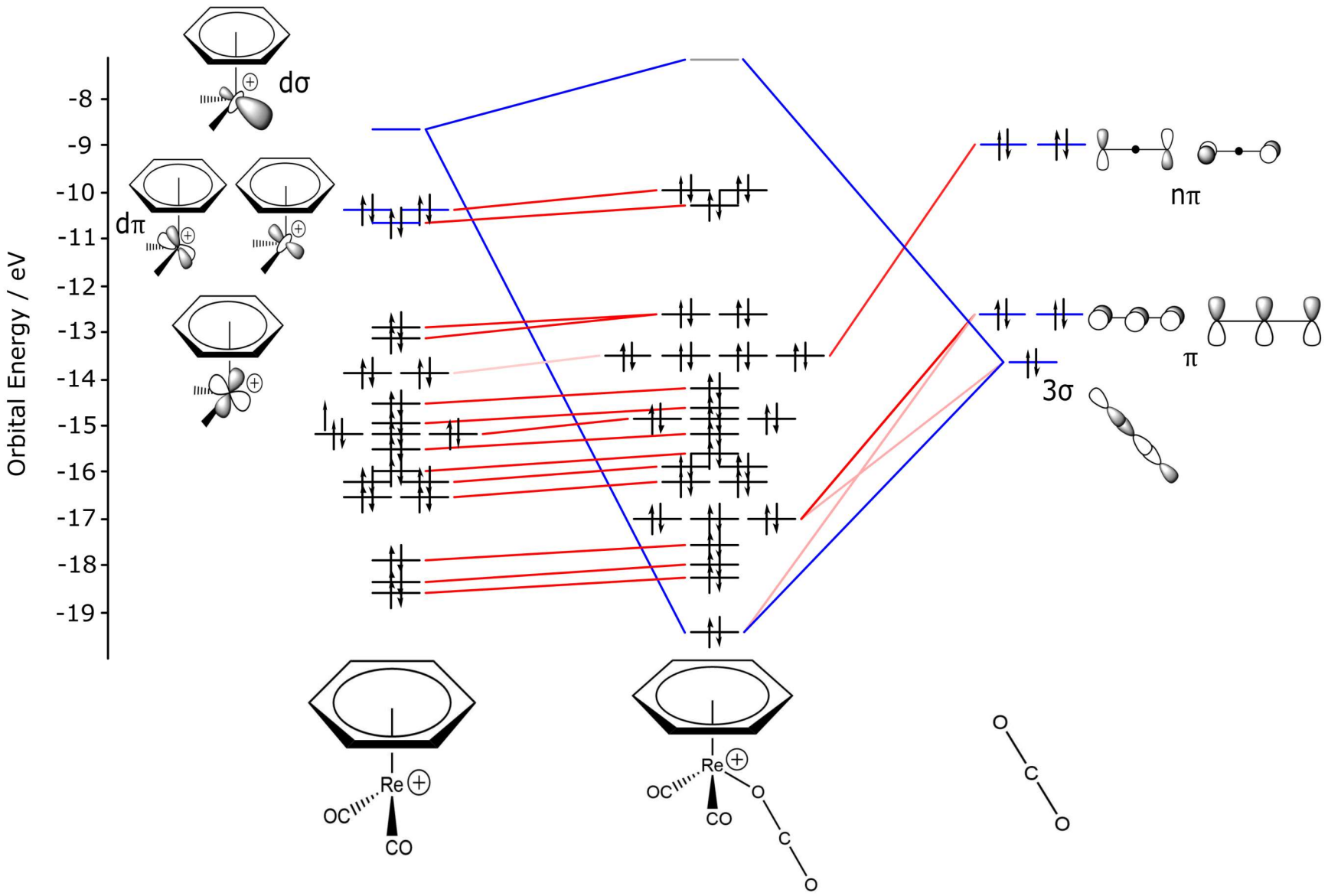

Figure 3.13: Schematic orbital interaction diagram between the orbitals of the $[BnRe(CO)_2]^+$ fragment and the orbitals of a linear CO_2 molecule.

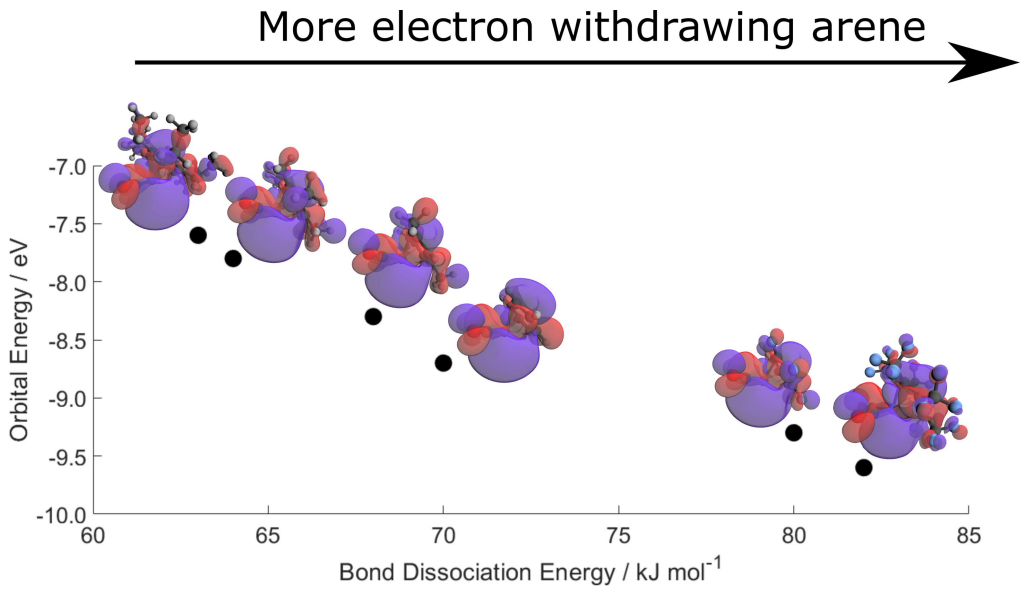

Figure 3.14: Calculated Re-CO_2 bond dissociation energies plotted against the energy of the metal fragment d_σ LUMO for [(HEB)Re(CO)$_2$(η^1-OCO)], [(HMB)Re(CO)$_2$(η^1-OCO)], [(Mes)Re(CO)$_2$(η^1-OCO)], [BnRe(CO)$_2$(η^1-OCO)], [(C_6F_6)Re(CO)$_2$(η^1-OCO)] and [($C_6(CF_3)_6$)Re(CO)$_2$(η^1-OCO)] (from left to right)

arene onto the metal centre, which in turn decreases the strength of the electrostatic interaction between the positively charged metal centre and the electronegative oxygen atom on CO_2. The metal fragments in Figure 3.14 with electron donating substituents have a higher energy metal d_σ LUMO orbital meaning its overlap with the interacting CO_2 orbital at -13.7 eV is less. The opposite is also found to be true where the electron withdrawing substituents on the arene cause a smaller amount of electron density to be donated from the arene onto the metal centre, which in turn increases the strength of the electrostatic interaction between the positively charged metal centre and the electronegative oxygen atom on CO_2. This can again be seen in Figure 3.14 where the metal fragments with electron withdrawing have a lower energy metal d_σ LUMO orbital meaning they are closer in energy to the -13.7 eV CO_2 σ orbital.

Comparisons of Functionalised Pianostool Complexes

[(HMB)Re(CO)$_2$(CO_2)]$^+$ can be used as a model complex with an arene containing electron donating substituents and [(C_6F_6)Re(CO)$_2$(CO_2)]$^+$ as a model

complex with an arene containing electron withdrawing substituents. These two structures are shown in Figure 3.15 along with selected bond lengths in Table 3.4. The carbonyl bond lengths for $[(HMB)Re(CO)_2(CO_2)]^+$ can be compared with $[(HMB)Re(CO)_3]^+$ to first gain a benchmark for the system and it is found that the Re-C bonds are 1.940 Å long and the C-O bonds are 1.141 Å long. It can be seen that the Re-C bonds in $[(HMB)Re(CO)_2(CO_2)]^+$ are 1.931 Å, which is 0.009 Å shorter than that of their tricarbonyl parent molecule and the carbonyl C-O bonds are 1.146 Å long, which is 0.005 Å longer than the tricarbonyl parent. This can be explained by carbonyl backbonding where the more electron rich arene is donating electron density onto the metal centre resulting in a stronger Re-C bond and a weaker C-O bond through metal to CO_2 $d_\pi \rightarrow \pi^*$ donation. This can be further seen by looking at the calculated ν(C-O) bands from Table 3.3 and comparing to calculated ν(C-O) bands for $[(HMB)Re(CO)_3]^+$ which are found at 2078, 2018 and 2016 cm^{-1}. It can be seen that the ν(C-O) bands have shifted down in wavenumber by around 52 and 34 cm^{-1} upon coordination of CO_2 which is consistent with a more electron rich metal weakening the C-O bonds by backbonding.

$[(C_6F_6)Re(CO)_2(CO_2)]^+$ can be compared with its tricarbonyl parent as a benchmark again and it is found that the Re-C bonds are 1.971 Å long and the C-O bonds are 1.132 Å long in $[(C_6F_6)Re(CO)_3]^+$. It can be seen that the Re-C bonds in $[(C_6F_6)Re(CO)_2(CO_2)]^+$ are 0.005 Å longer than that of their tricarbonyl parent molecule and the carbonyl C-O bonds are 0.001 Å longer than the tricarbonyl parent. This is unusual as usually a longer C-O bond is accompanied by a shorter M-C bond because of a larger degree of backbonding, this suggests that another factor is primarily influencing the bonding in this system instead of just backbonding. The calculated ν(C-O) bands for $[(C_6F_6)Re(CO)_3]^+$ are found at 2127, 2081 and 2079 cm^{-1}, which when compared to the CO_2 bound dicarbonyl species bands at 2099 and 2066 cm^{-1} it can be seen that upon CO_2 coordination there is the usual downward shift in wavenumber. These shifts of

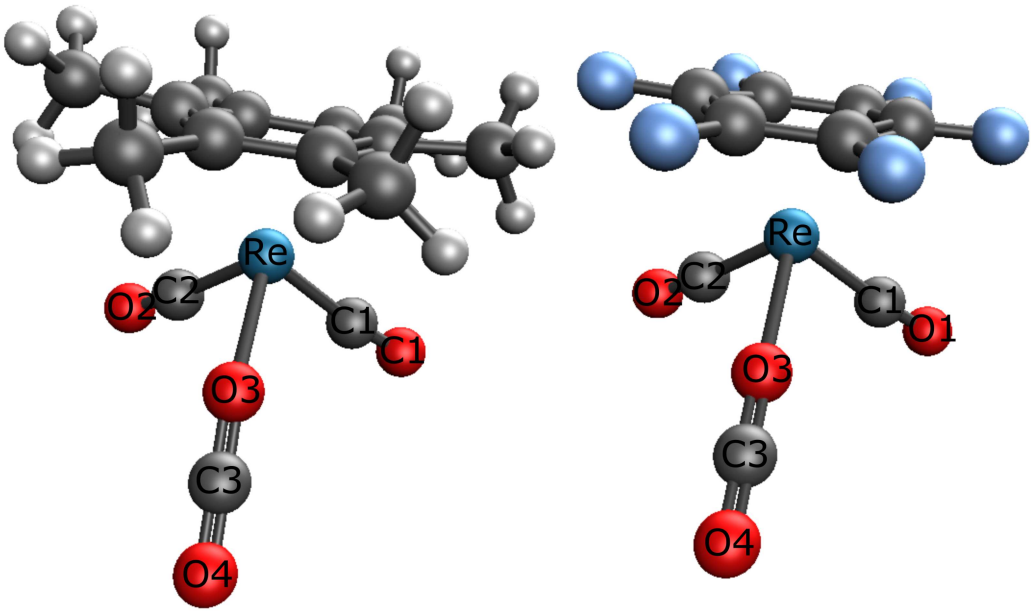

Figure 3.15: Optimised structures obtained at the DFT-M06/LANL08(f) (metals) and 6-311++G** level for $[(HMB)Re(CO)_2(CO_2)]^+$ (left) and $[(C_6F_6)Re(CO)_2(CO_2)]^+$ (right) showing the preferential η^1-OCO end-on binding mode.

around 28 and 14 cm^{-1} are smaller than the shifts that were found for the HMB arene complex. This reduction in shift is due to the more electron withdrawing arene reducing the effect of the CO_2 coordination and electron donation to the rest of the system.

Bond Length /Å	$[(HMB)Re(CO)_2(CO_2)]^+$	$[(C_6F_6)Re(CO)_2(CO_2)]^+$
Re-C1	1.931	1.976
Re-C2	1.931	1.976
Re-O3	2.310	2.273
C1-O1	1.146	1.133
C2-O2	1.146	1.133
O3-C3	1.166	1.167
C3-O4	1.143	1.141

Table 3.4: Table of non-arene bond lengths for $[(HMB)Re(CO)_2(CO_2)]^+$ and $[(C_6F_6)Re(CO)_2(CO_2)]^+$.

The calculated CO_2 IR band in complexes displaying η^1-OCO binding from Table 3.3 also display a visible trend. The complexes with more electron donating arenes have their CO_2 band at a lower wavenumber and the complexes with electron withdrawing arenes have their CO_2 band at a higher wavenumber. The change in the CO_2 frequencies is significantly smaller than the other ν(C-O) shifts.

The CO_2 bands have shifted 20 cm^{-1} between the most electron donating and withdrawing arenes but the other carbonyl bands have a variation of 91 cm^{-1} between the same two complexes.

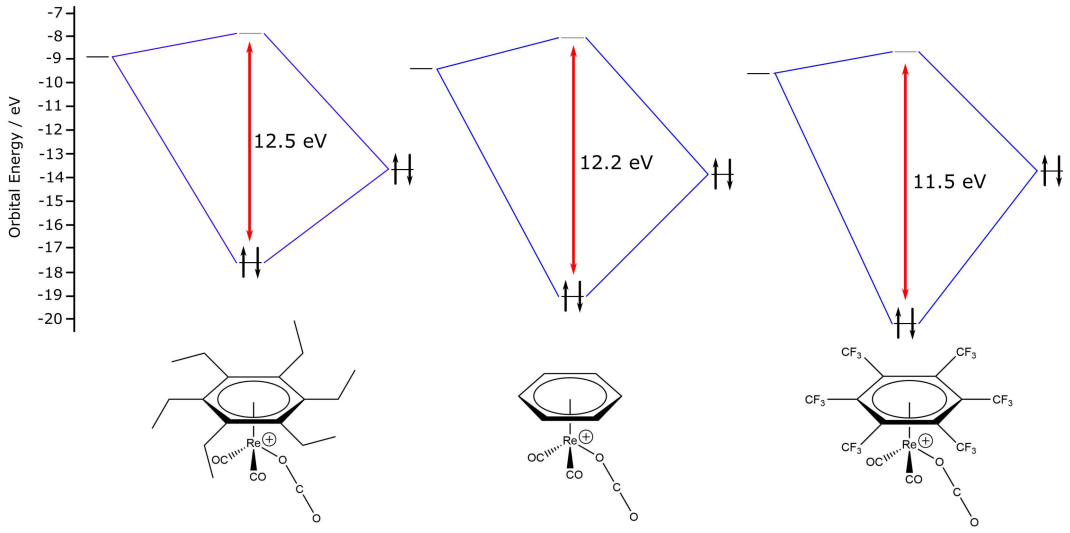

Figure 3.16: Simplified orbital interaction diagram displaying the frontier orbitals involved in end-on CO_2 coordination for $[(HEB)Re(CO)_2(\eta^1\text{-}OCO)]^+$, $[BnRe(CO)_2(\eta^1\text{-}OCO)]^+$ and $[(C_6(CF_3)_6)Re(CO)_2(\eta^1\text{-}OCO)]^+$ and the energy gap between them.

In Figure 3.16 a trend showing that the CO_2 complexes become more stable with more electron withdrawing arenes can be seen. The more electron donating arene has a higher energy metal fragment which in turn means the metal LUMO is located further in energy from the CO_2 orbital, which increases the energy difference between the bonding and antibonding orbitals on the CO_2 complex. The opposite can be seen for the complex with the more electron withdrawing arene and the unfunctionalised arene sits in the middle of the two complexes.

3.2.3 DFT Investigation of Neutral Mn and Re α-Diimine Complexes

Mn Complex Geometry Optimisations, Bond Lengths and Bond Strengths

Next a different set of complexes, with a proven ability to photochemically or electrochemically reduce CO_2, is investigated.[115,146–148] Geometry optimisations

were performed on the four different isomers of [(bpy)Mn(CO)$_2$(Cl)(CO$_2$)] with frequency calculations to ensure true energy minima had been obtained. These resulting structures can be seen in Figure 3.17. The calculated systems are all neutral and display the predicted lowest energy binding mode of CO_2 to be the end-on η^1-OCO binding mode. It can be seen that in the three cases where the CO_2 and Cl ligands are located *cis* to each other, the CO_2 ligand moves towards the Cl atom. The CO_2 molecule itself remains linear but the M-O-C bond angle is found to be 123 ± 2° whereas in the molecule with both CO_2 and Cl in axial positions the M-O-C angle is 173°.

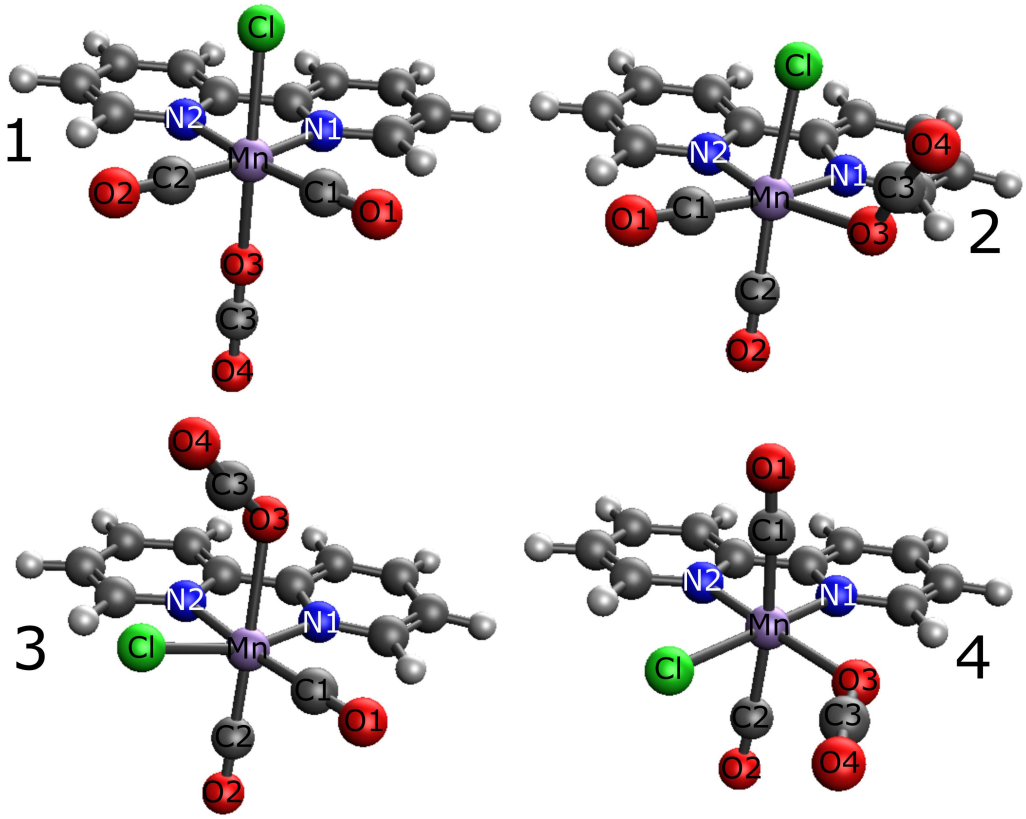

Figure 3.17: Optimised structures obtained at the DFT-M06/LANL08(f) (metals) and 6-311++G** level for [(bpy)Mn(CO)$_2$(ax-Cl)(ax-CO$_2$)] (**1**) (top left), [(bpy)Mn(CO)$_2$(ax-Cl)(eq-CO$_2$)] (**2**) (top right), [(bpy)Mn(CO)$_2$(eq-Cl)(ax-CO$_2$)] (**3**) (bottom left) and [(bpy)Mn(CO)$_2$(eq-Cl)(eq-CO$_2$)] (**4**) (bottom right) showing the preferential η^1-OCO end-on binding mode.

In Table 3.5 the different bond lengths of each of the four displayed isomers from Figure 3.17 can be seen and there is significant variation in bond lengths between isomers. The length of the Mn-C1 and Mn-C2 bonds can be explained

by the *trans* influence. This effect arises due to the differences in the way electron density is reorganised in a complex under the influence of a specific ligand. This ligand, by decreasing the need for electron density at the *trans* position, weakens the associated metal-ligand bond and as such leads to an increase in the bond length or kinetics.[149] It can be seen that the Mn-C1 and Mn-C2 bonds are longest in isomer **4** at 1.878 Å, where the two CO ligands are bound *trans* to each other. CO ligands have a large *trans* influence and as such result in these bonds being quite long. The two Mn-C1 and Mn-C2 bonds in isomer **1** are 0.09 Å shorter and are both *trans* to the bpy ligand, which has a much smaller *trans* influence. For isomer **2** Mn-C1 is found to be longer than Mn-C2, where Mn-C1 is *trans* to the bpy ligand and Mn-C2 is *trans* to the Cl ligand. This is because Cl has a greater *trans* influence than bpy, but not as large as the CO ligand.[150] Finally in isomer **3** Mn-C1 is *trans* to the bpy ligand and Mn-C2 is *trans* to the CO_2 ligand and as such M-C1 is longer than Mn-C2 due to very low *trans* influence exhibited by the CO_2 ligand.

Bond Length /Å	**1**	**2**	**3**	**4**
Mn-C1	1.788	1.791	1.781	1.878
Mn-C2	1.788	1.785	1.761	1.878
Mn-O3	2.182	2.258	2.225	2.221
Mn-N1	2.057	2.044	1.990	1.982
Mn-N2	2.057	1.976	2.064	1.982
C1-O1	1.152	1.152	1.152	1.143
C2-O2	1.152	1.153	1.152	1.143
O3-C3	1.156	1.168	1.166	1.167
C3-O4	1.153	1.147	1.148	1.147

Table 3.5: Table of bond lengths for the four isomers of [(bpy)Mn$(CO)_2$(Cl)(CO_2)] from Figure 3.17.

The Mn-N1 and Mn-N2 bonds can be analysed in a similar way, using the *trans* influence. In isomer **1** both bpy N atoms are *trans* to CO ligands and as such display matching and increased bond lengths. In isomer **2** Mn-N1 is the longer bond, which is *trans* to a CO ligand and in isomer **3** M-N2 is the longer bond as it is again *trans* to a CO ligand. In isomer **4** neither Mn-N bond is *trans* to a CO ligand and as such neither are significantly lengthened. The C1-O1 and

C2-O2 bonds in isomers **1**, **2** and **3** are all quite similar since none of these CO ligands are located *trans* to any other CO ligands with very large *trans* influences. In isomer **4** the C1-O1 and C2-O2 bonds are notably shorter due to them being *trans* to each other weakening their interaction with the metal centre and as such decreasing the amount of backbonding taking place.

The Mn-O3 bond lengths are best understood by using the bond dissociation energy calculations given in Table 3.6. The BDE values for each isomer align with the M-O3 bond lengths with isomer **1** having the shortest bond length, at 2.182 Å, and strongest Mn-OCO bond and isomer **2** having the longest bond length, at 2.258 Å, and weakest Mn-OCO bond. It can also be noted from Table 3.6 that there is a similar trend to that displayed for the pianostool complexes, where the presence of electron donating groups on the bpy ligand causes a decrease in Mn-OCO bond strength and electron withdrawing groups on the bpy cause an increase in Mn-OCO bond strength. The difference between the most electron donating and electron withdrawing groups is only 5 kJ mol^{-1} which is notably smaller than the differences for the pianostool complexes of 17 kJ mol^{-1}. This is potentially because there are only two additional functional groups in the bpy complexes compared with six additional functional groups for the pianostool complexes where every carbon atom of the arene was functionalised but this is not synthetically viable for bpy complexes.

Mn Complex Orbital Interactions and Vibrational Frequencies

The bonding orbitals involved in isomers **1-4** were investigated, to do this, MO diagrams of each isomer were constructed, see Figures 3.18, 3.19, 3.20 and 3.21. The bonding found in isomer **1** is very similar to that found in the pianostool complexes where the metal fragment LUMO d_σ orbital is interacting with the CO_2 σ orbital which has resulted in the strongest and shortest bond of the four isomers. In isomers **2**, **3** and **4** the binding to the CO_2 molecule appears to be an interaction with the same metal fragment d_σ orbital, which is now slightly

Complex	BDE / kJ mol^{-1}	ν(CO_2 and CO) /cm^{-1}
(bpy)Mn(CO)$_2$(ax-CO_2)(ax-Cl)	29	2426, 1975, 1925
(bpy)Mn(CO)$_2$(eq-CO_2)(ax-Cl)	14	2381, 1978, 1932
(bpy)Mn(CO)$_2$(ax-CO_2)(eq-Cl)	23	2375, 1980, 1927
(bpy)Mn(CO)$_2$(eq-CO_2)(eq-Cl)	28	2380, 2033, 1966
(dmbpy)Mn(CO)$_2$(ax-CO_2)(ax-Cl)	27	2425, 1973, 1921
(dmbpy)Mn(CO)$_2$(eq-CO_2)(ax-Cl)	14	2379, 1975, 1927
(dmbpy)Mn(CO)$_2$(ax-CO_2)(eq-Cl)	23	2375, 1977, 1923
(dmbpy)Mn(CO)$_2$(eq-CO_2)(eq-Cl)	28	2379, 2030, 1962
(dtbpy)Mn(CO)$_2$(ax-CO_2)(ax-Cl)	27	2425, 1972, 1920
(dtbpy)Mn(CO)$_2$(eq-CO_2)(ax-Cl)	14	2378, 1974, 1925
(dtbpy)Mn(CO)$_2$(ax-CO_2)(eq-Cl)	23	2375, 1976, 1921
(dtbpy)Mn(CO)$_2$(eq-CO_2)(eq-Cl)	28	2377, 2026, 1955
(dfbpy)Mn(CO)$_2$(ax-CO_2)(ax-Cl)	31	2427, 1984, 1938
(dfbpy)Mn(CO)$_2$(eq-CO_2)(ax-Cl)	15	2384, 1990, 1947
(dfbpy)Mn(CO)$_2$(ax-CO_2)(eq-Cl)	24	2380, 1988, 1940
(dfbpy)Mn(CO)$_2$(eq-CO_2)(eq-Cl)	30	2381, 2044, 1983
(dftbpy)Mn(CO)$_2$(ax-CO_2)(ax-Cl)	32	2428, 1984, 1939
(dftbpy)Mn(CO)$_2$(eq-CO_2)(ax-Cl)	15	2384, 1990, 1947
(dftbpy)Mn(CO)$_2$(ax-CO_2)(eq-Cl)	24	2380, 1991, 1943
(dftbpy)Mn(CO)$_2$(eq-CO_2)(eq-Cl)	30	2381, 2044, 1983

Table 3.6: Table of BDE computed values for the M-CO_2 bond between [(4,4'-R_2-2,2'-bpy)Mn(CO)$_2$(Cl)] and CO_2 and their calculated ν(CO) and CO_2 vibrational frequencies.

increased in energy and as such is now the LUMO+1 orbital of the fragment, and interacts with the CO_2 nπ orbitals.

The calculated IR bands for five (L)Mn(CO)$_2$(CO_2)(Cl) complexes and their isomers are given in Table 3.6 and a similar trend to that of the pianostool complexes is noted. The complexes bearing more electron donating groups have their CO_2 band shifted to a lower wavenumber, while the presence of electron withdrawing groups causes the CO_2 band to shift up to higher wavenumbers. The shift of these CO_2 bands has a maximum range of 3 cm^{-1} which is less than predicted for the pianostool complexes. This is due to the lower degree of functionalisation for the bpy complexes where there are only two additional functional groups where there are six additional functional groups for the pianostool complexes. The wavenumber of the CO_2 vibrational frequency varies between isomers with the band in isomer **1** appearing at a much higher wavenumber than in isomers **2**, **3** and **4**. This is related to the trend noted in Figure 3.17, where the M-O-C bond

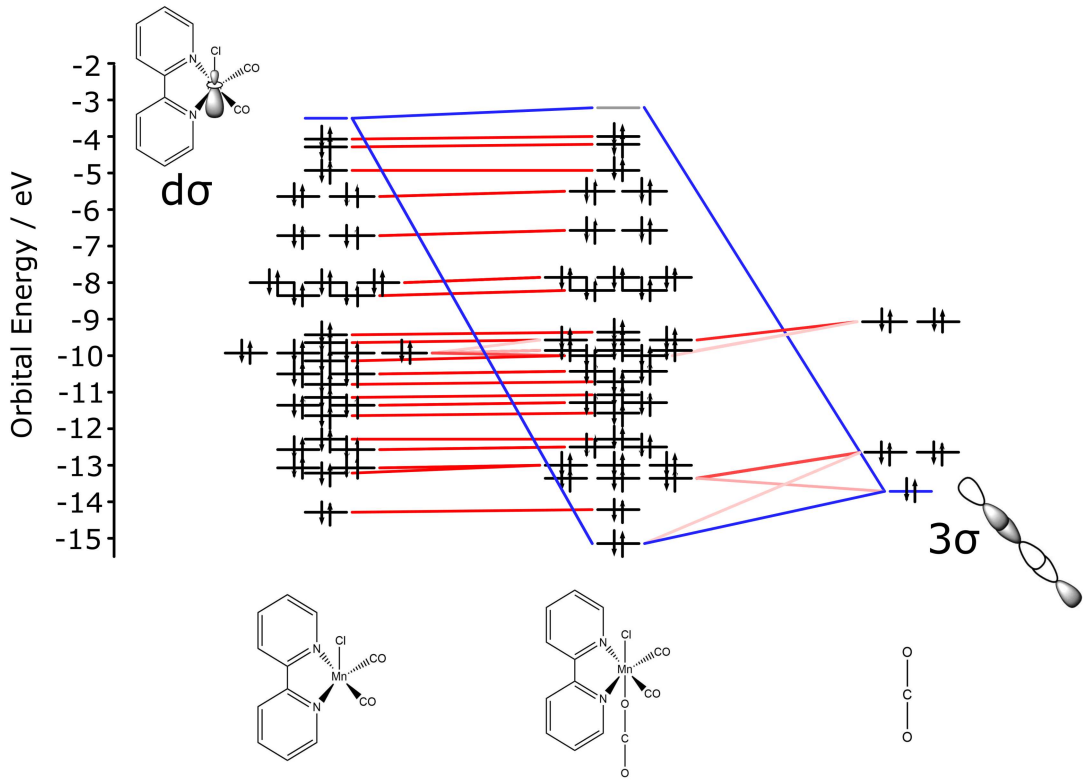

Figure 3.18: Schematic orbital interaction diagram between the orbitals of the [(bpy)Mn(CO)$_2$(ax-Cl)] fragment with an axial vacant site and the orbitals of a linear CO_2 molecule. Isomer **1**

angle is significantly smaller for isomers **2**, **3** and **4**. From the data in Table 3.5 it can be seen that this causes the O3-C3 and C3-O4 bonds to be more similar in length in isomer **1** when compared with the other isomers which in turn causes the antisymmetric stretch, which is the vibration responsible for this IR band, to be excited at a higher energy, closer to that of free CO_2 (2565 cm^{-1}). The calculated ν(CO) bands display the same trend for the bound CO_2 with more electron donating groups causing ν(CO) bands to shift to a lower wavenumber and the presence of electron withdrawing groups causes the reverse. It can also be seen that isomers **1**, **2** and **3** all have both their carbonyl bands between 1984 - 1972 cm^{-1} and 1939 - 1920 cm^{-1}, but for isomer **4** the carbonyl bands are found between 2044 - 2026 cm^{-1} and 1983 - 1955 cm^{-1}. This is because of the previously mentioned *trans* influence which causes the carbonyl bands in isomer **4** to interact with the manganese centre less strongly, therefore resulting in stronger C-O bonds appearing at higher wavenumbers.

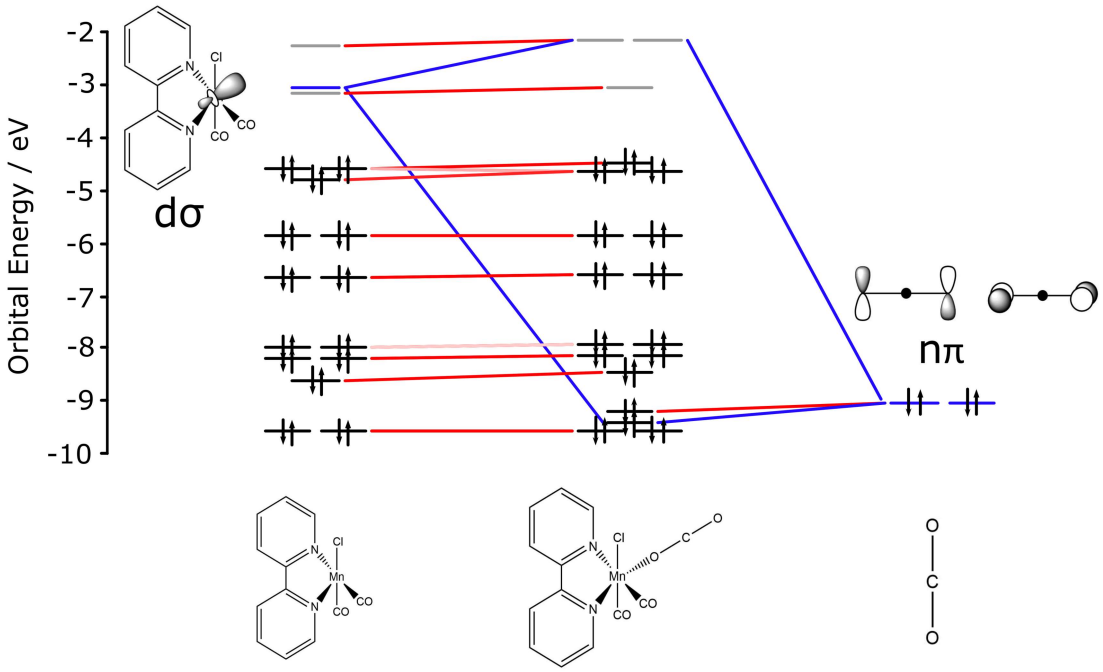

Figure 3.19: Schematic orbital interaction diagram between the orbitals of the [(bpy)Mn(CO)$_2$(ax-Cl)] fragment with an equatorial vacant site and the orbitals of a linear CO_2 molecule. Isomer **2**

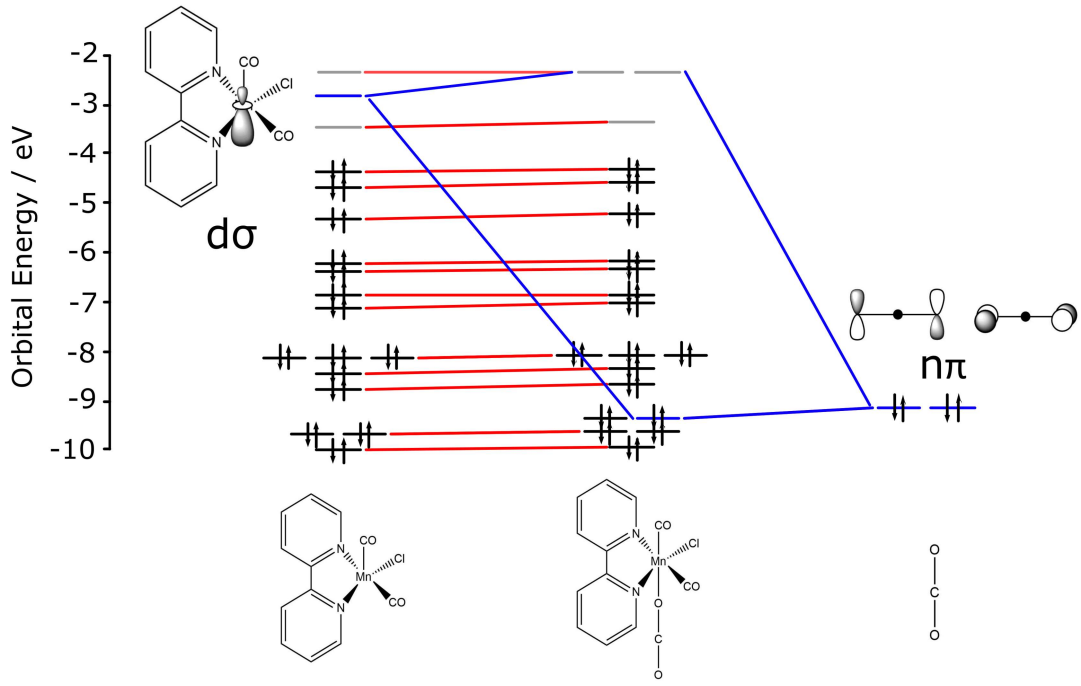

Figure 3.20: Schematic orbital interaction diagram between the orbitals of the [(bpy)Mn(CO)$_2$(eq-Cl)] fragment with an axial vacant site and the orbitals of a linear CO_2 molecule. Isomer **3**

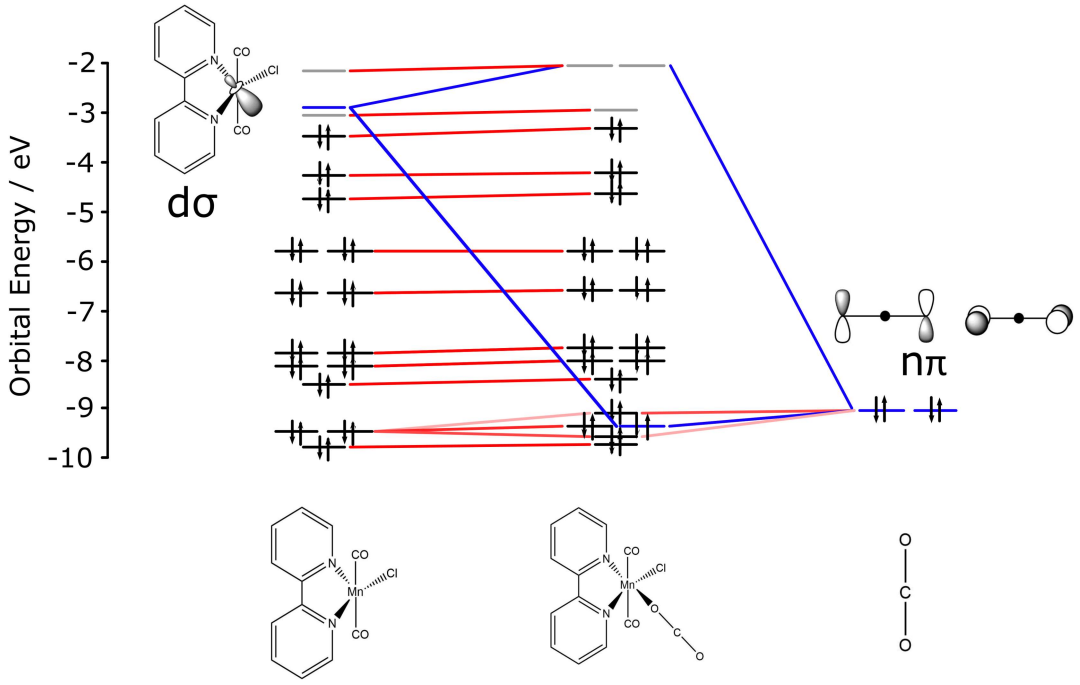

Figure 3.21: Schematic orbital interaction diagram between the orbitals of the [(bpy)Mn(CO)$_2$(eq-Cl)] fragment with an equatorial vacant site and the orbitals of a linear CO_2 molecule. Isomer **4**

The data in Figure 3.22 reveals a trend showing that the CO_2 complexes become more stable with more electron withdrawing groups attached to the bpy ligand for isomer **1**. The presence of a more electron withdrawing bpy results in a lower energy metal fragment, which in turn decreases the energy gap between the unoccupied bonding orbital of the metal fragment and the CO_2 bonding orbital. This effect also decreases the energy difference between the bonding and antibonding orbitals of the CO_2 complex. This effect is less noticeable than it was for the pianostool complexes. The same trend was found to also be true for isomers **2**, **3** and **4**, with a comparatively equal energy change found between electron donating and electron withdrawing bpy substituents.

Re Complex Geometry Optimisations, Bond Lengths and Bond Strengths

For the previously studied pianostool complexes, it was found that the neutral rhenium and manganese complexes had different preferential binding modes to

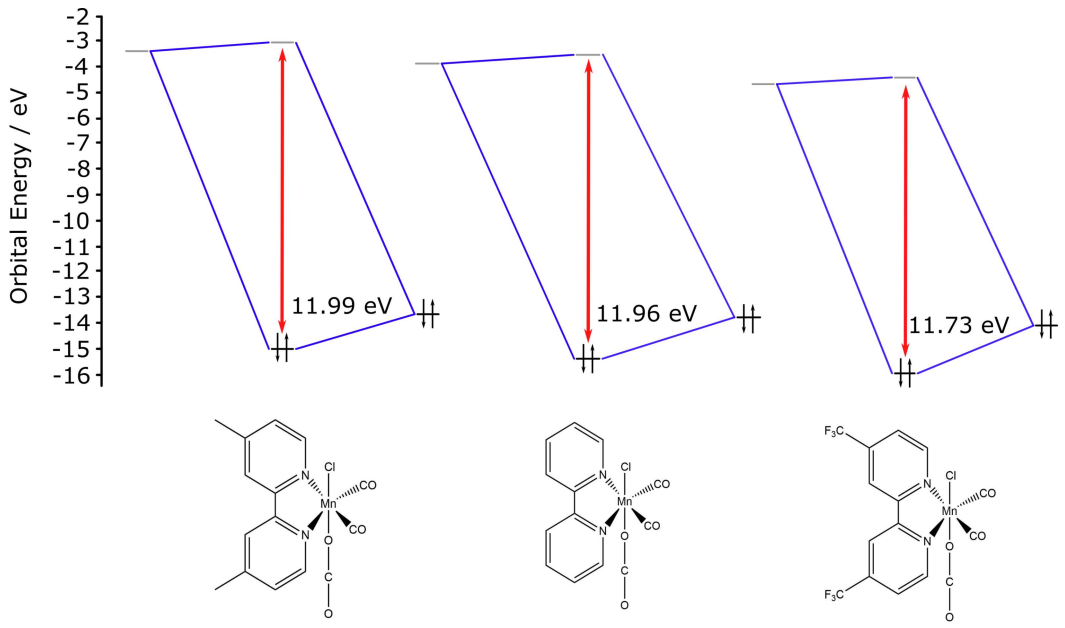

Figure 3.22: Simplified frontier orbital interaction diagram displaying the orbitals involved in end-on CO_2 coordination for [(4,4'-H_2-2,2'-bpy)Mn(CO)$_2$(Cl)], [(4,4'-Me_2-2,2'-bpy)Mn(CO)$_2$(Cl)] and [(4,4'-$(CF_3)_2$-2,2'-bpy)Mn(CO)$_2$(Cl)] and the energy gap between them.

CO_2. In order to further investigate whether the change from a neutral to cationic complex has an influence on the preferred CO_2 binding mode, DFT calculations were performed on the rhenium variants of the same set of complexes. The resulting structures of the four isomers of [(bpy)Re(CO)$_2$(Cl)(CO_2)] are given in Figure 3.23. It is observed that the η^1-OCO binding mode is also calculated to be the lowest energy for this set of cationic complexes too. The Re-O-C bond angle is smaller when CO_2 and Cl are *cis* to each other in isomers **6**, **7** and **8**, displaying a bond angle of 123 ± 3°.

Bond Length /Å	**5**	**6**	**7**	**8**
Re-C1	1.891	1.894	1.886	1.993
Re-C2	1.891	1.889	1.859	1.994
Re-O3	2.315	2.343	2.478	2.353
Re-N1	2.198	2.191	2.102	2.099
Re-N2	2.198	2.063	2.207	2.052
C1-O1	1.161	1.160	1.162	1.146
C2-O2	1.161	1.161	1.160	1.147
O3-C3	1.158	1.169	1.167	1.168
C3-O4	1.152	1.146	1.146	1.147

Table 3.7: Table of bond lengths for the four isomers of [(bpy)Re(CO)$_2$(Cl)(CO_2)] from Figure 3.23.

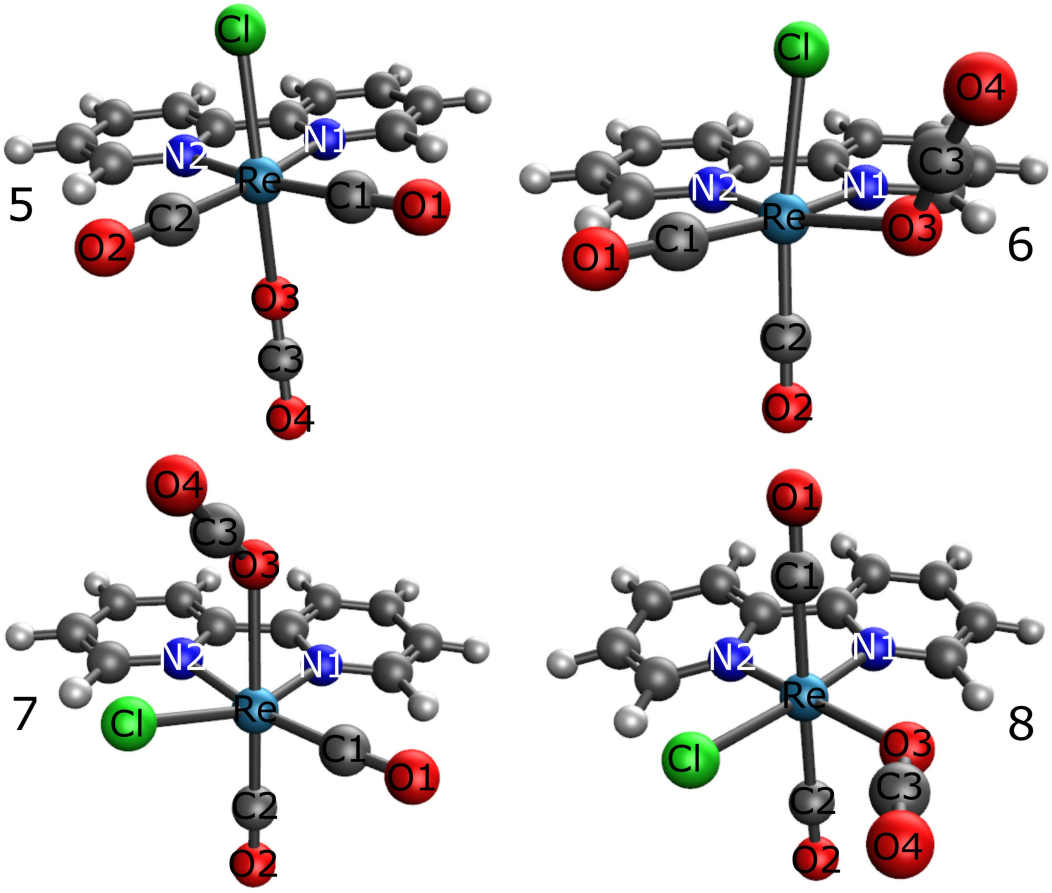

Figure 3.23: Optimised structures obtained at the DFT-M06/LANL08(f) (metals) and 6-311++G** level for [(bpy)Re(CO)$_2$(ax-Cl)(ax-CO$_2$)] (**5**) (top left), [(bpy)Re(CO)$_2$(ax-Cl)(eq-CO$_2$)] (**6**) (top right), [(bpy)Re(CO)$_2$(eq-Cl)(ax-CO$_2$)] (**7**) (bottom left) and [(bpy)Re(CO)$_2$(eq-Cl)(eq-CO$_2$)] (**8**) (bottom right) showing the preferential η^1-OCO end-on binding mode.

The data in Table 3.7 shows the different bond lengths of each of the four isomers described in Figure 3.23; again, there is noticeable variation in bond lengths between the isomers. The length of Re-C1 and Re-C2 bonds can again be explained by the *trans* influence. Re-C1 and Re-C2 are longest in isomer **8** and are shorter in isomer **5**. In isomers **6** and **7**, Re-C1 is found to be longer than Re-C2, which also match up with the manganese isomers for the same reasons relating to the *trans* influence.

The shortest Re-O3 bond is found in isomer **5**, which shown in Table 3.8 is the strongest bond of the four isomers by a significant margin. This is the strongest Re-O bond because the CO_2 molecule is not located *trans* to a destabilising CO ligand and has a higher energy antibonding orbital at -1.6 eV and a much

lower energy bonding orbital at -15.4 eV as shown in Figure 3.24. Isomer **6** has a weaker CO_2 bond than isomer **5**, along with a longer Re-O3 bond. The antibonding orbital of isomer **6** is also found at -1.6 eV, but its bonding orbital is found at a higher energy of -14.9 eV, c.f isomer **5**, so there is less of a stabilising effect from this bonding interaction. Isomer **7** has a Re-O3 bond length longer than all of the other isomers, but still a strong R-O bond. This is due to the fact the CO_2 ligand is located *trans* to a CO ligand, which causes this bond to be lengthed by the structural *trans* influence. The Re-O bond strength is helped by its high energy antibonding orbital, at -1.4 eV, which stabilises this interaction into being more favourable. Isomer **8** has the weakest Re-O bond and a longer Re-O3 bond length when compared to its closest analogue isomer **6**, as both have CO_2 ligands located *trans* to the bpy ligand. This is due the fact that the antibonding orbital of isomer **8** is found at the lowest energy, at -2.1 eV, meaning this bonding interaction is not as stabilising as it is for isomer **6** and hence causing the longer and weaker bond. It can also be seen from the data in Table 3.8 the same trend resulting from the presence of electron donating groups on the bpy ligand causing a decrease in Re-OCO bond strength; electron withdrawing groups on the bpy causing an increase in Re-OCO bond strength. The difference that this increase in bond strength based on bpy functional group change makes for these rhenium bpy complexes is a smaller change than was noted for the manganese bpy complexes.

Re Complex Vibrational Frequencies and Orbital Interactions

The calculated CO_2 IR bands reported in Table 3.8 follow the same trend as for the manganese bpy complexes where the complexes with more electron donating groups have their CO_2 band shifted to a lower wavenumber and the presence of electron withdrawing groups causes the CO_2 band to shift up in wavenumber. The value of the CO_2 vibrational frequency varies between isomers with the band in isomer **5** appearing at a much higher wavenumber than in isomers **6**, **7** and

Complex	BDE / kJ mol^{-1}	ν(CO_2 and CO) /cm^{-1}
(bpy)Re(CO)$_2$(ax-CO_2)(ax-Cl)	41	2422, 1943, 1884
(bpy)Re(CO)$_2$(eq-CO_2)(ax-Cl)	16	2384, 1952, 1892
(bpy)Re(CO)$_2$(ax-CO_2)(eq-Cl)	26	2381, 1952, 1889
(bpy)Re(CO)$_2$(eq-CO_2)(eq-Cl)	5	2378, 2022, 1923
(dmbpy)Re(CO)$_2$(ax-CO_2)(ax-Cl)	41	2421, 1940, 1880
(dmbpy)Re(CO)$_2$(eq-CO_2)(ax-Cl)	16	2384, 1948, 1886
(dmbpy)Re(CO)$_2$(ax-CO_2)(eq-Cl)	25	2381, 1948, 1883
(dmbpy)Re(CO)$_2$(eq-CO_2)(eq-Cl)	4	2378, 2015, 1916
(dtbpy)Re(CO)$_2$(ax-CO_2)(ax-Cl)	41	2418, 1940, 1880
(dtbpy)Re(CO)$_2$(eq-CO_2)(ax-Cl)	16	2383, 1945, 1883
(dtbpy)Re(CO)$_2$(ax-CO_2)(eq-Cl)	26	2380, 1947, 1882
(dtbpy)Re(CO)$_2$(eq-CO_2)(eq-Cl)	6	2377, 2011, 1911
(dfbpy)Re(CO)$_2$(ax-CO_2)(ax-Cl)	43	2425, 1954, 1899
(dfbpy)Re(CO)$_2$(eq-CO_2)(ax-Cl)	17	2386, 1966, 1907
(dfbpy)Re(CO)$_2$(ax-CO_2)(eq-Cl)	27	2385, 1963, 1905
(dfbpy)Re(CO)$_2$(eq-CO_2)(eq-Cl)	10	2380, 2038, 1944
(dftbpy)Re(CO)$_2$(ax-CO_2)(ax-Cl)	43	2425, 1955, 1898
(dftbpy)Re(CO)$_2$(eq-CO_2)(ax-Cl)	17	2387, 1967, 1907
(dftbpy)Re(CO)$_2$(ax-CO_2)(eq-Cl)	27	2386, 1965, 1904
(dftbpy)Re(CO)$_2$(eq-CO_2)(eq-Cl)	9	2383, 2039, 1944

Table 3.8: Table of BDE values for the M-CO_2 bond between [(4,4'-R_2-2,2'-bpy)Re(CO)$_2$(Cl)] and CO_2 and their calculated ν(CO) and CO_2 vibrational frequencies.

8, which is again related to the trend noted in Figure 3.17 where the M-O-C bond angle is altered. The calculated ν(CO) vibrational frequencies display the same trend as for the CO_2 bonds with more electron donating groups have their ν(CO) vibrational frequencies shifted to a lower wavenumber and the presence of electron withdrawing groups causes the ν(CO) vibrational frequencies to shift to higher wavenumber. This effect is far more noticeable for the CO ligands when compared with CO_2 as the CO ligand and its ability to strongly backbond with the metal centre means it is more sensitive to changes at the metal centre. The CO vibrational frequencies for isomers **5**, **6** and **7** all have their carbonyl ν(CO) values between 1967 - 1940 cm^{-1} and 1907 - 1880 cm^{-1}, but for isomer **8** the carbonyl vibrational frequencies are found between 2039 - 2011 cm^{-1} and 1944 - 1911 cm^{-1}. This is again due to the previously mentioned *trans* influence.

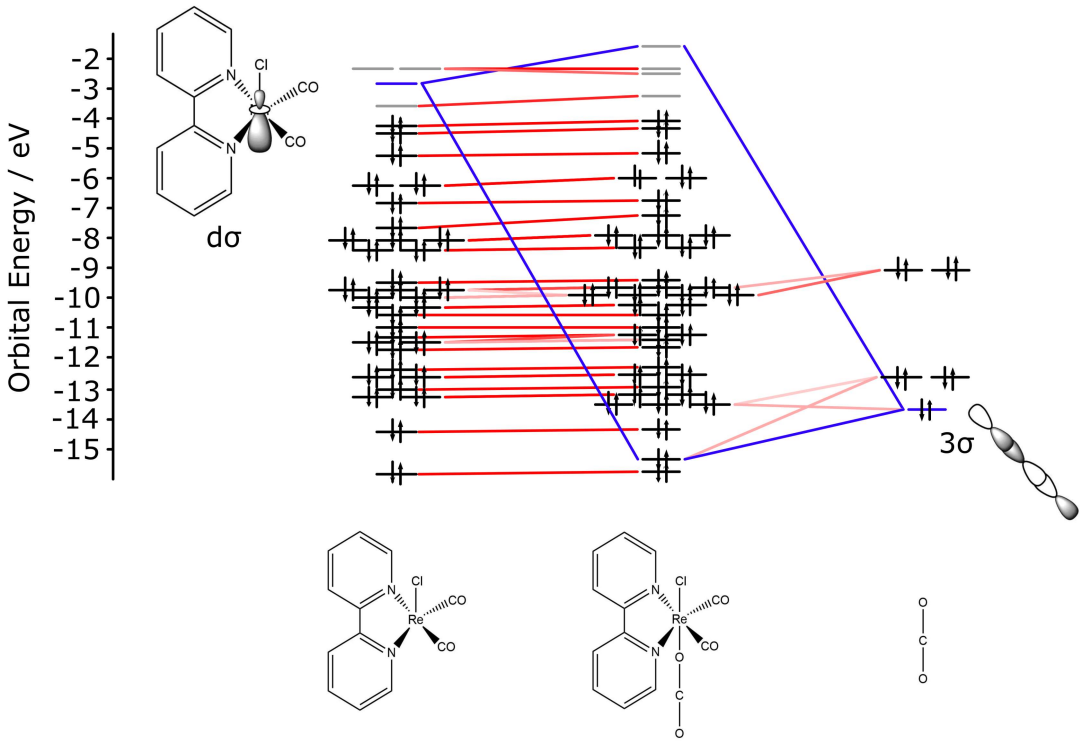

Figure 3.24: Schematic orbital interaction diagram between the orbitals of the [(bpy)Re(CO)$_2$(ax-Cl)] fragment with an axial vacant site and the orbitals of a linear CO_2 molecule. Isomer **5**

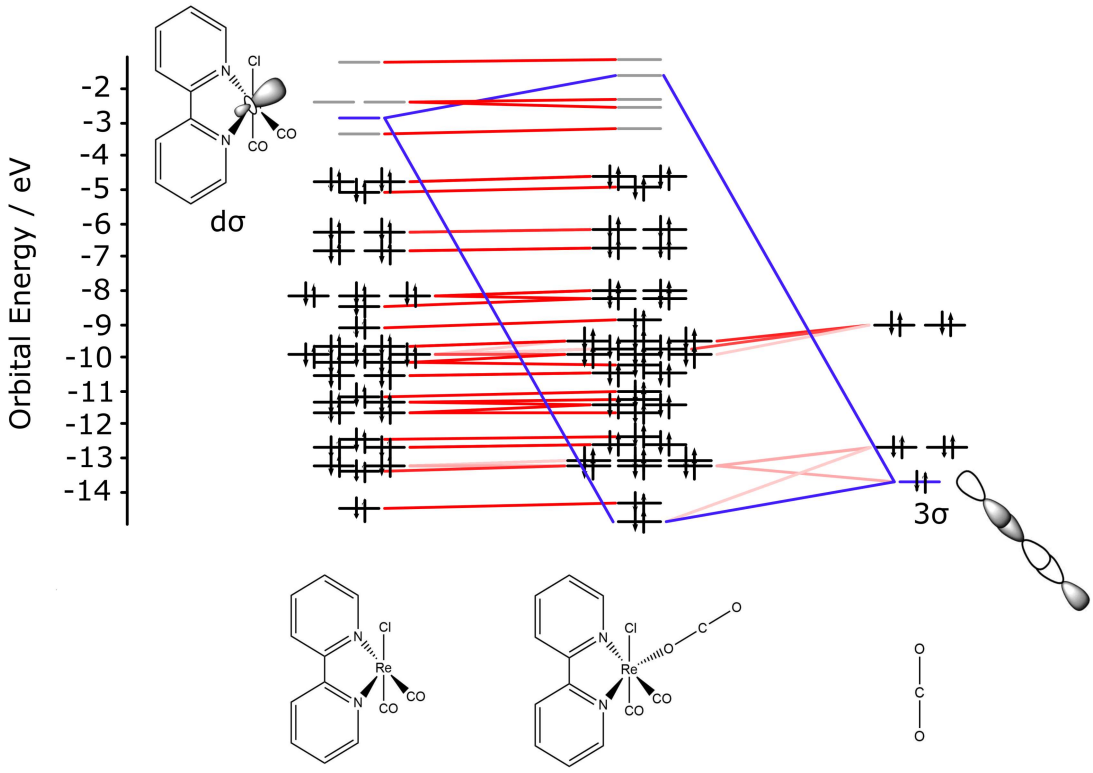

Figure 3.25: Schematic orbital interaction diagram between the orbitals of the [(bpy)Re(CO)$_2$(ax-Cl)] fragment with an equatorial vacant site and the orbitals of a linear CO_2 molecule. Isomer **6**

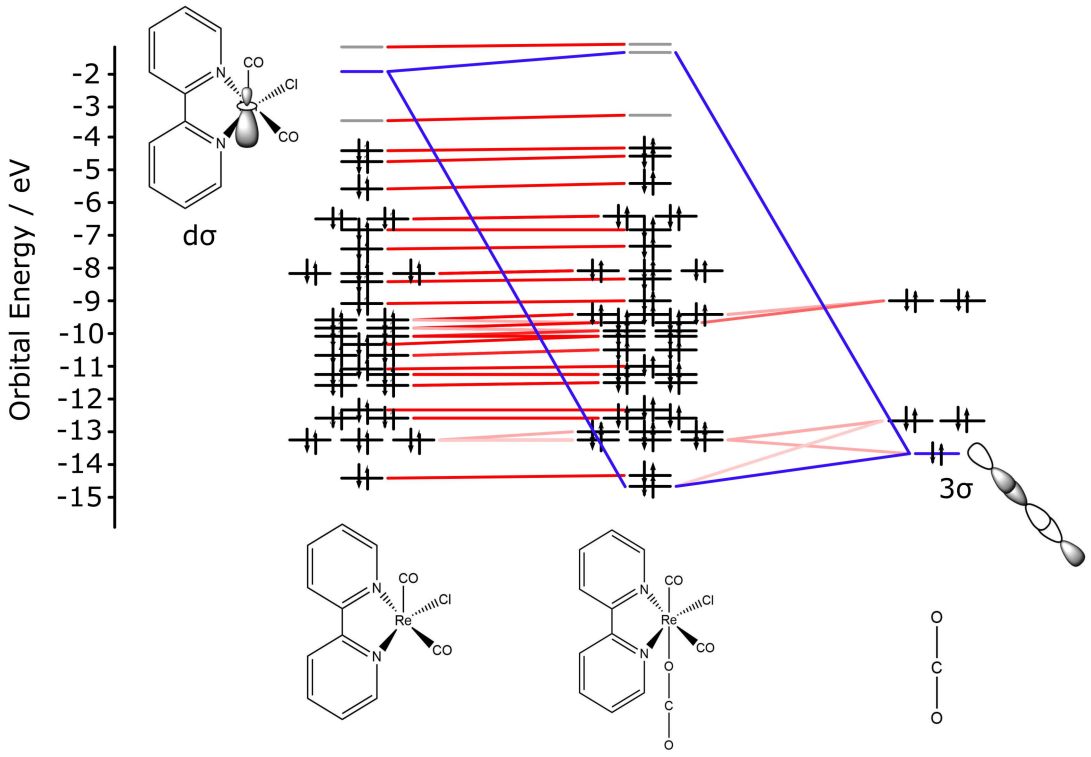

Figure 3.26: Schematic orbital interaction diagram between the orbitals of the [(bpy)Re(CO)$_2$(eq-Cl)] fragment with an axial vacant site and the orbitals of a linear CO_2 molecule. Isomer **7**

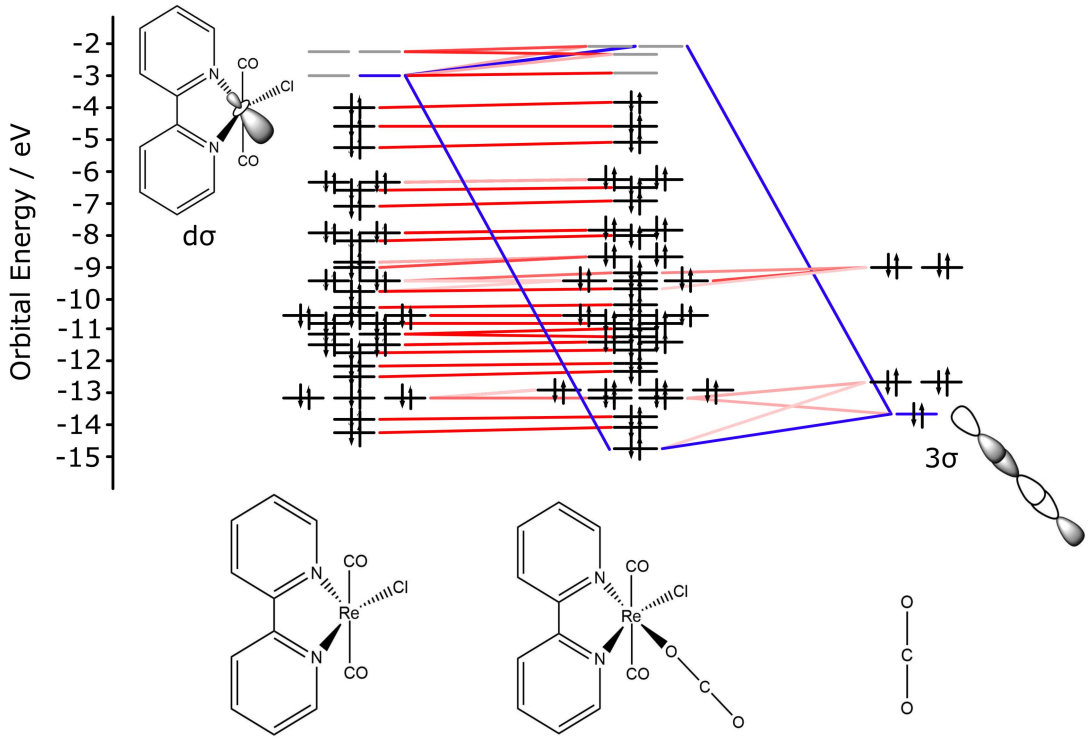

Figure 3.27: Schematic orbital interaction diagram between the orbitals of the [(bpy)Re(CO)$_2$(eq-Cl)] fragment with an equatorial vacant site and the orbitals of a linear CO_2 molecule. Isomer **8**

Relaxation Energies

From the data in Table 3.8, the stability of the complexes can be understood by examining the geometry and energy of the intermediate species of the structure [(bpy)Re(CO)$_2$(Cl)] which would be formed before CO_2 coordination. These structures are given in Figure 3.28; in each case the structure is optimised from a starting geometry with a vacant site and Cl ligand in each of the different axial or equatorial positions. In the isomers where the vacant site and the Cl atom start off *cis* to each other, the Cl atom appears to relax into the vacant site causing this structure to be more stable. In the isomer with the Cl and vacant site are *trans* to each other, there is very little relaxation of the Cl atom as it is locked into position by the coplanar carbonyl ligands. The carbonyls do not relax into the vacant site as this change in geometry would make their orbital overlap, and therefore backbonding with the metal significantly weaker. This lack of relaxation of the Cl atom into the vacant site makes this isomer of the intermediate species much higher energy than the other three. This means when CO_2 binds into the vacant site of any of the isomers with the *cis* relation between CO_2 and the Cl, there is the gain in stability of the CO_2 binding, but also a decrease in stability as the relaxation of the Cl can no longer occur. In the isomer where the vacant site and the Cl atom are *trans* there is only the extra stabilisation gained from the binding of the CO_2, and no competing increase in energy from the Cl atom not being able to relax.

The relaxation energies of each isomer can be calculated for comparison for the complexes with the vacant site and the CO_2 bound complex. For isomer **5** the relaxation energy of its intermediate species is just under 1 kJ mol^{-1}, which is much lower than the values of 40 kJ mol^{-1}, 17 kJ mol^{-1} and 45 kJ mol^{-1} for isomers **6**, **7** and **8**, respectively. This trend of decreasing relaxation energy, which results in a stronger CO_2 bond is found to fit the trend in the data presented in Table 3.8 perfectly.

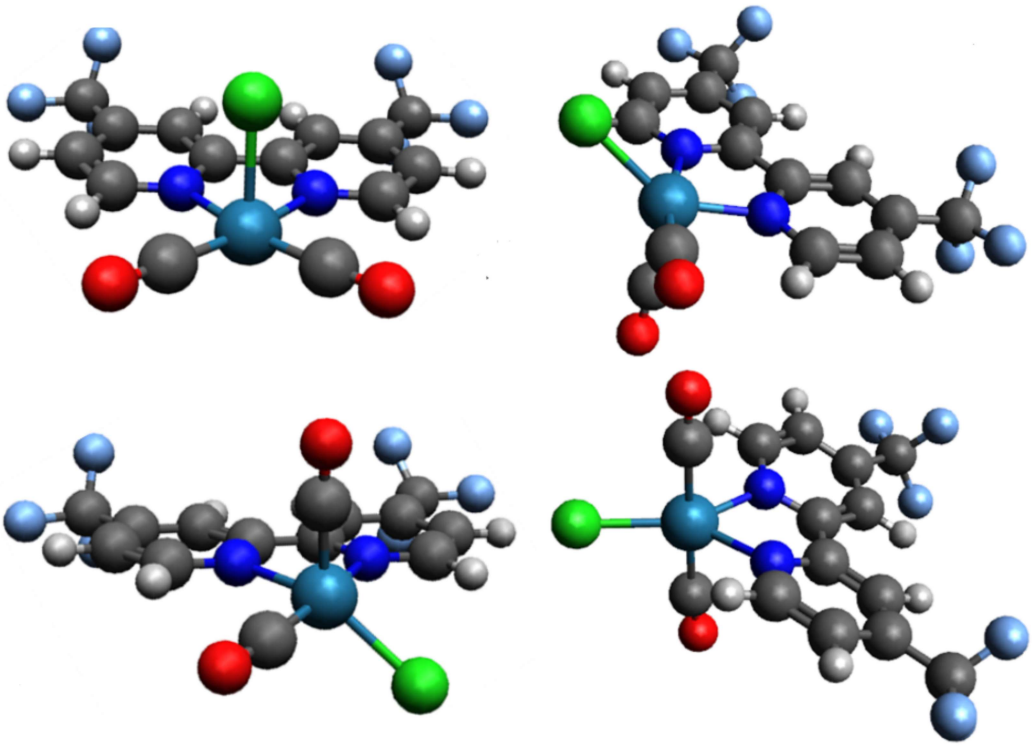

Figure 3.28: Four optimised structures obtained at the DFT-M06/LANL08(f) (metals) and 6-311++G** level for [(dfbpy)Re(CO)$_2$(Cl)] with different Cl and vacant site positions. Cl and vacant site axial (top left), Cl axial and vacant site equatorial (top right), Cl equatorial and vacant site axial (bottom left), Cl and vacant site equatorial (bottom right).

Influence of Bipyridine Functionalisation on Complex Stability

For the neutral rhenium complexes, the change in orbital energy gap as the bpy substituents change was investigated. The same trend as seen for the manganese complexes was found, where the more electron withdrawing bpy has a lower energy metal fragment, which in turn lowers the energy gap between the unoccupied bonding orbital of the metal fragment and the CO_2 bonding orbital. This effect again also decreases the energy difference between the bonding and antibonding orbitals of the CO_2 complex. For the rhenium complexes the orbital energy gap for dmbpy is 12.16 eV, for bpy is 12.12 eV and for dfbpy is 11.95 eV which are slightly larger numbers than for the manganese complexes but the trend remains the same.

Mn and Re Complex Bond Length Comparisons

Table 3.9 allows for a comparison between the data for each of the manganese and rhenium isomers when looking at bond lengths where isomers **1-4** are the manganese complexes and isomers **5-8** are the rhenium complexes. For the rhenium complexes, the M-X bonds are longer than the corresponding M-X bonds in the manganese analogues which is due to the fact that rhenium has a much larger ionic radius than that of manganese. The M-C bonds are on average 0.11 Å longer in the rhenium complexes than the manganese complexes but the C-O bonds of the carbonyls are on average only 0.008 Å longer in the rhenium complexes. For isomers **1** and **5**, the M-N bond is consistently longer by 0.141 Å in the rhenium complex over the manganese analogues, which is due to the previously mentioned difference in ionic radii between the two metals. For isomers **2** and **6** the difference in length for M-N1 is 0.147 Å, which is similar to that seen between isomers **1** and **5**, but the difference in length for M-N2 is 0.087 Å. This difference is due to the coordination of the CO_2 ligand in the position *trans* to M-N2, this is also observed for isomers **4** and **8** where M-N1 has a larger difference in length than M-N2. For isomers **3** and **7** the opposite is seen, where the Re-N1 bond is longer than Mn-N1 bond by 0.112 Å, but the Re-N2 bond is longer than the Mn-N2 bond by a greater amount of 0.143 Å. This is again due to differences in the *trans* influence as the larger shift is seen from the M-N bond located *trans* to the carbonyl ligand.

Bond Length /Å	**1**	**5**	**2**	**6**	**3**	**7**	**4**	**8**
M-C1	1.788	1.891	1.791	1.894	1.781	1.886	1.878	1.993
M-C2	1.788	1.891	1.785	1.889	1.761	1.859	1.878	1.994
M-O3	2.182	2.315	2.258	2.343	2.225	2.478	2.221	2.353
M-N1	2.057	2.198	2.044	2.191	1.990	2.102	1.982	2.099
M-N2	2.057	2.198	1.976	2.063	2.064	2.207	1.982	2.052
C1-O1	1.152	1.161	1.152	1.160	1.152	1.162	1.143	1.146
C2-O2	1.152	1.161	1.153	1.161	1.152	1.160	1.143	1.147
O3-C3	1.156	1.158	1.168	1.169	1.166	1.167	1.167	1.168
C3-O4	1.153	1.158	1.147	1.146	1.148	1.146	1.147	1.147

Table 3.9: Table of bond lengths for isomers **1-8** with each manganese and rhenium isomer grouped together.

For isomers **1** and **5** the M-O3 bond is 0.133 Å longer for the rhenium complex than the manganese one, which is again due to the difference in ionic radii between the metals, an effect similar to that seen in isomers **4** and **8** where the difference is 0.132 Å. For isomers **2** and **6** the M-O3 bond is 0.085 Å longer for the rhenium complex than the manganese one which is a smaller difference than other isomers. For isomers **3** and **7** the M-O3 bond is 0.253 Å longer for the rhenium complex than the manganese one which is a much greater difference than other isomers. This increased difference for isomers **3** and **7** is related to the same observation made for the M-N bonds where the bond located *trans* to a carbonyl ligand is lengthened more in the rhenium complex than it is in the manganese analogue. This variation in M-O3 bond length between metals and isomers is generally impactless on the length of both the O3-C3 and C3-O4 bonds of the CO_2 ligand where the mean difference in length for the O3-C3 and C3-O4 bonds between the rhenium and manganese complexes is 0.001 Å.

Cyclopentane Re Complexes

This Thesis also has a focus on alkane complexes and a such cyclopentane was also briefly investigated and the bond lengths of these complexes are documented in Table 3.10. Cyclopentane was chosen over other alkanes because its a commonly available lab solvent, easily dried, and less toxic than many non cyclic alkanes while also not being too large and therefore computationally intensive. Some other ligands,Xe, Kr and Ar, and their coordination to the [(bpy)Re$(CO)_2$(Cl)(L)] framework were also briefly investigated. The geometry optimisations did not minimise towards a structure where the noble gas atoms were coordinated to the metal which suggested that these complexes would not be formed.

The first thing to note is that the Re-C1, Re-C2, C1-O1 and C2-O2 bond lengths are all very similar to those seen for the rhenium CO_2 complex analogues and the same can be said for the Re-N1 and Re-N2 bond lengths that have slightly more variance, but still all similar. The other bonds that are analysed

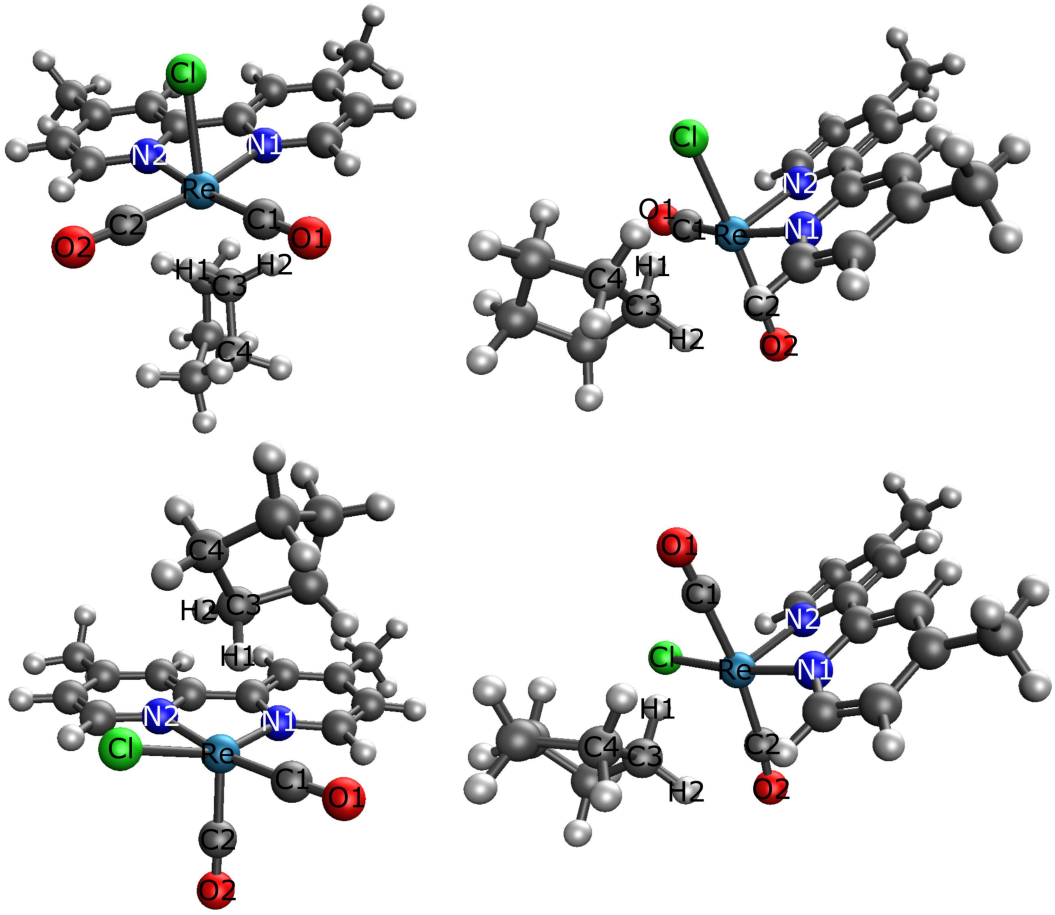

Figure 3.29: Optimised structures obtained at the DFT-M06/LANL08(f) (metals) and 6-311++G** level for [(dmbpy)Re(CO)$_2$(ax-Cl)(ax-C$_5$H$_{10}$)] (**5**-C$_5$H$_{10}$, top left), [(dmbpy)Re(CO)$_2$(ax-Cl)(eq-C$_5$H$_{10}$)] (**6**-C$_5$H$_{10}$, top right), [(dmbpy)Re(CO)$_2$(eq-Cl)(ax-C$_5$H$_{10}$)] (**7**-C$_5$H$_{10}$, bottom left) and [(dmbpy)Re(CO)$_2$(eq-Cl)(eq-C$_5$H$_{10}$)] (**8**-C$_5$H$_{10}$, bottom right).

are all directly related to the cyclopentane ligand and as such a comparison to free cyclopentane is beneficial. C-C bonds are 1.543 Å long in free cyclopentane and the C-H bonds are 1.095 Å long. It can be seen that bond between the H atom closest to the metal centre and its coordinated C atom in cyclopentane is elongated compared with the 1.095 Å of free cyclopentane. A likely cause of this is an interaction between the H atom and the metal increasing the electron density in the C-H σ^* orbital. Further evidence of this interaction is that as the Re-H bond length gets shorter as the C-H bond length gets larger. It can also be seen that the bond C3-H2 bond length for all isomers is smaller than the free cyclopentane bond length of 1.095 Å. This suggests that the C-H bond between the non-metal-interacting H atom and the C atom closest to the metal is stronger

post ligand coordination. This trend of shortening of bonds can also be seen in neighbouring C atoms on the cyclopentane, where the C3-C4 bond length is also found to be shorter than in free cyclopentane.

Bond Length /Å	**5**-C_5H_{10}	**6**-C_5H_{10}
Re-C1	1.893	1.893
Re-C2	1.893	1.890
Re-N1	2.197	2.209
Re-N2	2.197	2.078
Re-H1	1.928	1.964
C1-O1	1.161	1.160
C2-O2	1.161	1.163
C3-H1	1.142	1.131
C3-H2	1.089	1.091
C3-C4	1.531	1.532
Bond Length /Å	**7**-C_5H_{10}	**8**-C_5H_{10}
Re-C1	1.884	1.991
Re-C2	1.858	1.991
Re-N1	2.111	2.112
Re-N2	2.210	2.066
Re-H1	2.180	1.973
C1-O1	1.164	1.149
C2-O2	1.161	1.149
C3-H1	1.111	1.127
C3-H2	1.093	1.090
C3-C4	1.533	1.534

Table 3.10: Table of bond lengths for all four isomers for [(dmbpy)Re(CO)$_2$(Cl)(C_5H_{10})] from Figure 3.29.

The data in Table 3.11 show the calculated BDE values and calculated ν(CO) vibrational frequencies for the different isomers of [(dmbpy)Re(CO)$_2$(Cl)(C_5H_{10})]. This data shows that the trend when compared with the CO_2 complexes is different. The isomer with both Cl and C_5H_{10} bound in axial positions displays a Re-H bond strength of 21 kJ mol^{-1} greater than the Re-O interaction strength as seen in the dmbpy analogue of isomer **5** but the other isomers are no stronger than 3 kJ mol^{-1}. There is also a difference in the calculated ν(CO) vibrational frequencies where the isomer with both Cl and C_5H_{10} bound in axial positions is found to have both its bands at slightly higher wavenumber when compared with the dmbpy variant of isomer **5** by 4 cm^{-1}. The other three cyclopentane complex isomers are all predicted to have their ν(CO) vibrational frequencies between 2

to 6 cm^{-1} lower in wavenumber compared with those of the dmbpy variants of isomers **6**, **7** and **8**. The calculated IR spectra for the cyclopentane complexes are all predicted to display a small peak between 2432 and 2600 cm^{-1}, which is due to the C-H stretch of the H atom that is interacting with the metal centre which may act as a signal peak for any experimental work in this field in the future.

Complex	BDE / kJ mol^{-1}	ν(CO) /cm^{-1}
(dmbpy)Re$(CO)_2$(ax-C_5H_{10})(ax-Cl)	62	1944, 1884
(dmbpy)Re$(CO)_2$(eq-C_5H_{10})(ax-Cl)	19	1946, 1880
(dmbpy)Re$(CO)_2$(ax-C_5H_{10})(eq-Cl)	26	1945, 1887
(dmbpy)Re$(CO)_2$(eq-C_5H_{10})(eq-Cl)	6	2010, 1911

Table 3.11: Table of BDE values for the M-CO_2 bond between [(dmbpy)Re$(CO)_2$(Cl)] and C_5H_{10} and their calculated ν(CO) vibrational frequencies.

3.2.4 DFT Investigation of Cationic Mn and Re α-Diimine Complexes

Mn Complex Geometry Optimisations, Bond Lengths and Bond Strengths

Geometry optimisations of both *fac*-[(bpy)Mn$(CO)_3(CO_2)]^+$ (**9**) and *mer*-[(bpy)Mn$(CO)_3(CO_2)]^+$ (**10**) were performed together with frequency calculations to ensure the optimised structures were at the energy minimum. The resulting structures from these calculations are shown in Figure 3.30. These calculated structures again show a clear preference for η^1-OCO end-on binding of CO_2 and have an M-O-C angle of 155 $\pm$ 3°, which is less linear than that determined for the neutral isomer **1**, but more linear than found for isomers **2**, **3** and **4** where there was a Cl group located *cis* to the CO_2 ligand.

The data in Table 3.12 shows the different bond lengths of both isomers **9** and **10** from Figure 3.30. For isomer **9**, the bond distances Mn-C1 and Mn-C2 are the same since both carbonyl ligands are located *trans* to the same groups and have the same chemical environment. However, Mn-C3 bond is shorter as

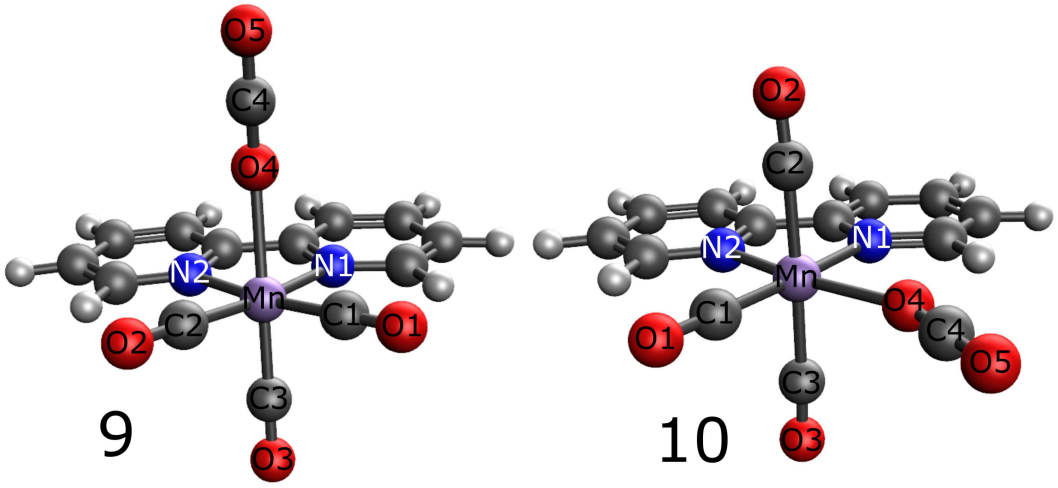

Figure 3.30: Optimised structures obtained at the DFT-M06/LANL08(f) (metals) and 6-311++G** level for *fac*-[(bpy)Mn(CO)$_3$(CO$_2$)]$^+$ (left) and *mer*-[(bpy)Mn(CO)$_3$(CO$_2$)]$^+$ (right) showing the preferential η^1-OCO end-on binding mode.

it is located *trans* to the CO_2 ligand, which has an even smaller *trans* influence than bpy. This trend is the same as that for the neutral isomer **3**, but for the neutral complexes these bonds are approximately 0.040 and 0.029 Å shorter than the bonds found in the cationic isomer **9**. The similarities to isomer **3** continue when looking at the C1-O1, C2-O2 and C3-O3 bond lengths. Despite the Mn-C bond length changing, the C-O bond lengths remain the same at a consistent 1.140 Å for the cationic species, compared with 1.152 Å in the neutral isomer **3**. This is expected due to the shorter C-O bonds meaning a greater degree of backbonding. For isomer **10** the same trend is noted where the Mn-C1 bond is shorter than the Mn-C2 and Mn-C3 bonsds due to the *trans* influence, which is the same trend noted for the neutral isomer **4**, where the neutral Mn-C bonds were again found to be longer. The C1-O1 bond in isomer **10** is seen to be 0.010 Å longer than C2-O2 and C3-O3 because of its greater degree of backbonding to the manganese centre since it is not located *trans* to a carbonyl ligand. This difference of 0.010 Å is in agreement with comparison to the neutral complexes where isomer **4** had a longer C1-O1 bond compared with isomers **1**, **2** and **3**.

In isomer **9**, both the Mn-N1 and Mn-N2 bonds are the same length since

Bond Length /Å	**9**	**10**
Mn-C1	1.821	1.812
Mn-C2	1.821	1.887
Mn-C3	1.790	1.887
Mn-O4	2.226	2.196
Mn-N1	2.049	2.057
Mn-N2	2.049	2.016
C1-O1	1.140	1.144
C2-O2	1.140	1.134
C3-O3	1.140	1.134
O4-C4	1.164	1.165
C4-O5	1.145	1.144

Table 3.12: Table of bond lengths for both isomers **9** and **10** of $[(bpy)Mn(CO)_3(CO_2)]^+$ from Figure 3.30

both are located *trans* to carbonyl ligands, but this time these Mn-N bonds are 0.008 Å longer than those in isomer **1**. This stronger Mn-N interaction for the cationic complexes is due to the electron donating nature of the N atoms on the bpy ligand interacting more strongly with a cationic metal when compared with a neutral one. In isomer **10** the Mn-N1 and Mn-N2 bonds are 0.041 Å different in length due to being located *trans* to different ligands although this is a much smaller disparity than that seen in its neutral analogue where the difference is 0.068 Å. This disparity is related to the fact that the carbonyl ligands in the neutral complex bind stronger than in the cationic complexes, as indicated by the shorter Mn-C bond distances. This stronger interaction between the metal and the carbonyl causes a greater *trans* influence and so therefore the Mn-N bonds located *trans* to the carbonyl ligands in the neutral complex are lengthened more than in the cationic complex.

For isomer **9**, the Mn-O4 bond distance is 2.226 Å with the bond located *trans* to a carbonyl ligand, which is virtually identical to that seen in isomer **3** where the Mn-O3 bond length is 2.225 Å and the O4-C4 and C4-C5 bond lengths are also almost identical at 1.164 and 1.165 Å. For isomer **10** the Mn-O4 bond is shorter than in isomer **9** because it is not located *trans* to a carbonyl and is shorter than its neutral analogues where the CO_2 is bound *trans* to the bpy ligand. This suggests a potential stronger binding for the cationic complexes than seen for the

neutral complexes. The O4-C4 and C4-O5 bond lengths for isomer **10** are almost identical to those found in isomer **9**, which suggests that the CO_2 IR stretching band for these two complexes would be very close in frequency. This is confirmed by the data reported in Table 3.13 where a set of bond dissociation energies and frequency calculations for both isomers of five different manganese complexes is reported. The calculated CO_2 IR bands for isomers **9** and **10** are predicted to be at 2421 and 2418 cm^{-1}, respectively. These calculated wavenumbers for the CO_2 band are found to be lower than the neutral isomer **1** by only a few wavenumbers, but much higher than the CO_2 band for isomers **2**, **3** and **4**.

Complex	BDE / kJ mol^{-1}	$\nu(CO_2$ and CO) /cm^{-1}
fac-[(bpy)Mn$(CO)_3(CO_2)]^+$	39	2421, 2079, 2017, 2010
mer-[(bpy)Mn$(CO)_3(CO_2)]^+$	50	2418, 2105, 2038, 2003
fac-[(dmbpy)Mn$(CO)_3(CO_2)]^+$	36	2421, 2076, 2013, 2006
mer-[(dmbpy)Mn$(CO)_3(CO_2)]^+$	48	2419, 2102, 2033, 1999
fac-[(dtbpy)Mn$(CO)_3(CO_2)]^+$	34	2422, 2075, 2011, 2004
mer-[(dtbpy)Mn$(CO)_3(CO_2)]^+$	48	2420, 2102, 2033, 1995
fac-[(dfbpy)Mn$(CO)_3(CO_2)]^+$	43	2420, 2082, 2023, 2017
mer-[(dfbpy)Mn$(CO)_3(CO_2)]^+$	52	2418, 2110, 2046, 2010
fac-[(dftbpy)Mn$(CO)_3(CO_2)]^+$	42	2420, 2082, 2023, 2015
mer-[(dftbpy)Mn$(CO)_3(CO_2)]^+$	52	2418, 2112, 2048, 2010

Table 3.13: Table of BDE values for the M-CO_2 bond between [Mn(4,4'-R_2-2,2'-bpy)$(CO)_3]^+$ and CO_2 and their calculated ν(CO) values.

Mn Complex Orbital Interactions and Vibrational Frequencies

The calculated ν(C-O) bands are presented in Table 3.13 and it should be noted that the majority lie above 2000 cm^{-1}, which is quite different to values for the neutral manganese complexes. This much higher frequencies for the ν(C-O) stretches is characteristic of a cationic and more electron deficient metal centre resulting in a reduction of M $\rightarrow$CO back-bonding.

For isomer **9** there are two ν(C-O) stretches with lower wavenumber than isomer **10** and one with higher. This is consistent with the different C-O bond lengths where isomer **9** has two C-O bonds which are longer and one C-O bond which is shorter than isomer **10**. It can also be seen that as the substituent

changes on the bpy for these cationic complexes the ν(C-O) bands are found to shift up in wavenumber for the electron withdrawing substituents and shift down in wavenumber for the electron donating substituents. The shifts in these carbonyl bands vary by a maximum of 15 cm^{-1}, which is less than the maximum variation caused by changing substituents for the neutral manganese complexes where the difference was 28 cm^{-1}. It is also worth noting that in the experimental spectra of this type of complexes, when taken in non-polar solvents, the FWHM of the IR peaks in solution are approximately 8 cm^{-1}. This means that the *fac* CO_2 complex would likely display only two clearly distinct CO bands, with one probably being broader than the other due to an overlap of peaks. The *mer* isomer has peaks which are spaced far enough apart that is far more likely that this isomer would display three distinct bands.

Bpy	CO_2 Complex Diff / kJ mol^{-1}	Intermediate Diff / kJ mol^{-1}
dtbpy	51	63
dmbpy	50	62
bpy	48	58
dfbpy	46	55
dftbpy	46	55

Table 3.14: Table of calculated energy differences. The left column is the difference between the more stable *fac* and less stable *mer* isomers of the cationic CO_2 complexes. The right column is the difference between the more stable *fac* and less stable *mer* isomers after having undergone CO loss (the intermediate complex, briefly formed with a vacant site, before CO_2 coordination).

The BDE values for isomers **9** and **10** are given in Table 3.13, it can be seen that the *fac* isomer is consistently predicted to bind to CO_2 9-14 kJ mol^{-1} more weakly than the *mer* isomer. This is due to the *trans* influence causing the CO_2 in the *fac* isomer to be a lot more labile than in the *mer* isomer. The strong *trans* influence of both CO ligands destabilising each other found in the *mer* isomer makes the *fac* isomer lower in energy and therefore more stable. The intermediate species formed following CO loss but before the CO_2 is coordinated is also found to be lower in energy and more stable for the *fac* isomer compared with the *mer* isomer. The CO_2 complex *fac* isomer is found to be more stable than the *mer*

isomer by 51 to 46 kJ mol^{-1}, depending on the bpy substituent. The intermediate tricarbonyl species for the *fac* isomer is found to be more stable than the *mer* isomer by 63 to 55 kJ mol^{-1}, depending on the bpy substituent. The energy differences for each isomer and each bpy substituent can be seen in Table 3.14. The greater difference in stability between isomers for the intermediate species compared with the CO_2 complex suggests that the binding of CO_2 stabilises the *mer*- isomer more than it stabilises the *fac*- isomer as the difference gets smaller upon CO_2 binding. This difference of 12 to 9 kJ mol^{-1} is similar to the difference seen between the strength of the M-CO_2 interaction for the isomers represented in Table 3.13 which is between 10 to 14 kJ mol^{-1}, depending on the bpy substituent. Another minor factor is the relaxation energy differences between vacant site species and CO_2 coordinated species which were very dominant for the neutral bpy complexes. This is a much smaller factor for the cationic complexes than it was for the neutral complexes as now there is no Cl group. The Cl group is a primarily σ bonding ligand which gives it a lot greater geometric freedom to relax into positions which limit the steric instability of the complex. The CO ligands coordinated to the metal are involved in back-bonding which is both a π and σ interaction. This means its geometric freedom is a lot more limited as maintaining a good orbital overlap is now not possible if the CO ligand deviates from the plane of the metal. This lack of ability for the CO ligand to relax to a more favourable steric position means that the relaxation energy lost upon CO_2 coordination is a lot smaller for the cationic complexes compared with the neutral, Cl containing, complexes. The relaxation energy lost from CO_2 coordination is greater for the *fac* isomers (4 kJ mol$^-$1) compared with the *mer* isomers (2 kJ mol$^-$1) meaning that the intermediate species for the *mer* isomers are giving up less relaxation compared with the *fac* isomers and as such display a stronger CO_2 bond. This is further reinforced by the previous point mentioned where it was showed that the *fac* intermediate species is more stable than the *mer* intermediate.

It can be also be seen that both cationic isomers have a higher M-CO_2 bond

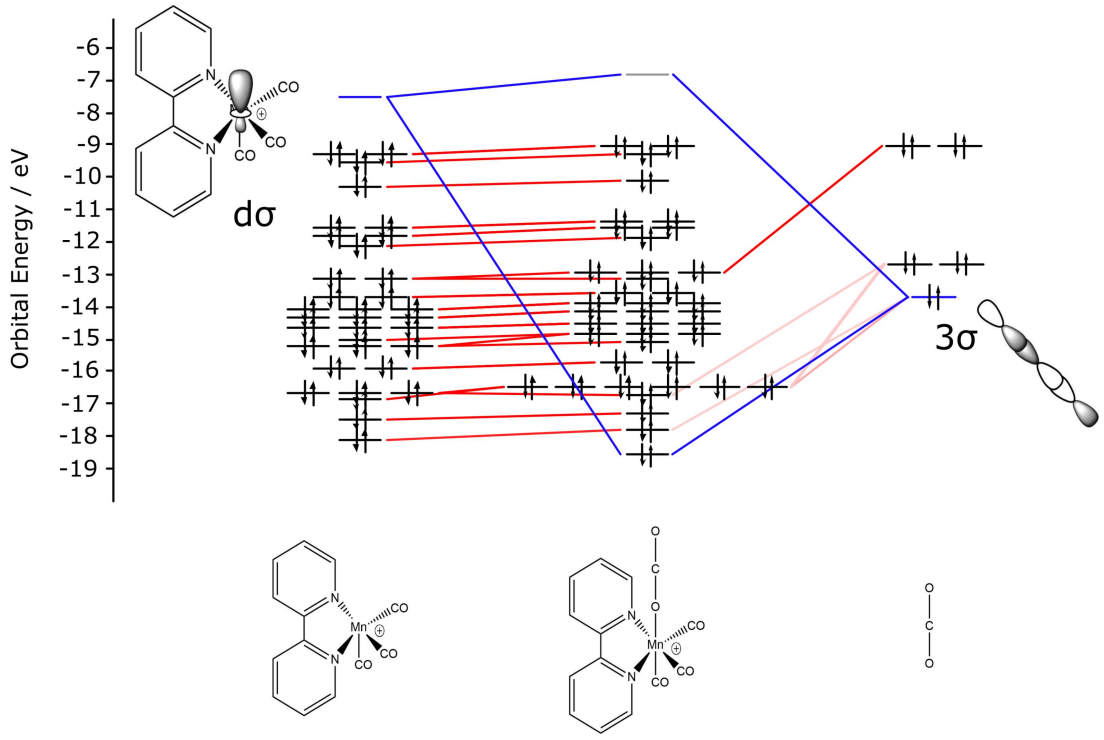

Figure 3.31: Schematic orbital interaction diagram between the orbitals of the $[(bpy)Mn(CO)_3]^+$ fragment with an axial vacant site and the orbitals of a linear CO_2 molecule. Isomer **9**

strength than any of the neutral manganese complexes. The explanation for this can be seen from Figures 3.31 and 3.32, which show MO diagrams describing the interaction of orbitals of $[(bpy)Mn(CO)_3]^+$ fragments and the orbitals of the linear CO_2 molecule for each isomer. It can be seen that the energy of the metal fragment LUMO is lower in energy by around 4 eV when compared with the neutral manganese isomers. This means that the interacting metal d_σ orbital is now much closer in energy to the -13.7 eV CO_2 σ orbital. This decrease in energy causes this interaction where the σ lone pair on the CO_2 donates electron density onto the metal d_σ orbital more easily than it did for the neutral complex and as such results in a stronger M-η^1-OCO interaction.

From the data in Table 3.13 the impact of changing substituents on these cationic manganese complexes can be seen; the same trend noted for the neutral complexes is seen where a more electron withdrawing bpy increases the metal to CO_2 binding strength and a more electron donating bpy decreases the metal to

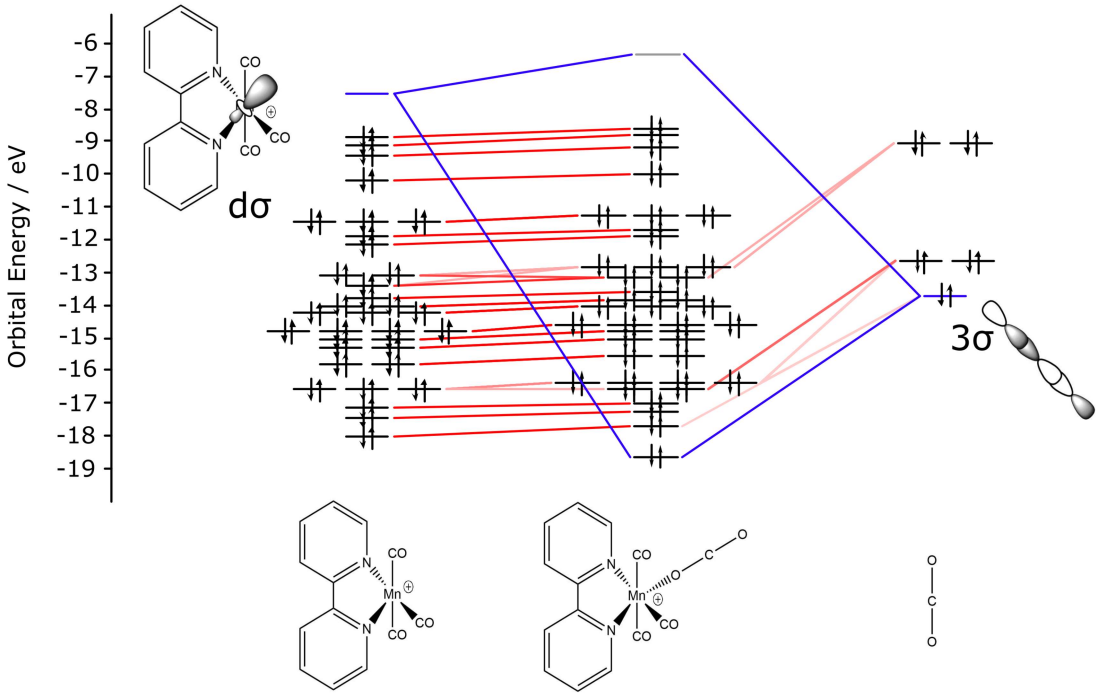

Figure 3.32: Schematic orbital interaction diagram between the orbitals of the $[(bpy)Mn(CO)_3]^+$ fragment with an equatorial vacant site and the orbitals of a linear CO_2 molecule. Isomer **10**

CO_2 binding strength. The *fac* isomers vary in strength by 8 kJ mol^{-1} and the *mer* isomers vary by 4 kJ mol^{-1}, which are slightly larger variations than seen from altering substituents for the neutral manganese complexes.

In Figure 3.33 a simplified diagram containing only the orbitals involved in bonding for three *fac* isomers with differently functionalised bpys is given. A trend can be noted where the *fac* cationic manganese CO_2 complexes become more stable with more electron withdrawing groups attached to the bpy ligand. The more electron withdrawing bpy has a lower energy metal fragment resulting in a smaller energy gap between the unoccupied bonding orbital of the metal fragment and the CO_2 bonding orbital. For these *fac* cationic manganese complexes the effect of changing the substituents on the bpy ligand is significantly less than when changing the substituents on the arene of the pianostool complexes. The increase in stability when changing the substituents for the *fac* cationic manganese complexes from more electron donating to electron withdrawing is slightly less than the increase in stability for the neutral manganese bpy complexes too.

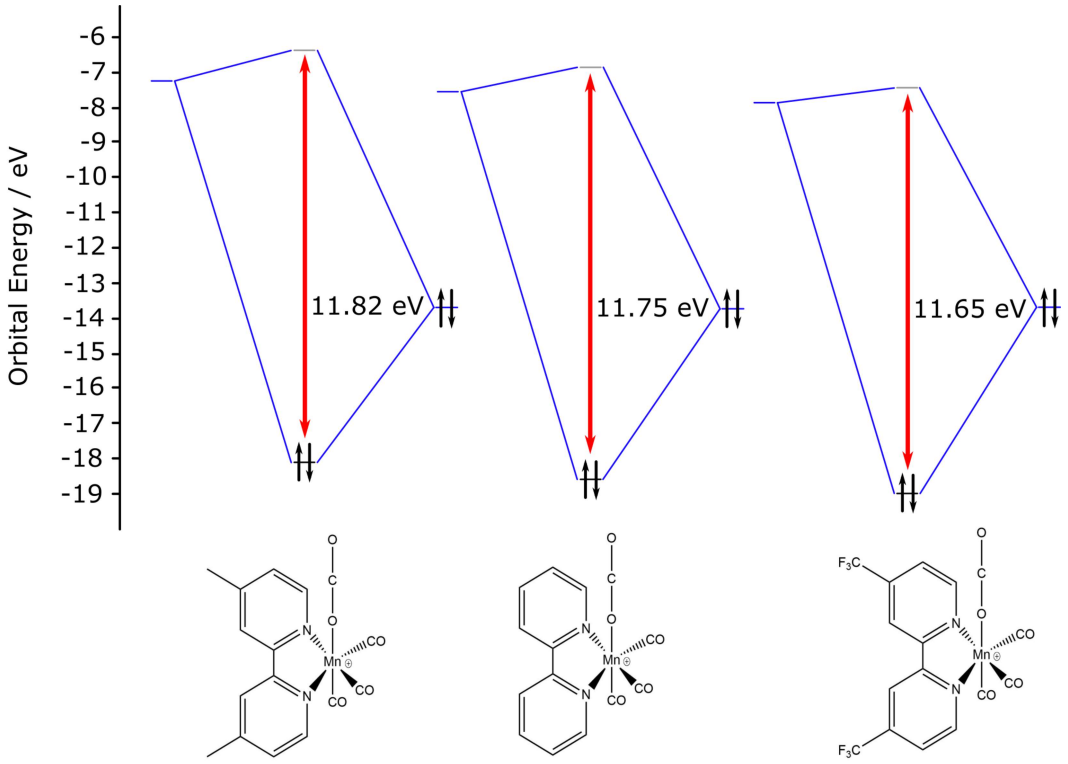

Figure 3.33: Simplified frontier orbital interaction diagram showing the orbitals involved in end-on CO_2 coordination for the *fac* isomers of [(4,4'-H_2-2,2'-bpy)$Mn(CO)_3$]$^+$, [(4,4'-Me_2-2,2'-bpy)$Mn(CO)_3$]$^+$ and [(4,4'-$(CF_3)_2$-2,2'-bpy)$Mn(CO)_3$]$^+$ and the energy gap between them.

The metal fragment orbital energies are on average approximately 4 eV lower in energy for the cationic complexes when compared with the neutral ones, but the gap between the bonding and antibonding orbital remains similar in magnitude.

The data in Figure 3.34 shows the same trend as seen for the *fac* isomers from Figure 3.33, but this time the difference caused from changing the substituent on the bpy is incredibly minor. The bonding-antibonding orbital energy gap for these *mer* isomers is also larger than it was for the *fac* isomers. The bonding orbital is almost identical in energy to the *fac* isomers but the antibonding orbital is higher in energy. This higher energy antibonding orbital also confirms that the *mer* isomers should bind more strongly to CO_2 than the *fac* isomers.

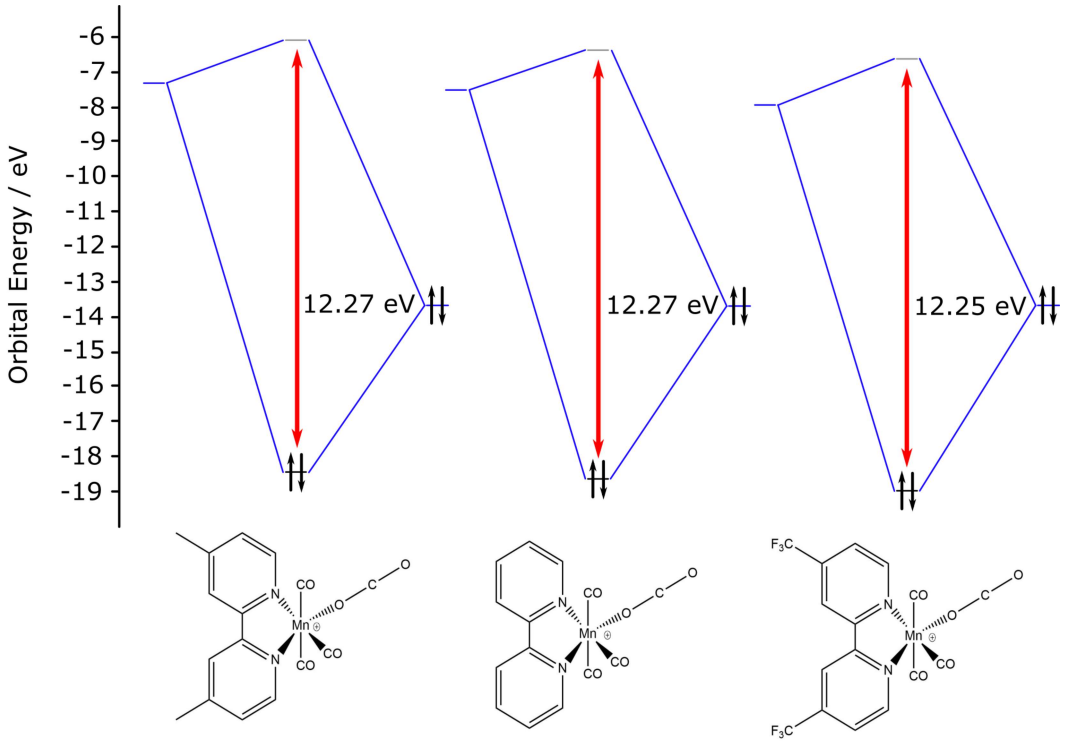

Figure 3.34: Simplified frontier orbital interaction diagram displaying the orbitals involved in end-on CO_2 coordination for the *mer* isomers of [(4,4'-H_2-2,2'-bpy)$Mn(CO)_3$]$^+$, [(4,4'-Me_2-2,2'-bpy)$Mn(CO)_3$]$^+$ and [(4,4'-$(CF_3)_2$-2,2'-bpy)$Mn(CO)_3$]$^+$ and the energy gap between them.

Re Complex Geometry Optimisations, Bond Lengths and Bond Strengths

Geometry optimisations of both *fac*-[(bpy)$Re(CO)_3(CO_2)$]$^+$ (**11**) and *mer*-[(bpy)$Re(CO)_3(CO_2)$]$^+$ (**12**) were performed together with frequency calculations to ensure the optimised structures had been obtained. The resulting structures from these calculations are given in Figure 3.35. These calculated structures again show a clear preference for η^1-OCO end-on binding of CO_2 to these complexes and have an M-O-C angle of 153 ± 2°, which is less linear than for the neutral isomer **5** but more linear than for isomers **6**, **7** and **8** where there was a Cl group located *cis* to the CO_2 ligand.

The data in Table 3.15 shows the different bond lengths of both isomers **11** and **12** from Figure 3.35 can be seen. For isomer **11** the Re-C1 and Re-C2 bonds are the same length as both carbonyl ligands are located *trans* to the same groups and have the same chemical environment, but Re-C3 is shorter as it is located

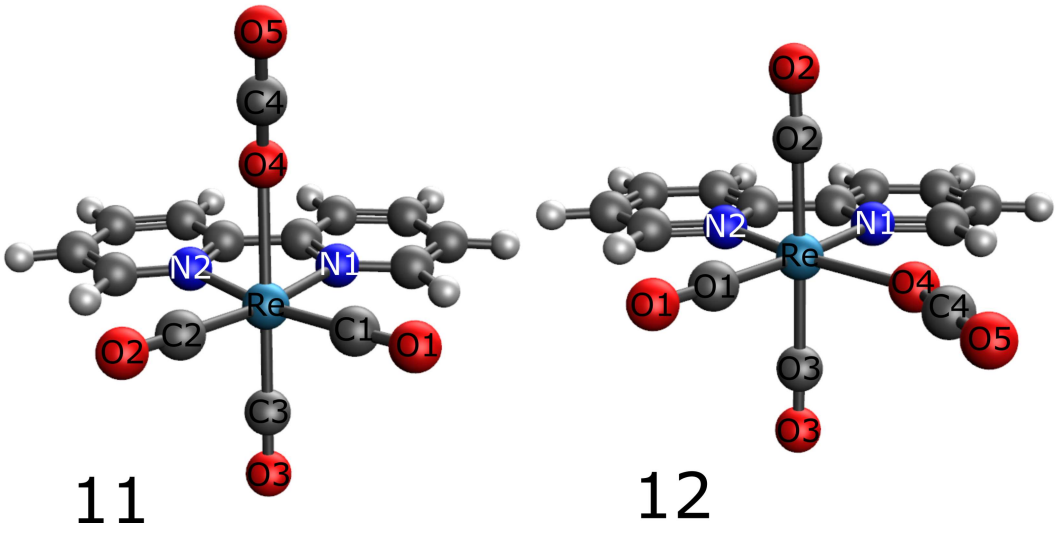

Figure 3.35: Optimised structures obtained at the DFT-M06/LANL08(f) (metals) and 6-311++G** level for *fac*-[(bpy)Re(CO)$_3$(CO$_2$)]$^+$ (left) and *mer*-[(bpy)Re(CO)$_3$(CO$_2$)]$^+$ (right) showing the preferential η^1-OCO end-on binding mode.

trans to the CO$_2$ ligand, which has an even smaller *trans* influence than bpy. This is the same as the trend seen for the neutral isomer **7**, but for the neutral complexes, Re-C1 and Re-C2 were found to be 0.049 and 0.033 Å shorter than the bonds found in the cationic isomer **9**. The C1-O1 and C2-O2 bond distances are found to be the same length at 1.145 Å, which is in agreement with the same Re-C bond lengths, but C3-O3 is found to be a very minor 0.001 Å longer. There is also a minor bond length difference found in isomer **7** too of 0.002 Å, but the cationic species had 0.016 ± 0.001 Å shorter C-O bond lengths which is expected due to the longer Re-C bonds. For isomer **12** the same trend is noted where the Re-C1 bond is shorter than the Re-C2 and Re-C3 bonds due to the *trans* influence, which is comparable to the neutral isomer **8** where the Re-C bonds were again found to be longer. The C1-O1 bond in isomer **12** is 0.013 Å longer than C2-O2 and C3-O3 bonds because of its greater degree of backbonding to the rhenium centre.

In isomer **11** both the Re-N1 and Re-N2 bonds are the same length since both are located *trans* to carbonyl ligands and both are also the identical lengths of the Re-N bonds found in the neutral isomer **5** which also has both Re-N1 and

Re-N2 bonds located *trans* to carbonyl ligands. In isomer **12** the Re-N1 and Re-N2 bonds have a difference in length of 0.090 Å due to being located *trans* to different ligands (CO_2 and CO) although the difference is smaller than that seen in isomer **6** where Re-N1 and Re-N2 were also located *trans* to CO_2 and CO but had a difference in length of 0.117 Å. This disparity is related to the fact that the carbonyl ligands in the neutral complex bind more strongly than in the cationic complexes, as evidenced by the shorter Re-C bond distances and, as such, have a greater *trans* influence and so cause the bonds located *trans* to it to lengthen more than they do in the cationic complex.

Bond Length /Å	**11**	**12**
Re-C1	1.935	1.916
Re-C2	1.935	2.011
Re-C3	1.892	2.011
Re-O4	2.367	2.318
Re-N1	2.198	2.202
Re-N2	2.198	2.112
C1-O1	1.145	1.151
C2-O2	1.145	1.138
C3-O3	1.146	1.138
O4-C4	1.166	1.166
C4-O5	1.143	1.143

Table 3.15: Table of bond lengths for both isomers of $[(bpy)Re(CO)_3(CO_2)]^+$ from Figure 3.35

For isomer **11** the Re-O4 bond was found to be 2.367 Å and is located *trans* to a carbonyl ligand, which can be compared with isomer **7** where the Re-O3 bond length is 2.478 Å and also located *trans* to a carbonyl ligand. The O4-C4 and O4-C5 bond lengths in each of these isomers are very similar despite the variation of the Re-O bond length. For isomer **12** the Re-O4 bond, 2.318 Å, is shorter as the CO_2 is not located *trans* to a carbonyl ligand and is again shorter than that of its closest neutral analogues where the CO_2 is bound *trans* to the bpy ligand. The shorter Re-O bond lengths for the cationic complexes again suggests a stronger M-CO_2 bonding than seen for the neutral complexes. The O4-C4 and C4-O5 bond lengths for isomer **12** are almost identical to those found in isomer **11**, which again suggests that the frequency of the CO_2 stretching IR band for

these two complexes would be very similar. This can be seen from the data in Table 3.16 where a set of bond dissociation energies and frequency calculations for both isomers of five different rhenium complexes are presented. The calculated CO_2 bands for each isomer are calculated to appear at 2418 and 2419 cm^{-1} which are found to be slightly lower than neutral isomer **5** but higher than isomers **6**, **7** and **8**.

Complex	BDE / kJ mol^{-1}	$\nu(CO_2$ and CO) /cm^{-1}
fac-[(bpy)Re(CO)$_3$(CO_2)]$^+$	53	2418, 2074, 1989, 1986
mer-[(bpy)Re(CO)$_3$(CO_2)]$^+$	66	2419, 2095, 2006, 1976
fac-[(dmbpy)Re(CO)$_3$(CO_2)]$^+$	50	2418, 2072, 1984, 1982
mer-[(dmbpy)Re(CO)$_3$(CO_2)]$^+$	64	2420, 2092, 2001, 1971
fac-[(dtbpy)Re(CO)$_3$(CO_2)]$^+$	48	2418, 2070, 1983, 1980
mer-[(dtbpy)Re(CO)$_3$(CO_2)]$^+$	63	2421, 2092, 1999, 1969
fac-[(dfbpy)Re(CO)$_3$(CO_2)]$^+$	57	2417, 2078, 1995, 1993
mer-[(dfbpy)Re(CO)$_3$(CO_2)]$^+$	69	2419, 2100, 2014, 1983
fac-[(dftbpy)Re(CO)$_3$(CO_2)]$^+$	56	2419, 2078, 1995, 1994
mer-[(dftbpy)Re(CO)$_3$(CO_2)]$^+$	68	2421, 2100, 2014, 1983

Table 3.16: Table of BDE values for the M-CO_2 bond between [(4,4'-R_2-2,2'-bpy)Re(CO)$_3$]$^+$ and CO_2 and their calculated ν(CO) values.

Re Complex Orbital Interactions and Vibrational Frequencies

The calculated ν(C-O) bands can be seen in Table 3.16 and it can be seen that the bands all lie at significantly higher wavenumbers than the neutral complexes which is in agreement with the bond length analysis suggesting that the carbonyl bands interact with the metal stronger in the neutral complexes. For isomer **11** there are two ν(C-O) stretches with lower wavenumber than isomer **12** and one with higher, which is in agreement with the different C-O bond lengths where isomer **11** has two C-O bonds which are longer than isomer **12** which are therefore weaker bonds which absorb at lower wavenumber and one C-O bond which is shorter which would absorb at higher wavenumber. From the data in Table 3.16, it can be seen that as the substituent on the bpy changes from electron donating to electron withdrawing the ν(C-O) bands are found to shift up in wavenumber. The difference between the most blue and red shifted IR frequencies is 15 cm^{-1},

which is the same maximum shift as seen for the cationic manganese complexes but smaller than the variation from the neutral rhenium complexes, which was 33 cm^{-1}. It is also worth noting again that in the experimental spectra of this type of complexes, when taken in non-polar solvents, the FWHM of the IR peaks in solution are approximately 8 cm^{-1}. This means that the *fac* CO_2 complex would likely display only two clearly distinct CO bands, with one probably being broader than the other due to an overlap of peaks. The *mer* isomer has peaks which are spaced far enough apart that is far more likely that this isomer would display three distinct bands.

The BDE values for isomers **11** and **12** are given in Table 3.16 and it can be seen that the *fac* isomer is consistently predicted to bind to CO_2 12-15 kJ mol^{-1} more weakly than the *mer* isomer. This is due to the *trans* influence causing the CO_2 in the *fac* isomer to be a lot more labile than in the *mer* isomer. These cationic rhenium complexes display the same trend as seen for the cationic manganese complexes with the differences in stability between the complexes and intermediate species which can be seen in Table 3.17. The CO_2 complex *fac* isomer is found to be more stable than the *mer* isomer by 85 to 80 kJ mol^{-1} depending on the bpy substituent whereas the intermediate tricarbonyl species for the *fac* isomer is found to be more stable than the *mer* isomer by 99 to 90 kJ mol^{-1}. This difference of 14 to 10 kJ mol^{-1} is also very similar to the difference seen between the strength of the M-CO_2 interaction between the *fac* and *mer* isomers from Table 3.16.

Bpy	CO_2 Complex Diff / kJ mol^{-1}	Intermediate Diff / kJ mol^{-1}
dtbpy	85	99
dmbpy	85	98
bpy	83	94
dfbpy	80	91
dftbpy	80	90

Table 3.17: Table of calculated energy differences. The left column is the difference between the more stable *fac* and less stable *mer* isomers of the cationic CO_2 complexes. The right column is the difference between the more stable *fac* and less stable *mer* isomers after having undergone CO loss (the intermediate complex, briefly formed with a vacant site, before CO_2 coordination).

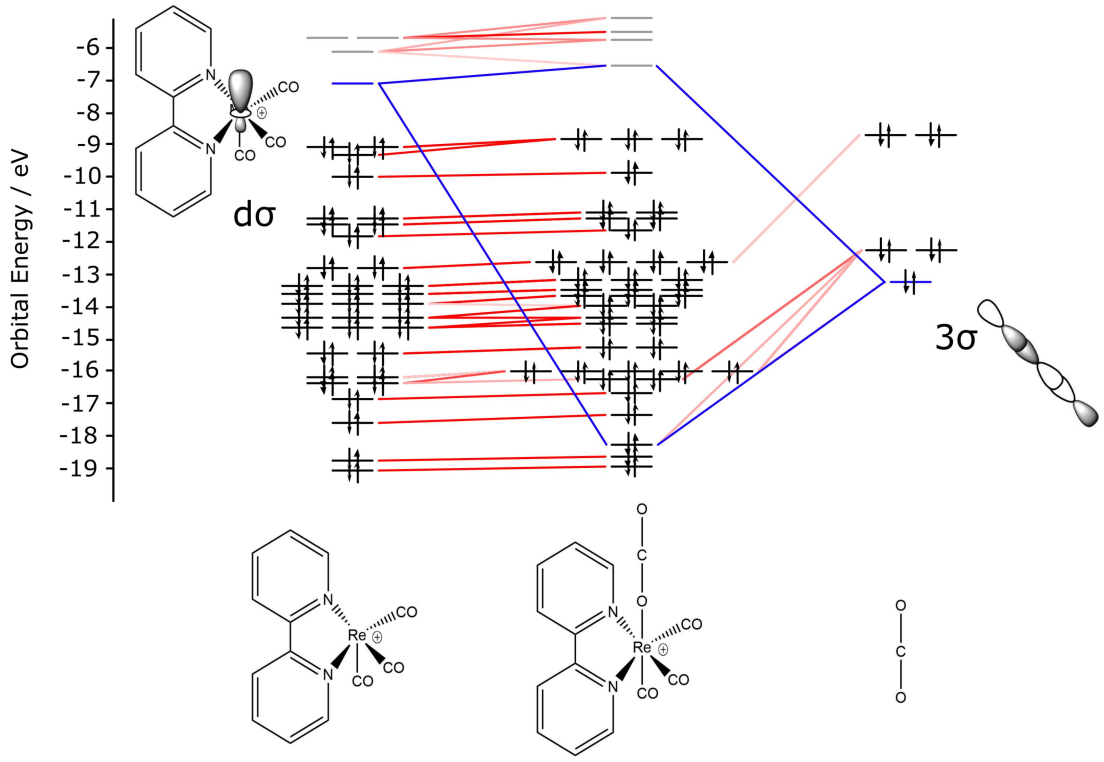

Figure 3.36: Schematic orbital interaction diagram between the orbitals of the $[(bpy)Re(CO)_3]^+$ fragment with an axial vacant site and the orbitals of a linear CO_2 molecule. Isomer **11**

From Table 3.16 it can be seen again that the cationic rhenium complexes have a stronger Re-CO_2 bond than the neutral complexes. The explanation for this can be seen from Figures 3.36 and 3.37, which show MO diagrams describing the interaction of the orbitals of $[(bpy)Re(CO)_3]^+$ fragments with the orbitals of the linear CO_2 molecule for each isomer. The metal fragment LUMO orbital is again shifted down in energy compared with the neutral complex by around 4 eV decreasing the energy gap between the interacting orbitals.

The data in Table 3.16 also shows the difference in bond energies as the substituents on the bpy group change and again it can be seen that a more electron withdrawing bpy increases the metal to CO_2 binding strength and a more electron donating bpy decreases the metal to CO_2 binding strength. The *fac* isomers vary in strength by 9 kJ mol^{-1} and the *mer* isomers vary by 5 kJ mol^{-1}, which are slightly larger variations than seen in the neutral rhenium bpy complexes when changing the substituents and a 1 kJ mol^{-1} larger variation

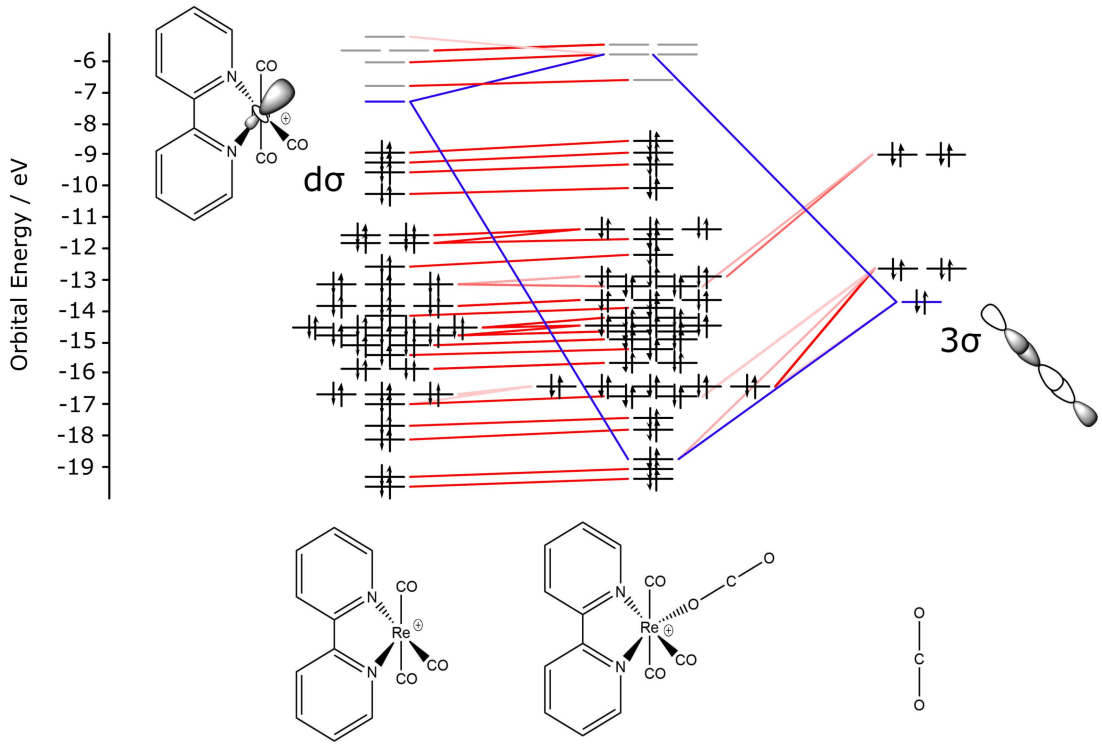

Figure 3.37: Schematic orbital interaction diagram between the orbitals of the $[(bpy)Re(CO)_3]^+$ fragment with an equatorial vacant site and the orbitals of a linear CO_2 molecule. Isomer **12**

compared with the cationic manganese bpy complexes for both isomers.

Influence of Bipyridine Functionalisation on Complex Stability

For the cationic rhenium complexes the change in orbital energy gap as the bpy substituents change was investigated. The same trend as seen again where the more electron withdrawing bpy has a lower energy metal fragment which in turn lowers the energy gap between the unoccupied bonding orbital of the metal fragment and the CO_2 bonding orbital. For the *fac* isomers the bonding-antibonding orbital energy gap for dmbpy is 12.09 eV, for bpy is 12.00 eV and for dfbpy is 11.84 eV, which slightly smaller energy gaps than the neutral rhenium bpy complexes which were 12.16, 12.12 and 11.95 eV, respectively. For the *mer* isomers the bonding-antibonding orbital energy gap for dmbpy is 12.83 eV, for bpy is 12.83 eV and for dfbpy is 12.82 eV, where it can be seen that the variation between different substituents is close to zero.

Mn and Re Complex Bond Length Comparisons

The data in Table 3.18 allows for comparison of bond lengths between the different manganese and rhenium complexes when comparing the same isomers. The rhenium complexes, $[(L)Re(CO)_3(CO_2)]^+$, all have longer M-X bonds than the manganese complexes, $[(L)Mn(CO)_3(CO_2)]^+$, which is the same situation as seen for the neutral bpy complexes. The M-C bonds are on average 0.111 Å longer in the rhenium complexes compared with the manganese analogues, with some variation depending on what group is located *trans* to the CO ligand. The carbonyl C-O bonds in the rhenium complexes are only on average 0.006 Å longer than the cationic manganese ones. For isomers **9** and **11** the M-N1 and M-N2 bonds are consistently longer by 0.149 Å in the rhenium complex compared to the manganese complexes, due to the previously mentioned difference in ionic radii. For isomers **10** and **12** there is more differences when comparing the M-N1 and M-N2 bond distance. For isomer **10** M-N1 is 2.057 Å and M-N2 is 2.016 Å which is a 0.041 Å difference from being located *trans* to different ligands but for isomer **12** M-N1 is 2.202 Å and M-N2 is 2.112 Å which is a 0.090 Å difference.

Bond Length /Å	**9**	**11**	**10**	**12**
M-C1	1.821	1.935	1.812	1.916
M-C2	1.821	1.935	1.887	2.011
M-C3	1.790	1.892	1.887	2.011
M-O4	2.226	2.367	2.196	2.318
M-N1	2.049	2.198	2.057	2.202
M-N2	2.049	2.198	2.016	2.112
C1-O1	1.140	1.145	1.144	1.151
C2-O2	1.140	1.145	1.134	1.138
C3-O3	1.140	1.146	1.134	1.138
O4-C4	1.164	1.166	1.165	1.166
C4-O5	1.145	1.143	1.144	1.143

Table 3.18: Table of bond lengths for isomers **9-12** with each manganese and rhenium isomer grouped together.

The M-O4 distances reported Table 3.18 are larger for the rhenium isomers **11** and **12** compared with the manganese isomers **9** and **10**, despite being stronger bonds for the rhenium isomers. These greater M-O4 bond distances are due to the

previously mentioned difference in ionic radii. For isomers **9** and **11** the difference in M-O4 bond length is 0.141 Å, but for isomers **10** and **12** the difference in M-O4 bond length is 0.122 Å. The M-O bonds in *mer* isomers **10** and **12** are shorter than their *fac* counterparts due to stronger M-O bonds. Much smaller differences are seen in the O4-C4 and C4-O5 bonds between isomers, but it is noted that the stronger the M-O bond the slightly longer the O4-C4 bond is and then in turn the shorter the C4-O5 bond is.

When comparing the calculated IR bands for isomers **9-12** there are some trends that can be noted. The first of which is that the position of the CO_2 band does not vary more than 3 cm^{-1} between metal or isomer, this is much less than the variation in the different shifts calculated for all the carbonyl ligands. The first carbonyl band in isomer **9** is found at 2079 cm^{-1} and in isomer **10** at 2105 cm^{-1} whereas in isomer **11** this band is found at 2074 cm^{-1} and in isomer **12** 2095 cm^{-1}. It can be seen that this band has shifted down in wavenumber for the rhenium isomers compared with the values for the manganese isomers and these shifts are by 5 cm^{-1} for the *fac* isomer and by 10 cm^{-1} for the *mer* isomer. This lower wavenumber for the rhenium isomers is expected due to the weaker C-O bond. The second carbonyl band in isomer **9** is found at 2017 cm^{-1}, in isomer **10** at 2038 cm^{-1}, in isomer **11** at 1989 cm^{-1} and in isomer **12** at 2006 cm^{-1}. The bands in the rhenium complex are found at a lower wavenumber than those in the manganese one, but this time the shifts are 28 cm^{-1} for the *fac* isomer and 32 cm^{-1} for the *mer* isomer, which is much larger than for the first carbonyl band.

The BDE values for isomers **9-12** can be seen on previous pages in Tables 3.13 and 3.16 and the main trend to be noted is that all the BDE values are between 14-16 kJ mol^{-1} higher for the rhenium complexes than the manganese complexes. It can also be noted that for both the manganese and rhenium complexes the *mer* isomer is always predicted to have a stronger M-CO_2 bond than the *fac* isomer. This trend can be understood by examining the MO diagrams for the different metals shown in Figures 3.31 and 3.36. The main cause of rhenium complexes

displaying greater binding strength than manganese ones is that the rhenium CO_2 complex is more stable than its manganese analogue, which can be seen from the lower energy of the highlighted bonding orbital in Figure 3.36 where the orbital lies at -18.9 eV compared with the same orbital in the manganese complex from Figure 3.31 which lies at -18.6 eV. In both of these systems there is additionally a larger stabilisation energy when comparing the energy of the metal fragment LUMO with the CO_2 complex bonding orbital for the rhenium complex. This same trend is also noted in Figures 3.32 and 3.37 for the other isomers too and is also seen across all the tested bpy substituents.

Cyclopentane Complexes

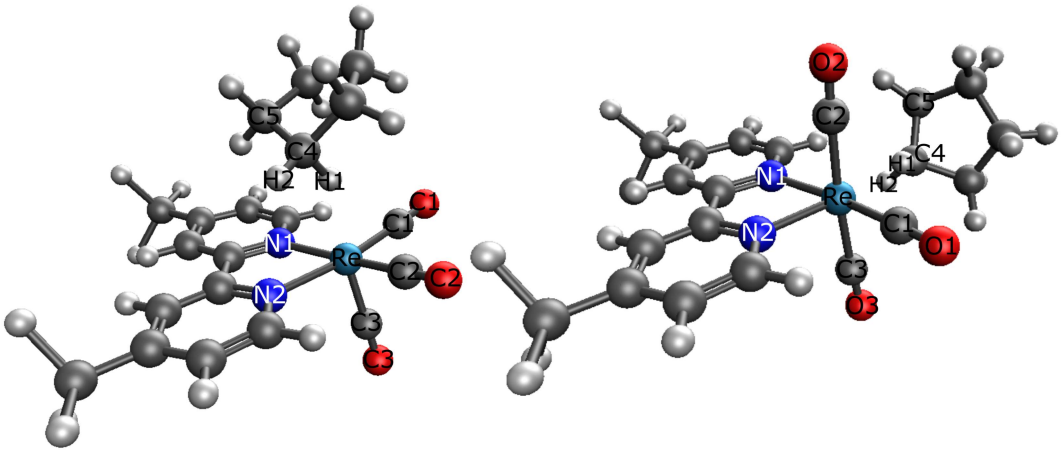

Figure 3.38: Optimised structures obtained at the DFT-M06/LANL08(f) (metals) and 6-311++G** level for [(dmbpy)Re(CO)$_3$(ax-C_5H_{10})] (**11**-C_5H_{10}, left) and [(dmbpy)Re(CO)$_3$(eq-C_5H_{10})] (**12**-C_5H_{10}, right).

Cyclopentane was again investigated, for the same reasons as explained previously, as a potential alkane ligand, as it was for (dmbpy)Re(CO)$_2$(Cl)(C_5H_{10}) and the structures of these two complexes can be seen in Figure 3.38 and their bond lengths can be seen in Table 3.19. Much like the situation when comparing the neutral alkane complexes with neutral CO_2 complexes the Re-C, C-O and Re-N bonds are all fairly similar in length to the cationic CO_2 complexes. These cationic alkane complexes have longer Re-C bonds than the neutral alkane complexes but very similar Re-N bond lengths. The Re-H bond lengths were found to

be longer for the cationic complexes despite showing a predicted binding strength of 63 kJ mol^{-1} for the *fac* isomer and 86 kJ mol^{-1} for the *mer* isomer which are greater than the binding strengths predicted for the neutral complexes.

Bond Length /Å	**11**-C_5H_{10}	**12**-C_5H_{10}
Re-C1	1.936	1.917
Re-C2	1.936	2.008
Re-C3	1.900	2.008
Re-N1	2.193	2.212
Re-N2	2.193	2.127
Re-H1	1.998	1.900
C1-O1	1.146	1.151
C2-O2	1.146	1.139
C3-O3	1.146	1.139
C4-H1	1.129	1.145
C4-H2	1.092	1.091
C4-C5	1.520	1.522

Table 3.19: Table of bond lengths for all four isomers for [(bpy)Re(CO)$_3$(C_5H_{10})] from Figure 3.38.

3.3 Conclusions and Future Perspectives

This Chapter has reported an extensive set of calculated bond strengths between manganese and rhenium metal centres and the CO_2 ligand of pianostool and α-diimine complexes. Most of these investigated complexes are predicted to display η^1-OCO binding between the metal and CO_2, a binding mode that is far less widely reported than η^1-CO_2 or η^2-CO_2 binding. It has been found that in all cases where the η^1-OCO binding is predicted the coordination always involves occupied orbitals on the CO_2 and unoccupied orbitals on the metal, meaning that electron density is being donated onto the metal from the CO_2.

For the pianostool and α-diimine complexes it was found that rhenium is a better choice of metal than manganese when trying to maximise the strength of interaction between the metal and a CO_2 ligand. This improvement when changing from manganese to rhenium was found to be true for both neutral and cationic complexes. It was also found that cationic complexes were found

to bind to CO_2 more strongly than neutral complexes, something that is due to the metal having a lower energy LUMO orbital, in the cationic complexes which allows for better orbital overlap with the occupied CO_2 orbitals. This lowering of energy of the metal LUMO can be further promoted by use of electron withdrawing substituents on ligands attached to the metal centres. This was found to be more effective for the pianostool complexes compared to the α-diimine systems. The situation for the α-diimine complexes, $(L)M(CO)_2(Cl)(CO_2)$ and $[(L)M(CO)_3(CO_2)]^+$, was found to be more complicated due to the presence of four different isomers for each neutral complex and two isomers for the cationic complexes. The overall trend for both neutral and cationic complexes is that the CO_2 ligand being located in the axial position resulted in the strongest binding to the metal centre.

A large number of calculated IR frequencies were also documented in this Chapter and these calculations will prove useful for any future work in this area as both benchmarks for other calculations and also in experimental attempts to try and investigate these complexes. To accompany these calculated IR frequencies a small selection of bond lengths were also discussed in this Chapter which could prove useful for any future experimentation in this area, especially when looking at crystal structures.

In the future some more calculations could be performed on significantly more electron donating substituents on both systems to see if the trend continues to fit along with something less electron withdrawing than CF_3 groups, examples could be NH_2 for strongly electron donating and Br for moderately electron withdrawing. Other work that could be done is investigating other metals outside of group seven to see if any of them predict even stronger M-CO_2 binding. Other work that could be done includes investigating what changes could be made on these systems to potentially tune the method of CO_2 binding to see if something as simple as a change of subtituents on a ligand or a different ligand system would cause a difference in binding mode of CO_2.

Chapter 4

Towards Isolation of Stable Organometallic CO_2 Complexes

4.1 Introduction

The aim of this Chapter is to synthesise organometallic carbonyl precursors in order to exploit the results of calculations from Chapter 3. These results indicated the generation of new η^1-OCO complexes may be possible from the frameworks of complexes targeted in this Chapter. This was started before the COVID lockdown and was initially focussing on organometallic alkane complexes but we had to pivot. This Chapter lays the foundation for experimental work, which is paired with the extensive DFT studies from Chapter 3.

4.1.1 Re α-Diimine Tricarbonyl Complexes

A family of complexes that have a proven ability to coordinate to CO_2 and act as a catalyst to help mediate reduction of CO_2 to CO is the rhenium α-diimine tricarbonyl complexes.[151,152] A number of studies have been performed in order to probe the mechanism of this reaction with many focussing on the photochemistry of this family of molecules.[146,147] In this section the photochemistry of this family of compounds will be introduced along with a brief summary of its photochemical

reactions with CO_2.

The photophysics of *fac*-[(α-diimine)Re(CO)$_3$X] complexes (X = halogen, phosphite, phosphine or amine; α-diimine = 2,2' or 4,4'-bipyridine) has been extensively studied over the last 40 years.[153–156] These complexes received much attention due to their potential applications in many areas such as photocatalytic reduction of CO_2 to CO, infrared probes of DNA damage and photosensitisers in solar cells.[157–161] The structure of this family of complexes is described in Figure 4.1.

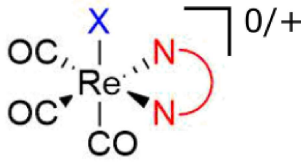

Figure 4.1: Generic molecular structure of *fac*-[(α-diimine)Re(CO)$_3$X] complexes.

Complexes of the type *fac*-[(bpy)Re(CO)$_3$Cl] are typically luminescent in solution at room temperature, emitting from a ^{3}MLCT excited state.[153] After excitation into the ^{1}MLCT absorption band, rapid intersystem crossing (<1 ps), facilitated by the heavy rhenium atom leads to population of the low lying ^{3}MLCT excited state.[153] This state is usually long-lived (40 ns to 1 μs, depending on solvent) and gives rise to emission in the visible region. Irradiation into these MLCT absorption bands does not lead to any CO loss photochemistry.

Ishitani *et al.* used ps-TRIR and photolysed *fac*-[(bpy)Re(CO)$_3$Cl] with 400 nm light in acetonitrile and the expected parent bands were bleached instantly leading to formation of three higher energy bands. These new bands were assigned to the formation of the ^{3}MLCT excited state. They were initially observed as broad spectral features, which rapidly narrowed and blue shifted by around 4 cm^{-1} due to vibrational cooling. The ν(CO) bands of the intially hot, photoexcited molecule are broad, but as the molecule cools, these bands become sharper and increase in intensity s the population of higher vibrational levels decreases and v = 0 increases.[153]

The formation of the CO loss products were investigated by using ns-TRIR

and photolysing *fac*-[(bpy)Re(CO)$_3$Cl] with 313 nm light in acetonitrile. The bands due to the ^{3}MLCT were still present as described for the ps-TRIR and decay with a lifetime of 43 ns to partially reform the parent. Two further bands were also present at lower wavenumbers, which were not due to an excited state, but rather the CO loss product [(bpy)Re(CO)$_2$Cl(MeCN)].[153]

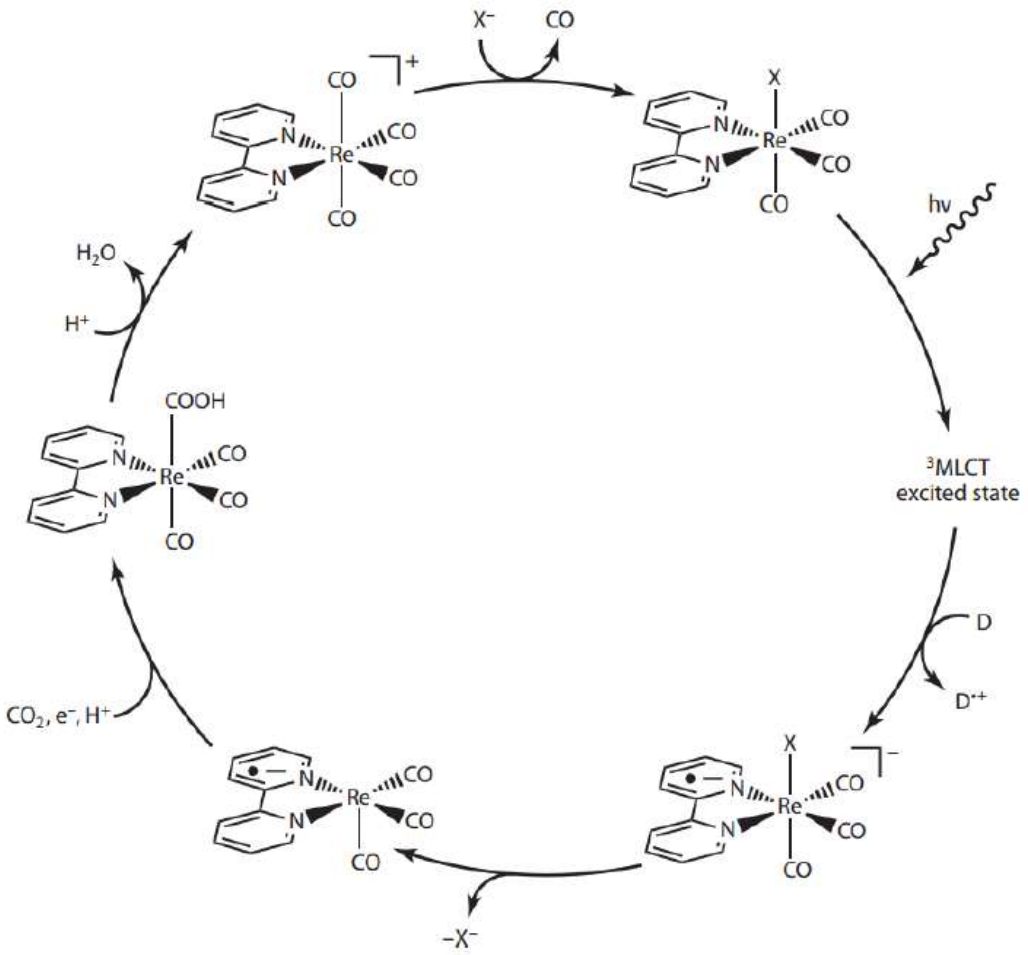

Figure 4.2: Proposed mechanism of *fac*-[(bpy)Re(CO)$_3$X] catalysed photoreduction of CO_2 to CO.[162]

In 1983 Ziessel *et al.* found that *fac*-[(bpy)Re(CO)$_3$Cl] was capable of reducing CO_2 to CO in the presence of water and further showed that improved turnover numbers in the presence of a sacrificial amine donor could be achieved. This was probed by 385 nm irradiation and therefore went *via* the ^{3}MLCT excited state pathway.[158] In 1986 Ziessel *et al.* reported that when exposing a DMF/TEOA (5 : 1 v/v) solution of *fac*-[(bpy)Re(CO)$_3$Cl] to light under a CO_2 atmosphere,

CO gas was generated from the CO_2 reduction reaction with a quantum yield of 0.14.[148] It was then later reported by Ishitani *et al.* in 2008 that when the Cl ligand is changed to an SCN group under similar conditions the CO_2 to CO reduction quantum yield was increased to 0.30.[163] Interestingly, it was found that when the Cl ligand is changed for a CN group the complex displays no catalytic activity at all.[163] Commonly, a CO_2 reduction system requires two components' a photosensitiser and catalyst, but it has been found that most Re^I α-diimine tricarbonyl complexes have the ability to act as both the photosensitiser and catalyst for the reduction of CO_2. A commonly reported mechanism of CO_2 reduction by use of a Re^I α-diimine tricarbonyl catalyst is given in Figure 4.2.

The initial step involves photochemical generation of the ^{3}MLCT excited state, which is then quenched by an electron transfer process from a sacrificial electron donor to generate the catalytically active one-electron reduced species $[(bpy)Re(CO)_3L]^+$. This is the step that can be attributed to the small amount of CO_2 reduction when L was CN, because this cyano intermediate was quite stable and as such only a little CN ligand dissociation happened. This small amount of ligand is then replaced by a CO_2 which is then reduced to CO, this does require another electron and this is typically supplied by another one electron reduced species.[163]

The aim of part of the work conducted in this report is to investigate whether such rhenium α-diimine complexes can be used to form a long-lived η^1-O CO_2 or alkane complex. Unfortunately *fac*-$[(bpy)Re(CO)_3Cl]$ is completely insoluble in non-polar solvents such as CO_2, alkanes or PFMCH and so to overcome this, a large fluorinated bpy was synthesised which is detailed later on in this Chapter.

4.1.2 Re α-Diimine Tetracarbonyl Complexes

Previous, currently unpublished, work in the group on $[(bpy)Re(CO)_4][PF_6]$ showed that it exhibited a unique reaction pathway for photodissociation arising from the ^{3}MLCT excited state following 355 nm irradiation and resulting in

the formation of a *fac*- tricarbonyl solvated photoproduct. The family of *fac*-[(α-diimine)Re(CO)$_3$X] complexes usually require a photoexcitation source of much lower wavelength (216 - 313 nm) to undergo the CO loss pathway.[153] This implies that the photogenerated one electron intermediate is much more accessible from [(bpy)Re(CO)$_4$][PF$_6$] than from their tricarbonyl analogues. This means that [(bpy)Re(CO)$_4$][PF$_6$] has the potential to be utilised as a type of photocatalyst for the reduction of CO_2 to CO.[164] Additional to this, [(bpy)Re(CO)$_4$]$^+$ has been observed as an essential intermediate in *fac*-[(bpy)Re(CO)$_3$Cl]-catalysed CO_2 reduction reactions, suggesting that their photoinduced properties might be able to give further insight of the mechanism behind the corresponding catalytic cycle.[165] The general structure of [(bpy)Re(CO)$_4$]$^+$ complexes is given in Figure 4.3.

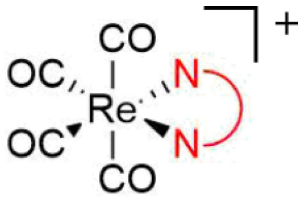

Figure 4.3: Generic molecular structure of *fac*-[(α-diimine)Re(CO)$_4$] complexes.

Due to the C_{2V} geometry of these Re^I α-diimine tetracarbonyl complexes there are four ν(CO) bands corresponding to four different IR active carbonyl modes. The FTIR spectrum of [(dmbpy)Re(CO)$_4$][OTf] is presented in Figure 4.4 and shows four ground state bands, which are assigned left to right as 1A$_1$, B$_1$, 2A$_1$ and B$_2$.[166] The two A$_1$ modes are described as an in-phase motion of axial and equatorial carbonyls, the B$_1$ mode is described as the out of phase motion of the axial carbonyls, and the B$_2$ vibrational mode is assigned as the out of phase motion of the equatorial carbonyls.

The first investigation into the photophysical behaviour of Re^I α-diimine tetracarbonyl complexes was carried out by Shaver *et al.* using [(α-diimine)Re(CO)$_4$][OTf], where α-diimine = 2,2'-bipyrimidine (bpm), bpy, dmbpy and 1,10-phenanthroline (phen).[167] It was reported that [(bpm)Re(CO)$_4$][OTf] exhibited a strong luminescence from its lowest energy ^{3}MLCT excited state, which

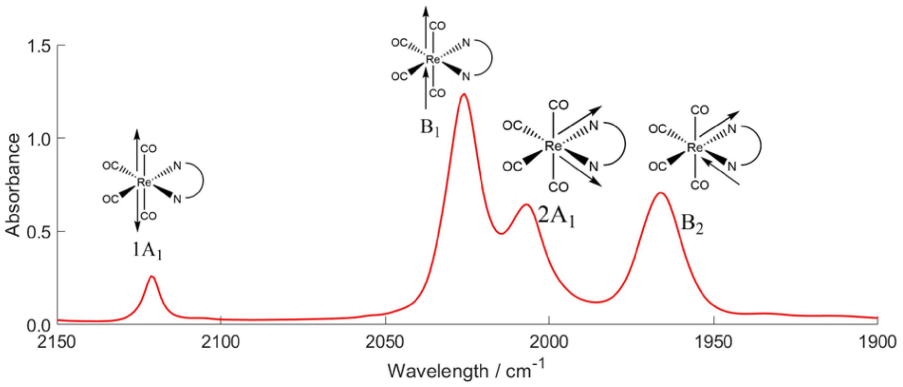

Figure 4.4: Ground state FTIR spectrum of the carbonyl region of [(dmbpy)Re(CO)$_4$][OTf] displaying the four vibrational modes of the CO ligands. This spectrum was recorded in CH_2Cl_2. From left to right: $1A_1$, B_1, $2A_1$ and B_2 vibrational modes.

had a lifetime of 390 ns. This lifetime is an entire order of magnitude greater than was observed for *fac*-[(bpy)Re(CO)$_3$Cl], which indicates that the changing of the Cl ligand to a CO massively reduces the rate of non-radiative decay and also increases the rate of radiative decay in the relaxation of the ^{3}MLCT excited state.

The first TRIR study of these types of complex was performed by Bernhard *et al.* in 2000.[166] After 355 nm excitation, the lower energy B_1, $2A_1$ and B_2 bands showed an increase in wavenumber by between 3 to 5 cm^{-1}, while the $1A_1$ decreased in energy by around 10 cm^{-1}. The shift of the $1A_1$ is within the typical shift range of a triplet ligand-centred (LC) $\pi \rightarrow \pi^*$ transition suggesting that the lowest excited state has some triplet LC $\pi \rightarrow \pi^*$ character. The typical ^{3}MLCT(Re$\rightarrow$diimine) transitions cause a decrease in the amount of electron density on the metal which results in less backbonding and strenghtens the CO bond and therefore blueshift the bands. The blueshift of the other three B_1, $2A_1$ and B_2 bands suggests that there is some MLCT character. Therefore these studies proved that the lowest excited state in this [(bpy)Re(CO)$_4$]$^+$ system was a mixed state of ^{3}MLCT(Re$\rightarrow$diimine)/^{3}LF($\pi \rightarrow \pi^*$).[166] These results were rationalised further with specific orbital explanations. The promotion of an electron from the metal d_{xy} orbital to the bpy π^* orbital (MLCT) causes an electron vacancy in the xy plane, the plane of the bpy. This vacancy leaves an 'electron hole' and there-

fore the $2A_1$ and B_2 modes of the equatorial carbonyls had a significant blueshift. The $1A_1$ mode was least affected by the hole and hence was more likely to be affected by the LF $\pi \rightarrow \pi^*$ transition, which is why this band is redshifted. The B_1 mode was influenced less than the $2A_1$ and B_2 modes, but more so than the $1A_1$ mode; as this band blueshifted too the B_1 mode was said to more reflect the ^{3}MLCT character in the mixed state.[166]

4.1.3 Cationic Complexes and Non-Coordinating Anions

Many of the complexes in this report are cationic. This electron deficiency in the metal centre can be used to our advantage and increase the strength of the electrostatic interaction with the oxygen atoms of CO_2, therefore making the η^1-O binding mode more favourable. The cationic complexes will also have a lower energy LUMO d_σ orbital, which will then have a better overlap with the n_π orbital and therefore be favourable. The metal HOMO d_π donation into the CO_2 π^* orbital makes η^2-CO binding more preferable. This increased orbital overlap and bond strength should then increase the lifetime of the complex and make it easier to study and obtain spectroscopic measurements.[122]

The primary drawback from using cationic species in this type of work is their poor solubility in non-polar media such as CO_2, alkane solvents and perfluoro methylcyclohexane (PFMCH). More polar solvents containing oxygen and nitrogen atoms are often ideal for solubulising cationic species, but these risk displacing ligands from the coordination sphere and would readily bind to reactive intermediates in the place of desired ligands of interest such as CO_2 or alkanes. Pianostool complexes are generally more soluble in non-polar solvents than the bpy systems in this report due to their much smaller size, polarisability and dipole moment. One of the ways to increase a compounds solubility in PFMCH or CO_2 is to increase the fluorous content of the complex. Exactly why this helps increase solubility in CO_2 is still not fully understood but it is generally known that the presence of fluorine creates molecules with weak self-interaction, render-

ing miscibility with CO_2 more readily possible and that electronegative fluorine exhibits specific interactions with CO_2's electron poor carbon atom.[168] The presence of fluorine will also affect the acidity of neighbouring protons, allowing for the possibility of specific interactions between these protons and CO_2's oxygen atoms.[33]

There are two different methods in which the fluorous content of the complexes has been increased in this work. The first of which is adding fluorinated carbon chains onto the organic parts of the complex, while making use of non fluorinated alkane spacers to leave the electronic properties of the complex unchanged. The second of these methods is changing the complexes anion to something which has a high fluorous content. The perfluoroalkoxyaluminate anion used in this work is shown in Figure 4.5 which contains 36 fluorine atoms. This anion is importantly also very non-coordinating owing to the large number of fluorine atoms essentially shielding the anion and making coordination very unlikely. This is important as when a reactive intermediate is formed the anion will not bind over the ligand of interest. This anion has been used before by Ball *et al.* when investigating a cationic transition metal alkane complex by NMR spectroscopy.[169]

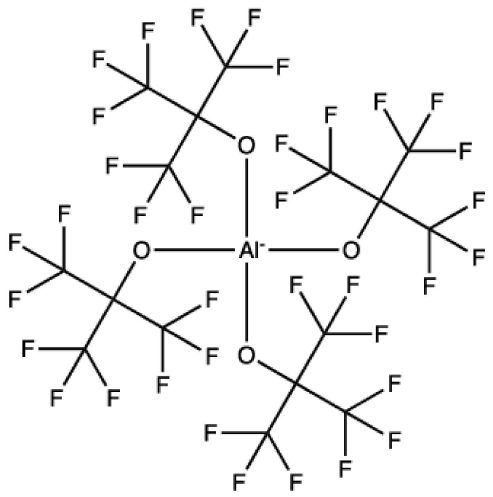

Figure 4.5: Structural formula of $[Al(OC(CF_3)_3)_4]^-$.

4.1.4 Ionic Liquids

Ionic liquids ideally consist of ionic species only, usually with significant molecular asymmetry in at least one of the ions, and form a liquid phase with a melting temperature lower than 100 °C.[48,170,171] In ionic liquids, the ordering of the ions into a solid crystalline phase is hindered not only by the molecular asymmetry, but also by the hydrogen bonded network established between the cations and suitable anions.[172,173] Ionic liquids have many tunable properties and can be modified to have desirable characteristics such as low toxicity, high polarity and non-coordination.[174,175] They are able to dissolve many metal complexes, catalysts and organic molecules. More recently ionic liquids have started to be used in reactions involving organometallic catalysts showing the potential these solvents could have in the future of organometallic photochemistry.[176–181]

4.1.5 Aims and Objectives

The work in this Chapter describes a series of synthetic attempts to isolate and purify some of the complexes investigated by DFT in this Thesis, with a primary focus on the rhenium pianostool and bpy complexes. If these complexes can be isolated then their solubilities in non-coordinating solvents such as alkanes and liquid CO_2 will be tested using FTIR as a characterising technique. The results from these solubility tests can then be used to modify the structure of the subsequent generation of target compounds and thus inform the synthetic strategy. PFMCH has a high gas solubility capability, due to its fluorinated nature, could be used to dope things like CO_2 into solution. Once in solution these complexes could be photochemically activated to form short-lived intermediate species and techniques such as TRIR and matrix isolation could be used to analyse the nature and photophysics of these compounds. We have used the following strategy to address the aims above:

1) Undertake the synthesis of a selection of both pianostool and α-diimine rhenium complexes.

2) If these complexes can be isolated and purified test their solubilities in non-polar media such as alkanes, PFMCH and liquid CO_2.

3) Use the results of these solubility tests to inform future syntheses while trying to minimise effects on the electronic structure of the systems.

4) If any of these systems are sufficiently soluble in the non-polar media, these complexes can be photolysed at low temperature to undergo 'CO loss' in an attempt to form a bond between the metal atom and the ligand of interest, such as CO_2.

This research was affected by the COVID-19 shutdown and the constraints of the pandemic have hampered the synthesis and ability to study the photophysics and photochemistry of these complexes.

4.2 Results and Discussion

4.2.1 Cationic Pianostool Complexes

Two different synthetic routes for making the cationic pianostool complexes were attempted and are summarised in Scheme 4.1. The top route utilises a metal triflate to form the desired pianostool complex, where the formation of AgBr is the driving force of the reaction. The triflate is a labile ligand, which can be displaced by benzene to form $[BnMn(CO)_3][OTf]$ under mild conditions.[182] The bottom route requires the reagents to be heated at reflux in decane at high temperatures, followed by an anion exchange. Although this route uses more harsh conditions, based on our tests, it is higher yielding than the top route and the top route cannot be used to make rhenium pianostool complexes as the $Re(CO)_5OTf$ intermediate species appears to be too stable to react with the arene up to temperatures of 60 °C. Therefore the bottom route was chosen as the preferable synthetic route when making all other pianostool complexes, unless stated otherwise. $[BnMn(CO)_3][OTf]$ was successfully synthesised but $[BnRe(CO)_3]^+$ was unable to be synthesised and isolated.

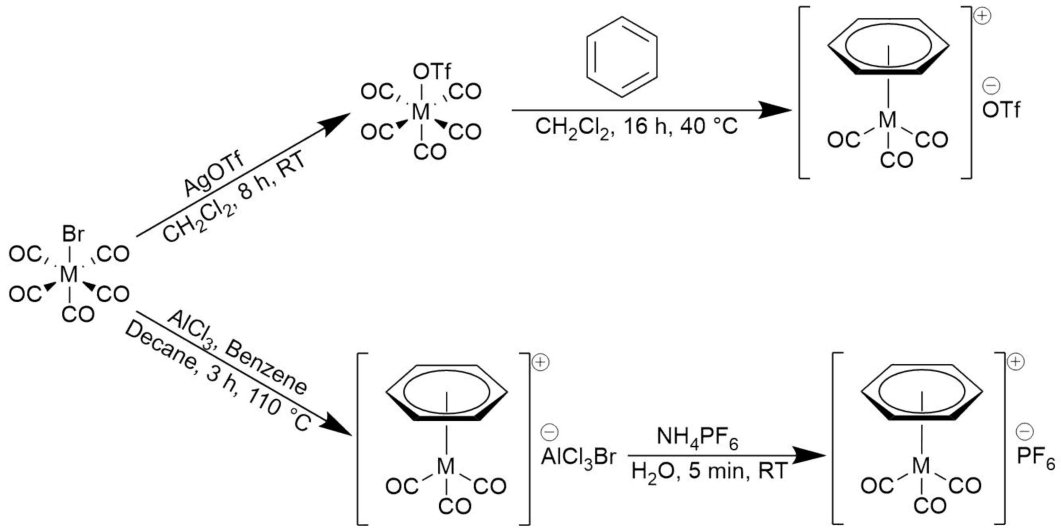

Scheme 4.1: Reaction schemes for the two tested synthetic routes for the synthesis of cationic pianostool complexes, where M = Re or Mn.

To synthesise a rhenium pianostool complex a different approach was trialled, which involved stabilising the rhenium analogues of these compounds by using a more bulky arene such as Mes, HMB and HEB. The complexes $[(Mes)Re(CO)_3][PF_6]$, $[(HMB)Re(CO)_3][PF_6]$ and $[(HEB)Re(CO)_3][PF_6]$ were successfully synthesised and the carbonyl region in the FTIR spectra of the successfully isolated rhenium pianostool complexes is given in Figure 4.6. The peak shapes of the three complexes (Figure 4.6) are not all uniform suggesting that these complexes are not pure and may also have impurities present.

An anion exchange from $[PF_6]^-$ to $[Al(OC(CF_3)_3)_4]^-$ was attempted, to both aid solubility and reduce the chance of coordination of $[PF_6]^-$. For this reaction, the compound $[Li][Al(OC(CF_3)_3)_4]$ is synthesised (Scheme 4.2) and stirred in diethyl ether along with the the cationic complex. This is reported in more detail in Chapter 6.

Figure 4.7 shows the FTIR spectra of $[(HMB)Re(CO)_3][PF_6]$ and product of the $[(HMB)Re(CO)_3]^+$ anion exchange in CH_2Cl_2. The red spectrum for $[(HMB)Re(CO)_3][PF_6]$ has two CO bands at 2059 and 1987 cm^{-1}, whereas following anion exchange, CO bands are observed at 2065, 2020, 2009 and 1900 cm^{-1}. The large differences between these spectra are not expected as there should be no difference in the covalent bonds of the molecule. This is likely due to the pres-

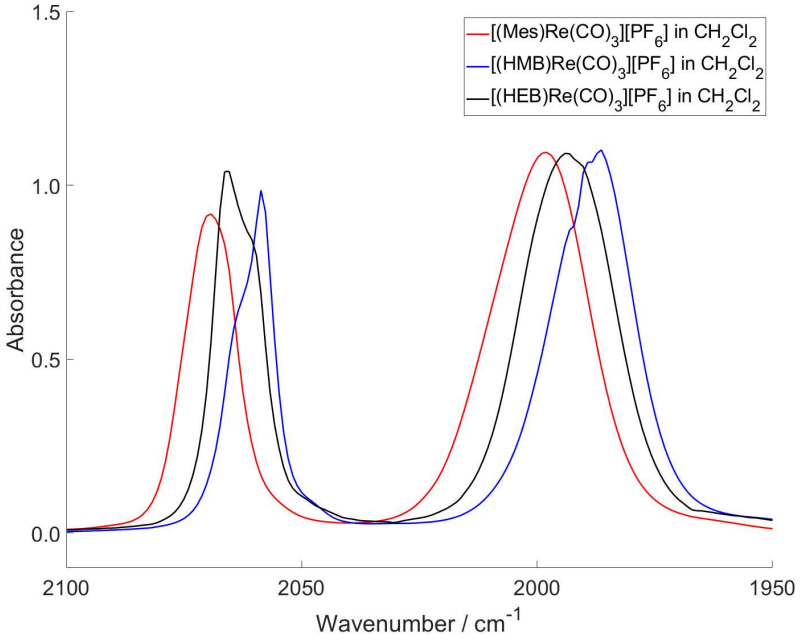

Figure 4.6: FTIR spectra of the carbonyl region of $[(Mes)Re(CO)_3][PF_6]$ (red), $[(HMB)Re(CO)_3][PF_6]$ (blue) and $[(HEB)Re(CO)_3][PF_6]$ (black) in CH_2Cl_2.

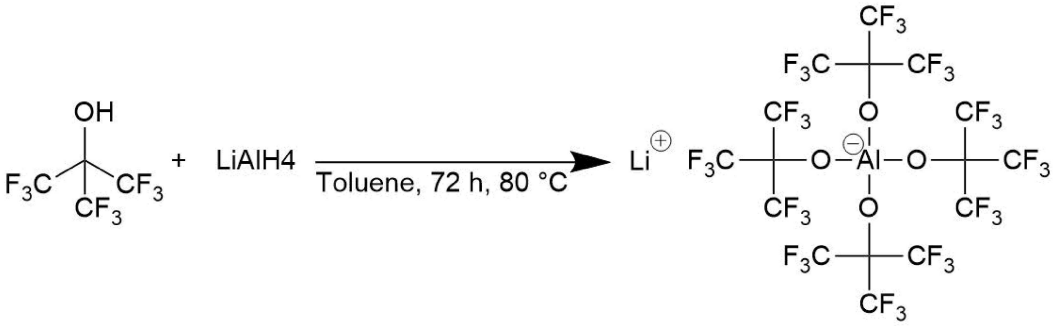

Scheme 4.2: Reaction scheme for the synthesis of $[Li][Al(OC(CF_3)_3)_4]$ adapted from Krossing's method.[183]

ence of multiple species, many of which will have likely be various decomposed complexes, such as dimers, from the original $[(HMB)Re(CO)_3]^+$. These species could not be separated by recrystallisation, washing or column chromatography and consequently no single pure product could be isolated.

When the anion exchange was carried out on $[(HEB)Re(CO)_3][PF_6]$ more success was achieved. The FTIR spectrum for $[(HEB)Re(CO)_3][PF_6]$ and the product of the $[(HEB)Re(CO)_3]^+$ anion exchange is given in Figure 4.8. Following the anion exchange, the CO bands do not shift by a large amount and a successful anion exchange was confirmed by MS. However two small bands are observed at

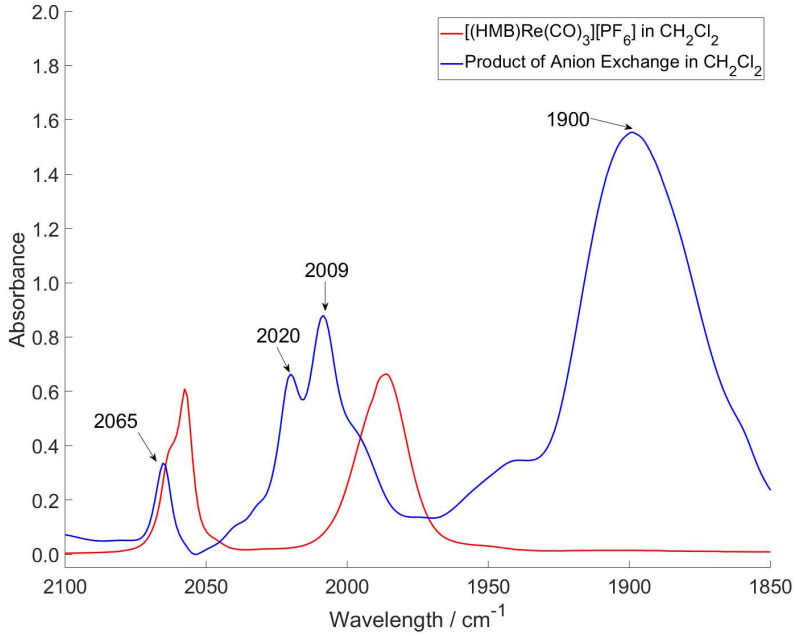

Figure 4.7: FTIR spectra of the carbonyl region of $[(HMB)Re(CO)_3][PF_6]$ (red) and the product of the $[(HMB)Re(CO)_3]^+$ anion exchange (blue) in CH_2Cl_2

1955 and 1895 cm^{-1}. The greater stability of $[(HEB)Re(CO)_3]^+$ over the other arenes is likely due to the structure of hexaethylbenzene and its '3-up/3-down' structure where the downwards pointing ethyl groups can help to act as a 'pincer' on the metal.[184]

Due to the difficulties in synthesis of a stable rhenium pianostool complex, the focus of this work moved to rhenium α-diimine complexes.

4.2.2 Neutral α-Diimine Complexes

A series of complexes of the general formula *fac*-$[(4,4'\text{-}R_2\text{-bpy})Re(CO)_3Cl]$ were synthesised using the route shown in Scheme 4.3. The complexes synthesised were: $[(bpy)Re(CO)_3Cl]$, $[(dmbpy)Re(CO)_3Cl]$ and $[(dtbpy)Re(CO)_3Cl]$. The reaction involves heating the reagents at reflux in an equal ratio in toluene for 3 h and then cooling until precipitate is formed and filtering, usually resulting in a pure product. This reaction only yields the *fac*- isomer of the product and no *mer*- isomer due to the *cis* effect.

These complexes were analysed by FTIR in CH_2Cl_2; the IR spectrum of

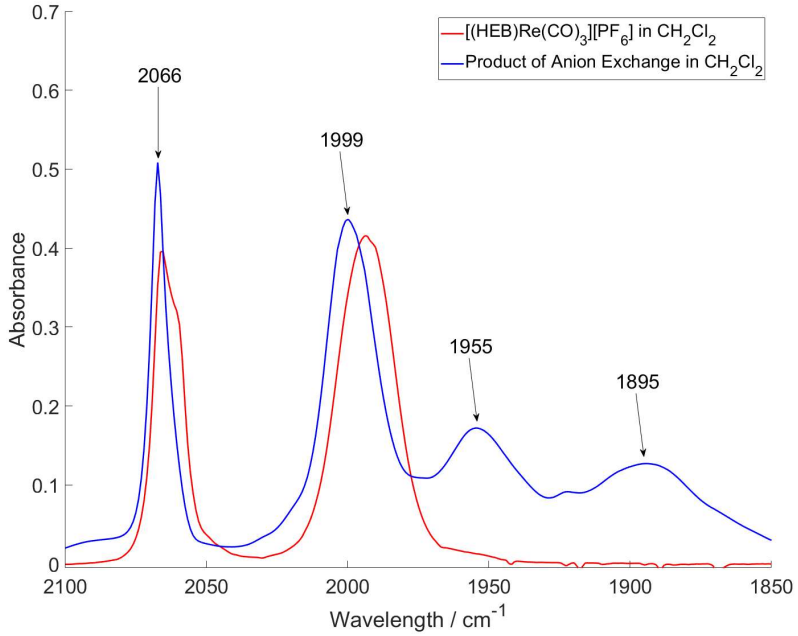

Figure 4.8: FTIR spectra of the carbonyl region of $[(HEB)Re(CO)_3][PF_6]$ (red) and the product of the $[(HEB)Re(CO)_3]^+$ anion exchange (blue) in CH_2Cl_2

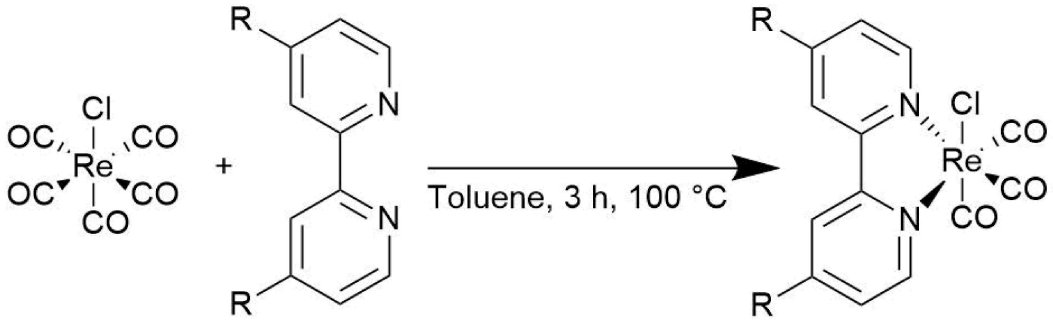

Scheme 4.3: Reaction scheme for the synthesis of *fac*-[(4,4'-R_2-bpy)$Re(CO)_3Cl$] where R = H (bpy), CH_3 (dmbpy) and ^{t}Bu (dtbpy).

$[(bpy)Re(CO)_3Cl]$ is presented in Figure 4.9 showing three clear CO bands at 2123, 2029 and 2010 cm^{-1}. The solubility of these complexes was then tested in a selection of non-polar solvents, hexane, cyclohexane, PFMCH and liquid CO_2, but unfortunately, using FTIR as the detection method of choice, no carbonyl peaks could be detected in the spectra due to a lack of solubility.

Fluorinated compounds have been shown to display higher solubility in CO_2 than their non-fluorous counterparts and as such the next ligand that was synthesised was a bpy ligand with two CF_3 groups located on the 4,4' positions (4,4'-perfluorodimethyl-2,2'-bipyridine, dfbpy). The 4,4' positions were chosen

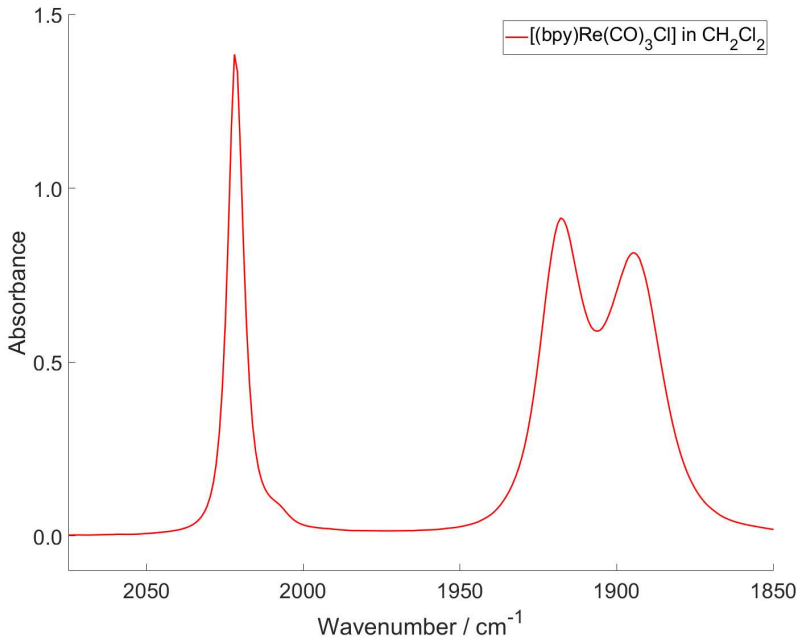

Figure 4.9: FTIR spectrum of the carbonyl region of $[(bpy)Re(CO)_3Cl]$ in CH_2Cl_2.

for a variety of reasons, which can be even more important when working with even larger and bulkier substituents. The distance between the substituent and the metal centre should be maximised to reduce the chance that the substituent directly interacts with the metal atom and potentially binds to the metal centre after undergoing 'CO loss' over the intended ligand. For this reason the 5 and 6 positions would be worse than the 4 positions. The other primary factor to consider is the steric strain on the ligand and having bulky substituents in the 3 positions could cause a large degree of steric hindrance. These points are illustrated in Figure 4.10.

The new dfbpy ligand was synthesised from the route shown in Scheme 4.4. The dfbpy ligand could then be used in the same procedure as before from Scheme 4.3 to generate $[(dfbpy)Re(CO)_3Cl]$. This complex then had its solubility tested in liquid CO_2, but the FTIR spectrum did not show any carbonyl bands, suggesting it was not soluble.

In order to boost the fluorous content of the complex, to try and boost solubility in CO_2, fluorinated chains were added to dmbpy, something that was achieved using the route shown in Scheme 4.5.[185] The extra CH_2 spacers between

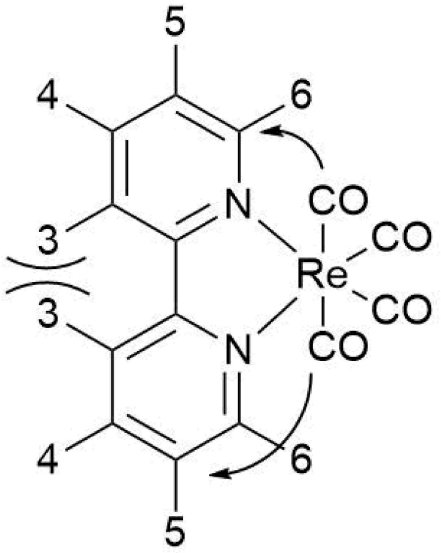

Figure 4.10: Structure of the $[(bpy)Re(CO)_4]$ framework showing the potential issues with positions 2,3 and 5 for bpy substituents.

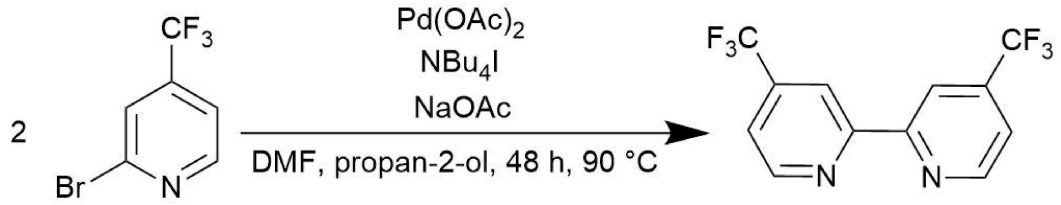

Scheme 4.4: Reaction scheme for the synthesis of dfbpy by a Pd-catalysed coupling reaction.

the fluorinated carbons and the aromatic part of the molecule were incorporated to ensure that the electronic properties of the bpy remain unaffected.

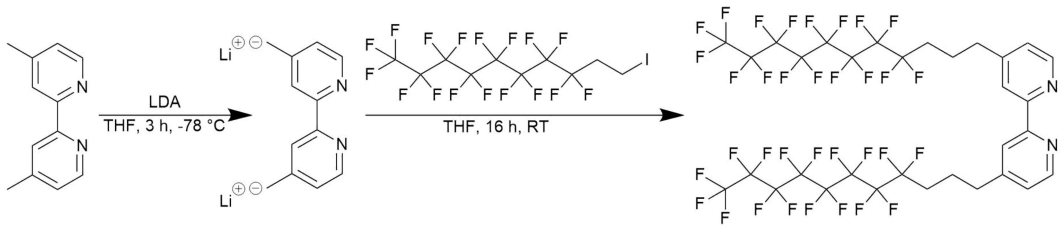

Scheme 4.5: Reaction scheme for the synthesis of dnb-F_{34} from addition of a fluorinated chain onto dmbpy.[185]

When attempting to make a bpy with longer fluorinated chains, as shown in Scheme 4.6, the exclusive product of this reaction is a mono-substituted product. This reaction fails to produce the doubly-substituted product in a multitude of other conditions including heating of the reaction and adding up a five times excess of the fluorinated alkyl iodide.

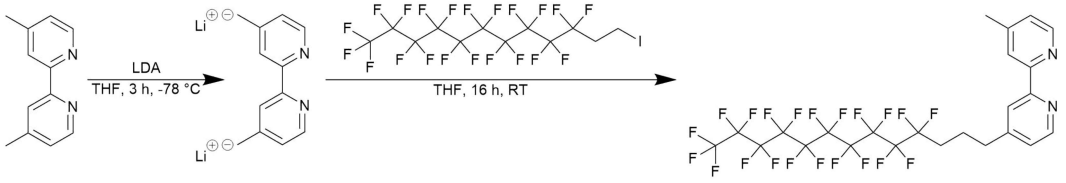

Scheme 4.6: Reaction scheme for the attempted synthesis dnb-F_{42} but resulting in 4- [1H, 1H, 2H, 2H, 3H, 3H- perfluorotridecyl] -4'-methyl-2,2'-bipyridine.

The yield of this reaction shown in Scheme 4.5 is relatively low at 11 %. Many different column chromatography solution systems were tested in order to separate out the three main expected components of reaction; unreacted dmbpy, mono-substituted product and the desired dnb-F_{34}. A successful system at separating out these three was found and it was using pure CH_2Cl_2 : 0.01 mL of aq ammonia solution in 4 % methanol in CH_2Cl_2 slowly increased on a gradient to a 50 : 50 mixture over a 30 column volume period and then ran at 50 : 50 for 15 more column volumes. This method can be used to isolate pure mono-substituted product and recover unreacted dmbpy, but there was unfortunately still an impurity present in the sample of dnb-F_{34}. The structure of this impurity is shown in Figure 4.11. This impurity can be identified in the ^{1}H NMR spectrum by the presence of a doublet of triplets at 5.62 ppm with a J^3_{FH} of 33.2 and J^3_{HH} of 7.8 Hz.

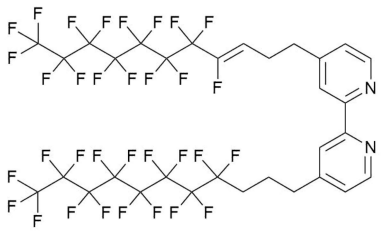

Figure 4.11: Structure of the impurity that could not be separated from dnb-F_{34} by column chromatography.

Experiments were performed to investigate which reagent was causing this elimination of HF from the product. A sample of pure dnb-F_{34} was stirred in diisopropylamine for three hours but this caused no changes in the ^{1}H NMR spectrum. Next, a sample of pure dnb-F_{34} was stirred in a mixture of ^{n}BuLi and diisopropylamine and this caused the growth of the previously noted dou-

blet of triplets at 5.62 ppm. Finally, a sample was stirred in ^{n}BuLi in THF and this caused no changes in the ^{1}H NMR spectrum. This means that it was the LDA specifically causing this HF elimination and not either the ^{n}BuLi or diisopropylamine. The reaction was then tried with an excess of diisopropylamine and substoichiometric amounts of ^{n}BuLi, the doublet of triplets at 5.62 ppm were present in the spectrum but at a lower intensity than previously but the yield was proportionally smaller too.

The [(dnb-F_{34})Re(CO)$_3$Cl] complex was synthesised and its solubility was tested in liquid CO_2. The resulting FTIR spectrum is given in Figure 4.12, which shows that the above modifications were a success, demonstrating that the presence of the fluorinated chains on the bpy ligand, has a positive effect on the solubility of the complex in CO_2. It is acknowledged that this spectrum has quite a poor signal-to-noise ratio and that the peaks are at a very low absorbance. This is due to the limit of solubility of this complex in CO_2 as the solution is as saturated as could be achieved. Multiple photolysis experiments were performed, with up to a 3 mm cell pathlength to maximise absorbance, but the signal to noise ratio was too poor to produce any sets of spectra that contained reliable and repeatable results.

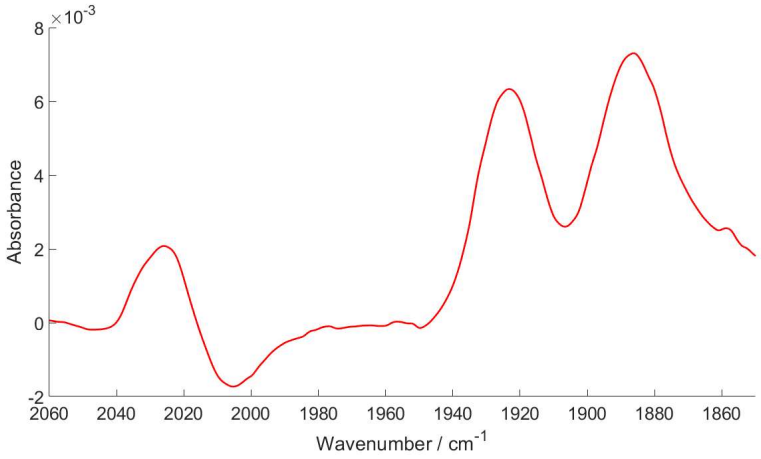

Figure 4.12: FTIR spectrum of the carbonyl region of [(dnb-F_{34})Re(CO)$_3$Cl] in liquid CO_2 (1000 psi) at 230 K.

Figure 4.13 shows the carbonyl region in an FTIR spectrum for both

[(bpy)Re(CO)$_3$Cl] and [(dnb-F$_{34}$)Re(CO)$_3$Cl] and it can be seen that the shift in carbonyl bands between the two complexes is minimal. Figure 4.14 shows electronic absorption spectra of both [(bpy)Re(CO)$_3$Cl] and [(dnb-F$_{34}$)Re(CO)$_3$Cl], which again show very similar peak positions. This helps to confirm that the presence of the three CH_2 spacers between the aromatic section of the bpy and the fluorinated carbon atoms is sufficient to cause little to no change to the electronic structure of the bpy and does not affect the positions of the carbonyl bands. This also means that the calculated vibrational frequencies for [(bpy)Re(CO)$_3$Cl] should be a suitable match for comparison between experiment and theoretical values when studying [(dnb-F$_{34}$)Re(CO)$_3$Cl].

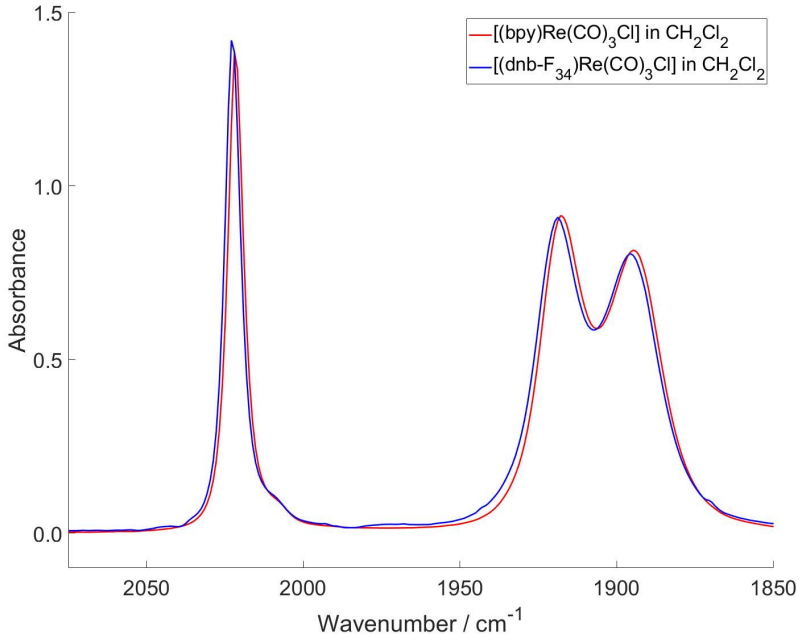

Figure 4.13: FTIR spectra of the carbonyl region of [(bpy)Re(CO)$_3$Cl] (red) and [(dnb-F$_{34}$)Re(CO)$_3$Cl] (blue) in CH_2Cl_2.

In a paper by Yang *et al.* THF was used as an alternative to CO_2 as a simple σ-coordinating ligand, binding through a lone pair on its oxygen atom. This was done to compare carbonyl shifts with a CO_2 complex as part of their evidence for showing η^1-O end-on coordination of CO_2.[122] From previous work in this area it is known that excitation into the band centred at 245 nm leads to CO loss.[186] This THF solvated complex, [(bpy)Re(CO)$_2$Cl(THF)], can then react with detached

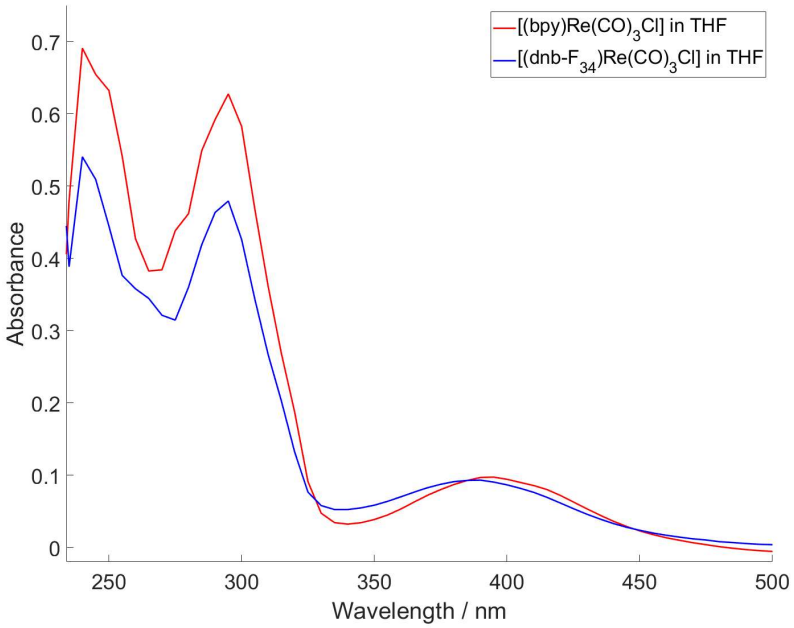

Figure 4.14: Electronic absorption spectra of *fac*-[(bpy)Re(CO)$_3$Cl] (red) and *fac*-[(dnb-F$_{34}$)Re(CO)$_3$Cl] (blue) in neat THF.

CO again to give both the original species and *mer*-[(bpy)Re(CO)$_3$Cl].[153]

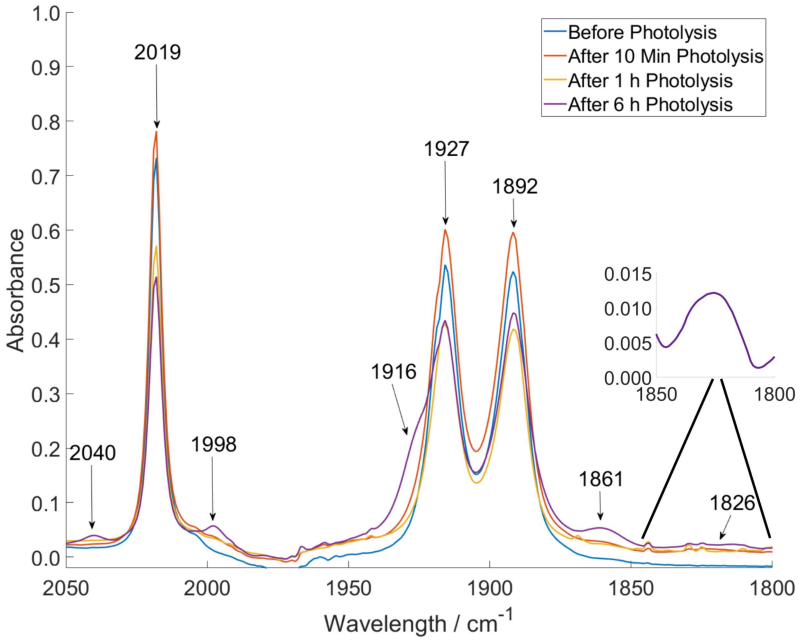

Figure 4.15: FTIR spectra of the carbonyl region at different intervals during photolysis of [(dnb-F$_{34}$)Re(CO)$_3$Cl] in THF using 254 nm light.

The resulting FTIR spectra from this photolysis experiment is given in Figure 4.15 and it can be seen that there is little change in the FTIR bands over 6

h of photolysis. Previous unpublished work from the George group found that when these long fluorinated chains are in solution, when the concentration is sufficient, they can aggregate and change the photochemistry of the system. This aggregation inhibits the loss of the CO ligand which in turn changes the potential reactions that can occur in solution. This is not predicted to be an issue when dissolving in liquid CO_2 as the complex is only sparingly soluble and as such the concentration should not reach the threshold to significantly inhibit CO loss. There is a gradual decrease in intensity of the original parent bands, as the experiment progresses over the 6 h, at 2019, 1927 and 1892 cm^{-1} along with growth of new peaks observed at 2040, 1998, 1916, 1861 and 1826 cm^{-1}. The small broad peak around 1826 cm^{-1} is found close to where a peak was noted by Sato *et al.* at 1828 cm^{-1} when photolysing [(bpy)Re(CO)$_3$Cl] in THF using 266 nm light.[153] This peak was assigned to a CO vibrational band of the bis-carbonyl rhenium complex [(bpy)Re(CO)$_2$Cl(THF)]. This suggests the formation of [(bpy)Re(CO)$_2$Cl(THF)] and this experiment and the observed bands could potentially prove as a preliminary benchmark for any future experiments where *fac*-[(dnb-F_{34})Re(CO)$_3$Cl] is photolysed in CO_2. There is likely a mixture of complexes present in solution including unreacted *fac*-[(dnb-F_{34})Re(CO)$_3$Cl] along with both *mer*-[(dnb-F_{34})Re(CO)$_3$Cl] and [(bpy)Re(CO)$_2$Cl(THF)].

4.2.3 Cationic α-Diimine Complexes

A series of complexes of the general formula [(4,4'-R_2-bpy)Re(CO)$_4$][OTf] were synthesised using the route shown in Scheme 4.7. The metal triflate is required to be formed first, which can then be reacted at quite mild conditions to form the desired product. $AgBF_4$ was also tried as an alternative to AgOTf in one experiment, but the resulting $[BF_4]^-$ containing complex was unable to undergo anion exchange with $[Al(OC(CF_3)_3)_4]^-$ without impurities forming. Four different complexes were initially synthesised, which were [(bpy)Re(CO)$_4$][OTf], [(dmbpy)Re(CO)$_4$][OTf], [(dtbpy)Re(CO)$_4$][OTf] and [(dfbpy)Re(CO)$_4$][OTf].

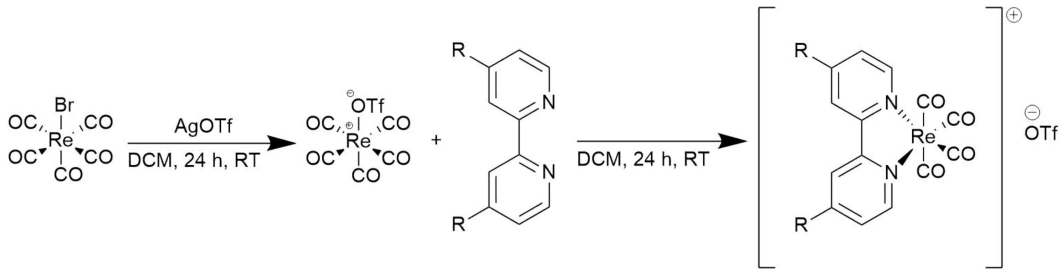

Scheme 4.7: Reaction scheme for the synthesis of [(4,4'-R_2-bpy)Re(CO)$_4$][OTf].

In Figure 4.16 the FTIR spectrum of both [(dtbpy)Re(CO)$_4$][OTf] and [(dtbpy)Re(CO)$_4$][Al(OC(CF$_3$)$_3$)$_4$] is shown. The anion exchange was successfully performed for [(bpy)Re(CO)$_4$]$^+$, [(dmbpy)Re(CO)$_4$]$^+$ and [(dtbpy)Re(CO)$_4$]$^+$ as confirmed by FTIR spectroscopy and MS, but for [(dfbpy)Re(CO)$_4$]$^+$ some impurities in the FTIR spectrum formed that could not be removed.

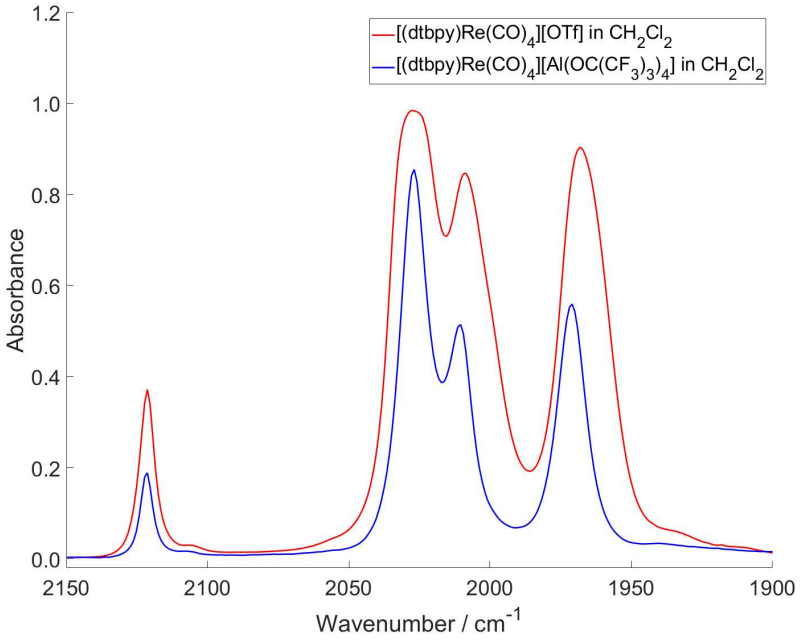

Figure 4.16: FTIR spectra of the carbonyl region of [(dtbpy)Re(CO)$_4$][OTf] (red) and [(dtbpy)Re(CO)$_4$][Al(OC(CF$_3$)$_3$)$_4$] (blue) in CH_2Cl_2.

The solubilities of these pure complexes were then tested in cyclohexane, hexane, PFMCH and liquid CO_2, but unfortunately none of the complexes were observable in those solvents when using FTIR as the detection method. The next step was to try and use the previously synthesised dnb-F_{34} ligand to further increase the complexes fluorous content to improve solubility in both liquid CO_2

and PFMCH.

The synthesis of [(dnb-F_{34})Re(CO)$_4$][OTf] was first attempted by using the method from Scheme 4.7; and the FTIR spectrum of the resulting crude product is shown in Figure 4.17. The desired product peaks are 2121, 2027, 2008 and 1967 cm^{-1}, a peak from unreacted [Re(CO)$_5$(OTf)] is seen at 2059 cm^{-1} and then a tricarbonyl impurity, seen at 2034, 1934 and 1913 cm^{-1}. The complex [Re(CO)$_5$(OTf)] is neutral and can be removed by dissolving the sample in CH_2Cl_2 and precipitating by slow addition of hexane. A variety of purification techniques were trialled to try and remove the tricarbonyl impurity.

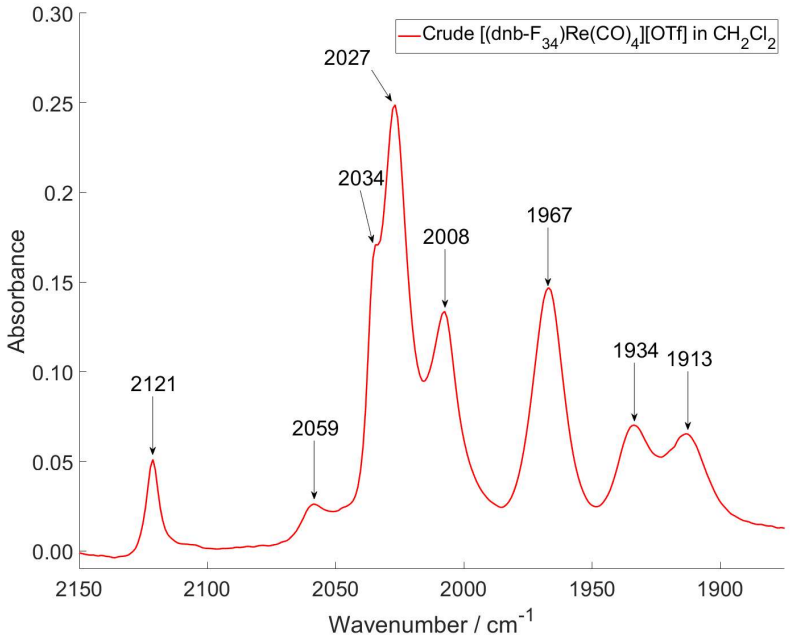

Figure 4.17: FTIR spectrum of the carbonyl region of [(dnb-F_{34})Re(CO)$_4$][OTf] and impurities in CH_2Cl_2.

A variety of purification methods were attempted to try and remove this impurity including recrystallisations, silica, alumina column chromatography, size exclusion chromatography, and heating the tricarbonyl compound at reflux in a variety of solvents and temperatures under an atmosphere of CO. The synthesis of the complex was also attempted using 4- [1H, 1H, 2H, 2H, 3H, 3H- perfluorotridecyl] -4'-methyl-2,2'-bipyridine as the ligand that only has the fluorinated chain on one side of the bpy. The same set of impurities were formed following

this synthetic approach and unfortunately the same problem was encountered and they could not be separated out.

Due to the persisting issues with purification of this complex, a change of methodology was applied and instead matrix isolation, by encapsulation of the complex in a polymer matrix, was next attempted. This has been reported in the literature with different complexes.[187–189] The first step was to dissolve the complex of interest, $[(dtbpy)Re(CO)_3(CO_2)][Al(OC(CF_3)_3)_4]$, in the minimum volume of CH_2Cl_2 and soaking a number of 100, 250 and 500 μm polyethylene discs in this solution over 72 h. FTIR spectra of these impregnated discs were then obtained to verify that the complex had permeated the discs and then compared with ATR-FTIR spectra of $[(dtbpy)Re(CO)_3(CO_2)][Al(OC(CF_3)_3)_4]$. The most similar disc spectrum to the ATR-FTIR was from one of the 100 μm discs and the FTIR and compared ATR-FTIR can be seen in Figure 4.18.

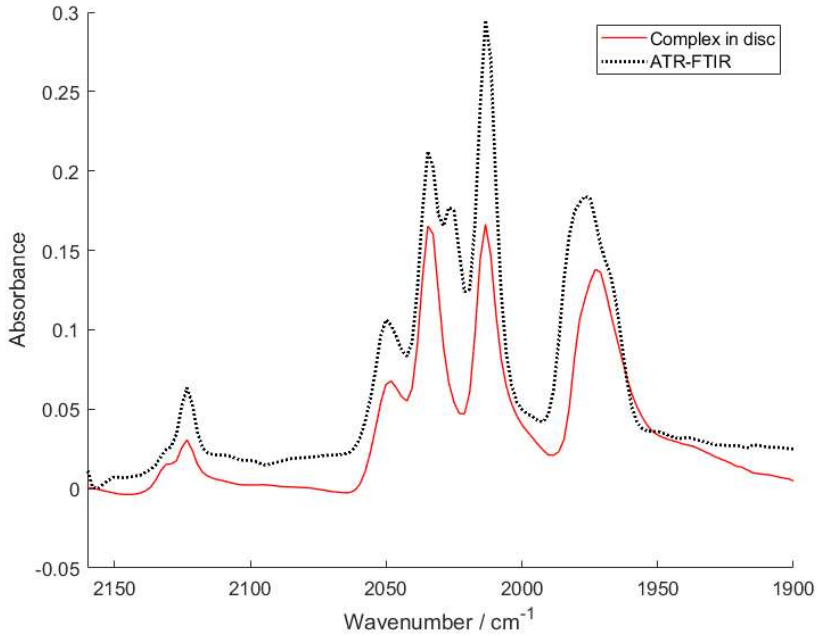

Figure 4.18: FTIR spectra of the carbonyl region for three polyethylene discs after being soaked in a ca. 50 mol dm^{-3} solution of $[(dtbpy)Re(CO)_4][Al(OC(CF_3)_3)_4)]$ in CH_2Cl_2 over 72 h, with a blank disc taken as a background. 100 μm (red), 250 μm (black) and 500 μm (blue).

In Figure 4.19 the FTIR difference spectrum from 1900 to 2280 cm^{-1} of the 100 μm disc containing $[(dtbpy)Re(CO)_4)][Al(OC(CF_3)_3)_4]$ after 35 min photolysis in

a 50 psi atmosphere of CO_2 at 260 K using 254 nm light can be seen. There is clear depletion of original parent bands and new peaks growing in at 2046, 1950 and 1933 cm^{-1} along with an additional peak at 2270 cm^{-1}. The calculated μ(C-O) vibrational frequencies for *fac*-[(dtbpy)Re$(CO)_3$)(CO_2)]$^+$ were 2070, 1983 and 1980 and for *mer*-[(dtbpy)Re$(CO)_3$)(CO_2)]$^+$ were 2092, 1999 and 1969. Neither of these sets of numbers align well with the experimentally observed peaks and as such more evidence needed to be obtained to untangle what was happening.

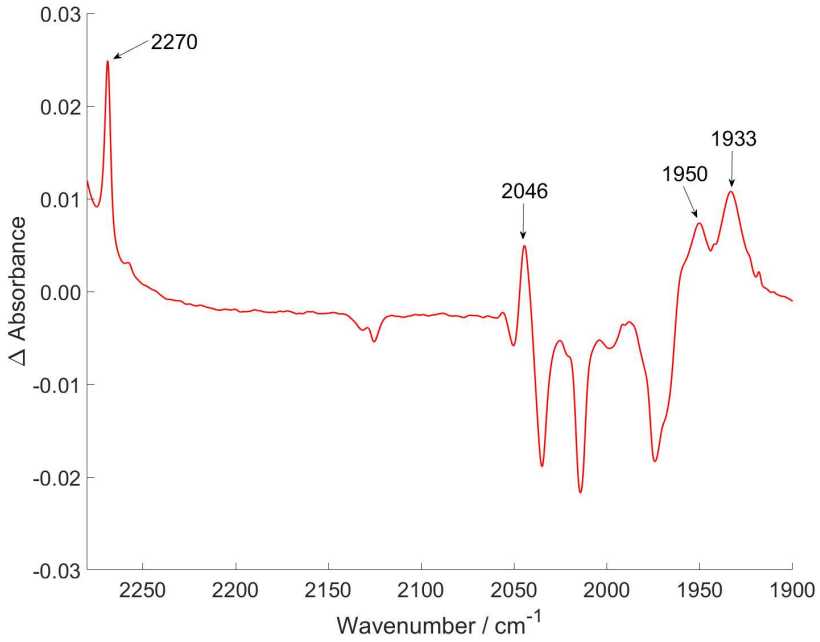

Figure 4.19: FTIR difference spectrum from 1900 to 2280 cm^{-1} of the 100 μm disc containing [(dtbpy)Re$(CO)_4$)][Al$(OC(CF_3)_3)_4$] after 35 min photolysis in a 50 psi atmosphere of CO_2 at 260 K using 254 nm light.

From the spectrum shown in Figure 4.20, it can be seen there is also some bleaching and growth of some CO_2 bands. There are three fundamental vibrations of CO_2 and these are; v_1 = 1337 cm^{-1} (symmetric stretch), v_2 = 667 cm^{-1} (doubly degenerate in and out of plane bending) and v_3 = 2349 cm^{-1} (antisymmetric stretch). Near-IR absorption of CO_2 between 3200 and 5600 cm^{-1} consists of two band systems, one of which is centred around 3650 cm^{-1}. This absorption is assigned to the v_1+v_3, $2v_2^0$+v_3 fermi dyad. This fermi resonance of two vibrational bands that have nearly the same energy and symmetry results in quantum

mechanical mixing and this mixing causes shifts in the energies and intensities of the absorption bands.[190] In this region, two bleaches and the growth of two peaks at 3681 and 3587 cm^{-1} can be seen. Each of the bleaches are split again due to rotational excitations, these are the R ($\Delta J = +1$) and P (ΔJ = -1) bands of the CO_2 showing rotational freedom. The two bands that are growing in are likely due to this same fermi dyad of CO_2. These peaks which have grown in do not display the rotational freedom that the bleaches do and as such would imply that the CO_2 has restricted rotation. This could realistically be for a few reasons, one being that the CO_2 has been rotationally locked inside of the polymer disc, or is interacting with potentially unsaturated polymer bonds. Another possibility is that the CO_2 is rotationally locked due to its coordination with the metal complex. If these bands are due to the latter reason this would mean that the CO_2 would still have its bending and symmetric vibrational modes available to it, even when coordinated.

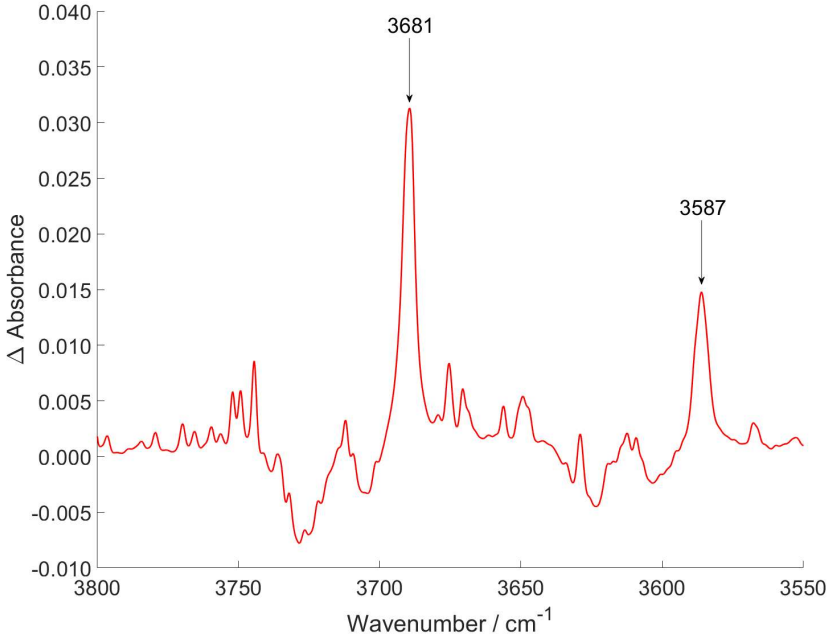

Figure 4.20: FTIR difference spectrum from 3550 to 3800 cm^{-1} of the 100 μm disc containing [(dtbpy)Re(CO)$_4$)][Al(OC(CF$_3$)$_3$)$_4$] after 35 min photolysis in a 50 psi atmosphere of CO_2 at 260 K using 254 nm light.

To try and distinguish between a metal-coordinated CO_2 molecule and CO_2

interacting with the polymer disc a very similar photolysis experiment was performed, but this time the disc did not contain any complex. The resulting difference spectra from this can be seen in Figures 4.21 and 4.22. The peak at 2270 cm^{-1} still grew in and there was the same pattern shown between 4000 to 3450 cm^{-1} showing the rotational restriction of some CO_2 molecules. The absorbance of the peaks in this experiment were also higher, which agrees with it being CO_2 locked into the disc given that this disc will have more space to fit CO_2 in without the complex.

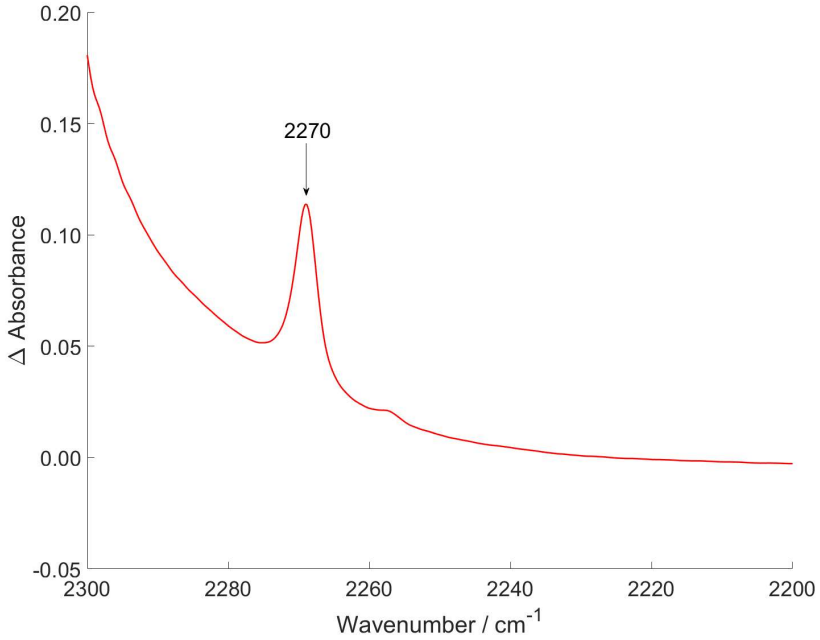

Figure 4.21: FTIR difference spectrum from 2200 to 2300 cm^{-1} of a blank the 100 μm disc after 30 min photolysis in a 65 psi atmosphere of CO_2 at 260 K using 254 nm light.

The final experiment performed using $[(dtbpy)Re(CO)_3(CO_2)][Al(OC(CF_3)_3)_4]$ in a polymer disc was a photolysis under an atmosphere of N_2 using 254 nm light. This is a stronger binding ligand than CO_2 and as such could give more input as to how strongly the polymer disc was potentially interacting with the complex, if at all. The difference spectrum of this photolysis experiment can be seen in Figure 4.23. The bleaching of the same parent bands could be seen but some of the bands that grew in were at different wavenumbers. There were

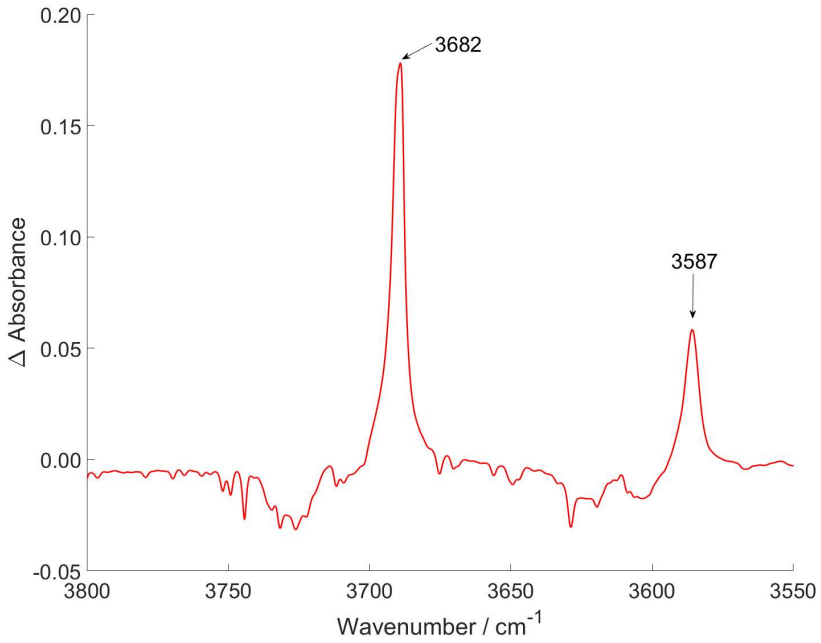

Figure 4.22: FTIR difference spectrum from 3550 to 3800 cm^{-1} of a blank the 100 μm disc after 30 min photolysis in a 65 psi atmosphere of CO_2 at 260 K using 254 nm light.

still peaks at 1950, 1933 and 2046 cm^{-1}, the same as when performed in CO_2 but there was also two additional peaks, one at at 1960 cm^{-1} and the other at 2056 cm^{-1}. The peak at 2270 cm^{-1} was not present in this N_2 experiment confirming that this peak was due to CO_2. Based on previous work along with other unpublished experimental work in the group with N_2 complexes and DFT calculations a coordinated N_2 FTIR band usually falls between 2220 to 2100 cm^{-1} and no such band could be seen.[191] The presence of the same three peaks in both the N_2 and CO_2 experiments suggests that there is a common species forming in both of these experiments. This species is likely a tricarbonyl species that has undergone 'CO loss' and the now vacant site is reacting with the polymer disc, likely at some of the unsaturated sites where a C=C bond could still be present. The presence of additional bands in this N_2 experiment does also suggest the formation of a new species, which could take the form $[(dtbpy)Re(CO)_3(N_2)][Al(OC(CF_3)_3)_4]$ but was potentially not formed in great enough quantity to be able to detect the N-N vibration by FTIR but the intense

carbonyl vibrations still could be observed.

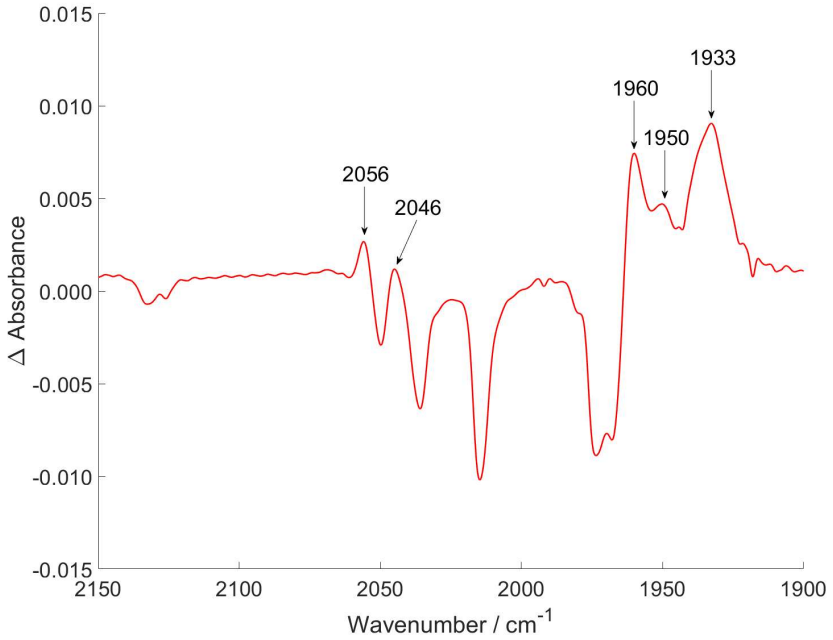

Figure 4.23: FTIR difference spectrum from 1900 to 2150 cm^{-1} of the 100 μm disc containing $[(dtbpy)Re(CO)_4)][Al(OC(CF_3)_3)_4]$ after 35 min photolysis in a 50 psi atmosphere of N_2 at 260 K using 254 nm light.

A further experiment was performed where a similar THF photolysis on the cationic system as was performed for the neutral system earlier in this Chapter. To do the same for this cationic system the $[OTf]^-$ anion needed to be changed to a weakly coordinating anion such as $[PF_6]^-$. $[(bpy)Re(CO)_4][PF_6]$ is a good candidate for this photolysis, although not soluble in CO_2 itself, if $[(dnb\text{-}F_{34})Re(CO)_4][Al(OC(CF_3)_3)_4]$ can be isolated and purified and ends up being soluble in CO_2 then this could provide valuable information.

$[(bpy)Re(CO)_4][PF_6]$ was photolysed with 254 nm light in THF and the difference spectra can be seen in Figure 4.24. The bleaching of the original compound peaks at 2120, 2024, 2001 and 1961 cm^{-1} can be seen as a very clear peak growth at 1920 cm^{-1}. There also looks like there is some peak growth being suppressed by the bleach around 2030 cm^{-1} and another small peak growing in at 1828 cm^{-1}. The peak being suppressed at 2030 cm^{-1} can be seen in Figure 4.25. The peak pattern of a narrower peak at 2030 cm^{-1} and a broader peak around 1920 cm^{-1}

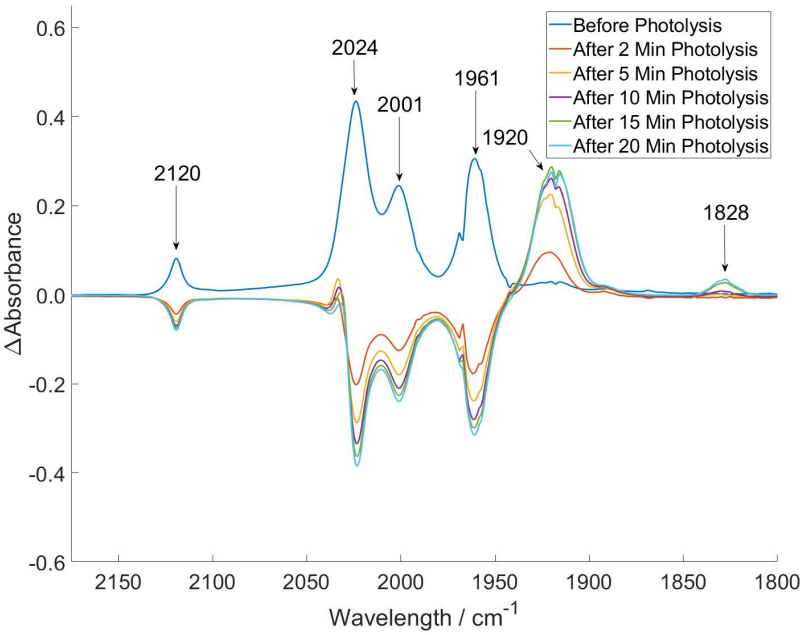

Figure 4.24: FTIR difference spectra in the carbonyl region showing the change in absorbance of the peaks at different intervals during photolysis of $[(bpy)Re(CO)_4][PF_6]$ in THF using 254 nm light.

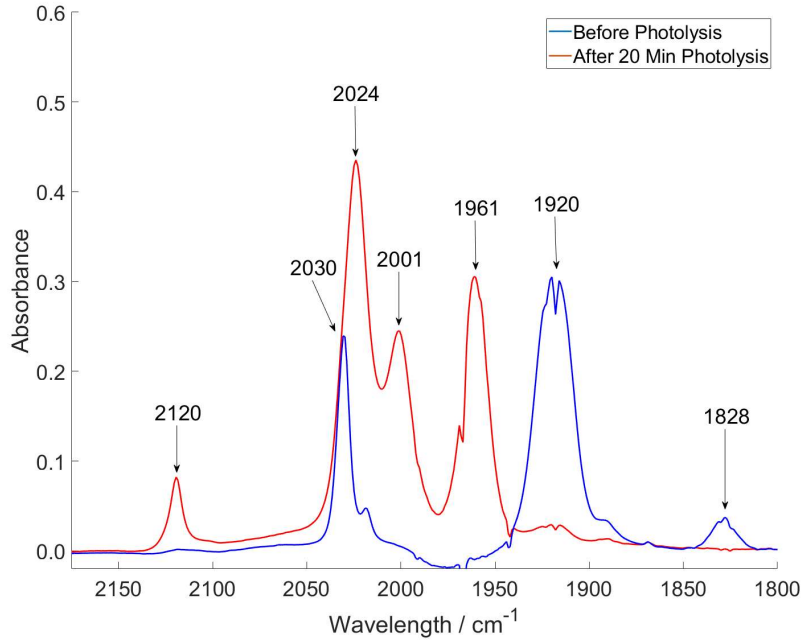

Figure 4.25: FTIR spectra from 1800 to 2175 cm^{-1} showing $[(bpy)Re(CO)_4][PF_6]$ before (red) and after 20 mins (blue) of photolysis in THF using 254 nm light.

is very similar to a tricarbonyl species for this system. The calculated ν(C-O) vibrational frequencies for $[(bpy)Re(CO)_3(CO_2)]^+$ are 2074, 1989 and 1986 cm^{-1}, which are similar distances apart as the experimentally observed peaks, but are

at a bit too high wavenumber. In the introduction it was discussed how using the harmonic approximation often leads to overestimation of vibrational frequencies. If we apply an anharmonic correction in the form of a scale factor of 0.975 the new calculated vibrational frequencies are found to be 2022, 1939 and 1936 cm^{-1} which is a much closer match. The peak at 1828 cm^{-1} is at the same wavenumber as a peak previously mentioned in this Thesis, noted by Sato *et al.*, which was assigned to the unsymmetrical CO vibrational band of the bis-carbonyl-rhenium complex [(bpy)Re$(CO)_2$Cl(THF)]. The presence of this peak in this experiment could indicate the formation of a neutral photoproduct with similar electronic properties to that of [(bpy)Re$(CO)_2$Cl(THF)].

4.2.4 Organometallic Complexes in Ionic Liquids

While undertaking the work in this Chapter, it was discovered that many of the complexes synthesised in this Chapter were soluble in trihexyltetradecylphosphonium chloride, an ionic liquid. It was also discovered that this ionic liquid could be mixed with non-polar media such as alkane solvents and then the metal complexes dissolved in this new solution although trihexyltetradecylphosphonium chloride is not miscible with PFMCH or PFTEA.

The improvement in solubility of [(bpy)Re$(CO)_3$Cl] in cyclohexane by presence of trihexyltetradecylphosphonium chloride can be seen in Figure 4.26 where [(bpy)Re$(CO)_3$Cl] is not observable by FTIR in pure cyclohexane. This also works for cationic complexes, which were previously insoluble in cyclohexane such as [(HEB)Re$(CO)_3$][PF_6].

Two other ionic liquids were also synthesised using the method shown in Scheme 4.8 from Licence *et al.*.[192] These were trihexyltetradecylphosphonium tetrafluoroborate and trihexyltetradecylphosphonium hexafluorophosphate, which were both formed by very similar methods. The original trihexyltetradecylphosphonium chloride is added to water and then a salt containing the desired anion, such as $NaBF_4$ or NH_4BF_4, is dissolved in water and then slowly added to

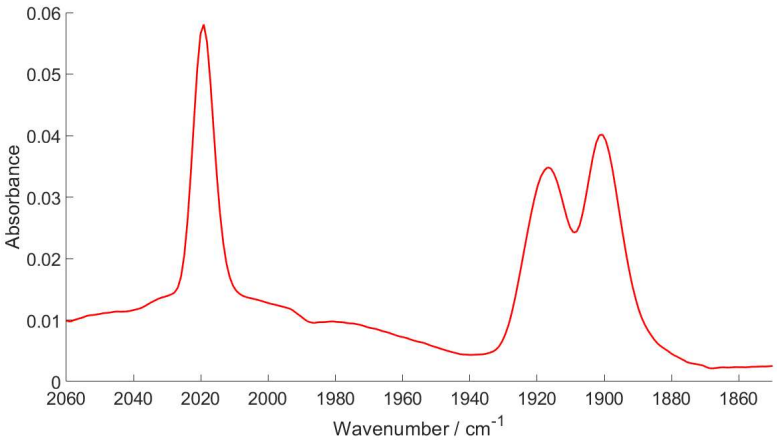

Figure 4.26: FTIR spectra of the carbonyl region of [(bpy)Re(CO)$_3$Cl] dissolved in a cyclohexane + trihexyltetradecylphosphonium chloride mixture.

the solution at 0 °C. The desired product is then extracted into ether and dried under a 5×10^{-5} mbar vacuum down to 50 ppm water remaining in the ionic liquid. Previous work has shown that the changing of the anion can dramatically alter an ionic liquids properties. For ionic liquids with 1,3-dialkylimidazolium cations, with a hexafluorophosphate anion the liquid is hydrophobic, but with a tetrafluoroborate anion the liquid is hydrophilic.[193]

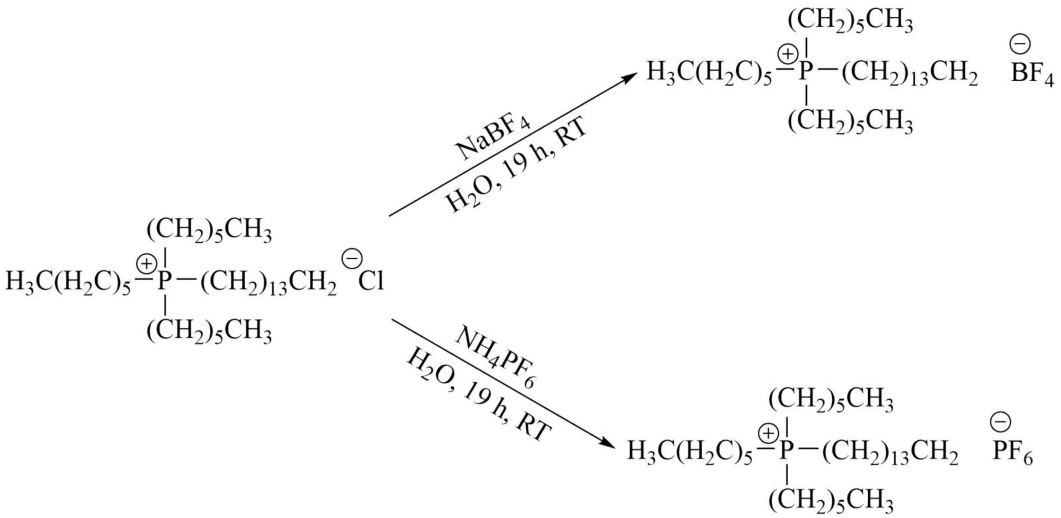

Scheme 4.8: Reaction scheme for the synthesis of trihexyltetradecylphosphonium tetrafluoroborate (top) and trihexyltetradecylphosphonium hexafluorophosphate (bottom) from trihexyltetradecylphosphonium chloride.[192]

These two newly synthesised compounds both had different properties at room temperature. Trihexyltetradecylphosphonium hexafluorophosphate is a solid at

room temperature whereas trihexyltetradecylphosphonium tetrafluoroborate is a liquid. None of the complexes tested, which were soluble in trihexyltetradecylphosphonium chloride, both neutral and cationic, were found to be soluble in the newly synthesised trihexyltetradecylphosphonium tetrafluoroborate. The trihexyltetradecylphosphonium hexafluorophosphate could be melted at a low temperature of 40 °C, but unfortunately still none of the complexes were soluble in this liquid either. Due to the increased fluorous nature of these new ionic liquds their miscibility with the previously mentioned fluorinated solvents, PFMCH and PFTEA were tested. Neither of these new ionic liquids were soluble with PFMCH or PFTEA at either room temperature or at 40 °C.

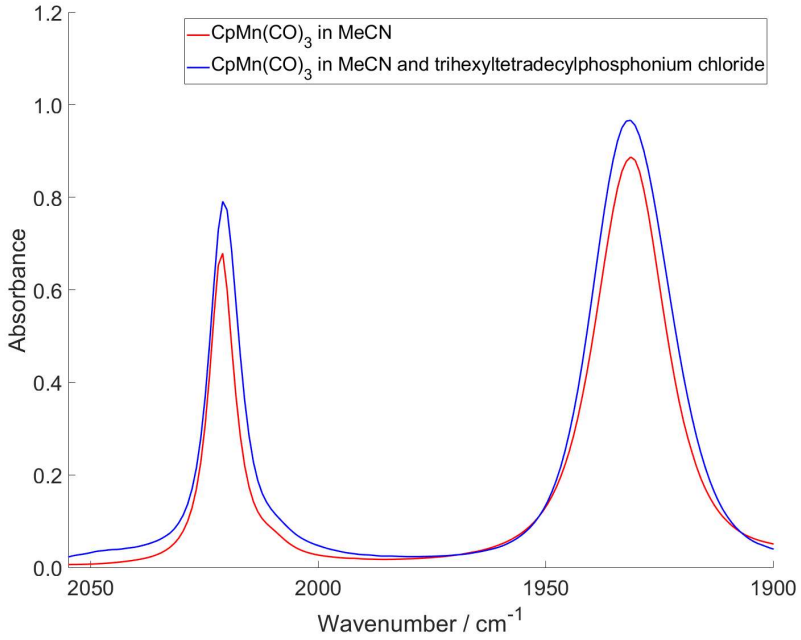

Figure 4.27: FTIR spectra of the carbonyl region of $CpMn(CO)_3$ dissolved in neat acetonitrile (red) and an acetonitrile + trihexyltetradecylphosphonium chloride mixture (blue).

The FTIR spectra of the complexes dissolved in trihexyltetradecylphosphonium chloride + solvent mixtures can look quite different depending on the solvent involved. In Figure 4.27 the FTIR spectra of $CpMn(CO)_3$ dissolved in both neat acetonitrile and an acetonitrile + trihexyltetradecylphosphonium chloride mixture can be seen. These spectra look very similar with close to identical

wavenumber peaks and very similar peak shapes. In Figure 4.28 the FTIR spectra of $CpMn(CO)_3$ dissolved in both neat cyclohexane and a cyclohexane + trihexyltetradecylphosphonium chloride mixture can be seen. Comparing these spectra, in Figure 4.27, it appears as if the $CpMn(CO)_3$ is entirely dissolved in the MeCN part of the solvent mixture whereas in Figure 4.28 the $CpMn(CO)_3$ is dissolved in both the cyclohexane and trihexyltetradecylphosphonium chloride.

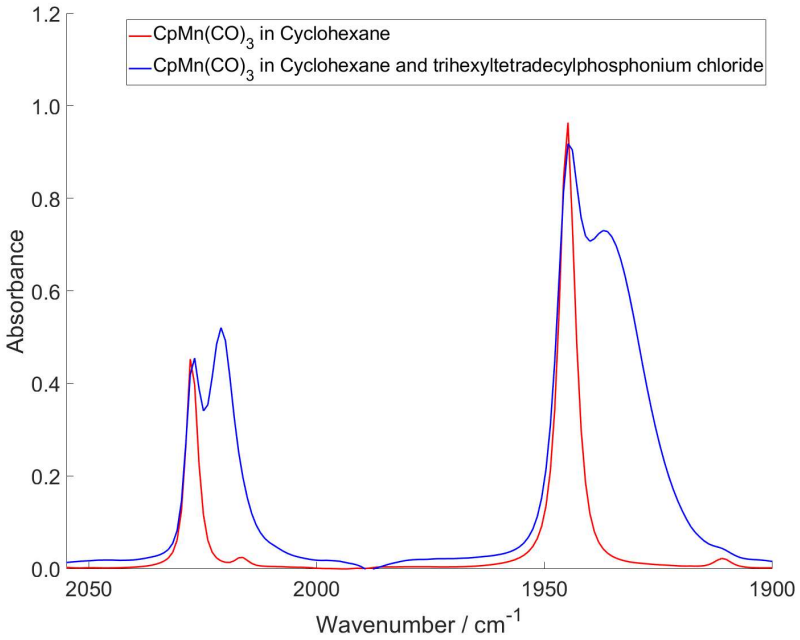

Figure 4.28: FTIR spectra of the carbonyl region of $CpMn(CO)_3$ dissolved in neat cyclohexane (red) and a cyclohexane + trihexyltetradecylphosphonium chloride mixture (blue).

In Figure 4.29 the formation of $CpMn(CO)_2(NCCH_3)$ by photolysis of $CpMn(CO)_3$ in neat acetonitrile can be seen by the growth of the peak at 1860 cm^{-1}. The other peak of $CpMn(CO)_2(NCCH_3)$ overlaps with the 1930 cm^{-1} peak of $CpMn(CO)_3$. After 30 min of photolysis most of the original $CpMn(CO)_3$ is converted and the $CpMn(CO)_2(NCCH_3)$ photoproduct is long-lived. In Figure 4.30 the same 1860 cm^{-1} peak can be seen, but at a much lower intensity but also in this experiment, the $CpMn(CO)_2(NCCH_3)$ is only found at the 5 min spectra and not in 30 min spectra. This suggests the presence of trihexyltetradecylphosphonium chloride either causes a further reaction, as there is no regeneration of

parent peaks so something new must be forming. Some potential ideas are that the trihexyltetradecylphosphonium chloride directly reacts with the photolysed $CpMn(CO)_2(NCCH_3)$ to form a Cl-bound anionic species with a corresponding trihexyltetradecylphosphonium counter cation or the high water content in the ionic liquid reacts with the $CpMn(CO)_2(NCCH_3)$ forming water-bound species.

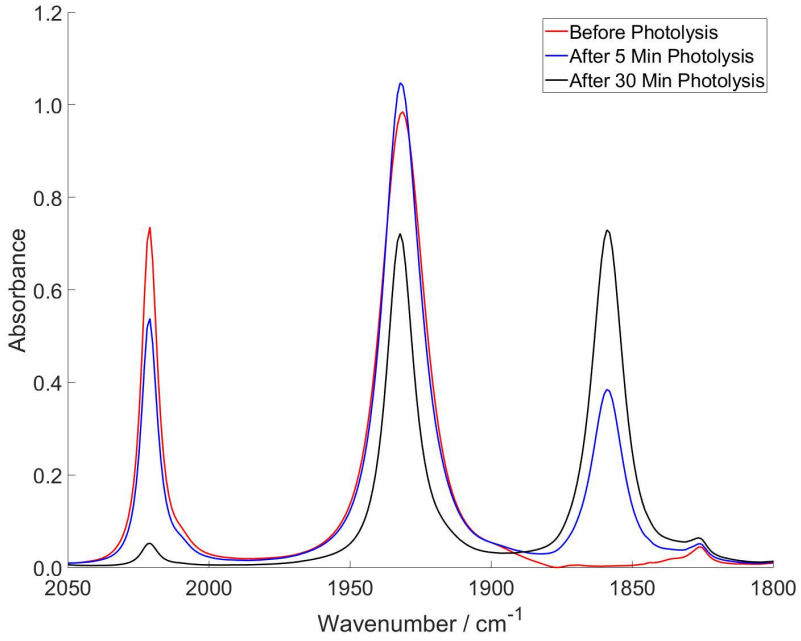

Figure 4.29: FTIR spectra of the carbonyl region showing the different peaks present during the photolysis of $CpMn(CO)_3$ in neat acetonitrile before photolysis (red), after 5 min (blue) and after 30 min (black) using 254 nm light.

In the spectra shown in Figure 4.31 there is clear depletion of the parent $CpMn(CO)_3$ peaks and no growth of any other peaks. This is due to the very short lifetime of $CpMn(CO)_2(C_6H_{12})$, which is not stable at room temperature on a timescale where FTIR spectra can be obtained using conventional lab techniques. In Figure 4.32 there is depletion of parent bands, with bands from the complex in cyclohexane and trihexyltetradecylphosphonium chloride depleting at the same rate. This time there is growth of new peaks, which are seen in the spectra taken at 1 min and at 5 min, but not in the 30 min spectrum. This again suggests that the presence of the ionic liquid in the solution is changing the reaction occuring with again potential formation of an anionic Cl bound species or a water bound

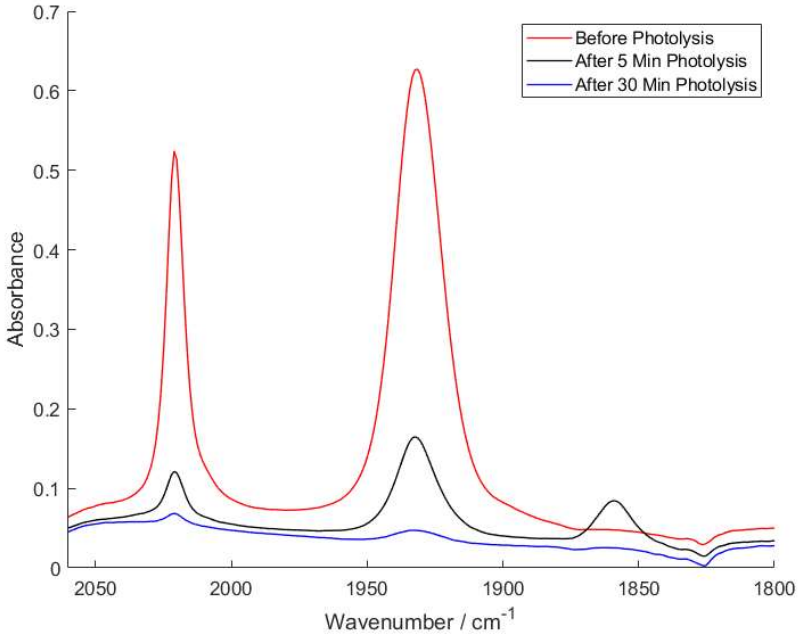

Figure 4.30: FTIR spectra of the carbonyl region showing the different peaks present during the photolysis of $CpMn(CO)_3$ in a mixture of acetonitrile and trihexyltetradecylphosphonium chloride before photolysis (red), after 5 min (blue) and after 30 min (black) using 254 nm light.

species.

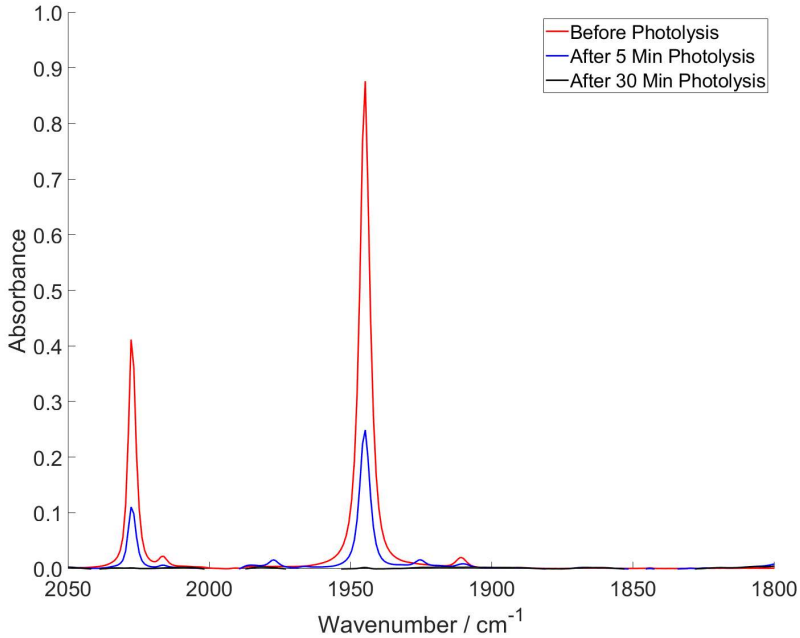

Figure 4.31: FTIR spectra of the carbonyl region showing the different peaks present during the photolysis of $CpMn(CO)_3$ in neat cyclohexane before photolysis (red), after 5 min (blue) and after 30 min (black) using 254 nm light.

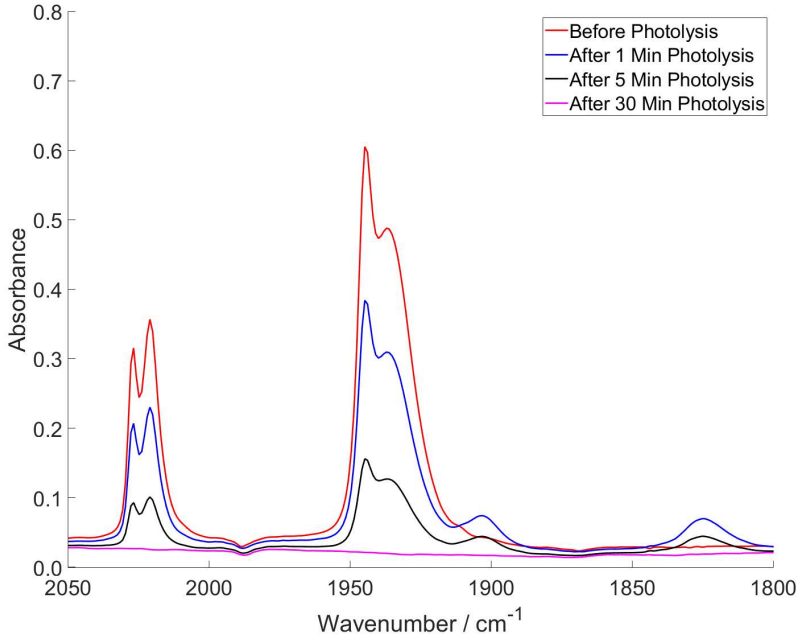

Figure 4.32: FTIR spectra of the carbonyl region showing the different peaks present during the photolysis of $CpMn(CO)_3$ in a mixture of cyclohexane and trihexyltetradecylphosphonium chloride before photolysis (red), after 1 min (blue) and after 5 min (black) and after 30 min (magenta) using 254 nm light.

These above experiments clearly show that the presence of the trihexyltetradecylphosphonium chloride ionic liquid alters the photoproducts obtained from photolysis experiments of $CpMn(CO)_3$. If ionic liquids were to be a viable idea for use in helping to dissolve compounds into non-polar, non-coordinating solvents they should be as unintrusive as possible to the chemistry being probed. This effect of ionic liquids altering observed photochemistry opens the door for future work where ionic liquids could potentially be added into current photochemical systems with potential use to help alter or tune photochemical pathways.

4.3 Conclusions and Future Perspectives

Two different routes to synthesise cationic pianostool complexes were tested and a cationic manganese pianostool complex was synthesised. The direct rhenium analogue of this complex could not be isolated in air due to nucelophillic attack on the larger rhenium atom. Bulkier arenes were used to synthesise a small library

of cationic rhenium pianostool complexes. A highly fluorous non-coordinating bulky anion, to aid with complex solubility in CO_2, was synthesised and anion exchanges were attempted. The anion exchange for all but one of the complexes failed, for $[(HEB)Re(CO)_3]^+$ the exchange was successful, but impurities were also formed.

A series of neutral rhenium α-diimine complexes were synthesised by using the same synthetic route, where the *fac-* isomer was exclusively formed due to the *cis* effect but these were insoluble in CO_2. To address this a range of fluorinated bpy ligands were synthesised, dfbpy, dnb-F_{34} and 4- [1H, 1H, 2H, 2H, 3H, 3H- perfluorotridecyl] -4'-methyl-2,2'-bipyridine. Different purification techniques were tested to try and improve on the current method for dnb-F_{34}, but no suitable alternative was found, but a way to obtain one of the potentially useful side products was achieved by column chromatography. The highly fluorinated bpy ligand was reacted with $Re(CO)_5Cl$ and $[(dnb\text{-}F_{34})Re(CO)_3Cl]$ was successfully isolated. $[(dnb\text{-}F_{34})Re(CO)_3Cl]$ was dissolved in liquid CO_2, which showed that the addition of the large fluorinated chains onto the bpy ligand does improve the solubility in CO_2. The solubility was still too low to conduct repeatable low temperature photolysis experiments. $[(dnb\text{-}F_{34})Re(CO)_3Cl]$ was photolysed in THF for a long time, but it took around 6 h for there to be any amount of noticeable change. This is believed to be due to a concentration effect where the concentration was too high causing the fluorinated chains to aggregate in solution which previous unpublished work in the group has shown can change the photophysics of these compounds.[194]

A series of cationic rhenium α-diimine complexes were synthesised by using the similar synthetic routes. The anion exchanges were attempted with these rhenium α-diimine complexes and all were successful aside from $[(dfbpy)Re(CO)_4]^+$ where impurities were also formed. After the anion exchanges these complexes were still not soluble in CO_2 so the previously synthesised highly fluorinated ligand, dnb-F_{34}, was used to try and synthesise the corresponding α-diimine com-

plex. This product was formed along with impurities, that could not be removed despite attempting a variety of techniques. A matrix isolation experiment was performed on $[(dtbpy)Re(CO)_4][Al(OC(CF_3)_3)_4]$ in a polyethylene disc since the complex was not soluble in CO_2. The complex was successfully inserted inside of the polymer matrix by soaking in CH_2Cl_2 for 72 h and the FTIR spectrum compared to an ATR-FTIR spectrum to confirm no reaction had occured between the matrix and the complex. Upon photolysis under an atmosphere of CO_2 there was growth of new carbonyl bands and an additional band at 2270 cm^{-1}. There was also growth of some new rotationally locked bands from CO_2 implying that the CO_2 had become rotationally restricted. Unfortunately, when the experiment was repeated on a blank disc, these bands showing rotational restriction of CO_2 appeared again along with the additional band at 2270 cm^{-1} suggesting the CO_2 was interacting with the disc and not the complex. A photolysis was performed with the complex in another disc under an atmosphere of N_2 and a similar set of carbonyl bands grew in, but there was no coordinated N_2 stretching frequency observed. A photolysis experiment on $[(dmbpy)Re(CO)_4][PF_6]$ was performed in THF and there was a clear bleach of parent bands and growth of two new bands. It was observed that the photostability of this cationic complex was significantly lower than that of its neutral analogue.

Some preliminary work involving using an ionic liquid, trihexyltetradecylphosphonium chloride, as a cosolvent for improving solubility in non-polar solvents was conducted. It was found to be miscible with alkane solvents, but not perfluorinated alkanes, and improved the solubility of both neutral and cationic compounds in alkanes. Two more ionic liquids were synthesised, trihexyltetradecylphosphonium hexafluorophosphate and trihexyltetradecylphosphonium tetrafluoroborate, but neither of these made for suitable solvents for dissolving the tested organometallic complexes. Photolysis experiments were performed on $CpMn(CO)_3$ in both neat solvents and solvent and ionic liquid mixtures and in the mixtures the presence of the ionic liquid was found to change the resulting

photochemistry of $CpMn(CO)_3$.

For the pianostool complexes a potential future experiment could be attempting the anion exchange on $[(HEB)Re(CO)_3][PF_6]$ again with a larger variety of conditions to see if the reaction can be performed without forming any impurity, even if it comes at a large cost to the overall yield. Use of a larger arene may be used in a future experiment to test if this makes the anion exchange reaction more reliable, and if functionalised with large electron withdrawing groups this could also potentially optimise the complex for a stronger M-CO_2 bond. If the solubility needs to be improved further then the large fluorinated chains, used in the bpy experiments, could be attached to the pianostool arene to increase the fluorous content, though this may risk intramolecular reactions when the complex undergoes CO loss.

For the neutral α-diimine complexes a future experiment could be trying to further improve the solubility of the complex in CO_2 by further modification of the bpy ligand which may improve the absorbance in the FTIR spectrum. Potentially a branched fluorinated chain instead of a straight carbon chain could also be used to further increase fluorous content.

For the cationic α-diimine complexes a new synthetic route may need to be tried to achieve a pure, highly fluorinated, cationic complex. If the halogen were removed from the previously purified $[(dnb\text{-}F_{34})Re(CO)_3Br]$. then the resulting complex heated in a highly coordinating solvent such as MeCN. a likely product would be $[(dnb\text{-}F_{34})Re(CO)_3(MeCN)][OTf]$. This may be an easier route to a pure cationic complex, but whether the photophysics of this complex would more closely resemble the current tricarbonyl or tetracarbonyl complexes is not known. The anion exchange could then also be attempted to further increase fluorous content and remove the highly coordinating OTf anion. Matrix experiments could also potentially be performed again but a much less reactive polymer matrix must be found in order to minimise the interaction between the metal complex and the matrix.

For the work with ionic liquids a good future next step may be to try and synthesise an ionic liquid which should be less coordinativley competitive while also still being a good cosolvent to aid in complex solubility in alkanes. This may reduce the effect that the presence of the ionic liquid has on the photochemistry of the molecule and could potentially allow for doping of weakly binding ligands such as CO_2 or Xe to also be used in neat ionic liquids.

Very recently Ball *et al.* report an example of a long lived methane complex formed by directly binding methane as a ligand to a reactive organometallic complex.[195] Photo-ejection of carbon monoxide from a cationic osmium-carbonyl complex dissolved in an inert hydrofluorocarbon solvent saturated with methane at 90 °C gives $[\eta^5\text{-CpOs(CO)}_2(CH_4)]^+$. This work could also be used as a baseline for some future experiments where solubility could be tested in CO_2 or CO_2 could be doped into hydrofluorocarbon solvents.

Chapter 5

Summary, Implications and Future Outlook

This Chapter will summarise the findings that are reported within this Thesis and will outline the implications of the work that have originated from the research. Furthermore, the future direction of the work and potential areas for investigation have been discussed.

5.1 Summary of Work Completed

In Chapter 2 a photochemical and photophysical study of $Co(CO)_3(NO)$ was conducted by using high and low concentration TRIR experiments on both the nanosecond and picosecond timescale utilising both 400/355 and 266 nm excitation. The results obtained were compared and contrasted to previous work performed by Harris who conducted a ps-TRIR experiment on $Co(CO)_3(NO)$ following 400 nm excitation.[1] There were both similarities and differences when comparing our results with those of Harris *et al.* The triplet states of $Co(CO)_3(NO)$ observed by Harris *et al.* were not observed in our experiments but the S1 state of $Co(CO)_3(NO)$ was observed along with $^3Co(CO)_2(NO)$, $Co(CO)_2(NO)$(*n*-heptane) and $Co(CO)_3$. All of the species observed in both our experiments, and those performed by Harris *et al.*, displayed different vastly kinetics. One of the

contributing factors to this is due to a large concentration difference between the experiments performed by ourselves and Harris. The results of our high concentration experiments allowed for many more species to be observed compared with our low concentration experiments with also much faster decays and kinetics found in the high concentration experiments. DFT calculations were performed to try and make suggestions of the identities of a number of the observed unassigned species such as $(CO)_2(NO)Co(\mu\text{-}CO)Co(CO)_2(NO)$.

The work in Chapters 3 and 4 focussed on the optimisation of properties of group 7 compounds in an effort to work towards isolating long-lived η^1-OCO coordinated organometallic complexes.

In Chapter 3 a computational study was performed that focussed on the optimisation of properties for maximising the strength of the end-on M-η^1-OCO bond. Some of the main findings were that rhenium was better than manganese for maximising the end-on M-η^1-OCO bond strength. The introduction of electron withdrawing groups onto either the arene in a pianostool complex, or the bpy in a α-diimine complex, where the tested groups were -CF_3 and -$C(CF_3)_3$, also increased the end-on M-η^1-OCO bond strength. This increase based on functionalisation of ligands is limited in its ability to influence bond strength by both how close the groups are to metal and also the number of functionalised groups attached to the ligand. Another primary finding was the large jump (around 20 kJ mol $^{-1}$) in end-on M-η^1-OCO bond strength when going from a neutral to a cationic complex due to the significantly better overlap between the LUMO of the metal and the HOMO of the CO_2.

Chapter 4 primarily focussed on the synthesis and spectroscopic measurements of both manganese and rhenium cationic pianostools with modified arenes, along with neutral and cationic α-diimine complexes with modified bpy ligands. It was found that for the cationic pianostool complexes, the larger the steric bulk of the coordinated arene, where the smallest tested arene was benzene and the largest was HEB, the more stable the complex is to both arene displacement

and nucleophillic attack. None of the complexes initially synthesised were soluble in CO_2, alkanes or perfluorinated solvents and so modifications were made in order to improve solubility. The synthesis and purification is reported of a highly fluorinated bpy ligand, dnb-F_{34}, containing carbon spacers to limit the effect on the electronic properties of the complex. It was shown that the addition of these large fluorinated groups onto the bpy ligand was sufficient to solubilise [(dnb-F_{34})Re(CO)$_3$Cl] in liquid CO_2, where [(bpy)Re(CO)$_3$Cl] was previously insoluble. The solubility needs to be further improved to allow for future reaction monitoring in solution by FTIR in CO_2. [(dnb-F_{34})Re(CO)$_3$Cl] was photolysed in THF, but showed remarkable photostability, which was attributed to an aggregation of fluorinated chains in solution inhibiting CO loss.

The cationic α-diimine complexes, [(bpy)Re(CO)$_4$][OTf], [(dmbpy)Re(CO)$_4$][OTf] and [(dtbpy)Re(CO)$_4$][OTf] appeared to be more stable in the $[Al(OC(C(CF_3)_3)_4]^-$ anion exchange reaction than the pianostool complexes, [(Mes)Re(CO)$_3$][PF_6] and [(HMB)Re(CO)$_3$][PF_6]. [(HEB)Re(CO)$_3$][PF_6] and [(dfbpy)Re(CO)$_4$][OTf] were also used in anion exchange reactions, where based on MS, reactions were a success. In both cases though, significant amounts of impurity were formed, meaning no single pure product could be isolated. The solubilities of [(bpy)Re(CO)$_4$][Al(OC(C(CF_3)$_3$)$_4$], [(dmbpy)Re(CO)$_4$][Al(OC(C(CF_3)$_3$)$_4$] and [(dtbpy)Re(CO)$_4$][Al(OC(C(CF_3)$_3$)$_4$] were all tested in CO_2, alkanes and perfluorinated solvents but all were not sufficiently soluble to be observable by FTIR. When trying to synthesise [(dnb-F_{34})Re(CO)$_4$][Al(OC(C(CF_3)$_3$)$_4$], there were purification difficulties that hindered progress significantly. A matrix isolation experiment utilising [(dtbpy)Re(CO)$_4$][Al(OC(CF_3)$_3$)$_4$] in a polyethylene disc was conducted, but it appeared that the polymer matrix was likely reacting with the complex and the CO_2 molecules were also interacting with the polymer matrix.

Brief work with ionic liquids was performed involving testing the solubilities of [(bpy)Re(CO)$_3$Cl] in trihexyltetradecylphosphonium chloride, trihexyl-

tetradecylphosphonium hexafluorophosphate and trihexyltetradecylphosphonium tetrafluoroborate and was only successfully dissolved in trihexyltetradecylphosphonium chloride. It was then further found that trihexyltetradecylphosphonium chloride is miscible with alkane solvents, but not perfluorinated alkanes, and improved the solubility of both neutral and cationic compounds in alkanes. Photolysis experiments were performed on $CpMn(CO)_3$ in both neat hexane and MeCN and compared with photolysis experiments on $CpMn(CO)_3$ in mixtures of ionic liquid and hexane or MeCN. It was found that the presence of the ionic liquid changed the resulting photochemistry of $CpMn(CO)_3$ where $CpMn(CO)_2(MeCN)$ was slower to form in the presence of ionic liquid and the decay of $CpMn(CO)_3$ in hexane was slower in the presence of ionic liquid.

5.2 Implications and Future Work

Chapter 2 teaches us that the photophysics and photochemistry of $Co(CO)_3(NO)$ is far more complex than it appeared on initial inspection and there is a clear need for much more work in this area to fully understand this complex. It is clear that both CO loss and NO loss pathways are induced upon photolysis, but the ratio of which ligand dissociation occurs is unknown. There is also a clear concentration element to consider in all future experiments. The concentration of future experiments may also be varied to help untangle complex reaction dynamics along with variations in laser strength, excitation wavelength, solvents and temperature.

From Chapter 3 a few conclusions can be drawn, which if taken into account in future research in this area, should help to increase the lifetime of any complexes formed. The use of rhenium over manganese should be noted, to maximise the strength of the end-on M-η^1-OCO bond. Cationic complexes should also ideally be used as the decreased CO_2 HOMO, metal LUMO energy gap for the cationic systems also helps to maximise the strength of the end-on M-η^1-OCO bond. Future work should also consider the use of electron withdrawing groups, such as

CF_3, which should help increase the end-on M-η^1-OCO bond strength, which if can be done with large numbers of fluorine atoms, may also aid in solubility.

The results observed in Chapter 4 demonstrate the known ability of fluorinated carbon chains to improve the solubility of organometallic complexes in CO_2. This could help with work towards isolation of long-lived η^1-OCO complexes and also alkane and Xe complexes through doping. With further modifications to the bpy ligand or a pianostool arene, to allow for a further increase in fluorous content, a new area of research could be opened. This area may help the goal of synthesising a long-lived cationic η^1-OCO complex be more readily attainable, which could be analysed using standard spectroscopic techniques. An issue that could potentially arise is the inhibition of CO loss due to presence of the fluorinated chains, but the increase in lability of the CO ligand when comparing the cationic tetracarbonyl compounds with neutral tricarbonyl compounds may solve this issue.

Chapter 6

Experimental

6.1 Chapter 2 - Time Resolved Infra-Red Spectroscopy

6.1.1 Nottingham Ultrafast TRIR apparatus

All of the ultrafast TRIR experiments reported in this Thesis from Chapter 4 were performed using the Nottingham ultrafast TRIR apparatus and in collaboration with Drs. Xue-Zhong Sun and Surajit Kayal. This experimental set-up is discussed in detailed in the literature, so only a brief introduction is given in this section.[20]

In the Nottingham ultrafast TRIR apparatus, 800 nm laser pulses (2.3 mJ, 1 kHz, 140 fs) are produced with the combination of a Ti:sapphire oscillator (MaiTai, Spectra Physics) and a regenerative amplifier system (Spitfire Pro, Spectra Physics). These pulses are then split into two beams. One beam, which is the 'pump', produces a pulse with tunable wavelength (266 or 400 nm in this Thesis) by harmonic generation (TimePlate Tripler, 6-3, Minioptic Technology inc.). The other beam is used to pump a TOPAS-C optical parametric amplifier (Light Conversion), which is followed by a difference frequency generator that can produce tuneable mid-IR pulses (180 cm^{-1} fwhm and approx 2μJ at 2000 cm^{-1}).

By using a Ge beam splitter, these mid-IR pulses are split into two halves: one going to a single-element MCT detector (Kolmar Technology) to be recorded as a reference; the other half is used as the 'probe' and passes through the sample directly. In order to investigate photoinduced transient species at a specific time delay, the pump beam can be optically delayed on a translation state (LMA Actuator, Aerotech) that allows for time delays up to approx 2 ns. Afterwards, a small amount of the transmitted IR probe that passes through the sample is dispersed by a 250 mm IR monochromator (DK240, Spectra Products) with 150 L/mm gratings (giving approx 4 cm^{-1} resolution) onto a two linear 128 MCT detector array (Infrared Associates). The signals were amplified with a 144-channel amplifier (Infrared Associates Inc.) and converted by a 16-bit analog-to-digital converter (IR0144, Infrared Systems Development Corp.).

For the ns-TRIR measurements, the output of a Q-switched Nd:YVO laser (1064 nm, 600 ps, Advanced Optical Technology) was frequency quadrupled to produce a pump pulse with either 266 or 355 nm wavelength. The pump and probe pulses are synchronised and the delay is controlled by a pulse generator (DG535, Stanford Research Systems). Delays between pump and probe from 0.5 ns to 100 μs can be obtained. In order to ensure the excitation of the portion of the excited sample is uniform, the diameter of the pump beam (approx 500 μm) is greater than the IR probe beam (approx 200 μm).

6.1.2 Sample Preparation

All solution TRIR samples measured in this Thesis were prepared under an Ar atmosphere using standard Schlenk line techniques with the use of dry solvents, which were dried over CaH_2, degassed with Ar, and stored under an Ar atmosphere (n-heptane).

These samples were prepared with both Uv-Vis and IR absorbance less than 0.6 at both the pump and probe wavelength. An infrared solution cell (Harrick Scientific Products Inc.) with CaF_2 windows (25 $\times$ 2 mm, Crystran Ltd.) were

equipped with a pathlength of 390 μm. Teflon tubing was used to circulate the sample during the experiment to minimise the degredation caused by the high repetition rate of the lasers.

6.1.3 Computational Methods

The DFT calculations performed in this Chapter were performed using the exchange-correlation functional M06 and the LANL08(f) basis set was used for Co and the 6-311(2+,2+)G** Pople basis set was used for all other atoms; H, C, N and O. The corresponding LANL08(f) effective core potential was used for Co to make calculations run considerably faster with minimal loss of computational accuracy.

Excited state analysis calculations were run with unrestricted DFT calculations using the exchange-correlation functional CAM-B3LYP. The LANL08(f) basis set was used for Co and the 6-311++G** Pople basis set was used for all other atoms; H, C, N and O. The corresponding LANL08(f) effective core potential was used for Co to make calculations run considerably faster with very minimal loss of computational accuracy. The geometry optimisation for the S_1 state of $Co(CO)_3(NO)$ was run using the maximum overlap method (MOM), which was designed to force oscillating SCF calculations to 'choose' a configuration.[94] MOM occupies SCF orbitals by maximum overlap with the previous set of occupied orbitals instead of the traditional occupation of lowest energy orbitals. In the calculation of the S_1 state of $Co(CO)_3$ a configuration where an electron is promoted to a higher energy orbital is chosen and the excited state configuration can be converged.

All ECPs and basis sets were taken from the EMSL basis set exchange database.[196]

6.2 Chapter 3 - Computational Methods

DFT as implemented in the Q-CHEM 5.0 quantum-chemical software package was used for all calculations.[197] All calculations were performed in the ground state *in vacuo* with the exception of the excited state analysis. The counterpoise correction method was used for all bond dissociation energy calculations. Figure 6.1 shows a schematic version of the cycles that were performed to obtain energies for use in bond dissociation energy calculations.

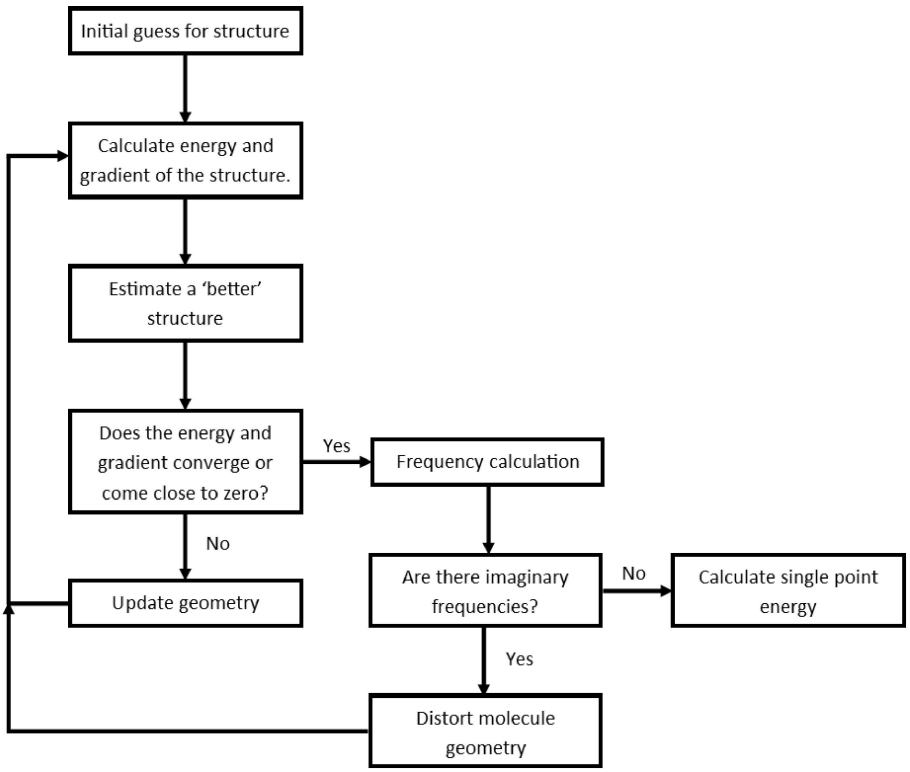

Figure 6.1: Schematic interpretation of the steps performed to obtain energies for use in bond dissociation energy calculations.

All bond dissociation energy calculations were run with restricted DFT calculations using the exchange-correlation functional M06. The LANL08(f) basis set was used for manganese and rhenium and the 6-311++G** Pople basis set was used for all other atoms; H, C, N, O, F and Cl. The corresponding LANL08(f) effective core potential was used for both manganese and rhenium to make calculations run considerably faster at very minimal loss of computational accuracy.

Excited state analysis calculations were run with unrestricted DFT calcu-

lations using the exchange-correlation functional CAM-B3LYP. The LANL08(f) basis set was used for rhenium and the 6-311(2+,2+)G** Pople basis set was used for all other atoms; H, C, N, O, F, and Br. The corresponding LANL08(f) effective core potential was used for rhenium to make calculations run considerably faster at very minimal loss of computational accuracy.

All ECPs and basis sets were taken from the EMSL basis set exchange database.[196]

The MO diagrams were calculated and exported using ADFinput using the fragment analysis technique.[198]

6.3 Chapter 4 - Spectroscopy

6.3.1 Fourier Transform Infra-red Spectroscopy

FTIR spectra were recorded using a Nicolet 6700 FTIR spectrometer at 2 cm^{-1} resolution, with an MCT or TGS detector in solution cells (Harrick Scientific Products, Inc.) with CaF_2 windows and a 0.39 or 1.00 mm path length. FTIR spectra for the matrix experiments were taken on a Nicolet IS50R FTIR spectrometer at 2 cm^{-1} resolution with an MCT detector in a copper high pressure cell with CaF_2 windows and a 2.00 mm path length.

6.3.2 UV/Visible Absorbance Spectroscopy

The UV/Vis spectra were performed on an Agilent Technologies Cary 60 UV/Vis spectrometer with 1 mm path length quartz cuvettes.

6.3.3 NMR Spectroscopy

All NMR spectroscopy was carried out on Bruker AV400, AV(III)400 and AV500 spectrometers. Chemical shifts are quoted in parts per million relative to TMS for ^{1}H and $^{13}C\{^{1}H\}$ NMR and $CFCl_3$ for ^{19}F NMR.

6.3.4 Photolysis Experiments

Photolysis experiments at room temperature were performed using a Hg arc lamp emitting 254 nm light next to a Harrick Scientific Products cell with a 510 μm pathlength between CaF_2 windows purged with Ar.

Photolysis experiments at cold temperatures were performed using an Hg arc lamp emitting 254 nm light next to a copper cell with CaF_2 windows sealed with a lead gasket. The two halves of the cell containing the compound were joined together using 4 steel screws in each of the corners and tightened, compressing the lead and creating a seal. The cell was attached to a cold finger that has an inlet and outlet for gas to pass through the cell. Once leak proof, the cell was encased in a vacuum shroud and evacuated to approx 5×10-5 mbar. Once under vacuum, the cell was filled with CO_2 at room temperature and then cooled to 230 K using a helium compressor and the temperature controlled by a Scientific Instruments model 9700 controller, which was attached to a resistive heat band at the base of the cold finger.

6.4 Chapter 4 - Syntheses

6.4.1 Materials

Reagents were purchased from Sigma Aldrich, Strem Chemicals, Fisher Scientific and VWR International and used as received, unless stated otherwise. Solvents were purchased dry (max 5 ppm of H_2O) and degassed with Ar before use. All synthetic experiments were performed under anhydrous and anaerobic conditions using typical Schlenk line techniques under an atmosphere of Ar.

6.4.2 Synthetic Procedures

Synthesis of [MnBn(CO)$_3$][OTf]

A solution of $Mn(CO)_5Br$ (0.41 g, 1.45 mmol) and $AgOSO_2CF_3$ (0.31 g, 1.58 mmol) was heated at reflux in DCM (25 mL) at 40 °C for 1 h in the dark to give $Mn(CO)_5(OSO_2CF_3)$. The pale yellow solution was then isolated by filtration and benzene (1.02 g, 13.06 mmol) was added and the solution heated at reflux for a further 4 h. The reaction mixture was then evaporated to dryness to give a dark yellow solid, which was recrystallised from CH_2Cl_2 to precipitate [MnBn(CO)$_3$][OTf] as a pale yellow solid (0.14 g, 26 %). ν(CO)/cm^{-1} (CH_2Cl_2) 2085, 2038 and 2026; MS *m/z* - 216.9701 $[C_9H_6O_3Mn]^+$, 148.9524 $[CF_3O_3S]^-$.

Attempted Synthesis of [ReBn(CO)$_3$][PF$_6$]

A solution of $Re(CO)_5Br$ (0.40 g, 0.98 mmol), $AlCl_3$ (0.39 g, 2.92 mmol) and benzene (1.17 mL, 13.06 mmol) was heated at reflux in decane at 110 °C for 4 h resulting in a dark red tar underneath the solvent. The pale yellow solution was cooled in ice then decanted off and the tar washed with cyclohexane (3 × 10 mL) and dissolved in ice-cold water (10 mL). This was then filtered under gravity into an aqueous solution of water and NH_4PF_6 (0.1 g / 2 mL) which precipitated a white solid, which was then isolated by filtration and dissolved in the minimum amount of acetone and immediately precipitated with diethyl ether to precipitate a white solid, which was dried under vacuum (0.015 g, 3 %). ν(CO)/cm^{-1} (CH_2Cl_2) 2064, 2052 and 2002.

Synthesis of [Re(CO)$_3$(Mes)][PF$_6$]

A solution of $Re(CO)_5Br$ (0.50 g, 1.23 mmol), $AlCl_3$ (0.49 g, 3.69 mmol) and mesitylene (1.56 mL, 11.23 mmol) was heated at reflux in decane at 110 °C for 4 h resulting in a dark red tar underneath the solvent. The pale yellow solution was cooled in ice then decanted off and the tar washed with cyclohexane (3 × 10 mL) and dissolved in ice-cold water (10 mL). This was then filtered under gravity into

an aqueous solution of water and NH_4PF_6 (0.1 g / 2 mL) which precipitated a pale yellow solid, which was then isolated by filtration and dissolved in the minimum amount of acetone and immediately precipitated with diethyl ether to precipitate $[Re(CO)_3(Mes)][PF_6]$ as a pale yellow solid, which was dried under vacuum (0.22 g, 46 %). Calculated: C, 26.92 %; H, 2.26 % Found: C, 27.38 %; H, 2.49 %; ν(CO)/cm^{-1} (CH_2Cl_2) 2070 and 1998; MS *m/z* - 391.0349 $[C_{12}H_{12}O_3Re]^+$.

Synthesis of $[Re(CO)_3(HMB)][PF_6]$

A solution of $Re(CO)_5Br$ (0.50 g, 1.23 mmol), $AlCl_3$ (0.49 g, 3.69 mmol) and hexamethylbenzene (1.82 g, 11.23 mmol) was heated at reflux in decane at 110 °C for 4 h resulting in a dark red tar underneath the solvent. The pale yellow solution was cooled in ice then decanted off and the tar washed with cyclohexane (3 × 10 mL) and dissolved in ice-cold water (10 mL). This was then filtered under gravity into an aqueous solution of water and NH_4PF_6 (0.1 g / 2 mL) which precipitated a pale yellow solid, which was then isolated by filtration and dissolved in the minimum amount of acetone and immediately precipitated with diethyl ether to precipitate $[Re(CO)_3(HMB)][PF_6]$ as a pale yellow solid, which was dried under vacuum (0.10 g, 17 %). Calculated: C, 31.20 %; H, 3.14 % Found: C, 32.08 %; H, 3.52 %; ν(CO)/cm^{-1} (CH_2Cl_2) 2059 and 1987; ^{1}H NMR (400 MHz, $CDCl_3$) 2.64 (s, 18H); ^{13}C NMR (100 MHz, $CDCl_3$) 114.3 (Ar) 17.6 (CH_3); MS *m/z* - 433.0830 $[C_{15}H_{18}O_3Re]^+$, 144.9642 $[PF_6]^-$.

Synthesis of $[Re(CO)_3(HEB)][PF_6]$

A solution of $Re(CO)_5Br$ (0.40 g, 0.98 mmol), $AlCl_3$ (0.39 g, 2.95 mmol) and hexaethylbenzene (1.21 g, 4.92 mmol) was heated at reflux in decane at 110 °C for 4 h resulting in a dark red tar underneath the solvent. The pale yellow solution was cooled in ice then decanted off and the tar washed with cyclohexane (3 × 10 mL) and dissolved in ice-cold water (10 mL). This was then filtered under gravity into an aqueous solution of water and NH_4PF_6 (0.1 g / 2 mL) which precipitated

a pale yellow solid, which was then isolated by filtration and dissolved in the minimum amount of acetone and immediately precipitated with diethyl ether to precipitate $[Re(CO)_3(HEB)][PF_6]$ as a pale yellow solid, which was dried under vacuum (0.31 g, 51 %). Calculated: C, 38.12 %; H, 4.57 % Found: C, 38.73 %; H, 4.89 %; $\nu(CO)/cm^{-1}$ (CH_2Cl_2) 2065 and 1994; ^1H NMR (400 MHz, $CDCl_3$) 2.67 (CH_2, q, 12H, J^3_{HH} 7.6 Hz) 1.33 (CH_3, t, 18H, J^3_{HH} 7.6 Hz); MS *m/z* - 517.1744 $[C_{21}H_{30}O_3Re]^+$.

Synthesis of $[Re(bpy)(CO)_4][OTf]$

A solution of $Re(CO)_5Br$ (0.12 g, 0.30 mmol) and AgOTf (0.09 g, 0.30 mmol) in CH_2Cl_2 was stirred for 16 h at room temperature in the dark to give $Re(CO)_5(OTf)$. The pale yellow supernatant was then filtered off and 2,2'-bipyridine (0.06 g, 0.36 mmol) added and the mixture stirred for 16 h at room temperature in the dark. The reaction mixture was then concentrated under vacuum and precipitated with slow addition of excess ether. The pale yellow solid precipitate, $[Re(bpy)(CO)_4][OTf]$, was isolated by filtration then dried under vacuum (0.10 g, 58 %). Calculated: C, 29.85 %; H, 0.97 %; N, 4.64 % Found: C, 30.32 %; H, 1.62 %; N, 4.46 %; $\nu(CO)/cm^{-1}$ (CH_2Cl_2) 2123, 2029, 2010 and 1970; ^1H NMR (400 MHz, $CDCl_3$) 8.96 (6,6'-bpy, d, 2H) 8.75 (3,3'-bpy, d, 2H) 8.41 (4,4'-bpy, td, 2H) 7.76 (5,5'-bpy, td, 2H); MS *m/z* - 455.0187 $[C_{14}H_8O_4N_2Re]^+$.

Synthesis of $[Re(CO)_4(dmbpy)][OTf]$

A solution of $Re(CO)_5Br$ (0.12 g, 0.30 mmol) and AgOTf (0.09 g, 0.30 mmol) in CH_2Cl_2 was stirred for 20 h at room temperature in the dark to give $Re(CO)_5(OTf)$. The pale yellow supernatant was then filtered off and 4,4'-dimethyl-2,2'-bipyridine (0.06 g, 0.34 mmol) added and the mixture stirred for 24 h at room temperature in the dark. The reaction mixture was then concentrated under vacuum and precipitated with slow addition of excess ether. The

pale yellow solid precipitate, $[Re(CO)_4(dmbpy)][OTf]$, was isolated by filtration then dried under vacuum (0.04 g, 22 %). Calculated: C, 32.33 %; H, 1.92 %; N, 4.44 % Found: C, 32.89 %; H, 1.89 %; N, 4.14 %; ν(CO)/cm^{-1} (CH_2Cl_2) 2121, 2026, 2008 and 1967; ^{1}H NMR (400 MHz, $CDCl_3$) 8.96 (6,6'-bpy, d, 2H) 8.69 (3,3'-bpy, d, 2H) 7.47 (5,5'-bpy, td, 2H) 2.71 (CH_3, s, 6H); MS *m/z* - 483.0437 $[C_{16}H_{13}N_2O_4Re]^+$.

Synthesis of $[Re(CO)_4(dtbpy)][OTf]$

A solution of $Re(CO)_5Br$ (0.50 g, 1.23 mmol) and AgOTf (0.40 g, 1.62 mmol) in CH_2Cl_2 was stirred for 18 h at room temperature in the dark to give $Re(CO)_5(OTf)$. The pale yellow supernatant was then filtered off and 4,4'-di-tert-butyl-2,2'-bipyridine (0.40 g, 1.50 mmol) added and the mixture stirred for 38 h at room temperature in the dark. The reaction mixture was then concentrated under vacuum and precipitated with slow addition of excess ether. The pale yellow solid precipitate, $[Re(CO)_4(dtbpy)][OTf]$, was isolated by filtration then dried under vacuum (0.05 g, 5 %). Calculated: C, 38.60 %; H, 3.38 %; N, 3.91 % Found: C, 39.23 %; H, 3.47 %; N, 3.45 %; ν(CO)/cm^{-1} (CH_2Cl_2) 2122, 2028, 2009 and 1969; ^{1}H NMR (400 MHz, $CDCl_3$) 8.82 (6,6'-bpy, d, 2H) 8.55 (3,3'-bpy, s, 2H) 7.55 (5,5'-bpy, td, 2H) 1.45 (CH_3, s, 18H); MS *m/z* - 567.1294 $[C_{22}H_{24}N_2O_4Re]^+$.

Synthesis of $[Re(CO)_4(dfbpy)][OTf]$

A solution of $Re(CO)_5Br$ (0.41 g, 1.00 mmol) and AgOTf (0.31 g, 1.20 mmol) in CH_2Cl_2 was stirred for 24 h at room temperature in the dark to give $Re(CO)_5(OTf)$. The pale yellow supernatant was then filtered off and 4,4'-perfluorodimethyl-2,2'-bipyridine (1.46 g, 5.00 mmol) added and the mixture heated at reflux at 45 °C for 48 h in the dark. The reaction mixture was then concentrated under vacuum until precipitate started to form. The solution was then filtered under gravity to leave a grey powder. The grey solid was then washed

with diethyl ether (3 × 20 mL) to give a pale yellow solid, $[Re(CO)_4(dfbpy)][OTf]$ (0.06 g, 8 %). Calculated: C, 27.61 %; H, 0.82 %; N, 3.79 % Found: C, 29.82 %; H, 1.13 %; N, 4.21 %; $\nu(CO)/cm^{-1}$ (CH_2Cl_2) 2127, 2039, 2010 and 1973; ^1H NMR (400 MHz, CD_3CN) 9.26 (6,6'-bpy, d, 2H) 8.94 (3,3'-bpy, s, 2H) 8.05 (5,5'-bpy, td, 2H); ^{19}F NMR (376 MHz, CD_3CN) -79.4 (CF_3-bpy) -75.6 (OTf); MS *m/z* - 590.9835 $[C_{16}H_6N_2O_4F_6Re]^+$

Attempted Synthesis of $[Re(CO)_4(dnb\text{-}F_{34})][OTf]$

A solution of $Re(CO)_5Br$ (0.16 g, 0.38 mmol) and AgOTf (0.13 g, 0.50 mmol) in CH_2Cl_2 was stirred for 24 h at room temperature in the dark to give $Re(CO)_5(OTf)$. The pale yellow supernatant was then filtered off and 4,4'-bis [1H, 1H, 2H, 2H, 3H, 3H- perfluoroundecyl] -2,2'-bipyridine (0.50 g, 0.46 mmol) added and the mixture heated at reflux at 45 °C for 48 h in the dark. The reaction mixture was then filtered under gravity and hexane added to the solution to precipitate a pale yellow powder (0.08 g). $\nu(CO)/cm^{-1}$ (CH_2Cl_2) 2121, 2059, 2035, 2027, 2007, 1967, 1934 and 1913.

Attempted Synthesis of [Re(4- [1H, 1H, 2H, 2H, 3H, 3H- perfluorotridecyl] -4'-methyl-2,2'-bipyridine)$(CO)_4$] [OTf]

A solution of $Re(CO)_5Br$ (0.25 g, 0.62 mmol) and AgOTf (0.21 g, 0.82 mmol) in CH_2Cl_2 was stirred for 24 h at room temperature in the dark to give $Re(CO)_5(OTf)$. The pale yellow supernatant was then filtered off and 4- [1H, 1H, 2H, 2H, 3H, 3H- perfluorotridecyl] -4'-methyl-2,2'-bipyridine (0.55 g, 0.75 mmol) added and the mixture heated at reflux at 45 °C for 48 h in the dark. The reaction mixture was then filtered under gravity and hexane added to the solution to precipitate a pale yellow powder (0.12 g). $\nu(CO)/cm^{-1}$ (CH_2Cl_2) 2121, 2046, 2034, 2027, 2007, 1966, 1924 and 1913.

Synthesis of [ReCl(CO)$_3$(dnb-F$_{34}$)]

A solution of $Re(CO)_5Cl$ (0.11 g, 0.29 mmol) and 4,4'-bis [1H, 1H, 2H, 2H, 3H, 3H- perfluorotridecyl] -2,2'-bipyridine (0.33 g, 0.30 mmol) was heated at reflux in 20 mL of toluene at 100 °C for 3 h. The yellow solution was then filtered under gravity and the solvent removed under vacuum to give a yellow solid. The solids were then washed with hexane to give a pure yellow powder (0.39 g, 97 %). ^{1}H NMR (400 MHz, $CDCl_3$) 8.97 (6,6'-bpy, d, 2H, J^3_{HH} 5.6 Hz) 8.00 (3,3'-bpy, s, 2H) 7.38 (5,5'-bpy, dd, 2H J^3_{HH} 5.7 Hz, J^4_{HH} 1.7 Hz) 2.94 (Ar-CH_2, t, 4H, J^3_{HH} 7.6 Hz) 2.16 ($CH_2CH_2CF_2$, m, 8H); ν(CO)/cm^{-1} (CH_2Cl_2) 2023, 1920 and 1898; MS *m/z* - 1383.0082 $[C_{35}H_{19}N_2O_3F_{34}ClRe]^+$.

Synthesis of [ReBr(CO)$_3$(dnb-F$_{34}$)]

[(dnb-F_{34})$Re(CO)_3Br$] was synthesised *via* an identical procedure to that reported above for [(dnb-F_{34})$Re(CO)_3Cl$] using $Re(CO)_5Br$ instead of $Re(CO)_5Cl$. The obtained [(dnb-F_{34})$Re(CO)_3Br$] complex is a bright yellow powder (93 %). ^{1}H NMR (400 MHz, $CDCl_3$) 8.99 (6,6'-bpy, d, 2H, J^3_{HH} 5.7 Hz) 7.99 (3,3'-bpy, s, 2H) 7.37 (5,5'-bpy, dd, 2H J^3_{HH} 6.0 Hz, J^4_{HH} 1.6 Hz) 2.95 (Ar-CH_2, t, 4H, J^3_{HH} 8.0 Hz) 2.17 ($CH_2CH_2CF_2$, m, 8H); ν(CO)/cm^{-1} (CH_2Cl_2) 2024, 1921 and 1899; MS *m/z* - 1426.9634 $[C_{35}H_{19}N_2O_3F_{34}BrRe]^+$.

Synthesis of [ReCl(bpy)(CO)$_3$]

[(bpy)$Re(CO)_3Cl$] was synthesised *via* an identical procedure to that reported above for [(dnb-F_{34})$Re(CO)_3Cl$] using 2,2'-bipyridine instead of 4,4'-bis [1H, 1H, 2H, 2H, 3H, 3H- perfluoroundecyl] -2,2'-bipyridine. The obtained [(bpy)$Re(CO)_3Cl$] complex is a bright yellow powder (98 %). ν(CO)/cm^{-1} (CH_2Cl_2) 2023, 1920 and 1896.

Synthesis of [ReCl(CO)$_3$(dmbpy)]

[(dmbpy)Re(CO)$_3$Cl] was synthesised *via* an identical procedure to that reported above for [(dnb-F$_{34}$)Re(CO)$_3$Cl] using 4,4'-dimethyl-2,2'-bipyridine instead of 4,4'-bis [1H, 1H, 2H, 2H, 3H, 3H- perfluoroundecyl] -2,2'-bipyridine. The obtained [(dmbpy)Re(CO)$_3$Cl] complex is a bright yellow powder (95 %). ν(CO)/cm^{-1} (CH_2Cl_2) 2022, 1920 and 1895.

Synthesis of [ReCl(CO)$_3$(dtbpy)]

[(dtbpy)Re(CO)$_3$Cl] was synthesised *via* an identical procedure to that reported above for [(dnb-F$_{34}$)Re(CO)$_3$Cl] using 4,4'-di-tert-butyl-2,2'-bipyridine instead of 4,4'-bis [1H, 1H, 2H, 2H, 3H, 3H- perfluoroundecyl] -2,2'-bipyridine. The obtained [(dtbpy)Re(CO)$_3$Cl] complex is a bright yellow powder (97 %). ν(CO)/cm^{-1} (CH_2Cl_2) 2021, 1919 and 1894.

Synthesis of [ReCl(CO)$_3$(dfbpy)]

[(dfbpy)Re(CO)$_3$Cl] was synthesised *via* an identical procedure to that reported above for [(dnb-F$_{34}$)Re(CO)$_3$Cl] using 4,4'-perfluorodimethyl-2,2'-bipyridine instead of 4,4'-bis [1H, 1H, 2H, 2H, 3H, 3H- perfluoroundecyl] -2,2'-bipyridine. The obtained [(dfbpy)Re(CO)$_3$Cl] complex is a bright orange powder (96 %). ν(CO)/cm^{-1} (CH_2Cl_2) 2028, 1931 and 1908.

Synthesis of [Li][Al(OC(CF$_3$)$_3$)$_4$]

$LiAlH_4$ (0.40 g, 10.59 mmol) was suspended in 70 mL of toluene then perfluoro-tert-butanol (10.00 g, 42.37 mmol) was added at 0 °C and stirred for 1 h. The reaction mixture was then heated at 80 °C for 72 h. The cloud solution was then cooled to -20 °C to precipitate the crude grey product and filtered under gravity. Purification was then performed by sublimation (150 °C at 5x10^{-2} mbar) to give a pure white powder (1.30 g, 12 %). ^{19}F NMR (376 MHz, $CDCl_3$) -76.9 (CF_3); MS *m/z* - 960.1490 [$C_{16}O_4F_{36}Al$]$^-$. These analyses are in agreement with

literature.[183]

Hexafluorophosphate Anion Exchange

The metal complex (1 eq) and NH_4PF_6 (8 eq) were dissolved in 25 mL of acetone and stirred at room temperature in the dark for 2 h. Water (20 mL) was then added and the mixture stirred for a further 48 h in the dark allowing slow evaporation of the acetone and crystallisation of the final product.

$[Al(OC(CF_3)_3)_4]$ Anion Exchange

The metal complex (1 eq) and $[Li][Al(OC(CF_3)_3)_4]$ (1.2 eq) were suspended in 30 mL of diethyl ether and stirred at room temperature in the dark for 24 h. The supernatant is filtered off and the solvent removed under vacuum resulting in the crude product as a pale yellow oil. The oil is then washed with hexane (5 × 5 mL), which is decanted off each time to leaving behind the pure product. This oil can sometimes be solidified by azeotroping with pentane.

Synthesis of Hexaethylbenzene

A solution of 3-hexyne (13.50 mL, 0.80 mol), trimethylsilyl chloride (13.50 mL, 1.26 mol) and solid Pd/C (10 %, 3.00 g, 0.32 mol) in THF was heated at reflux at 70 °C for 3 h. The resulting reaction mixture was filtered under gravity and evaporated under vacuum to yield an orange powder. This solid was then purified by recrystallised from ethanol then recrystallising again from *n*-heptane to give white needle crystals (2.08 g, 64 %). ^{1}H NMR (400 MHz, $CDCl_3$) 2.68 (CH_2, q, 12H, J^3_{HH} 7.5 Hz) 1.23 (CH_3, t, 18H, J^3_{HH} 7.5 Hz); ^{13}C NMR (100 MHz, $CDCl_3$) 137.9 (Ar) 22.2 (CH_2) 15.8 (CH_3); MS *m/z* - 246.3025 $[C_{18}H_{30}]^+$. These analyses match with literature.[Yasutaka1997]

Synthesis of 4,4'-perfluorodimethyl-2,2'-bipyridine (dfbpy)

To dimethylformamide (15 mL) and propan-2-ol (0.78 mL), $Pd(O_2CCH_3)_2$ (0.05 g) and tetrabutylammonium iodide (0.80 g) were added and stirred at 20 °C for 40 min. 2-bromo-4-(trimethylfluoro)pyridine (1.00 g, 2.22 mmol) and sodium acetate (0.37 g) were then added and the mixture was refluxed for 48 h. The black liquid was then added to water (300 mL) and filtered under vacuum to isolate a black solid. This solid was then washed with a hexane:ethyl acetate (10:1) solution (2 × 75 mL) and filtered under vacuum to afford a red liquid; the solvent mixture removed under vacuum to give a red solid. This red solid was then purified by column chromatography (hexane:ethyl acetate 10:1) to give a white powder (0.19 g, 59 %). ^{1}H NMR (400 MHz, $CDCl_3$) 8.85 (6,6'-bpy, d, 2H, J^3_{HH} 5.2 Hz) 8.70 (3,3'-bpy, s, 2H) 7.56 (5,5'-bpy, d, 2H, J^3_{HH} 5.2 Hz); ^{13}C NMR (100 MHz, $CDCl_3$) 156.2 (2,2'-bpy, s) 150.4 (6,6'-bpy, s) 139.75 (Ar-CF_3, q, J^2_{CF} 34.3 Hz) 123.1 (CF_3, q, J^1_{CF} 274.7 Hz) 120.01 (3,3'-bpy , q, J^3_{CF} 3.5 Hz) 117.2 (5,5'-bpy, q, J^3_{CF} 3.5 Hz); ^{19}F NMR (376 MHz, $CDCl_3$) -64.95 (CF_3); MS *m/z* - 293.0522 $[C_{12}H_7N_2F_6]^+$.

Synthesis of 4,4'-bis [1H, 1H, 2H, 2H, 3H, 3H- perfluoroundecyl] -2,2'-bipyridine (dnb-F_{34})

Diisopropylamine (3.70 mL, 26.40 mmol) was dissolved in THF (20 mL) and cooled to -78 °C; ^{n}BuLi (2.50 M in hexanes, 9.90 mL, 24.75 mmol) was then added dropwise and stirred for 40 min, the solution was then allowed to warm to 0 °C and stirred for another 20 min. The solution was then cooled back to -78 °C and a THF (80 mL) solution of 4,4'-dimethyl-2,2'-bipyridine (2.21 g, 11.98 mmol) is added to the reaction mixture and stirred at -78 °C for 1 h. The reaction is then allowed to warm up 0 °C and stirred for another 2 h. The reaction mixture is then cooled back to -78 °C and a THF (60 mL) solution of 1H, 1H, 2H, 2H-perfluorodecyl iodide (15.60 g, 27.18 mmol) is added and stirred for 1 h in the dark. The reaction is then allowed to warm up to room temperature for 18 h while

stirring. Brine (50 mL) is then added and the product is extracted into diethyl ether (15 × 150 mL), dried over $MgSO_4$, isolated by filtration and the solvent removed under vacuum to give a brown oil. This brown oil is then purified by a series of recrystallisations in trifluorotoluene to give a pure white powder (1.42 g, 11 %). ^{1}H NMR (400 MHz, $CDCl_3$) 8.60 (6,6'-bpy, d, 2H, J^3_{HH} 5.0 Hz) 8.28 (3,3'-bpy, s, 2H) 7.16 (5,5'-bpy, dd, 2H J^3_{HH} 5.0 Hz, J^4_{HH} 1.8 Hz) 2.81 (Ar-CH_2, t, 4H, J^3_{HH} 7.6 Hz) 2.08 ($CH_2CH_2CF_2$, m, 8H); ^{13}C NMR (100 MHz, $CDCl_3$) 156.4 (2,2'-bpy) 150.8 (4,4'-bpy) 149.5 (6,6'-bpy) 123.9 (3,3'-bpy) 121.3 (5,5'-bpy) 34.7 (Ar-CH_2) 30.6 (CF_2CH_2, t, J^2_{FH} 22 Hz) 21.2 (CH_2**C**H_2CH_2); ^{19}F NMR (376 MHz, $CDCl_3$) -131.1 (CF_2) -128.4 (CF_2) -127.7 (CF_2) -126.9 (CF_2) -126.7 (CF_2) -119.1 (CF_2) -85.7 (CF_3); MS *m/z* - 1077.1005 $[C_{32}H_{19}N_2F_{34}]^+$.

Attempted Synthesis of 4,4'-bis [1H, 1H, 2H, 2H, 3H, 3H- perfluorotridecyl] -2,2'-bipyridine (dnb-F_{42})

Diisopropylamine (3.70 mL, 26.40 mmol) was dissolved in THF (20 mL) and cooled to -78 °C; ^{n}BuLi (2.50 M in hexanes, 9.90 mL, 24.75 mmol) was then added dropwise and stirred for 40 min, the solution was then allowed to warm to 0 °C and stirred for another 20 min. The solution was then cooled back to -78 °C and a THF (80 mL) solution of 4,4'-dimethyl-2,2'-bipyridine (2.21 g, 11.98 mmol) is added to the reaction mixture and stirred at -78 °C for 1 h. The reaction is then allowed to warm up to 0 °C and stirred for another 2 h. The reaction mixture is then cooled back to -78 °C and a THF (60 mL) solution of 1H, 1H, 2H, 2H-perfluorododecyl iodide (18.32 g, 27.18 mmol) is added and stirred for 1 h in the dark. The reaction is then allowed to warm up to room temperature for 18 h while stirring. Brine (50 mL) is then added and the product is extracted into diethyl ether (5 × 50 mL) dried over $MgSO_4$, isolated by filtration and the solvent removed under vacuum to give a brown solid. This brown solid is then purified by a series of recrystallisations from trifluorotoluene to give a pure white powder (3.52 g, 23 %). ^{1}H NMR (400 MHz, $CDCl_3$) 8.60 (F-chain side 6,6'-bpy, d, 1H,

J^3_{HH} 5.2 Hz) 8.54 (unsubstituted side 6,6'-bpy, d, 1H, J^3_{HH} 4.8 Hz) 8.26 (F-chain side 3,3'-bpy, s, 1H) 8.25 (unsubstituted side 3,3'-bpy, s, 1H) 7.15 (5,5'-bpy, dd, 2H J^3_{HH} 5.0 Hz, J^4_{HH} 1.8 Hz) 2.81 (Ar-CH_2, t, 2H, J^3_{HH} 7.6 Hz) 2.45 (CH_3, s, 3H) 2.08 ($CH_2CH_2CF_2$, m, 4H); MS *m/z* - 731.0978 $[C_{24}H_{16}N_2F_{21}]^+$.

Synthesis of Trihexyltetradecylphosphonium Tetrafluoroborate

Trihexyltetradecylphosphonium chloride (5.2 g, 10.0 mmol) was added to water (15 mL) and stirred then $NaBF_4$ (1.3 g, 11.8 mmol) was dissolved in water (10 mL) and slowly added at 0 °C while stirring causing it to go viscous. This solution was then stirred for 19 h at rt and resulting in a clear solution with a yellow oil at the bottom. The clear solution was then extracted into diethyl ether (5 × 30 mL) and washed with water (6 × 50 mL). The ether was then removed under reduced pressure to give a translucent white oil, which went clear when dried and eventually solidified upon cooling (5.1 g, 91 %). ^{1}H NMR (400 MHz, $CDCl_3$) 0.87 - 0.92 (m, 12H), 1.26 - 1.34 (m, 32H), 1.44 - 1.59 (m, 16H) 2.13 - 2.23 (m, 8H); ^{13}C NMR (100 MHz, $CDCl_3$) 13.8, 14.2, 18.7, 21.6, 21.7, 22.4, 22.6, 28.9, 29.3, 29.5, 29.6, 30.2, 30.4, 30.6, 30.8, 30.9, 31.8; ^{19}F NMR (377 MHz, $CDCl_3$) -151.47 (q), -151.42 (br, s).

Synthesis of Trihexyltetradecylphosphonium Hexafluorophosphate

Trihexyltetradecylphosphonium chloride (5.0 g, 9.6 mmol) was added to water (30 mL) and stirred then NH_4PF_6 (1.3 g, 11.4 mmol) was dissolved in water (15 mL) and slowly added at 0 °C while stirring causing it to go viscous. This solution was then stirred for 19 h at rt and resulting in a clear solution with large spherical solid precipitate, which was extracted with diethyl ether (4 × 30 mL) and washed with water (6 × 50 mL). The ether was then removed under reduced pressure and dried *in vacuo* to give a white solid (4.6 g, 99 %). ^{1}H NMR (400 MHz, $CDCl_3$) 0.87 - 0.92 (m, 12H), 1.26 - 1.34 (m, 32H), 1.44 - 1.59 (m, 16H), 2.08 - 2.17 (m, 8H); ^{13}C NMR (100 MHz, $CDCl_3$) 13.8, 14.1, 18.4, 18.9, 21.4,

21.5, 22.3, 22.7, 28.8, 29.3, 29.5, 29.7, 30.2, 30.3, 30.5, 30.7, 30.9; ^{19}F NMR (377 MHz, $CDCl_3$) -72.09 (d).

Chapter 7

References

(1) K. R. Sawyer, R. P. Steele, E. A. Glascoe, J. F. Cahoon, J. P. Schlegel, M. Head-Gordon and C. B. Harris, *Journal of Physical Chemistry A*, 2008, **112**, 8505–8514.

(2) H. Ha and T. L. Gustafson, *Annual Review of Physical Chemistry*, 1994, **45**, 593–622.

(3) P. C. Ford, *Accounts of Chemical Research*, 1981, **14**, 31–38.

(4) Y. Sunada, H. Kawakami, T. Imaoka, Y. Motoyama and H. Nagashima, *Angewandte Chemie International Edition*, 2009, **48**, 9511–9514.

(5) V. A. Yaylayan, S. Harty-Majors and A. A. Ismail, *Journal of Agricultural and Food Chemistry*, 1999, **47**, 2335–2340.

(6) O. Faix, B. Andersons and G. Zakis, *Holzforschung*, 1998, **52**, 268–274.

(7) V. A. Yaylayan and A. A. Ismail, *Carbohydrate Research*, 1995, **276**, 253–265.

(8) D. V. Krupenya, E. O. Danilov, M. A. Rodgers and S. P. Tunik, *Journal of Physical Chemistry A*, 2003, **107**, 8867–8871.

(9) R. B. King, M. B. Bisnette and A. Fronzaglia, *Journal of Organometallic Chemistry*, 1966, **5**, 341–356.

(10) V. K. Kien, W. Chew, L. H. K. Lim, Y. F. Wai and K. L. Weng, *Bioconjugate Chemistry*, 2007, **18**, 1370–1374.

(11) L. Shao, L. Zhang, M. Zhou and Q. Qin, *Organometallics*, 2001, **20**, 1137–1143.

(12) B. H. Weiller, E. P. Wasserman, C. B. Moore and R. G. Bergman, *Journal of the American Chemical Society*, 1993, **115**, 4326–4330.

(13) C. K. Kim, K. A. Lee, C. K. Kim, B. Lee and H. W. Lee, *Chemical Physics Letters*, 2004, **391**, 321–324.

(14) H. Li, H. Feng, W. Sun, R. B. King and H. F. Schaefer, *Inorganic Chemistry*, 2013, **52**, 6893–6904.

(15) C. D. Montgomery, *Journal of Chemical Education*, 2007, **84**, 102–105.

(16) S. C. Avanzino, A. A. Bakke, H. Chen, W. L. Jolly, T. H. O. Lee and A. J. Ricco, *Inorganic Chemistry*, 1980, **19**, 1931–1936.

(17) L. E. O. J. Procopio, P. J. Carroll and D. H. Berry, *Science*, 1995, **14**, 45–55.

(18) R. Collins, M. J. H. Ojea, A. Mansikkamki, J. Tang and R. A. Layfield, *Inorganic Chemistry*, 2020, **59**, 642–647.

(19) I. Castro-Rodriguez, H. Nakai, L. N. Zakharov, A. L. Rheingold and K. Meyer, *Science*, 2004, **305**, 1757–1760.

(20) M. A. Alamiry, N. M. Boyle, C. M. Brookes, M. W. George, L. Conor, P. Portius, M. T. Pryce, K. L. Ronayne, X. Z. Sun, M. Towrie and Q. V. Khuong, *Organometallics*, 2009, **28**, 1461–1468.

(21) R. H. Crabtree, *Chemical Reviews*, 1985, **85**, 245–269.

(22) R. B. Hitam, K. A. Mahmoud and A. J. Rest, *Coordination Chemistry Reviews*, 1984, **55**, 1–29.

(23) A. I. Cooper and M. Poliakoff, *Chemical Physics Letters*, 1993, **212**, 611–616.

(24) C. Zybill and G. Muller, *Organometallics*, 1987, **6**, 2489–2494.

(25) J. S. M. Wai, I. Mark, J. S. Svendsen, M. G. Finn, E. N. Jacobsen and K. B. Sharpless, *Journal of the American Chemical Society*, 1989, **111**, 1123–1125.

(26) C. R. Kemnitz, E. S. Ball and R. J. Mcmahon, *Organometallics*, 2012, **31**, 70–84.

(27) B. M. A. Graham, M Poliakoff, J. J. Turner and L. Road, *Journal of the Chemical Society A: Inorganic, Physical, Theoretical*, 1971, 2939–2948.

(28) A. J. Rest, *Journal of Molecular Structure*, 1990, **222**, 87–93.

(29) R. Tyler and P. Petrylak, *Journal of Organometallic Chemistry*, 1981, **212**, 389–396.

(30) T. E. Bitterwolf, *Journal of Organometallic Chemistry*, 2004, **689**, 3939–3952.

(31) S. B. Duckett, M. W. George, O. S. Jina, S. L. Matthews, R. N. Perutz, X. Z. Sun and K. Q. Vuong, *Chemical Communications*, 2009, **2**, 1401–1403.

(32) G. E. Ball, T. A. Darwish, S. Geftakis, M. W. George, D. J. Lawes, P. Portius and J. P. Rourke, *Proceedings of the National Academy of Sciences of the United States of America*, 2005, **102**, 1853–1858.

(33) E. J. Beckman, *Chemical Communications*, 2004, **10**, 1885–1888.

(34) W. Hui, R. Mammucari and N. R. Foster, *Journal of Organometallic Chemistry*, 2013, **724**, 102–116.

(35) R. P. Hughes and H. A. Trujillo, *Organometallics*, 1996, **15**, 286–294.

(36) M. W. George, M. Poliakoff and J. J. Turner, *Analyst*, 1994, **119**, 551–561.

(37) M. K. Kuimova, W. Z. Alsindi, J. Dyer, D. C. Grills, O. S. Jina, P. Matousek, A. W. Parker, P. Portius, X. Z. Sun, M. Towrie, C. Wilson, J. Yang and M. W. George, *Dalton Transactions*, 2003, **21**, 3996–4006.

(38) M. Born and R. Oppenheimer, *Annalen der Physik*, 1927, **84**, 457–484.

(39) D. R. Hartree, *Mathematical Proceedings of the Cambridge Philosophical Society*, 1928, **24**, 89–110.

(40) J. C. Slater, *Physical Reviews*, 1950, **35**, 210–211.

(41) C. Roothaan, *Reviews of Modern Physics*, 1951, **23**, 69–89.

(42) G. G. Hall, *Proceedings of the Royal Society A*, 1951, **205**, 541–552.

(43) J. C. Slater, *Physical Reviews*, 1930, **36**, 57–64.

(44) S. F. Boys, *Proceedings of the Royal Society of London. Series A, Mathematical and Physical Sciences*, 1950, **200**, 542–554.

(45) W. J. Hehre, R. F. Stewart and J. A. Pople, *The Journal of Chemical Physics*, 1969, **51**, 2657–2664.

(46) R. Krishnan, J. S. Binkley, R. Seeger and J. A. Pople, *The Journal of Chemical Physics*, 1980, **72**, 650–654.

(47) P. C. Hariharan and J. A. Pople, *Theoretical Chemistry Accounts*, 1973, **28**, 213–222.

(48) M. J. Frisch, J. A. Pople and J. S. Binkley, *The Journal of Chemical Physics*, 1984, **80**, 3265–3269.

(49) H. Hellmann, *The Journal of Chemical Physics*, 1935, **3**, 61.

(50) H. Hellmann and W. Kassatotschkin, *Journal of Chemical Physics*, 1936, **4**, 324–325.

(51) Z. Zhang and R. M. Pitzer, *Journal of Physical Chemistry A*, 1999, **103**, 6880–6886.

(52) P. Hohenberg and W. Kohn, *Physical Reviews*, 1964, **136**, 864–871.

(53) W. Kohn and L. J. Sham, *Physical Reviews*, 1965, **140**, 1133–1139.

(54) S. Lehtola, C. Steigemann, M. J. Oliveira and M. A. Marques, *SoftwareX*, 2018, **7**, 1–5.

(55) H. Primas, *International Journal of Quantum Chemistry*, 1967, **1**, 493–519.

(56) S. H. Vosko, L. Wilk and M. Nusair, *Canadian Journal of Physics*, 1980, **58**, 1200–1211.

(57) A. D. Becke, *Physical Reviews: A*, 1988, **38**, 3098–3191.

(58) C. Lee, W. Yang and R. G. Parr, *Physical Reviews: B*, 1988, **37**, 785–790.

(59) A. D. Becke, *Journal of Physical Chemistry*, 1993, **98**, 5648–5652.

(60) J. Gerratt and I. M. Mills, *The Journal of Chemical Physics*, 1968, **49**, 1719–1729.

(61) K. Ruud, P. O. Strand and P. R. Taylor, *Journal of Chemical Physics*, 2000, **112**, 2668–2683.

(62) F. Jensen, *Introductional to Computational Chemistry*, John Wiley & Sons, 2007.

(63) E. B. Wilson, *The Journal of Chemical Physics*, 1939, **7**, 1047–1052.

(64) E. B. Wilson, J. C. Decius and P. C. Cross, *Molecular Vibrations*, 1955.

(65) Y. Unal, W. Nassif, B. C. Ozaydin and K. Sayin, *Vibrational Spectroscopy*, 2021, **112**, 103189–103195.

(66) J. P. Merrick, D. Moran and L. Radom, *Journal of Physical Chemistry A*, 2007, **111**, 11683–11700.

(67) G. Rauhut and P. Pulay, *Journal of Physical Chemistry*, 1995, **99**, 3093–3100.

(68) H. Y. Zhang, Y. M. Sun and X. L. Wang, *Chemistry - A European Journal*, 2003, **9**, 502–508.

(69) A. Fatima, T. Husain, M. Suhel, S. M. Prasad and V. P. Singh, *Journal of Plant Growth Regulation*, 2022, **41**, 163–177.

(70) J. Astier, J. Rossi, P. Chatelain, A. Klinguer, A. Besson-Bard, C. Rosnoblet, S. Jeandroz, V. Nicolas-Francs and D. Wendehenne, *Journal of Experimental Botany*, 2021, **72**, 781–792.

(71) L. Lamattina, C. Garca-Mata, M. Graziano and G. Pagnussat, *Annual Review of Plant Biology*, 2003, **54**, 109–136.

(72) S. J. Neill, R. Desikan and J. T. Hancock, *New Phytologist*, 2003, **159**, 11–35.

(73) J. A. McCleverty, *Chemical Reviews*, 2004, **104**, 403–418.

(74) R. H. Crabtree, *The Organometallic Chemistry of the Transition Metals by Robert H. Crabtree*, John Wiley & Sons, 2001.

(75) L. E. Laverman, A. Wanat, J. Oszajca, G. Stochel, P. C. Ford and R. V. Eldik, *Journal of the American Chemical Society*, 2001, **123**, 285–293.

(76) P. C. Ford and I. M. Lorkovic, *Chemical Reviews*, 2002, **102**, 993–1017.

(77) T. E. Bitterwolf, *Coordination Chemistry Reviews*, 2006, **250**, 1196–1207.

(78) P. Boulet, H. Chermette and J. Weber, *Inorganic Chemistry*, 2001, **40**, 7032–7039.

(79) M. Buchs, C. A. Daul, P. T. Manoharan and C. W. Schlpfer, *International Journal of Quantum Chemistry*, 2003, **91**, 418–431.

(80) W. D. Horrocks and R. C. Taylor, *Inorganic Chemistry*, 1963, **2**, 723–727.

(81) W. Evans and J. I. Zink, *Journal of the American Chemical Society*, 1981, **103**, 2635–2640.

(82) D. M. Rayner, A. S. Nazran, M. Drouin and P. A. Hackett, *Journal of Physical Chemistry*, 1986, **90**, 2882–2888.

(83) J. H. Enemark and R. D. Feltham, *Coordination Chemistry Reviews*, 1974, **13**, 339–406.

(84) W. Wang, F. Chen, J. Lin and Y. She, *Journal of the Chemical Society, Faraday Transactions*, 1995, **91**, 847–853.

(85) S. Georgiou and C. A. Wight, *Journal of Physical Chemistry*, 1990, **94**, 4935–4940.

(86) J. A. Bartz, T. O. Friday, B. R. Goodman, S. E. Kooi, R. G. Blair and W. F. Polik, *Journal of Physical Chemistry A*, 1998, **102**, 10697–10702.

(87) I. H. Sabherwal and A. B. Burg, *Journal of the Chemical Society D: Chemical Communications*, 1969, 853–854.

(88) G. E. Gadd, M. Poliakoff and J. J. Turner, *Organometallics*, 1987, **6**, 391–397.

(89) B. O. Crichton, A. J. Rest and L. Road, *Journal of the Chemical Society, Dalton Transactions*, 1977, 536–541.

(90) X. Wang and L. Andrews, *Journal of Physical Chemistry A*, 2001, **105**, 4403–4409.

(91) P. Coppens, I. Novozhilova and A. Kovalevsky, *Chemical Reviews*, 2002, **102**, 861–883.

(92) M. Atanasov and T. Schnherr, *Journal of Molecular Structure: THEOCHEM*, 2002, **592**, 79–93.

(93) E. Dombrowski, E. Peterson, D. D. Sesto and A. L. Utz, *Catalysis Today*, 2015, **244**, 10–18.

(94) A. T. Gilbert, N. A. Besley and P. M. Gill, *Journal of Physical Chemistry A*, 2008, **112**, 13164–13171.

(95) A. P. Scott and L. Radom, *Journal of Physical Chemistry*, 1996, **100**, 16502–16513.

(96) M. W. George, M. B. Hall, O. S. Jina, P. Portius, X. Z. Sun, M. Towrie, H. Wu, X. Yang and S. D. Zaric, *Proceedings of the National Academy of Sciences of the United States of America*, 2010, **107**, 20178–20183.

(97) J. A. Calladine, K. Q. Vuong, X. Z. Sun and M. W. George, *Pure and Applied Chemistry*, 2009, **81**, 1667–1675.

(98) J. A. Calladine, S. B. Duckett, M. W. George, S. L. Matthews, R. N. Perutz, O. Torres and K. Q. Vuong, *Journal of the American Chemical Society*, 2011, **133**, 2303–2310.

(99) A. J. Cowan and M. W. George, *Coordination Chemistry Reviews*, 2008, **252**, 2504–2511.

(100) G. Bor, U. K. Dietler and K. Noack, *Journal of the Chemical Society, Chemical Communications*, 1976, **5**, 914–916.

(101) L. A. Hanlan, H. Huber, E. P. Kndig, B. R. McGarvey and G. A. Ozin, *Journal of the American Chemical Society*, 1975, **97**, 7054–7068.

(102) J. Mascetti and M. Tranquille, *Journal of Physical Chemistry*, 1988, **92**, 2177–2184.

(103) J. Pacansky, U. Wahlgren and P. S. Bagus, *Journal of Chemical Physics*, 1975, **62**, 2740–2744.

(104) F. Solymosi, *Journal of Molecular Catalysis*, 1991, **65**, 337–358.

(105) M. Sodupe, V. Branchadell and A. Oliva, *Journal of Physical Chemistry*, 1995, **99**, 8567–8571.

(106) G. Paiaro and L. Pandolfo, *Comments on Inorganic Chemistry*, 1991, **12**, 213–235.

(107) D. C. Grills, *University of Nottingham Thesis*, 1999.

(108) G. J. Xia, J. Liu and Z. F. Liu, *Physical Chemistry Chemical Physics*, 2019, **21**, 19252–19268.

(109) A. E. Reed, F. Weinhold, L. A. Curtiss and D. J. Pochatko, *Journal of Chemical Physics*, 1986, **84**, 5687–5703.

(110) M. J. Hussey and A. J. Murray, *Journal of Physics B: Atomic, Molecular and Optical Physics*, 2005, **38**, 2965–2977.

(111) N. J. Brown, A. Garca-Trenco, J. Weiner, E. R. White, M. Allinson, Y. Chen, P. P. Wells, E. K. Gibson, K. Hellgardt, M. S. Shaffer and C. K. Williams, *ACS Catalysis*, 2015, **5**, 2895–2902.

(112) N. W. Kinzel, C. Werl and W. Leitner, *Angewandte Chemie - International Edition*, 2021, **60**, 11628–11686.

(113) N. Hazari, N. Iwasawa and K. H. Hopmann, *Organometallics*, 2020, **39**, 1457–1460.

(114) D. H. Apaydin, S. Schlager, E. Portenkirchner and N. S. Sariciftci, *ChemPhysChem*, 2017, **18**, 3094–3116.

(115) C. Sun, L. Rotundo, C. Garino, L. Nencini, S. S. Yoon, R. Gobetto and C. Nervi, *ChemPhysChem*, 2017, **18**, 3219–3229.

(116) J. C. Calabrese, T Herskovitz and J. B. Kinney, *Journal of the American Chemical Society*, 1983, **105**, 5914–5915.

(117) M Aresta, G Forti, H Tanaka, H Nagao, S. M. Peng, K Tanaka, S Gambarotta, C Floriani, A Chiesi-Villa, C Guastini, J. C. Calabrese, T Herskovitz, J. B. Kinney, G. S. Bristow, P. B. Hitchcock, M. F. Lappert, D. H. Gibson, M Ye, J. F. Richardson, F Arena, P. F. Zanazzi, F Ozawa, T Ito, Y Nakamura and A. J. Yamamoto, *Organometallics*, 1994, **13**, 407–409.

(118) D. H. Gibson, M. Ye and J. F. Richardson, *Journal of the American Chemical Society*, 1992, **114**, 9716–9717.

(119) J.-C. Tsai, M. Khan and K. M. Nicholas, *Organometallics*, 1989, **8**, 2967–2968.

(120) M. Aresta, F. C. Nobile, A. G. Vincenzo, F. Elisabetta and M. Mario, *Journal of the Chemical Society, Chemical Communications*, 1975, **8**, 636–637.

(121) A Dohring, P. W. Jolly, C Kruger and M. J. Romao, *Zeitschrift fur Naturforschung B*, 1985, **40**, 484–488.

(122) J. Yang, B. R. NGuessan, A. Dedieu, D. C. Grills, X.-Z. Sun and M. W. George, *Organometallics*, 2009, **28**, 3113–3122.

(123) Z. H. Kafafl, R. H. Hauge, L. Fredln and J. L. Margrave, *Journal of Physical Chemistry*, 1983, **87**, 797–800.

(124) Z. H. Kafafi, R. H. Hauge, W. E. Billups and J. L. Margrave, *Inorganic Chemistry*, 1984, **23**, 177–183.

(125) K. O. Hartman and I. C. Hisatsune, *Journal of Physical Chemistry*, 1966, **44**, 1920.

(126) L. Mino, G. Spoto and A. M. Ferrari, *The Journal of Physical Chemistry*, 2014, **118**, 25016–25026.

(127) J. Ye, C. Liu and Q. Ge, *The Journal of Physical Chemistry*, 2012, **116**, 7817–7825.

(128) M. J. Ajitha and C. H. Suresh, *The Journal of Organic Chemistry*, 2012, **77**, 1087–1094.

(129) H. Chen, Y. Guo, Y. Du, X. Xu, C. Su, Z. Zeng and L. Li, *Chemical Engineering Journal*, 2021, **415**, 128824–128838.

(130) T. Davran-Candan, *The Journal of Physical Chemistry*, 2014, **118**, 4582–4590.

(131) J. G. Shim, J. H. Kim, Y. H. Jhon, J. Kim and K. H. Cho, *Industral Engineering Chemistry Research*, 2009, **48**, 2172–2178.

(132) W. Guo, C. Michel, R. Schwiedernoch, R. Wischert, X. Xu and P. Sautet, *Organometallics*, 2014, **33**, 6369–6380.

(133) S. Lin and Z. Lin, *Organometallics*, 2019, **38**, 240–247.

(134) J. Mascetti, F. Galan and I. Pa, *Coordination Chemistry Reviews*, 1999, **190**, 557–576.

(135) M. Deepan, S. Sunny and M. Jaccob, *Journal of CO2 Utilization*, 2022, **57**, 101872–101881.

(136) Q. Ren, N. Wu, Y. Cai and J. Fang, *Organometallics*, 2016, **35**, 3932–3938.

(137) L. Dang, Z. Lin and T. B. Marder, *Organometallics*, 2010, **29**, 917–927.

(138) A. A. Sarantou, *Dalton Transactions*, 2021, **50**, 14797–14809.

(139) J. Agarwal, R. P. Johnson and G. Li, *The Journal of Physical Chemistry*, 2011, **115**, 2877–2881.

(140) S. Sakai, K. Kitaura and K. Morokuma, *Inorganic Chemistry*, 1982, **21**, 760–765.

(141) U. Pidun and G. Frenking, *Organometallics*, 1995, **14**, 5325–5336.

(142) X. Wu, Z. Liu, T. S. Murphy, X. Z. Sun, M. W. D. Hanson-Heine, M. Towrie, J. N. Harvey and M. W. George, *Faraday Discussions*, 2019, **220**, 86–105.

(143) T. F. Wang, C. C. Hwu, C. W. Tsai and K. J. Lin, *Organometallics*, 1997, **16**, 3089–3090.

(144) H. Yang, M. C. Asplund, K. T. Kotz, M. J. Wilkens, H. Frei, C. B. Harris and K. M. Smith, *Journal of the American Chemical Society*, 1998, **120**, 10154–10165.

(145) G. I. Childs, D. C. Grills, X. Z. Sun and M. W. George, *Pure and Applied Chemistry*, 2001, **73**, 443–447.

(146) C. Kutal, M. A. Weber, G. Ferraudi and D. Geiger, *Organometallics*, 1985, **4**, 2161–2166.

(147) C. Kutal, A. J. Corbin and G. Ferraudi, *Organometallics*, 1987, **6**, 553–557.

(148) J. Hawecker, J.. Lehn and R. Ziessel, *Helvetica Chimica Acta*, 1986, **69**, 1990–2012.

(149) F. Gugan, V. Tognetti, L. Joubert, H. Chermette, D. Luneau and C. Morell, *Physical Chemistry Chemical Physics*, 2015, **18**, 982–990.

(150) B. J. Coe and S. J. Glenwright, *Coordination Chemistry Reviews*, 2000, **203**, 5–80.

(151) M. S. Kablaoui, *Journal of the Chemical Society, Dalton Transactions*, 1974, **39**, 3696–3698.

(152) T. Scheiring, A. Klein and W. Kaim, *Journal of the Chemical Society. Perkin Transactions 2*, 1997, 2569–2571.

(153) S. Sato, Y. Matubara, K. Koike, M. Falkenstrm, T. Katayama, Y. Ishibashi, H. Miyasaka, S. Taniguchi, H. Chosrowjan, N. Mataga, N. Fukazawa, S. Koshihara, K. Onda and O. Ishitani, *Chemistry - A European Journal*, 2012, **18**, 15722–15734.

(154) M. K. Kuimova, W. Z. Alsindi, A. J. Blake, E. S. Davies, D. J. Lampus, P. Matousek, J. McMaster, A. W. Parker, M. Towrie, X. Z. Sun, C. Wilson and M. W. George, *Inorganic Chemistry*, 2008, **47**, 9857–9869.

(155) K. A. Walters, K. D. Ley, C. S. Cavalaheiro, S. E. Miller, D. Gosztola, M. R. Wasielewski, A. P. Bussandri, H. V. Willigen and K. S. Schanze, *Journal of the American Chemical Society*, 2001, **123**, 8329–8342.

(156) J. R. Shaw and R. H. Schmehl, *Journal of the American Chemical Society*, 1991, **113**, 389–394.

(157) S. L. L. Yoon and K. Y. Wong, *Journal of the Chemical Society, Chemical Communications*, 1984, **3**, 328–333.

(158) J. Hawecker, J.-M. Lehn and R. Ziessel, *Journal of the Chemical Society, Chemical Communications*, 1983, **286**, 536–538.

(159) A. E. Friedman, J. K. Barton, J. C. Chambron, J. P. Sauvage, N. J. Turro and J. K. Barton, *Journal of the American Chemical Society*, 1990, **112**, 4960–4962.

(160) A. S. Polo, M. K. Itokazu and I. N. Y. Murakami, *Coordination Chemistry Reviews*, 2004, **248**, 1343–1361.

(161) D. M. P. Mingos and V. W. W. Yam, *Photofunctional Transition Metal Complexes*, Springer, 2007.

(162) X. Wu, *University of Nottingham Thesis*, 2020.

(163) H. Takeda, K. Koike, H. Inoue and O. Ishitani, *Journal of the American Chemical Society*, 2008, **130**, 2023–2031.

(164) K. A. Grice, N. X. Gu, M. D. Sampson and C. P. Kubiak, *Dalton Transactions*, 2013, **42**, 8498–8504.

(165) A. J. Morris, G. J. Meyer and E. Fujita, *Accounts of Chemical Research*, 2009, **42**, 1983–1994.

(166) S. Bernhard, K. M. Omberg, G. F. Strouse and J. R. Schoonover, *Inorganic Chemistry*, 2000, **39**, 3107–3110.

(167) R. J. Shaver and D. P. Rillema, *Inorganic Chemistry*, 1992, **31**, 4101–4107.

(168) J. Peach and J. Eastoe, *Beilstein Journal of Organic Chemistry*, 2014, **10**, 1878–1895.

(169) H. M. Yau, A. I. McKay, H. Hesse, R. Xu, M. He, C. E. Holt and G. E. Ball, *Journal of the American Chemical Society*, 2016, **138**, 281–288.

(170) J. D. Holbrey and K. R. Seddon, *Clean Products and Processes*, 1999, **1**, 223–236.

(171) Z. Lei, B. Chen, Y. M. Koo and D. R. Macfarlane, *Chemical Reviews*, 2017, **117**, 6633–6635.

(172) R. Hayes, S. Imberti, G. G. Warr and R. Atkin, *Angewandte Chemie*, 2013, **125**, 4721–4725.

(173) P. A. Hunt, C. R. Ashworth and R. P. Matthews, *Chemical Society Reviews*, 2015, **44**, 1257–1288.

(174) V. A. Cocalia, K. E. Gutowski and R. D. Rogers, *Coordination Chemistry Reviews*, 2006, **250**, 755–764.

(175) R. Feng, D. Zhao and Y. Guo, *Journal of Environmental Protection*, 2010, **1**, 95–104.

(176) J. Dupont and J. D. Scholten, *Chemical Society Reviews*, 2010, **39**, 1780–1804.

(177) R. Ge, C. Hardacre, P. Nancarrow and D. W. Rooney, *Journal of Chemical and Engineering Data*, 2007, **52**, 1819–1823.

(178) J. D. Scholten, B. C. Leal and J. Dupont, *ACS Catalysis*, 2012, **2**, 184–200.

(179) J. P. Hallett and T. Welton, *Chemical Reviews*, 2011, **111**, 3508–3576.

(180) N. Yan, C. Xiao and Y. Kou, *Coordination Chemistry Reviews*, 2010, **254**, 1179–1218.

(181) K. L. Luska and A. Moores, *ChemCatChem*, 2012, **4**, 1534–1546.

(182) W. Dai, S. B. Kim, R. D. Pike, C. L. Cahill and D. A. Sweigart, *Organometallics*, 2010, **29**, 5173–5178.

(183) I. Krossing, *Chemistry - A European Journal*, 2001, **7**, 490–502.

(184) L. E. Harrington, J. F. Britten, K. Nikitin and M. J. McGlinchey, *ChemPlusChem*, 2017, **82**, 433–441.

(185) B. L. Bennett, K. A. Robins, R. Tennant, K. Elwell, F. Ferri, I. Bashta and G. Aguinaldo, *Journal of Fluorine Chemistry*, 2006, **127**, 140–145.

(186) C. Otero, A. Carreo, R. Polanco, F. M. Llancalahuen, R. Arratia-Prez, M. Gacita and J. A. Fuentes, *Frontiers in Chemistry*, 2019, **7**, 1–12.

(187) S. E. Goff, T. F. Nolan, M. W. George and M. Poliakoff, *Organometallics*, 1998, **17**, 2730–2737.

(188) A. I. Cooper, S. G. Kazarian and M. Poliakoff, *Chemical Physics Letters*, 1993, **206**, 175–180.

(189) M. J. Clarke, A. I. Cooper, S. M. Howdle and M. Poliakoff, *Journal of the American Chemical Society*, 2000, **122**, 2523–2531.

(190) M. Basire, F. Mouhat, G. Fraux, A. Bordage, J. L. Hazemann, M. Louvel, R. Spezia, S. Bonella and R. Vuilleumier, *Journal of Chemical Physics*, 2017, **146**, 134102–134114.

(191) W. A. King, X. L. Luo, B. L. Scott, G. J. Kubas and K. W. Zilm, *Journal of the American Chemical Society*, 1996, **118**, 6782–6783.

(192) R. K. Blundell and P. Licence, *Physical Chemistry Chemical Physics*, 2014, **16**, 15278–15288.

(193) P. J. Dyson, *Applied Organometallic Chemistry*, 2002, **16**, 495–500.

(194) K. E. A. Reynolds, *University of Nottingham Thesis*, 2019.

(195) J. D. Watson, L. D. Field and G. E. Ball, *Nature Chemistry*, 2022, **14**, 801–804.

(196) K. L. Schuchardt, B. T. Didier, T. Elsethagen, L. Sun, V. Gurumoorthi, J. Chase, J. Li and T. L. Windus, *Journal of Chemical Information and Modeling*, 2007, **47**, 1045–1052.

(197) Y. Shao, Z. Gan, E. Epifanovsky, A. T. Gilbert, M. Wormit, J. Kussmann, A. W. Lange, A. Behn, J. Deng, X. Feng, D. Ghosh, M. Goldey, P. R. Horn, L. D. Jacobson, I. Kaliman, R. Z. Khaliullin, T. Kuss, A. Landau, J. Liu, E. I. Proynov, Y. M. Rhee, R. M. Richard, M. A. Rohrdanz, R. P. Steele, E. J. Sundstrom, H. L. Woodcock, P. M. Zimmerman, D. Zuev, B. Albrecht, E. Alguire, B. Austin, G. J. Beran, Y. A. Bernard, E. Berquist, K. Brandhorst, K. B. Bravaya, S. T. Brown, D. Casanova, C. M. Chang, Y. Chen, S. H. Chien, K. D. Closser, D. L. Crittenden, M. Diedenhofen, R. A. Distasio, H. Do, A. D. Dutoi, R. G. Edgar, S. Fatehi, L. Fusti-Molnar, A. Ghysels, A. Golubeva-Zadorozhnaya, J. Gomes, M. W. Hanson-Heine, P. H. Harbach, A. W. Hauser, E. G. Hohenstein, Z. C. Holden, T. C. Jagau, H. Ji, B. Kaduk, K. Khistyaev, J. Kim, J. Kim, R. A. King, P. Klunzinger, D. Kosenkov, T. Kowalczyk, C. M. Krauter, K. U. Lao, A. D. Laurent, K. V. Lawler, S. V. Levchenko, C. Y. Lin, F.

Liu, E. Livshits, R. C. Lochan, A. Luenser, P. Manohar, S. F. Manzer, S. P. Mao, N. Mardirossian, A. V. Marenich, S. A. Maurer, N. J. Mayhall, E. Neuscamman, C. M. Oana, R. Olivares-Amaya, D. P. Oneill, J. A. Parkhill, T. M. Perrine, R. Peverati, A. Prociuk, D. R. Rehn, E. Rosta, N. J. Russ, S. M. Sharada, S. Sharma, D. W. Small, A. Sodt, T. Stein, D. Stuck, Y. C. Su, A. J. Thom, T. Tsuchimochi, V. Vanovschi, L. Vogt, O. Vydrov, T. Wang, M. A. Watson, J. Wenzel, A. White, C. F. Williams, J. Yang, S. Yeganeh, S. R. Yost, Z. Q. You, I. Y. Zhang, X. Zhang, Y. Zhao, B. R. Brooks, G. K. Chan, D. M. Chipman, C. J. Cramer, W. A. Goddard, M. S. Gordon, W. J. Hehre, A. Klamt, H. F. Schaefer, M. W. Schmidt, C. D. Sherrill, D. G. Truhlar, A. Warshel, X. Xu, A. Aspuru-Guzik, R. Baer, A. T. Bell, N. A. Besley, J. D. Chai, A. Dreuw, B. D. Dunietz, T. R. Furlani, S. R. Gwaltney, C. P. Hsu, Y. Jung, J. Kong, D. S. Lambrecht, W. Liang, C. Ochsenfeld, V. A. Rassolov, L. V. Slipchenko, J. E. Subotnik, T. V. Voorhis, J. M. Herbert, A. I. Krylov, P. M. Gill and M. Head-Gordon, *Molecular Physics*, 2015, **113**, 184–215.

(198) G. T. E. Velde, F. M. Bickelhaupt, E. J. Baerends, C. F. Guerra and S. J. A. V. A. N. Gisbergen, *Journal of Computational Chemistry*, 2001, **22**, 931–967.